Fundamental studies of diamond chemical vapour deposition: Plasma diagnostics and computer modelling.

James C. Richley

A dissertation submitted to the University of Bristol in accordance with the requirements for the award of the degree of Doctor of Philosophy in the Faculty of Science.

School of Chemistry

Abstract

This thesis reports experimental studies of the gas-phase chemistry within microwave plasma enhanced (MWPE) reactors used for the chemical vapour deposition (CVD) of diamond, as well as computational investigations into gas-surface and surface based chemical reactions which are likely to play a role in the growth and morphology of diamond films.

A combination of cavity ring down spectroscopy (CRDS) and optical emission spectroscopy (OES) has been applied to study $CH_4/H_2/Ar$ plasmas which contain a high proportion of Ar ($\approx$86.8%). Column densities were successfully measured for C_2(a) and CH(X) radicals, and for H(n=2) atoms as a function of height above the substrate, and for a range of process conditions (power, pressure, flow rates, *etc.*). Addition of Ar was found to have a large effect on the plasma's capacity to absorb the microwave power, which in turn resulted into a substantial increase in the plasma volume. Variation of the Ar fraction within the input gas mixture was found to have little effect on the average rotational temperatures derived from C_2(a) absorption, however.

CRDS has also been applied to study B atoms within $B_2H_6/H_2/Ar$ and $B_2H_6/CH_4/H_2/Ar$ plasmas. Column densities as a function of process conditions as well as their spatial profile were successfully measured. B atoms were found to be extensively distributed throughout the reactor volume spanning much wider regions than species like CH and C_2 radicals.

Electronically excited species within $CO_2/CH_4/H_2$ plasmas have been studied using OES. Spatial distributions of their emissions, as well as changes as a result of process conditions, have been measured. Preliminary CRDS measurements of C_2(a) and CH(X) column densities in these plasmas are also presented.

Quantum mechanical (QM) and Quantum mechanical/Molecular mechanical (QM/MM) studies have explored insertion reactions of C_xH_y (x=0-3, y=0-2), B atoms and BH radicals directly into C-H and C-C bonds on the diamond surface. Insertion of several of these species into C-H bonds on the diamond surface was found to be energetically feasible at typical growth temperatures. Such insertion reactions may play a role in diamond growth and/or doping, and serve to complement more traditional growth mechanisms, based on radical addition to surface radical sites. QM/MM studies have also explored the migration of CH_2 and BH groups on and between the reconstructed 2×1 $\{100\}$ and $\{111\}$ H-terminated surfaces.

Acknowledgement

I would like to thank my supervisor, Professor Mike Ashfold, for all his invaluable help and encouragement throughout my PhD, and I would like to thank Professor Jeremy Harvey for all his help and patience, in assisting me with the computational work. Also I would like to give special thanks to Dr Jie Ma for teaching me how to use CRDS and the microwave reactor and, to Dr Andy Cheesman for teaching me how to perform QM and QM/MM calculations. In addition I would like to thank Dr Oliver Fox, Mr. Mark Kelly, Mr. Ben Truscott, Dr James Smith and Mr. Keith Rosser for their many helpful discussions and assistance with experimental work and would like to thank Dr Yuri Mankelevich for his valuable advice and discussion. I wish to thank Element Six Ltd. for financial support and for loan of the microwave reactor.

Declaration

I declare that the work in this dissertation was carried out in accordance with the requirements of the University's Regulations and Code of Practice for Research Degree Programmes and that it has not been submitted for any other academic award. Except where indicated by specific reference in the text, the work is the candidate's own work. Work done in collaboration with, or with the assistances of, others, is indicated as such. Any view expressed in the dissertation are those of the author.

SIGNED: _____ DATE: _____

Contents

1 Introduction **1**
1.1 Diamond: Structure, Properties and potential uses . . . 1
1.2 Synthesis of diamond . . . 2
1.2.1 Chemical vapour deposition of diamond . . . 3
1.2.2 Chemical vapour deposition techniques . . . 4
1.2.2.1 Hot Filament CVD . . . 4
1.2.2.2 Microwave plasma enhanced CVD . . . 5
1.2.3 Gas-phase chemistry . . . 6
1.2.4 Surface chemistry . . . 8
1.2.4.1 $\{100\}$ surface . . . 9
1.2.4.2 $\{111\}$ surface . . . 13
1.2.4.3 $\{110\}$ surface . . . 14
1.2.4.4 β-Scission . . . 16
1.2.4.5 Surface migration . . . 16
1.3 Doping of diamond films . . . 19
1.3.1 p-type doping . . . 19
1.3.2 n-type doping . . . 19
1.4 Plasma modelling . . . 20
1.4.1 Bristol-Moscow model . . . 20
1.5 Aims . . . 23
References . . . 24

2 Computational methods, background spectroscopy, and experimental techniques **29**
2.1 Computational techniques . . . 29
2.1.1 The Schrödinger equation and the Hartree-Fock approximation . . . 30
2.1.2 Density functional theory . . . 32
2.1.3 Molecular mechanics . . . 37
2.1.4 QM/MM calculations . . . 40
2.1.5 Transition state theory . . . 41
2.2 Spectroscopy background . . . 42
2.2.1 Atomic and Molecular spectra . . . 42
2.2.1.1 Atomic Spectra . . . 43
2.2.1.2 Molecular Spectra . . . 46
2.2.1.3 Line intensity . . . 50
2.3 Experimental Techniques . . . 52
2.3.1 Lasers . . . 52
2.3.1.1 Nd:YAG laser . . . 53
2.3.1.2 Dye Lasers . . . 54
2.3.2 Spectroscopic methods . . . 54
2.3.2.1 Optical emission spectroscopy . . . 54

2.3.2.2 Absorption spectroscopy . . . 55
2.3.2.3 Cavity ring-down spectroscopy . . . 55
References . . . 57

3 Diagnostics of Ar-rich $CH_4/H_2/Ar$ plasmas **59**
3.1 Introduction . . . 59
3.2 Experimental . . . 60
3.3 Results and discussion . . . 63
3.3.1 Cavity ring down spectra of C_2(a), CH(X) and H(n=2) . . . 64
3.3.2 Column density calculations . . . 68
3.3.3 Column density measurements . . . 70
3.3.4 Optical emission measurements . . . 75
3.3.5 Results from plasma modelling . . . 80
3.3.6 Conclusions . . . 81
References . . . 83

4 Diagnostics of boron containing plasmas **85**
4.1 Introduction . . . 85
4.2 Experimental . . . 86
4.3 Results and discussion . . . 87
4.3.1 Typical B atom spectrum . . . 87
4.3.2 B atom profile . . . 89
4.3.3 Effect of process conditions . . . 90
4.4 Conclusions . . . 97
References . . . 97

5 OES and CRDS diagnostics of $CO_2/CH_4/H_2$ plasmas. **99**
5.1 Introduction . . . 99
5.2 Experimental . . . 100
5.3 Results and discussion . . . 101
5.4 Conclusion . . . 115
References . . . 115

6 Insertion reactions of C_xH_y species. **117**
6.1 Introduction . . . 117
6.2 Computational Method . . . 118
6.3 Results . . . 122
6.3.1 C(^{3}P) Atoms . . . 122
6.3.2 CH ($X^2\Pi$) radicals . . . 124
6.3.3 CH_2 . . . 126
6.3.4 C_2 . . . 128
6.3.5 C_3 . . . 128
6.3.6 Discussion . . . 129
6.3.7 Conclusions . . . 132
References . . . 133

7 Migration of CH_2 on and between diamond surfaces **135**
7.1 Introduction . . . 135
7.2 Computational Methods . . . 137
7.3 Results and discussion . . . 138
7.3.1 Migration on the {111} surface . . . 139

7.3.2 Migration between different surfaces . . . 140
7.3.2.1 Convex step edge . . . 141
7.3.2.2 Concave step edge . . . 143
7.3.3 Conclusions . . . 145
References . . . 145

8 Insertion of BH radicals and B atoms, and migration of BH radicals on diamond 147
8.1 Introduction . . . 147
8.2 Computational detail . . . 149
8.3 Results and discussion . . . 150
8.3.1 B and BH insertion . . . 150
8.3.1.1 C-H bonds . . . 150
8.3.1.2 C-C bonds . . . 153
8.3.1.3 Implications for CVD growth of boron doped diamonds . . . 154
8.3.2 BH surface migration . . . 155
8.3.2.1 C$\{100\}$:H 2×1 surface . . . 155
8.3.2.2 C$\{111\}$:H surface . . . 157
8.3.2.3 Migration at the step edge . . . 158
8.3.2.4 BH *vs.* CH_2 migration . . . 163
References . . . 163

9 Overview 165

A Important reactions in the Bristol-Moscow plasma model 169

B Constants for CRDS 171

C Calculated rates of C(^{3}P) and CH($X^2\Pi$) insertion into C-H bonds. 173

List of Figures

1.1 Illustrations of a) the unit cell of diamond, and b) three layers of graphite. 2

1.2 Phase diagram of elemental carbon from reference[11], highlighting the areas under which CVD and HPHT synthesis of diamond takes place. 3

1.3 Schematic of a typical HFCVD reactor. 4

1.4 Schematic of a typical MWPECVD reactor. 5

1.5 Illustration of a portion of the H-shifting reactions which occur within the gas phase of a CVD diamond reactor. The blue arrow indicates the trend of the H-shifting reactions in the cool region of the reactor, whilst the red arrow shows the trend of the reactions within the hot region. 7

1.6 Spatial profiles of C_2(a, v=0), CH(X, v=0) radicals and H(n=2) atoms within a MW-PECVD reactor. The red line and symbols show column densities when the hydrocarbon source gas was C_2H_2 whilst the black line shows column densities measured when the source gas was CH_4. Reactor parameters: Microwave Power = 1.5 kW, Pressure = 150 Torr, F(Ar) = 40 sccm, for CH_4 measurements, $F(H_2)$ = 500 sccm and $F(CH_4)$ = 25 sccm, for C_2H_2 measurements $F(H_2)$ = 512.5 sccm and $F(C_2H_2)$ = 12.5 sccm. Figure reproduced from Ma *et al.*[16] 8

1.7 A simple version of the Bachmann triangle, showing the diamond growth region, as well as the areas where no growth and non-diamond growth occurs. Figure adapted from reference 4. 9

1.8 a) An illustration of the H-terminated $\{100\}$ diamond surface with the 2×1 reconstruction. A dimer bond, a trough between dimer bonds, a dimer row (blue) and a dimer chain (red) on the surface are highlighted. b) Scanning tunnelling microscope image showing the 2×1 reconstruction on the $\{100\}$ surface. From reference 29. . . 11

1.9 Illustration of structures on the C$\{100\}$:H 2×1 surface involved in the a) the trough and b) the dimer mechanisms for the incorporation of a gaseous CH_3 group. Energetics and diagrams are from Cheesman *et al.*[34] and the former are in kJ mol^{-1}. 12

1.10 Mechanism proposed by Skokov *et al.* for the incorporation of acetylene at diradical sites on the C$\{100\}$:H 2×1 surface of diamond. Figure reproduced from reference 35. 13

1.11 a portion of the H-terminated $\{111\}$ diamond surface. 14

1.12 A portion of the $\{110\}$ surface. 15

1.13 $\{110\}$ growth mechanisms for both CH_3 and C_2H_4 from reference 27. 15

1.14 An illustration of two different β-scission pathways where attack by gaseous H atoms results in the removal of long hydrocarbon (C_xH_y, $x \geq 2$) chains from the surface. Figure from reference 27. 16

1.15 Energy profiles for a) migration along dimer chains and b) migration along dimer rows on the $\{100\}$:H 2×1 surface. Energies are in kJ mol^{-1} and are relative to the starting structures 1 and 6 for the migration along the chains and rows, respectively. Figure adapted from Cheesman *et al.*[34] 18

1.16 2D(r,z) plots of the calculated gas temperatures, T_{gas} (K) and H atom mole fraction (%), (left and right respectively) from the plasma model. The red colouring highlights regions of high temperature and high H atom mole fractions, whilst the pale yellow region denotes lower temperatures and H atom mole fractions. This figure is reproduced from reference 53. 22
1.17 2D(r,z) plots of the calculated C_2H_2 and CH_4 mole fractions, (left and right respectively) from the plasma model. The red colouring highlights regions with the highest mole fractions, whilst the pale yellow region denotes regions with a lower mole fraction . This figure is reproduced from reference 53. 23

2.1 A simplified illustration of a potential energy surface along the reaction coordinate. . 30
2.2 An illustration of the torsion (dihedral) angle ω between four atoms. 38
2.3 Illustration of the hydrogen atoms energy levels and a selection of lines from the Lyman and Balmer series. 45
2.4 The fine structure of the Hydrogen Balmer alpha absorption resulting from spin-orbit coupling and the selection rules. 46
2.5 Illustration of the spacing of electronic, vibration and rotational levels in a molecule . 47
2.6 The three different ways in which electromagnetic radiation can interact with two different energy levels (i and j) 51
2.7 Illustration of processes within a four level laser scheme 53
2.8 A diagram of a typical CRDS experimental setup 56

3.1 Cross section of the microwave CVD reactor and CRDS set-up used in the current investigations. 61
3.2 Photograph of the MWPECVD reactor used for cavity ring-down spectroscopy. The aperture used for OES can be seen in the foreground. 62
3.3 Images of the plasma ball seen through the front port of a MWPECVD reactor with differing $X_0(H_2)$, a) 92%, b) 36.9% and c) 9.2%. Other reactor conditions are kept constant, p=150 Torr, P=1.0 kW, $X_0(CH_4)$=0.5% and the balance in the gas mixture is made up using Ar. Pictures taken by O.J.L Fox. 64
3.4 Measured substrate temperatures and the temperature change (between input and output) of the cooling water flowing (at 1 l min^{-1}) through the base (ΔT_{base}) and side walls (ΔT_{wall}) of the MWPECVD reactor as a function of $X_0(H_2)$, other reactor parameters are; P=1.0 kW, p=150 Torr, $X_0(CH_4)$ = 0.5% and Ar as balance. 65
3.5 Typical spectra obtained for a) a portion of the C_2 ($d^3\Pi_g \leftarrow a^3\Pi_u$) (0,0) transition, b) a portion of the CH ($A^2\Delta \leftarrow X^2\Pi$) (0,0) transition and c) the H ($n = 3 \leftarrow n = 2$) transition. 66
3.6 CRDS spectra of a portion of the $C_2(d^3\pi_g \leftarrow a^3\Pi_u)$ (0,0) band measured for a) typical MCD growth conditions (H_2-rich, 4.4% CH_4 / 88.6% H_2 / 7% Ar, p = 150 Torr, P= 1.5 kW), b) base conditions in our present experiments (0.5%CH_4 /14.7%H_2 / 84.8%Ar, p = 150 Torr, P= 1.0 kW) and c) UNCD type growth conditions (0.5%CH_4 / 1%H_2 / 98.5%Ar, p = 150 Torr, P= 0.5 kW). The upper and low traces are PGOPHER simulations of the relevant portion of the transition assuming T_{rot} = 3000 and 2000 K, respectively. 67
3.7 Measured and calculated (filled and open symbols respectively) C_2(a, v=0), CH(X, v=0) and H(n=2) column densities as a function of z for the base conditions (0.5% CH_4/ 14.7% H_2/ 84.8% Ar p=150 Torr, P=1.0 kW). Also included for comparison are column densities of C_2(a, v=0), CH(X, v=0) and H(n=2) measured for typical MCD type growth conditions (4.4% CH_4/ 88.6% H_2/ 7% Ar, p=150 Torr, P=1.5 kW, from ref 12) 71

3.8 Measured and calculated (filled and open symbols, respectively) column densities of C_2(a, v=0), CH(X, v=0) and H(n=2) as a function of a) $X_0(H_2)$ and b) $X_0(CH_4)$ at a fixed height (z=9.5 mm) above the substrate. F_{Total} is kept at a constant by adjusting X_0(Ar) to compensate for adjustments in $X_0(H_2)$ and $X_0(CH_4)$. 73

3.9 Measured and calculated (filled and open symbols, respectively) column densities of C_2(a, v=0), CH(X, v=0) and H(n=2) as a function of a) pressure and b) applied microwave power at a fixed height (z=9.5 mm) above the substrate. 74

3.10 A typical emission spectra recorded at base conditions. Emissions associated with C_2(d→a), C_3(A→X) and CH(A→X) radicals as well as those of H(n=3→2) and H(n=4→2) atoms are highlighted. 76

3.11 Normalized relative H_α, H_β, C_2(d→a), CH(A→X) and C_3(A→X) emission intensities plotted as a function of a) $X_0(H_2)$ and b) $X_0(CH_4)$. As with CRDS measurements F_{Total} was kept constant by compensating any change in $X_0(H_2)$ or $X_0(CH_4)$ with Ar. 77

3.12 Normalized relative H_α, H_β, C_2(d→a), CH(A→X) and C_3(A→X) emission intensities plotted as a function of a) total pressure and b) applied microwave power. 78

3.13 Spatial profiles of the emission intensities of the C_2(d→a) and H_α transitions, when $X_0(H_2)$ is 1% and 15%, with P=0.5 kW and 1.0 kW, respectively, p=150 Torr and $X_0(CH_4)$=0.5%. 79

3.14 Variation of the average power density, Q, average electron temperature, T_e and [H]/[H_2] ratio as a function of $X_0(H_2)$ within the central hot region of the plasma (r=0, $z = z_C$ where z_C is the central region of the plasma, and z=0 is the location of the substrate). The points at 1, 14.7 and 25% $X_0(H_2)$ are all calculated with $X_0(CH_4)$=0.5%, a value of 4.4% is used when $X_0(H_2)$=88.6%. Q was estimated from the relationship $Q = \frac{P}{V}$, where V is the plasma volume. 80

3.15 2D(r, z) model distributions of CH_3 (left) and C_2(a) (right) number densities for the present base conditions. The vertical z and radial r dimension used when simulating the reactor were both 6 cm. 82

4.1 a) Typical CRD spectrum of the B($3^2S_{1/2}$←$2^2P_{1/2}$) and B($3^2S_{1/2}$←$2^2P_{3/2}$) transitions. b) Grotrian diagram illustrating the relevant energy levels of B atoms, and the two transitions. 88

4.2 Measured B($2^2P_{3/2}$) and ^{11}BH(X, v=0) column densities (blue circles and purple squares respectively) under base conditions for B_2H_6/H_2/Ar and B_2H_6/CH_4/H_2/Ar plasmas (filled and open symbols respectively) as a function of z. 90

4.3 Measured B($2^2P_{3/2}$) and ^{11}BH(X, v=0) column densities (blue circles and purple squares respectively) under base conditions for B_2H_6/H_2/Ar and B_2H_6/CH_4/H_2/Ar plasmas (filled and open symbols respectively) as a function of a) B_2H_6 flow rate and b) Ar flow rate. Red circles are measured B($2^2P_{1/2}$) column densities multiplied by a factor of two. 91

4.4 Measured B($2^2P_{3/2}$) and ^{11}BH(X, v=0) column densities (blue circles and purple squares respectively) under base conditions for B_2H_6/H_2/Ar and B_2H_6/CH_4/H_2/Ar plasmas (filled and open symbols respectively) as a function of a) applied microwave power and b) total pressure. 93

4.5 Measured B($2^2P_{3/2}$) and ^{11}BH(X, v=0) column densities (blue circles and purple squares respectively) under base conditions for B_2H_6/CH_4/H_2/Ar plasmas as a function of CH_4 flow rate. 94

5.1 A simplified version of the Bachmann triangle,[7] showing the diamond growth region, as well as the areas where no growth and non-carbon growth occurs. Also shown are the location of the current base conditions (red dot) and the direction traversed by varying the H_2 fraction or CO_2/CH_4 ratio. 100

5.2 Cross section of the MWPECVD reactor and the OES setup used in the current investigations. 102

5.3 OES spectrum showing the spectral features observed in a $CO_2/CH_4/H_2$ plasma operating at base conditions (this is constructed by combining two separate spectra due to the limited wavelength range ($\approx$ 300 nm) which can be captured before the grating requires adjustment). Emission from excited C_3(A) is not observed at base conditions but the feature becomes increasingly evident when CH_4 is in excess of CO_2. 103

5.4 a) Normalised emission intensities of the H_α, H_β, C_2(d-a), CH(A-X), C_3(A-X), CO(B-A) and OH(A-X) transitions and b) Column densities of C_2(a, v=0) and CH(X, v=0) at base conditions, as a function of height above the substrate, z. 105

5.5 a) Normalised emission intensities of the H_α, H_β, C_2(d$\rightarrow$a), CH(A$\rightarrow$X), C_3(A$\rightarrow$X), CO(B$\rightarrow$A) and OH(A$\rightarrow$X) transitions and b) C_2(a, v=0) and CH(X, v=0) column densities, z=10 mm, at a function of R, where R = $X_0(CH_4)/(X_0(CO_2) + X_0(CH_4))$. Other discharge parameters were kept fixed as their base values as R was varied. . . 106

5.6 Normalised emission intensities of the C_2(d$\rightarrow$a), CH(A$\rightarrow$X), C_3(A$\rightarrow$X), CO(B$\rightarrow$A), H_α, H_β, and OH(A$\rightarrow$X) transitions as a function of height above the substrate when: a) $R \approx 0.43$ and b) $R \approx 0.57$. Emission from OH(A) is not observed when $R \approx 0.57$ and C_3(A) is not observed when $R \approx 0.43$. 107

5.7 Effect of varying $X_0(H_2)$ on a) emission from C_2(d), CH(A), CO(B), OH(A), H(n=3) and H(n=4) species and b) column densities of C_2(a, v=0) and CH(X, v=0) at z=10 mm. C_2(a, v=0) column densities were obtained at R = 0.51. F_{CH_4} and F_{CO_2} are varied to keep F_{Total} and the $X_0(CH_4)$:$X_0(CO_2)$ ratio constant. 109

5.8 Normalised emission intensities of a) C_2(d$\rightarrow$a), b) H_α and H_β, c) CH(A$\rightarrow$X), d) CO(B$\rightarrow$A) and e) OH(A$\rightarrow$X) as a function of z when $X_0(H_2)$ = 95, 60 and 30% (red, green and blue points, respectively). F_{CH_4} and F_{CO_2} are varied to keep F_{Total} and the $X_0(CH_4)$:$X_0(CO_2)$ ratio constant. 110

5.9 Effect of varying P on a) emission from C_2(d), CH(A), CO(B), OH(A), H(n=3) and H(n=4) and b) column densities of C_2(a, v=0) and CH(X, v=0) at z = 10 mm. Emission intensities and CH(X, v=0) column densities were obtained with R = 0.5, C_2(a, v=0) column densities were obtained with R = 0.51. All other parameters were kept at base conditions. 112

5.10 Effect of varying p on a) emission from C_2(d), CH(A), CO(B), OH(A), H(n=3) and H(n=4) and b) column densities of C_2(a, v=0) and CH(X, v=0) at z = 10 mm. Emission intensities and CH(X, v=0) column densities were obtained with R = 0.5, C_2(a, v=0) column densities were obtained with R = 0.51. All other parameters were kept at base conditions. 113

5.11 Normalised emission intensities of a) C_2(d$\rightarrow$a), b) H_α and H_β, c) CH(A$\rightarrow$X), d) CO(B$\rightarrow$A) and e) OH(A$\rightarrow$X) as a function of z when p = 100, 150 and 200 Torr (red, green and blue points, respectively). All other parameters were kept at base conditions. 114

6.1 Bar chart showing the difference in the predicted number density of a number of species 0.5 mm above the growing substrate, from simulations of the plasma under MCD and UNCD conditions. Based on the data presented in Table 6.1. 119

6.2 Illustration showing the basic C_9H_{14} cluster and the two variants used in the QM calculations, as well as the five distinguishable C-H (HC1-HC5) and the four C-C (CC1-CC4) bonds on the diamond surface. 120

6.3 (a) shows an example of the QM/MM structure used in the current calculations. The MM network is shown in grey whilst the black central region is the structure treated with QM. (b) shows the QM region for the insertion of atomic carbon into a C-H bond on the diamond. The bond lengths highlighted are used to restrict q such that $q = a + b - c$. 121

6.4 Minimum energy pathways for the insertion of C(^{3}P) atoms into a C-H (HC1) and a C-C (CC1) bond, including B3LYP/6-31g(d) optimized structures for the entrance channel complex, transition state and final product. Energies are in kJ mol^{-1} and are from B3LYP/6-311g(d,p)//B3LYP/6-31g(d) calculations with zero point corrections caculated at the B3LYP/6-31g(d) level. 124

6.5 PES along reaction coordinate q, where $q = a + b - c$; a = the distance between the gas phase C atom and one of the surface C atoms, b = the distance between the gas phase C atom and the other surface C atom (*i.e.* not the one used to define a) and c = C-C bond length. A q value of ≈0.5 Å corresponds to the fully inserted product. Plotted energies are from B3LYP/6-311g(d,p) single point energies on B3LYP/6-31g(d):MM2 geometries. 125

6.6 PES along reaction coordinate q, where $q = a + b - c$; a = distance between gas phase $^1C_2$ species and the H atom of the C-H bond, b = the distance between the C and H atoms of the C-H bond and c = distance between gas phase $^1C_2$ species and the C atom of the C-H bond. A q value of ≈0.3 Å indicates the fully inserted product. Plotted energies are from B3LYP/6-311g(d,p) single point energies on B3LYP/6-31g(d):MM2 geometries. 129

6.7 Cartoon illustrating the insertion mechanism of $^1CH_2$ into a C-H bond. 130

7.1 An example of a base model used in the current set of calculations. The two C{100}:H 2×1 surfaces and the C{111}:H surface are highlighted. Also shown are the two different step edges which we identify as convex and concave. The orientation of the dimer bonds on the upper and lower surfaces is also illustrated where they lie parallel and perpendicular to the step edges, respectively. A number of similar models are used in this study with varying orientations of the dimer bonds. 136

7.2 Optimised initial, intermediate and final QM structures for the migration of CH_2 on the C{111}:H surface from the QM/MM calculations. The relative QM/MM B3LYP/6-311G(d,p):MM2 energies (kJ mol^{-1}) are defined relative to that of the initial structure. R_1 and R_2 shown on the initial structure are the bond lengths used to define the reaction coordinate, q. The crossing between the triplet and singlet potential energy surfaces is also highlighted. 139

7.3 Calculated minimum energy profiles for the migration of a surface CH_2 group from the C{100}:H 2×1 surface to the C{111}:H surface via a convex step edge where the dimer bonds are oriented either: a) perpendicular or b) parallel to the step edge. Depictions of the optimised QM regions returned by the QM/MM calculations for the initial, intermediate and final structures are included. Carbon atoms on the C{100}:H 2×1 surface are highlighted in blue whilst those on the C{111}:H are in green. The migrating group and the adjacent surface radical are shown in black. The energies (in kJ mol^{-1}) are from B3LYP/6-311g(d,p):MM2 calculations and defined relative to the initial structure. 142

7.4 Calculated minimum energy profiles for CH_2 migration from the C{111}:H surface to the C{100}:H 2×1 surface via a concave step edge. P1: dimer bonds on the C{100}:H 2×1 surface are perpendicular to the step edge (a); P2 and P3: dimer bonds are parallel to the step edge, starting structures with the CH_2 group facing the trough in between two dimer bonds and the centre of a dimer bond, are shown in b) and c), respectively. The migrating CH_2 group and the adjacent surface radical are highlighted in black. The energies (in kJ mol^{-1}) reported are from B3LYP/6-311g(d,p):MM2 calculations, defined relative to the initial structure in its triplet electronic state. 144

8.1 Reaction pathways for both the addition of various BH_x species and their incorporation into the diamond C{100}:H 2×1 surface. Calculated energetics are in kJ mol^{-1}. Figure reproduced from Cheesman *et al.*[3] 148

8.2 QM regions (with link atoms removed) used within the QM/MM calculations to study migration of pendant BH groups along the dimer chains (a) or dimer rows (b) present on the C{100}:H 2×1 surface. 149

8.3 (a) The C-H bond and (b) the C-C bond investigated for insertion of B and BH. . . . 151

8.4 An illustration of the potential energy surface involved in the insertion of B(^{2}P) atoms into a C-H bond on the C_9H_{14} cluster. Geometries of the transition state and products shown are from calculations at the B3LYP/6-31g(d) level of theory. Energetics are from calculations at the B3LYP/6-311g(d,p)//B3LYP/6-31g(d) level and include ZPC calculated at the B3LYP/6-31g(d) level. The energies are in kJ mol^{-1} and defined relative to that of the reactants. 152

8.5 An illustration of the potential energy surface involved in the insertion of BH($X^1\Sigma^+$) radicals into a C-H bond on the C_9H_{14} cluster. Geometries of the transition state and products shown are from calculations at the B3LYP/6-31g(d) level of theory. Energetics are from calculations at the B3LYP/6-311g(d,p)//B3LYP/6-31g(d) level of theory and include ZPC calculated at the B3LYP/6-31g(d) level. The energies are in kJ mol^{-1} defined relative to the reactants. 153

8.6 An illustration of the potential energy surface involved in the insertion of B (^{2}P) atoms into a C-C dimer bonds on the C_9H_{14} cluster. Geometries of the transition state and products shown are from calculations at the B3LYP/6-31g(d) level of theory. Energetics are at the B3LYP/6-311g(d,p)//B3LYP/6-31g(d) level of theory and include ZPC calculated at the B3LYP/6-31g(d) level. Energies are in kJ mol^{-1} and are defined relative to the reactants. 154

8.7 BH migration profiles along the dimer chains on the C{100}:H 2×1 surface, with optimised geometries of the QM region within the QM/MM calculations shown. Energies are in kJ mol^{-1} and are defined relative to the initial pre-incorporated structure in its triplet electronic state. 156

8.8 BH migration profiles along the dimer rows on the C{100}:H 2×1 surface, with the optimised geometries of the QM region within in the QM/MM calculations shown. Energies are in kJ mol^{-1} and are defined relative to the initial pre-incorporated structure in its triplet electronic state. 157

8.9 Optimised initial, intermediate and final structures of the QM region for the migration of BH on the C{111}:H surface from the QM/MM calculations. The relative QM/MM B3LYP/6-311g(d,p):MM2 energies (in kJ mol^{-1}) are defined relative to that of the initial structure. 158

8.10 Calculated minimum energy profiles for the migration of a pendant BH group from the upper C{100}:H 2 × 1 surface to the C{111}:H surface via the convex step edge, when the dimer bonds are oriented perpendicular to the step edge. Depictions of the optimised QM regions returned by the QM/MM calculations for the initial, intermediate and final structures are included. Carbon atoms in a dimer bond on the C{100}:H 2 × 1 surface are highlighted in blue, the migrating group BH group is shown in pink and the adjacent surface radical is shown in black (on the initial structure). The energies (in kJ mol^{-1}) are from B3LYP/6-311g(d,p):MM2 calculations and defined relative to the initial structure. 159

8.11 Calculated minimum energy profiles for the migration of a pendant BH group from the upper C{100}:H 2 × 1 surface to the C{111}:H surface via a convex step edge where the dimer bonds are oriented parallel to the step edge. Depictions of the optimised QM regions returned by the QM/MM calculations for the initial, intermediate and final structures are included. Carbon atoms in a dimer bond on the C{100}:H 2 × 1 surface are highlighted in blue, the migrating group BH group is shown in pink and the adjacent surface radical is shown in black (on the initial structure). The energies (in kJ mol^{-1}) are from B3LYP/6-311g(d,p):MM2 calculations and defined relative to the initial structure. 160

8.12 Calculated minimum energy profiles for BH migration from the C{111}:H surface to the C{100}:H 2 × 1 surface via a concave step edge. (a) P1: dimer bonds on the C{100}:H 2 × 1 surface are perpendicular to the step edge ; P2 and P3: dimer bonds are parallel to the step edge. Starting structures with the BH group facing the trough in between two dimer bonds or the centre of a dimer bond are shown in b) and c) respectively. The migrating BH group and adjacent surface radical are highlighted in pink and black, respectively. The energies (in kJ mol^{-1}) reported are from B3LYP/6-311g(d,p):MM2 calculations, defined relative to the initial structure. 162

List of Tables

1.1 Some properties of diamond.[4] 2

6.1 Predicted number densities of a variety of gas phase species 0.5 mm above the growing diamond surface from calculations presented in Ma *et al.*[2] (MCD) and Richley *et al.*[3] MCD process conditions: 4.4% CH_4, 7.1% Ar, 88.5% H_2, Pressure (p) = 150 Torr, Power (P) = 1.5 kW. UNCD process conditions: 0.5% CH_4, 1% H_2, 98.5% Ar, p = 170 Torr, P = 0.7 kW. 118

6.2 B3LYP/6-311g(d,p)//B3LYP/6-31g(d) energies including the ZPC calculated at the B3LYP/6-31g(d) level for the entrance channel complex ($E_{complex}$), transition states (E_{TS}) and the overall change in energy (ΔE) associated with insertion of C(^{3}P) into the C-H and C-C bonds shown in Figure 6.2. All energies are defined relative to those of the reactants. 123

6.3 B3LYP/6-311g(d,p)//B3LYP/6-31g(d) energies including the ZPC calculated at the B3LYP/6-31g(d) level for the entrance channel complex ($E_{complex}$), transition states (E_{TS}) and the overall change in energy (ΔE) associated with insertion of CH($X^2\Pi$) into the C-H and C-C bonds shown in Figure 6.2. All energies are defined relative to those of the reactants. 126

6.4 B3LYP/6-311g(d,p)//B3LYP/6-31g(d) energies including the ZPC calculated at the B3LYP/6-31g(d) level for transition states (E_{TS}) and the overall change in energy (ΔE) associated with insertion of $^1CH_2$ into the C-H and C-C bonds shown in Figure 6.2. All energies are defined relative to those of the reactants. 127

A.1 Absorbed power densities and reaction rates for important plasma-chemical reactions in the central hot region of the plasma (r=0, z=10.5 mm) for a typical MCD plasma (4.4% CH_4/88.6% H_2/ 7% Ar, p=150 Torr, P=1.5 kW), table reproduced from Mankelevich *et al.*[1] 169

A.1 (*continued*) 170

B.1 List of transitions and their associated wave numbers, Einstein A coefficients, upper and lower state degeneracies and PGOPHER coefficients investigated using CRDS spectroscopy. C_2 and CH PGOPHER coefficients are from simulations using PGOPHER and the Einstein A coefficients are from Wills *et al.*[1] Constants relating to the H(n=2) transitions are from the NIST atomic spectra database.[2] 171

C.1 Reaction rate coefficients of C(^{3}P) atoms inserting into C-H bonds, calculated from vibrational frequencies computed in the QM calculations using transition state theory. 173

C.2 Reaction rate coefficients of CH($X^2\Pi$) radicals inserting into C-H bonds, calculated from vibrational frequencies computed in the QM calculations using transition state theory. 173

1

Introduction

Diamond is a material best known for its use as a gemstone and is prized as a symbol of wealth due to its scarcity in nature. As well as making appealing gem stones diamond also possesses a number of physical properties which makes it attractive for a range of potential applications.

1.1 Diamond: Structure, Properties and potential uses

Diamond is one of a number of different forms that elemental carbon can take; others include graphite, fullerenes (such as C_{60}) and carbon nanotubes. Structures of both diamond and graphite are shown in Figure 1.1a and 1.1b respectively. The difference between just these two forms of carbon is quite stark, with diamond consisting of tetrahedrally bonded (sp^3 hybridized) carbon atoms, whilst graphite consists of layers of sp^2 bonded carbon sheets. As a consequence of the vastly different structures of these two carbon allotropes, they each possess vastly different properties. For example diamond is one of the hardest materials known to man, which makes it ideally suited to applications involving the cutting or machining of other materials. Graphite, on the other hand, is a rather soft material and finds common use as "lead" in pencils and as a dry lubricant. Graphite's ability to act as an effective dry lubricant is commonly attributed to the weak bonding between the carbon sheets, however, under conditions when certain gaseous species are absent, graphite shows increased friction and higher wear.[1] Experiments using surface x-ray diffraction[2] have leant support to the hypothesis[3] that the low wear rates commonly observed are a result of dangling bonds at the edges of the sheets becoming saturated by chemisorbed gas species.

A number of the physical properties of diamond are listed in table 1.1.

The high thermal conductivity and low thermal expansion coefficient of diamond makes it ideal for uses where dissipation of heat is important, such as in the creation of x-ray lenses[5] or Raman lasers.[6] Diamond finds use in optical windows[4] due to its lack of any significant absorption of

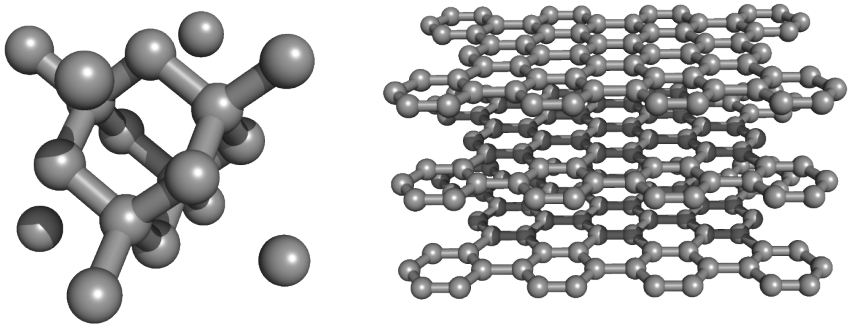

(a) Diamond unit cell

(b) Graphite

Figure 1.1: Illustrations of a) the unit cell of diamond, and b) three layers of graphite.

Table 1.1: Some properties of diamond.[4]

Property	Value
Mechanical hardness	90 GPa
Thermal conductivity	2000 $Wm^{-1}K^{-1}$
Band Gap	5.4 eV
High resistivity	10^{13} Ω cm
Thermal expansion coefficient	1×10^{-6} K^{-1}

electro-magnetic radiation (ranging from the far infra red to deep UV). Its high resistance to radiation, high density and chemical stability to hydrogen plasmas also makes diamond a promising material for use as shielding within fusion reactors.[7]

It is also possible to dope diamond and create a semiconductor. This combined with the chemical inertness and bio-compatibility of diamond allows for a number of potential applications in the production of bio-sensors[8] or bio-electronics, such as eye implants.[9]

1.2 Synthesis of diamond

Diamond under standard conditions (298 K, 1 atm) on the earth's surface is not the most thermodynamically stable form of carbon. Graphite is the stable allotrope (see phase diagram in Figure 1.2). Diamond is a metastable form of carbon though, and does not readily convert to graphite. This is due to a large energy barrier for the interconversion process. Diamond was initially only found naturally in deposits brought up to the earth's surface (from regions within the earth's core where diamond is the stable allotrope). This however changed in the 1950's when diamond was first successfully synthesised using a high pressure / high temperature (HPHT) technique[10]. This technique aims to

mimic the natural conditions under which diamond forms.

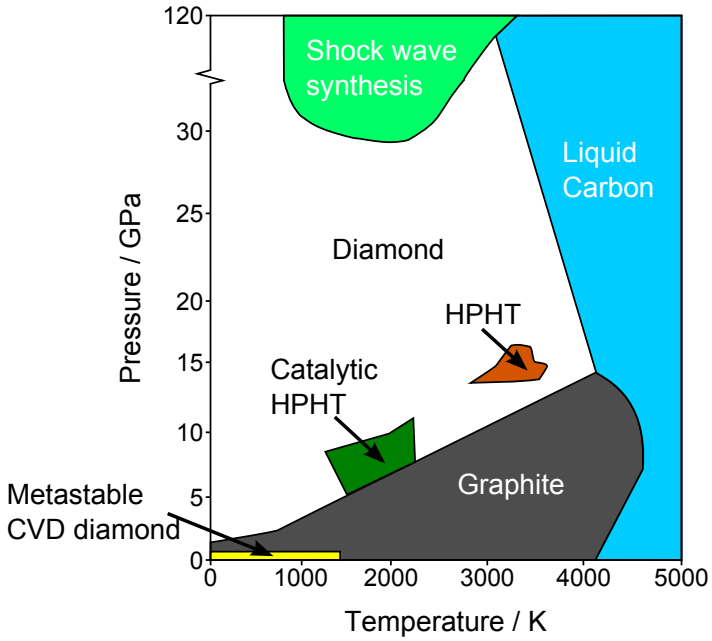

Figure 1.2: Phase diagram of elemental carbon from reference[11], highlighting the areas under which CVD and HPHT synthesis of diamond takes place.

The HPHT process involves heating carbon (normally in the form of graphite) to over 2000K whilst placing it under a significant pressure (>5GPa) within the presence of a metal catalyst. This leads to the formation of single crystal diamonds, the largest of which, being several millimetres in size.

1.2.1 Chemical vapour deposition of diamond

Another technique developed to grow diamond synthetically is chemical vapour deposition (CVD). CVD of diamond involves firstly the creation of an activated gas mixture which, followed by a variety of gas-surface and surface reactions, results in the growth of a diamond film. The growth process is normally carried out on a hot substrate (typically around 900-1500 K[12]). Diamond films can be grown both homoepitaxially (on diamond) or heteroepitaxially (on metals such as iridium[13] or molybdenum[14]). Homoepitaxial growth is commonly achieved by using small crystal seeds on a substrate such as silicon. Addition of gas phase species to the surface of these crystals results in their growth. Depending on the gas-phase conditions and the nucleation density either a large single crystal of diamond or a polycrystalline film (which can have a large variety of grain sizes ranging from μm to nm) are grown.

Growth of diamond via CVD can be split into three phases; firstly the activation of the gas mixture and reactions between gas phase species within the activated mixture; secondly gas-phase re-

actions and, finally, gas-surface and surface reactions which incorporate species into the bulk diamond.

1.2.2 Chemical vapour deposition techniques

A number of different techniques for activating the initial gas mixtures used for CVD of diamond are available. Two of the most common techniques used to activated the gas mixture are hot filament (HF) activation and microwave plasma enhanced (MWPE) activation.

1.2.2.1 Hot Filament CVD

HF CVD as suggested by its name relies on gas activation by metal filaments resistively heated to around 2000 K. The filament (typically tungsten or tantalum) heats the surrounding gas mixture (the initial gas mixture is usually a combination of CH_4 and H_2) and catalytically produces H atoms from the dissociation of H_2. Gas phase reactions and diffusion of species towards a substrate (commonly seeded silicon, which is heated to around 1000-1200 K) results in the growth of diamond.[4] A schematic of a HF CVD reactor is shown in Figure 1.3.

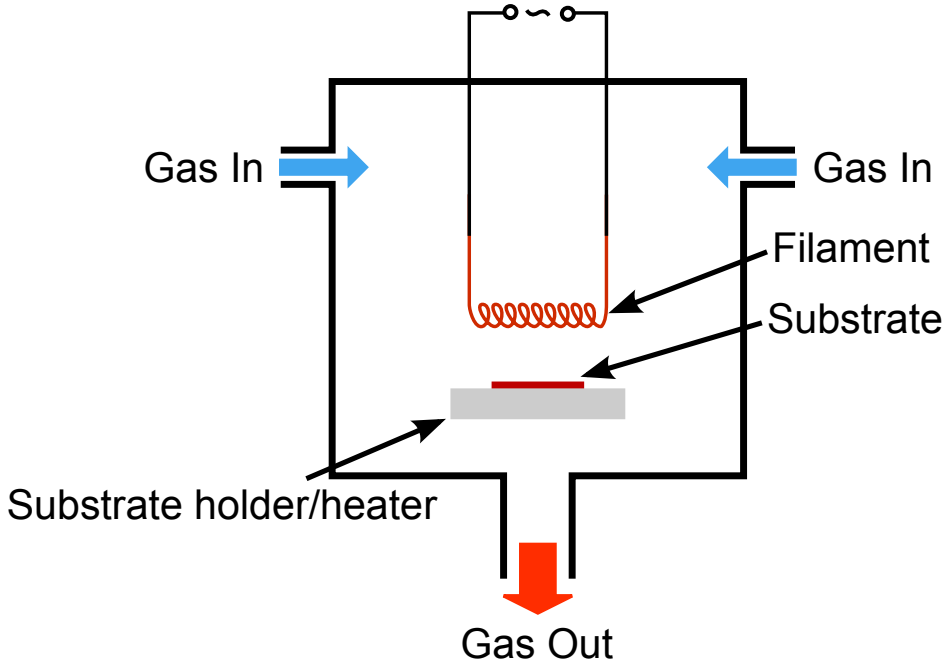

Figure 1.3: Schematic of a typical HFCVD reactor.

HF CVD is a relatively cheap method for the synthesis of diamond films, but it has its drawbacks. Firstly, due to the high temperatures involved, the filament will react with the gas mixture and will slowly degrade, influencing its efficiency at activating the gas mixture. The use of the filament

to activate the gas also restricts the input gases that can be used, as corrosive or oxidising gases will damage the filament. In addition, diamond films grown using HF CVD may be contaminated with the filament material, rendering the film unsuitable for some applications which require high quality material. In addition, the growth rate of diamond by HF CVD tends to be lower than other techniques.

1.2.2.2 Microwave plasma enhanced CVD

MWPE CVD is now one of the most frequently used methods for the creation of high quality synthetic diamond. The MWPECVD reactors function by coupling microwave power via a waveguide and antenna through a quartz window and into a chamber containing a low pressure (pressure ranges from around 20 to over 200 Torr depending on the reactor and gas composition) mixture of gases (commonly a CH_4 in H_2). A schematic of a MWPECVD reactor is shown in Figure 1.4.

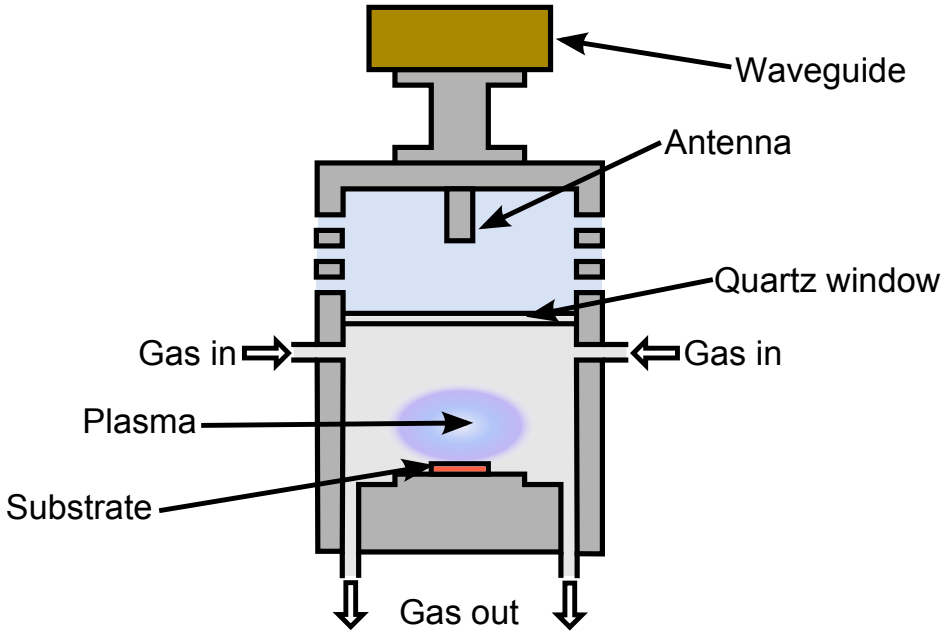

Figure 1.4: Schematic of a typical MWPECVD reactor.

The plasma is generated by electrons within the chamber picking up energy from the electric component of the microwave field. These then collide with gas phase species and transfer their energy. The collisions result in heating of the gas mixture and dissociation, excitation and ionisation of gas phase species. Subsequent reactions between the various gas phase atoms, molecules and ions results in a complex set of chemical reactions occurring within the gas phase environment. Diffusion of the gas phase species towards the substrate and their ensuing reactions with the surface results in the growth of diamond. MWPECVD reactors also tend not to require substrate heaters. Instead

the substrate is heated by the plasma to the temperatures required for diamond growth and its temperature is controlled by separating it from the base (usually with a wire), which is normally water cooled.

The major advantage of MWPECVD over HFCVD is that there is no filament used to activate the gas, and consequently no contamination of the diamond film. This clean environment for growth means that higher quality diamond can be produced. Another advantage of having no filament is that a much wider array of input gas mixtures can be used (including oxygen), as the degradation of the filament is no longer a factor. MWPECVD also affords relatively fast growth rates due to the high input power and high level of gas activation compared to HFCVD. The major drawback of these systems is their significantly higher cost to design and manufacture.

1.2.3 Gas-phase chemistry

The second stage in CVD of diamond involves creation of the growth species from the input gas mixture by reactions within the gas phase. The gas mixtures used typically involve a combination of a hydrocarbon with hydrogen (normally 1-5% CH_4 in H_2).[12] Activation of the gas mixture produces a large number of hydrogen atoms. These H atoms are thought to play key roles in many aspects of diamond growth via chemical vapour deposition.

A large proportion of the gas phase chemistry and consequently creation of various hydrocarbon species (whose addition to the surface results in diamond growth), is thought to be dependent on abstraction and addition of H atoms from the hydrocarbon species (H-Shifting reactions). These H-shifting reactions are driven by the high concentration of H atoms within the gas phase. The H-shifting reactions process the input hydrocarbon into a number of different species. By way of illustration, the conversion of CH_4 to other C_1H_x and C_2H_x species is shown in Figure 1.5. It has been shown via computational modelling of plasmas used for diamond CVD[15] that the direction of the H-shifting reactions between C_1 and C_2 species is highly dependant on the prevailing local temperature. In cooler regions CH_4 is favoured whilst C_2H_2 is favoured in the hotter regions.

The gas-phase chemistry and composition within a MWPECVD reactor has also been shown to have little dependence on the specific hydrocarbon used in the input gas mixture.[16] This has been shown in cavity ring down spectroscopy (CRDS) measurements of a number of species occurring within the plasmas when CH_4 and C_2H_2 are used as the hydrocarbon source gas. By adjusting the flow rates of both gases so that the C fraction is the same (*i.e.* 50% lower flow rate of C_2H_2 compared to CH_4) the spatial distribution and column densities of C_2(a), CH(X) radicals and H(n=2) atoms were shown to

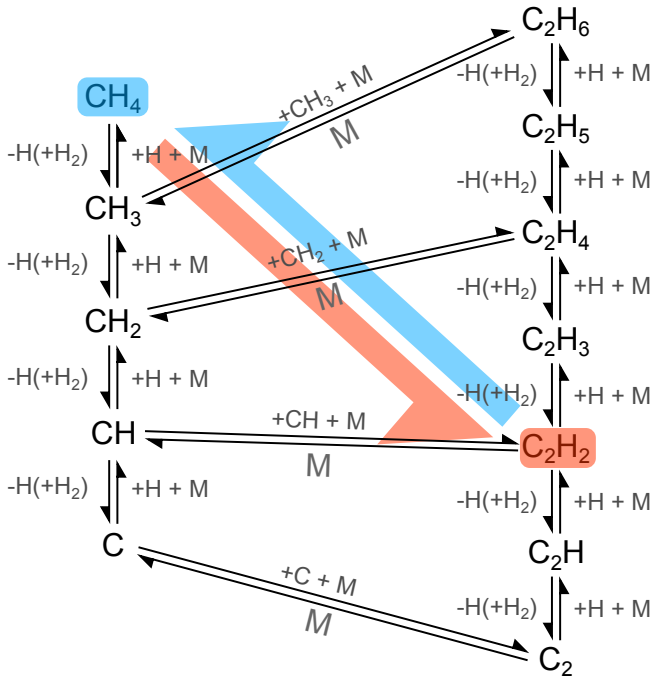

Figure 1.5: Illustration of a portion of the H-shifting reactions which occur within the gas phase of a CVD diamond reactor. The blue arrow indicates the trend of the H-shifting reactions in the cool region of the reactor, whilst the red arrow shows the trend of the reactions within the hot region.

be practically identical, see Figure 1.6.

Other gases have also been added to the source mixture to influence the growth of diamond and/or aid in the analysis of the plasmas. Examples include the addition of B_2H_6 to the gas phase to boron dope the diamond,[17] and addition of N_2 (which has been shown to increase the growth rates when added in low quantities[18]) and Ar, which was initially added to aid in various plasma diagnostic techniques such as actinometry.[19] The addition of Ar has also been used to dilute the gas phase such that the H_2 fraction is reduced and leads to the growth of films with small crystallite sizes.[20]

Addition of oxygen containing molecules into the gas phase offers a number of advantages over just a CH_4/H_2 gas mixture. These can include improved crystal morphology, an increased deposition rate[21] and the ability to grow diamond at low temperatures.[22,23] The effect of the O/H and O/C ratio within plasmas is summarised in the Bachmann triangle[24] (see Figure 1.7).

This diagram clearly shows that diamond growth occurs when the C:O ratio is close to 1. As the C:O ratio is increased from 1 the film becomes progressively lower in quality as an increased amount of non-diamond carbon is deposited, finally resulting in deposition of amorphous carbon. Whilst in the opposite direction increasing the oxygen fraction causes diamond growth to cease altogether.

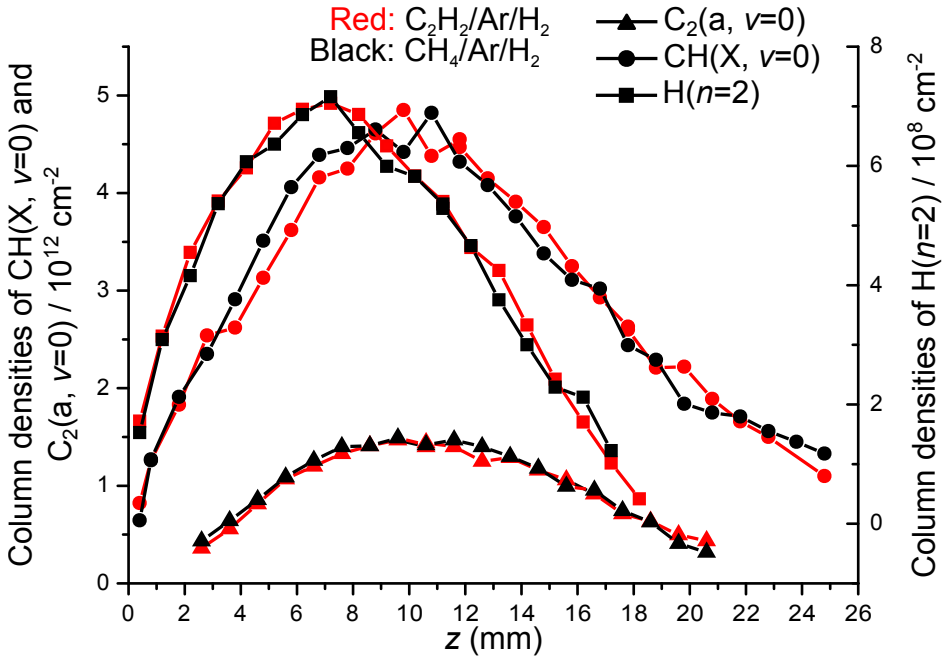

Figure 1.6: Spatial profiles of C_2(a, v=0), CH(X, v=0) radicals and H(n=2) atoms within a MWPECVD reactor. The red line and symbols show column densities when the hydrocarbon source gas was C_2H_2 whilst the black line shows column densities measured when the source gas was CH_4. Reactor parameters: Microwave Power = 1.5 kW, Pressure = 150 Torr, F(Ar) = 40 sccm, for CH_4 measurements, $F(H_2)$ = 500 sccm and $F(CH_4)$ = 25 sccm, for C_2H_2 measurements $F(H_2)$ = 512.5 sccm and $F(C_2H_2)$ = 12.5 sccm. Figure reproduced from Ma *et al.*[16]

1.2.4 Surface chemistry

The final stage in the growth of diamond by CVD is the reaction of gas-phase species with the substrate and subsequently their incorporation into the bulk diamond. The CH_3 radical is one of the prime candidates for the main growth species, due to its high concentration close to the substrate[12] and also its presence in both HF and MWPECVD reactors. As such, many studies have focused on reaction pathways resulting from the addition of gas phase CH_3 radicals to the growing surface and their incorporation into the diamond crystal lattice.

Under most conditions used for diamond CVD there is a large presence of H atoms directly above the substrate. This in turn leads to the growing diamond film having a surface terminated with hydrogen. In order for species such as CH_3 to add to the surface, the hydrogen atoms terminating the growing diamond surface must be removed. The high concentration of H atoms in the gas phase above the substrate (calculated at 8.14×10^{15} cm^{-3} for a gas mixture of 4.4% CH_4/ 88.6% H_2/ 7% Ar at T_{sub} ≈973 K[25]) is thought to play a significant role in the creation of surface radical sites (by hydrogen abstraction). The most probable fate for these surface radicals will be their recombination

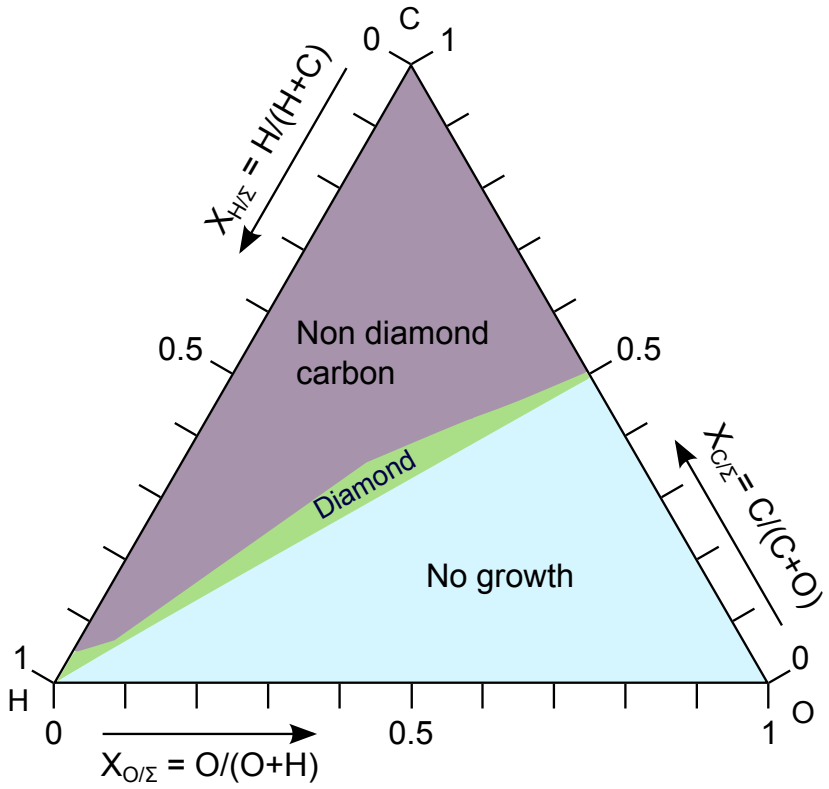

Figure 1.7: A simple version of the Bachmann triangle, showing the diamond growth region, as well as the areas where no growth and non-diamond growth occurs. Figure adapted from reference 4.

with gas phase H atoms due to the high flux of H atoms to the surface (10^4-10^7 s^{-1} per surface carbon[26]). At any one time though there will be ≈ 1-10% of the surface present as surface radicals on to which hydrocarbon species can add.[26] The rate of hydrocarbon addition to free surface sites is not dependent on the H atom concentration.[27]

1.2.4.1 {100} surface

The {100} diamond surface is one of the most commonly observed in diamond films grown using CVD. It tends to form smooth surfaces and has a low defect density.[28] It is also the only surface that requires addition of just one carbon atom on the surface to form part of a new layer.[12] For these reasons the {100} is one of the most studied surfaces of diamond.

H-terminated {100} diamond surfaces are known to form a 2×1 reconstruction[29] (henceforth represented as C{100}:H 2×1) where two adjacent carbon atoms form a bond between each other (termed a dimer bond). This results in the formation of rows and chains of these bonds across the C{100}:H 2×1 surface, an illustration is shown in Figure 1.8a. This rearrangement occurs as a result of high steric hindrance between adjacent surface hydrogen atoms on the unreconstructed surface. Mecha-

nisms for the formation of this reconstruction have been proposed involving either elimination of H_2 from the surface or atomic hydrogen[30].

A number of different growth mechanisms have been proposed for the $\{100\}$ surface from CH_3 radicals, the first of which by Harris[31] used bicyclononane as a model of the unreconstructed H-terminated $\{100\}$ surface. This was subsequently modified to account for the $\{100\}$ surface forming the 2×1 reconstruction. This pathway involves the incorporation of a CH_3 group across a trough on the C$\{100\}$:H 2×1 surface and is commonly referred to as the trough mechanism[32]. Another pathway known as the dimer mechanism proposed by Garrison *et al.*[33] involves the incorporation of a gaseous CH_3 group into a dimer bond on the C$\{100\}$:H 2×1 surface. A combination of both these mechanisms is required for the growth of a new layer of diamond on the C$\{100\}$:H 2×1 surface.[32]

Both pathways start with the same initial steps, *i.e.* the creation of a surface radical site by hydrogen abstraction followed by addition of a gaseous CH_3 radical to the site and one further H atom abstraction to form a pendant CH_2 group on the surface. The trough mechanism then involves a further H abstraction from the surface carbon atom on the other side of the trough, and a subsequent ring closing reaction between the two radical sites results in the incorporation of the CH_2 group into the diamond lattice. Incorporation into the dimer bond instead proceeds by a rearrangement reaction, which breaks the dimer bond and forms a double bond between the CH_2 group and the surface carbon to which it is attached and a radical site on the other carbon which was part of the dimer bond. Reaction between the CH_2 group and the radical then concludes with the incorporation of CH_2 into the crystal lattice. Both the trough mechanism and the dimer mechanism are illustrated in Figures 1.9a and 1.9b which include energetics from recent computational investigations by Cheesman *et al.*[34]

Due to the inherent randomness of the surface radical site locations created by interaction with gas phase H atoms, carbon atoms will add randomly across the diamond surface. Therefore if only the dimer and trough mechanisms are active, growth of diamond will occur in localised regions. This fails to account for the smooth C$\{100\}$:H 2×1 surfaces observed in experimentally grown material.[36] To account for this, it has been proposed that species are able to diffuse across the surface[32] (surface migration, see Section 1.2.4.5) and that growth occurs at steps between surfaces.[32]

Acetylene has also been proposed as a growth species on the C$\{100\}$:H 2×1 surface, and a mechanism for its incorporation has been advanced by Skokov *et al.*[35] (shown in Figure 1.10). The proposed C_2H_2 growth mechanism requires two adjacent surface radical sites (compared to the sin-

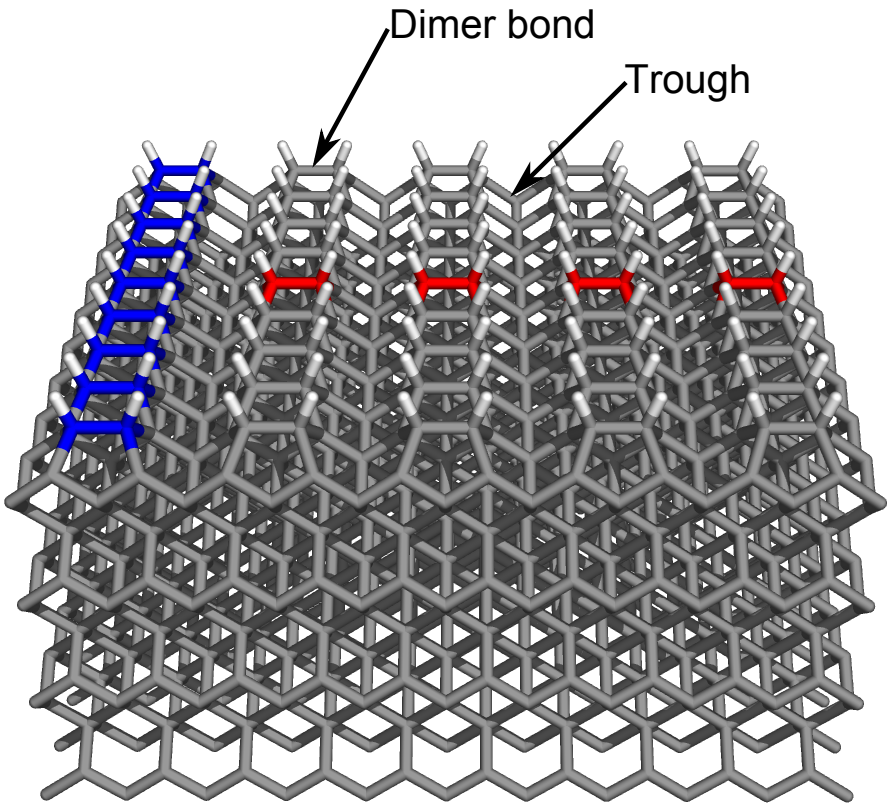

(a)

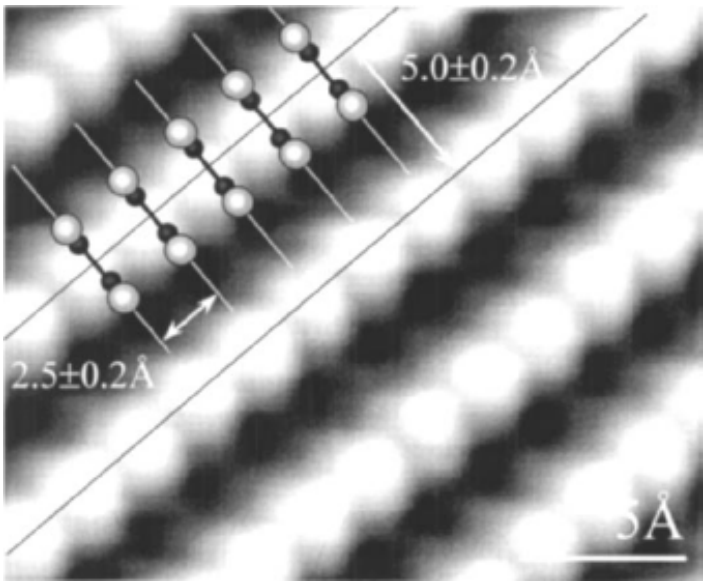

(b)

Figure 1.8: a) An illustration of the H-terminated $\{100\}$ diamond surface with the 2×1 reconstruction. A dimer bond, a trough between dimer bonds, a dimer row (blue) and a dimer chain (red) on the surface are highlighted. b) Scanning tunnelling microscope image showing the 2×1 reconstruction on the $\{100\}$ surface. From reference 29.

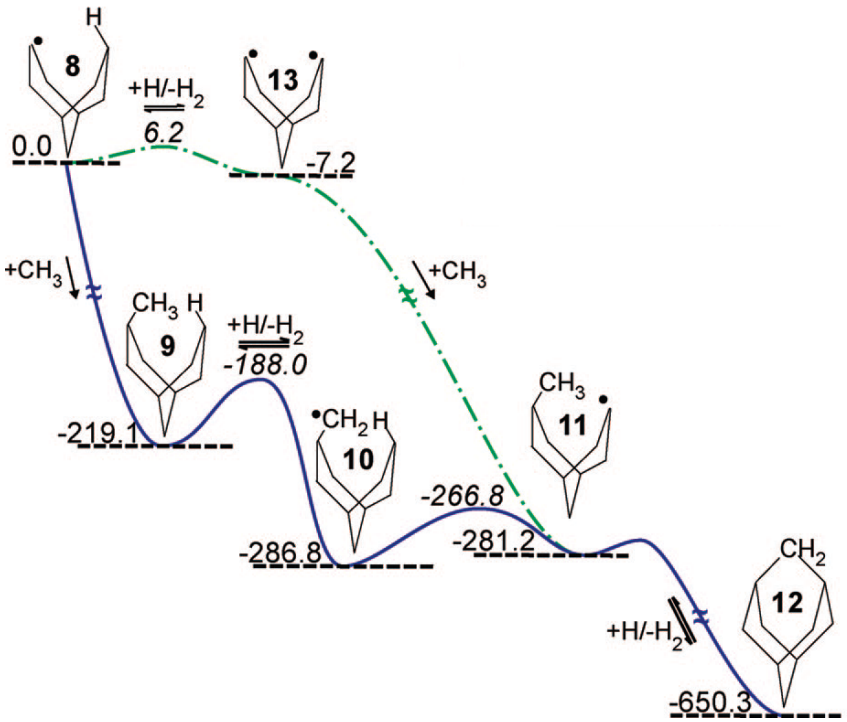

(a) Trough mechanism

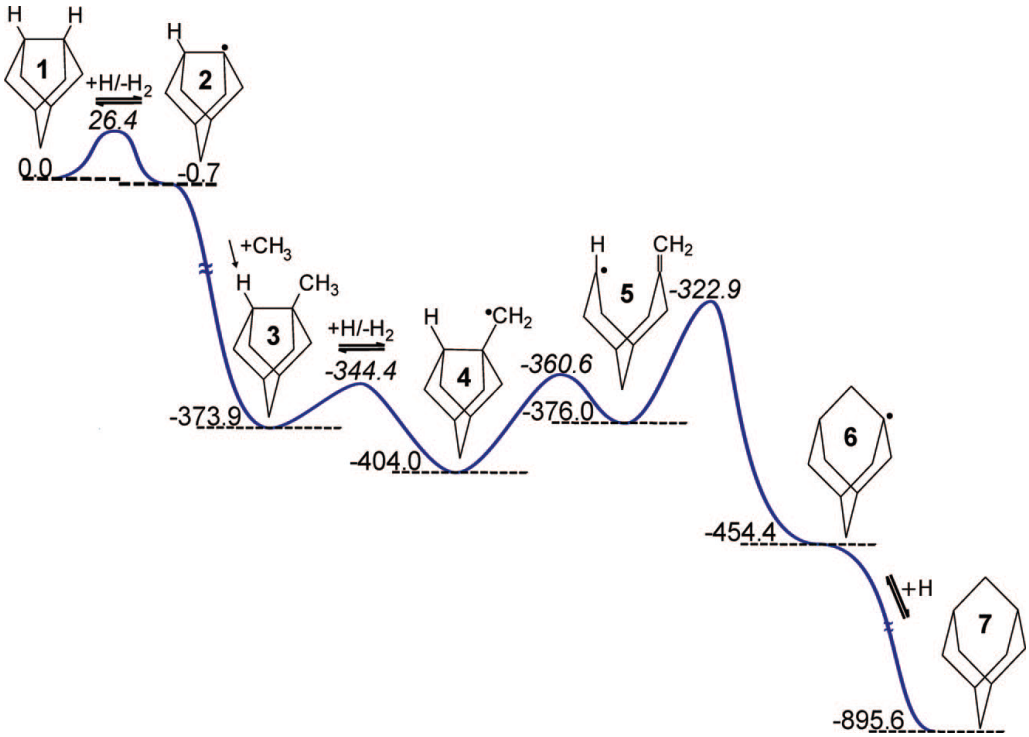

(b) Dimer mechanism

Figure 1.9: Illustration of structures on the C{100}:H 2×1 surface involved in the a) the trough and b) the dimer mechanisms for the incorporation of a gaseous CH_3 group. Energetics and diagrams are from Cheesman *et al.*[34] and the former are in kJ mol^{-1}.

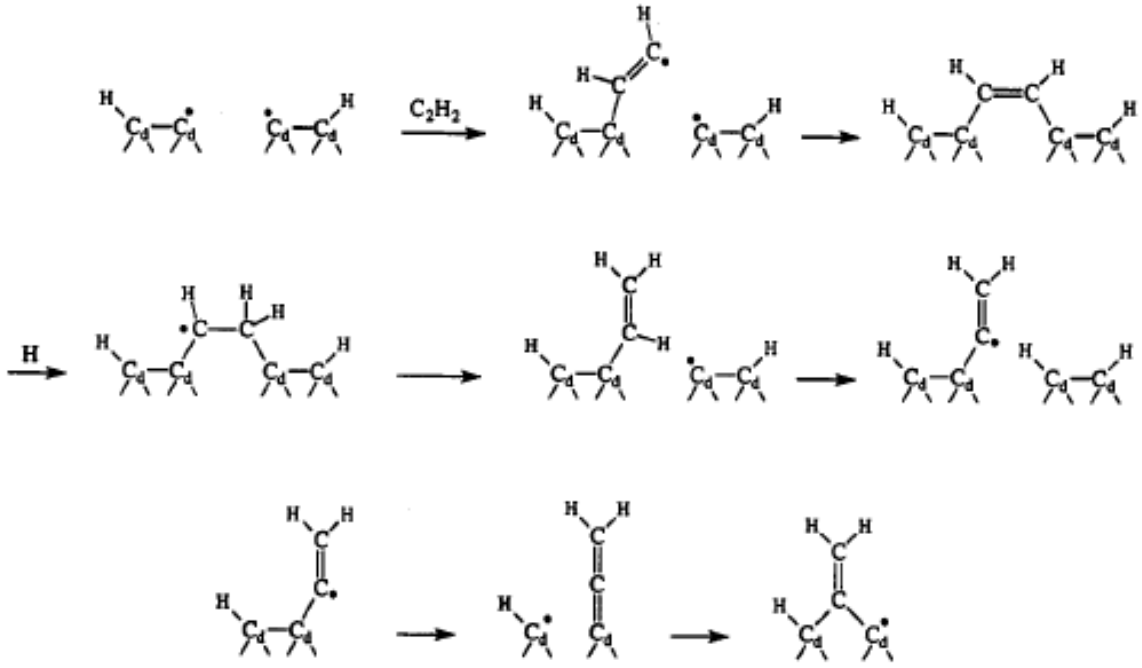

Figure 1.10: Mechanism proposed by Skokov *et al.* for the incorporation of acetylene at diradical sites on the C{100}:H 2 × 1 surface of diamond. Figure reproduced from reference 35.

gle radical site required for CH_3 incorporation). This is to prevent the adsorbed C_2H_2 group on the surface being removed via β-scission reactions (see Section 1.2.4.4). As a consequence, C_2H_2 incorporation via the proposed mechanism is restricted to the $\approx$1% of the surface that will have two adjacent radical sites.

1.2.4.2 {111} surface

Another surface that is commonly observed in as-grown films of CVD diamond is the H-terminated {111} surface (a portion of which is shown in Figure 1.11).

A growth mechanism for the {111}:H surface from methyl radicals was proposed by Tsuda *et al.*[37]. This mechanism requires the surface to be fully covered in adsorbed CH_3 groups, which upon addition of a final CH_3^+ forms a new layer of diamond on the {111}:H surface. This mechanism is thought to be unlikely due to the paucity of CH_3^+ cations and the high steric hindrance that would be encountered by the CH_3 groups on the surface.

To add a new layer of diamond on top of a {111}:H surface three carbon atoms are required to bond together in the appropriate way. Due to this requirement, growth from just CH_3 radicals is thought to be a slow process as the likelihood of three CH_3 radicals coming together and bonding on the surface

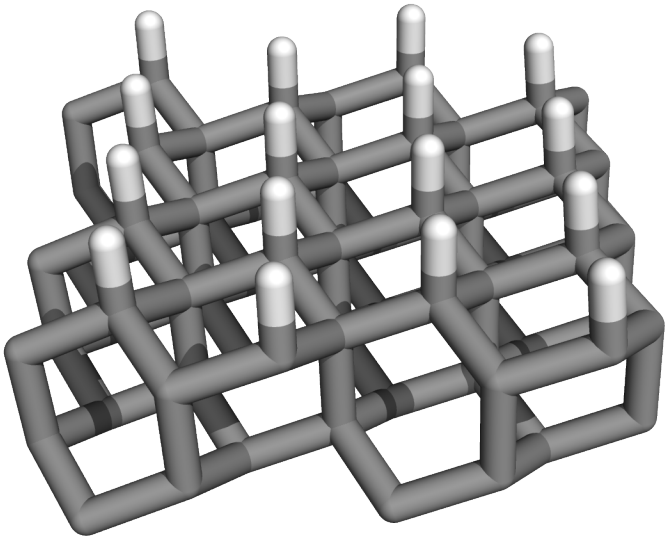

Figure 1.11: a portion of the H-terminated $\{111\}$ diamond surface.

to form the new layer will be low.[38] Once a new layer has been nucleated though, growth at the kinks and steps formed on the surface is thought to be quick, as only one or two carbon atoms (depending on the site) are required to extended the surface.[38] The rate limiting step involved in the growth of a new layer on the $\{111\}$:H surface is therefore thought to be the initial nucleation step and that once this has been achieved the rest of the layer is quickly formed via a step flow process. Steps towards the formation of a four atom nucleation point have been outlined by Butler and Oleynik[39] as well as explanations for the high defect concentrations and crystal twinning observed on $\langle 111 \rangle$ growth sectors. Butler and Oleynik also suggested that the enhancement in growth rate observed in diamond CVD by the addition of nitrogen into the gas phase is due to the chemisorbtion of CN radicals onto the diamond surface. These are less susceptible to β-scission (see Section 1.2.4.4) compared to longer hydrocarbons and are thus able to assist in the formation of a nucleation point and enhance the nucleation rate on the $\{111\}$ surface.

1.2.4.3 $\{110\}$ surface

The $\{110\}$ surface (see Figure 1.12) of diamond is one of the fastest growing[40] and macroscopic $\{110\}$ faces are not observed in diamond CVD due to the surface growing out, $\{110\}$ type ridges are however commonly observed at intersections between other surfaces.[27]

Growth mechanisms proposed for this surface involve bridging the troughs on the $\{110\}$:H surface by either the adsorption of two CH_3 radicals or species such as C_2H_4[27], C_2H_2[41] and C_2[42] followed

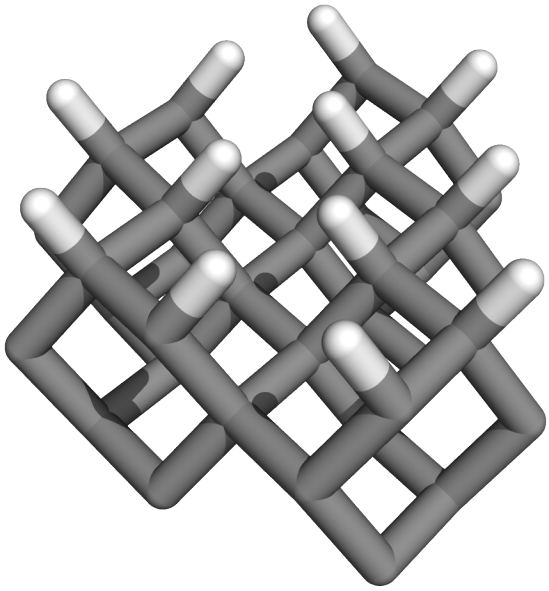

Figure 1.12: A portion of the $\{110\}$ surface.

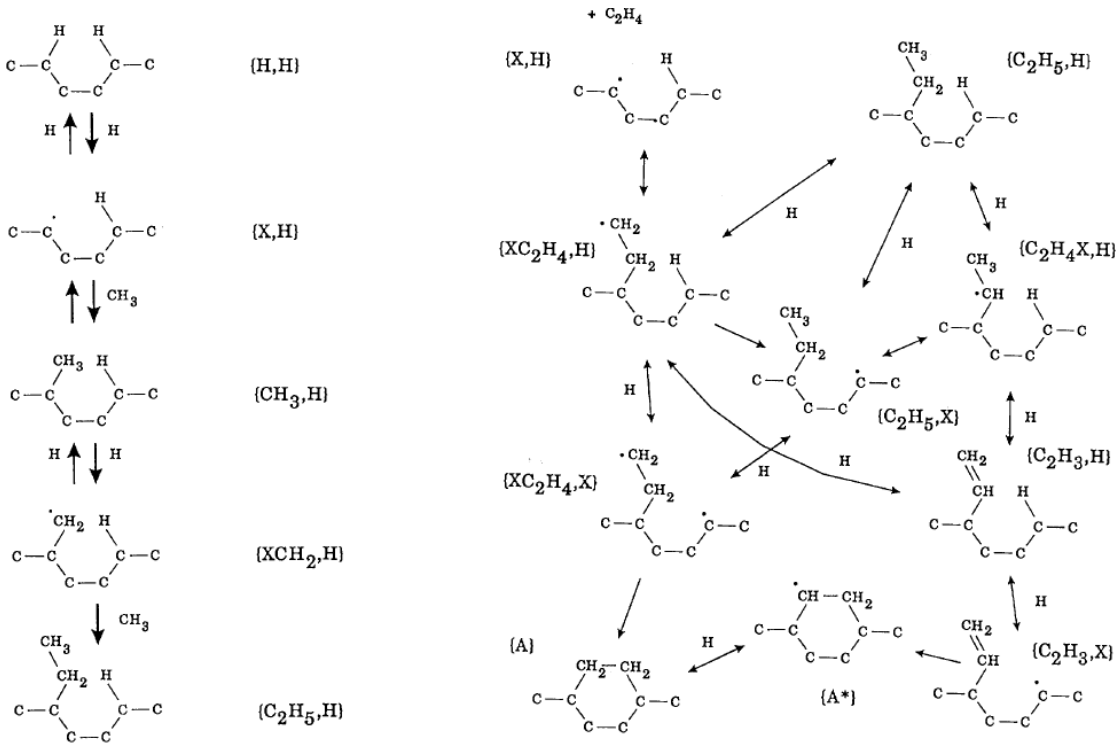

Figure 1.13: $\{110\}$ growth mechanisms for both CH_3 and C_2H_4 from reference 27.

by a number of hydrogen abstractions and rearrangement (Figure 1.13 shows reaction schemes for the incorporation of CH_3 and C_2H_4).

1.2.4.4 β-Scission

β-scission is a process whereby abstraction of an H atom from pendant hydrocarbon chains (C_xH_y, $x \geq 2$) results in their removal or conversion into C_1H_x species (see Figure 1.14).

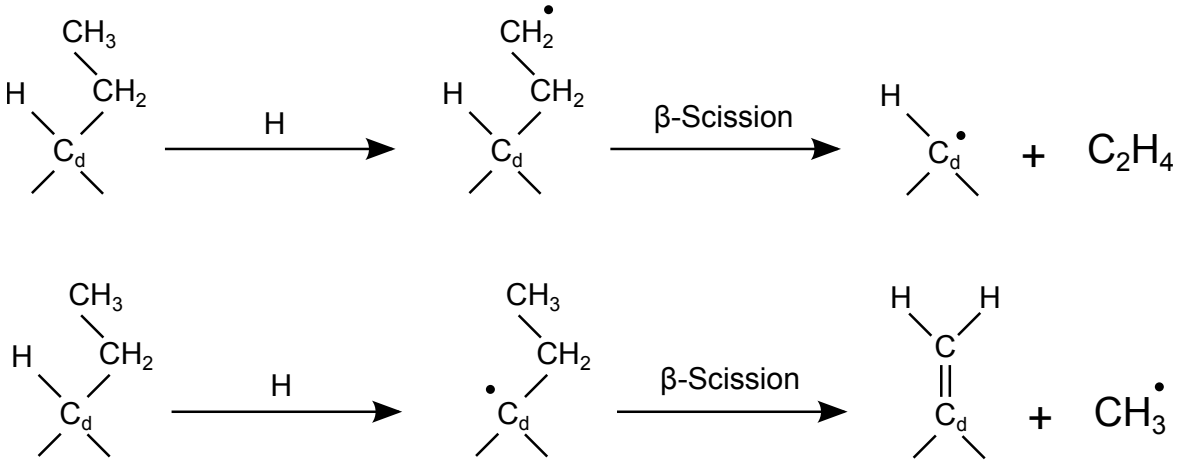

Figure 1.14: An illustration of two different β-scission pathways where attack by gaseous H atoms results in the removal of long hydrocarbon (C_xH_y, $x \geq 2$) chains from the surface. Figure from reference 27.

This process is another way in which gaseous H atoms above the growing diamond surface are important in the CVD of diamond. The selective removal of long hydrocarbon chains from the surface helps prevent deposition of non-diamond (sp^2) carbon. This type of preferential etching by H atoms of sp^2 carbon over sp^3 carbon has been previously observed experimentally.[43] This preferential removal is important in the metastable growth of diamond under CVD conditions.

1.2.4.5 Surface migration

The movement of surface bound (pendant) hydrocarbon species on the $\{100\}$:H 2×1 diamond surface was suggested by Frenklach *et al.*[44] as a possible explanation for the smooth morphologies observed on this surface. Migration of various hydrocarbon species on both the $\{100\}$:H 2×1[34,44,45] and the $\{111\}$:H[46] surfaces have previously been investigated. One of the most studied migration species is a pendant CH_2 created by H abstraction from a surface CH_3 group. Most migration reactions proposed involve diradical sites, *i.e.* sites where a radical is present on a surface carbon adjacent to the pendant CH_2 radical. The migration then proceeds via a ring-closing reaction on the surface;

subsequent opening of the ring results in either the movement of the CH_2 group along the surface by one carbon or its reversion to its original geometry. Energy profiles and structures required for migration of CH_2 radicals on the $\{100\}$:H 2×1 surface along the dimer chains and dimer rows are shown in Figure 1.15a and 1.15b respectively, reproduced from Cheesman *et al.*[34] A similar ring opening process was also proposed for migration of CH_2 on the $\{111\}$:H surface.[46]

The energetics calculated to be involved in the migration process by Cheesman *et al.* whilst large, involving energy barriers of $>$100 kJ mol^{-1} for some steps, should still be relatively facile under the substrate temperatures typically involved in the CVD growth of diamond ($\approx$ 1000 K). In both pathways, the rate limiting step is the initial creation of the pendant CH_2 group and reformation of the dimer bond (involving barriers of 145 and 115 kJ mol^{-1} for migration along the chain and row, respectively). A rough estimate for the rate of this process can then be calculated using the Arrhenius equation:

$$\ln k = \ln A - \frac{E_a}{RT} \tag{1.1}$$

Here k is the rate, A is a pre-exponential factor, E_a is the activation energy, R is the ideal gas constant and T is temperature. Assuming that the pre-exponential factor A is of the order of a vibrational period on the surface (1×10^{13} s^{-1}) and T=1000 K, the rate of migration along the dimer chain (E_a=145 kJ mol^{-1}) can be calculated to be $\approx 2.67\times10^{5}$ s^{-1}. The migration is therefore on a similar time-scale as that predicted for H atom collisions with the surface (10^4-10^7 s^{-1} per carbon atom[26]), which through addition to radical sites would prevent migration, but will also enable migration by abstraction of H atoms from nearby surface carbons.

Surface migration of species towards step edges and their subsequent incorporation at these sites leading to step flow growth, has been proposed as an explanation for the stepped surfaces observed during diamond CVD.[45]

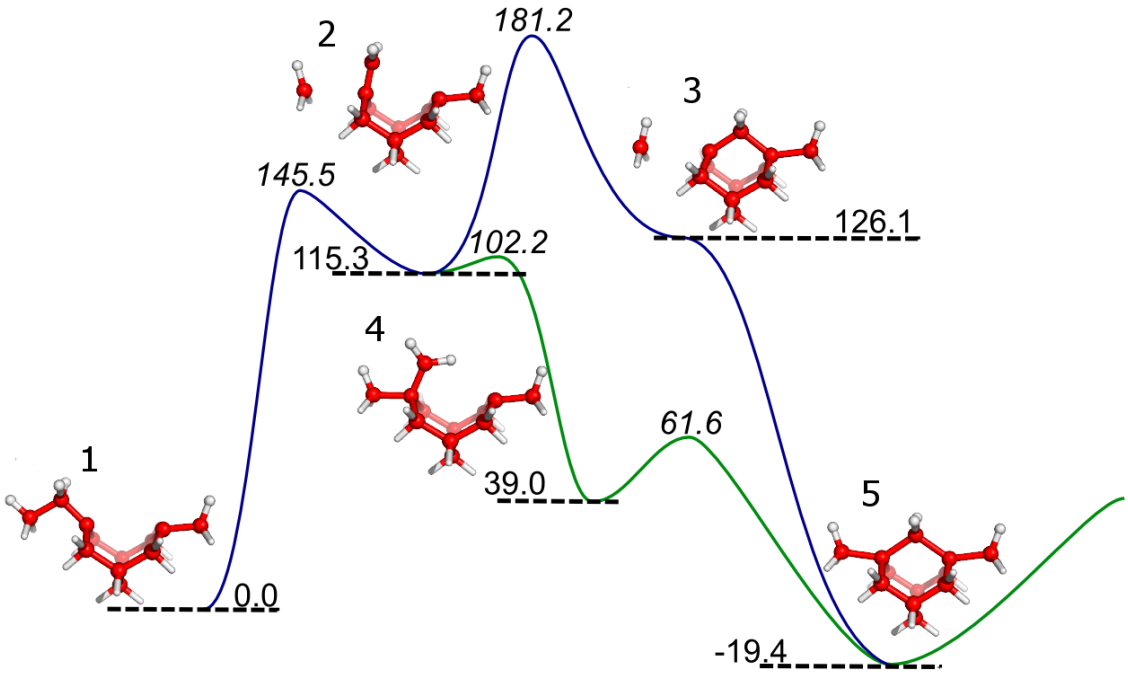

(a)

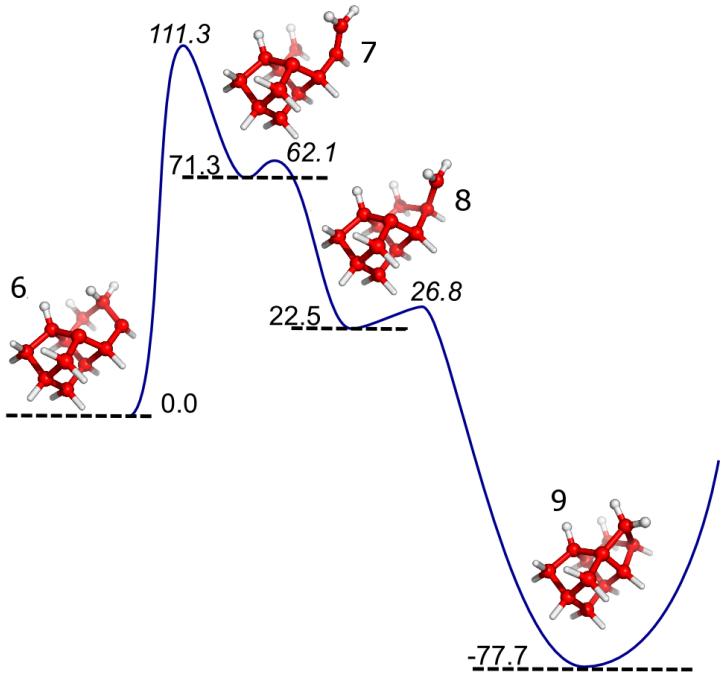

(b)

Figure 1.15: Energy profiles for a) migration along dimer chains and b) migration along dimer rows on the $\{100\}$:H 2×1 surface. Energies are in kJ mol^{-1} and are relative to the starting structures 1 and 6 for the migration along the chains and rows, respectively. Figure adapted from Cheesman *et al.*[34]

1.3 Doping of diamond films

Diamond has a large band gap (5.4 eV[47]) and is commonly thought of as an electrical insulator. The incorporation of atoms other than carbon into the diamond lattice introduces additional energy levels into the diamond band structure and, as a consequence, results in the diamond becoming conductive. These atoms can either be donors or acceptors, creating n-type or p-type semiconducting diamond respectively. The doping of diamond can be achieved either in-situ, during diamond growth, or post growth by techniques such as ion implantation.

1.3.1 p-type doping

Semiconducting p-type diamond is created by the introduction of acceptor levels just above the valence band of diamond. Promotion of electrons from the valence band to these new acceptor levels allows for the conduction due to the holes formed in the valence band.

The addition of boron into the diamond lattice is the most successful way of creating p-type diamond and occurs naturally in some diamonds.[48] Boron incorporation creates an acceptor level 0.37 eV above the energy of the valence band.[48] Boron can be easily incorporated into the diamond crystal lattice during the CVD process by the addition of small amounts of a precursor such as diborane or trimethylboron into the input gas mixture.

High levels of boron can be incorporated into diamond, with concentrations reaching $\geq 1 \times 10^{20}$ cm^{-3} ($\approx$0.06 % B). Diamond grown with such high levels of boron incorporation exhibit metallic behaviour and, at low temperatures, even becomes superconductive.[49]

1.3.2 n-type doping

In contrast to the ease with which p-type diamond is produced using boron as a dopant, the production of n-type diamond has met with much less success. Nitrogen as the donor would be an obvious choice with its additional electron compared to carbon, and it is commonly observed in natural diamonds. The donor level of substitutional nitrogen is however far too deep (1.6 eV below the conduction band[50]) and prevents conduction. Use of a number of other group V elements such as phosphorus and arsenic as substitutional donor atoms, or group I elements such as lithium and sodium as interstitial donor atoms, have also been attempted in order to create n-type diamond. However the results so far

have not been convincing.[17]

1.4 Plasma modelling

The plasmas used for the chemical vapour deposition of diamond are highly complex environments with a multitude of different chemical reactions taking place at the same time as well as collisions between species, diffusion of species, excitation/de-excitation of species and numerous other gas phase processes. Plasma diagnostic methods such as laser spectroscopy and optical emission spectroscopy only give information on a limited number of species which show characteristic absorptions or emissions in experimentally accessible wavelength regions. Many species are however difficult to study with these techniques, due to the wavelengths at which they absorb or emit light, and the degree to which their spectra can be resolved (normally limiting the species to either atoms or diatomic molecules). Neither do these techniques offer a direct measure of other parameters (e.g. the electron temperature T_e and the electron energy distribution function (EEDF)) that may effect the plasma composition, shape and size.

In order to gain further insight into the dynamic chemistry that is taking place within the plasma it is often useful to use computational models in conjunction with experimental diagnostic techniques. A number of models for various types of diamond CVD reactors exist such as those for bell jar type microwave reactors[51] or hot filament reactors.[52]

1.4.1 Bristol-Moscow model

The Bristol-Moscow model is described in detail by Mankelevich *et al.*[53] However, in brief, the Bristol-Moscow model of the Bristol MW-PECVD reactor is a 2D(r, z) model with a reactor height (z) and radius (r) of 6 cm and assumes cylindrical symmetry. The initial model concentrated on CH_4/ H_2/ Ar plasmas and included more than 38 species and over 240 direct and reverse reactions. This has recently been extended to include chemistry involving both boron and oxygen containing species.[54,55]

The model itself is comprised of three main blocks describing:

- Power absorption, gas heating, heat and mass transfer.
- Plasma activation of the gas mixture and diffusion of species.
- Gas-surface processes.

Rates of the various plasma activation reactions are dependent on the local electron energy distribution function, which in turn (at pressures $p \approx$ 75-150 Torr) is a function of the reduced electric field E/N. The model does not explicitly calculate E/N. Rather E/N and the electron temperature T_e are estimated from parameters within the model, describing the power absorption and the activation volume. The size of the plasma volume is guided by experimental spectroscopic measurements, whilst the absorbed power density, Q_J is calculated as a sum of power losses and gains associated with the interactions of electrons with other particles.

$$Q_J = \sum_i k_i N_j n_e \epsilon_e \tag{1.2}$$

k_i in eq. 1.2 is the rate coefficient associated with reaction i, n_e is the electron density, ϵ_e is the electron energy loss or gain associated with reaction i and N_j is the number density of the particle interacting with the electron.

A number of important plasma-chemical reactions (for a gas phase mixture of 4.4% CH_4 / 88.6% H_2/ 7% Ar at p = 150 Torr and power, P = 1.5 kW), their associated reaction rates and their contribution to the total absorbed power in the centre of the plasma region [*i.e.* radius, r = 0 mm the (the centre of the substrate) and height above the substrate surface, z = 10.5 mm] are shown in Appendix A. These processes determine the power density profiles, maximum electron densities ($n_e \approx 3 \times 10^{11}$ cm^{-3} in the centre of the plasma) and the gas temperature ($\approx$ 2930 K in the centre of the plasma).

The fraction of the absorbed power density shown for the various reactions in Appendix A highlights that the majority of the absorbed power density in the central region of the plasma (Q_J=30 W cm^{-3}) is used to either vibrationally ($\approx$66%) or rotationally ($\approx$27%) excite H_2 molecules, $\approx$5% is lost in elastic scattering of H_2+e, $\approx$1.6% is used to dissociate H_2 molecules and the remainder is used in the excitation and ionization of gas phase species. The majority of the input MW power in the model is thus dissipated by heating the gas via rotational-translation and vibrational-translation relaxation. The plasma model has shown that the production of H atoms within the plasma (which in turn drives the H-shifting reactions of the hydrocarbons in the gas phase) by thermal dissociation of H_2 is more than an order of magnitude greater than that produced by electron impact dissociation, under the high pressure conditions (p = 150 Torr) used in our reactor.[53]

Figure 1.16 shows a 2D false colour plot produced from the model output which shows the gas temperature as well as the H atom mole fraction (X_H %) as a function of r and z within the reactor volume. This figure serves to illustrate the inhomogeneity the gas temperature and H atom distribu-

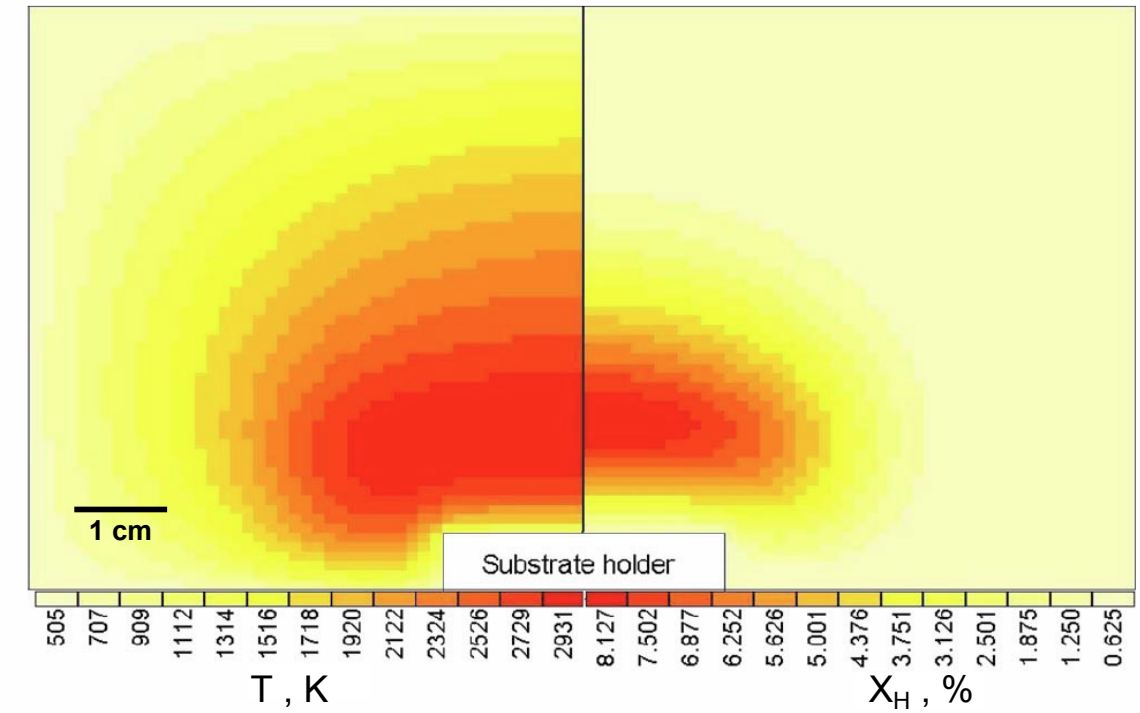

Figure 1.16: 2D(r,z) plots of the calculated gas temperatures, T_{gas} (K) and H atom mole fraction (%), (left and right respectively) from the plasma model. The red colouring highlights regions of high temperature and high H atom mole fractions, whilst the pale yellow region denotes lower temperatures and H atom mole fractions. This figure is reproduced from reference 53.

tion within the reactor; with the centre of the plasma ball being close 3000 K whilst close to the water cooled walls the gas temperature falls to near room temperature. It also illustrates how the majority of the H atoms are located within the high temperature region of the plasma ball.

As the pressure is constant throughout the reactor (p = 150 Torr) but T_{gas} declines by almost 10-fold between the centre and edge, the number density N/V must, as a consequence, increase by ≈10-fold (from the ideal gas law $pV = Nk_BT$, where k_B is the Boltzmann constant). Thus plots in terms of the mole fraction (e.g. Figure 1.16), exaggerates the spatial variation in species number density, and though X_H decreases by a factor of ≈13 between r = 0 and r= 6 cmm N_H only falls by a factor of ≈1.3.

Figure 1.17 shows 2D plots of the C_2H_2 and CH_4 mole fractions. The model was able to demonstrate how the plasma chemistry changed between the hot and cool regions of the plasma, with the most stable hydrocarbon species switching from CH_4 in the cooler plasma region to C_2H_2 in the hot region.

The model and its comparison with available experimental data is therefore a vital tool in under-

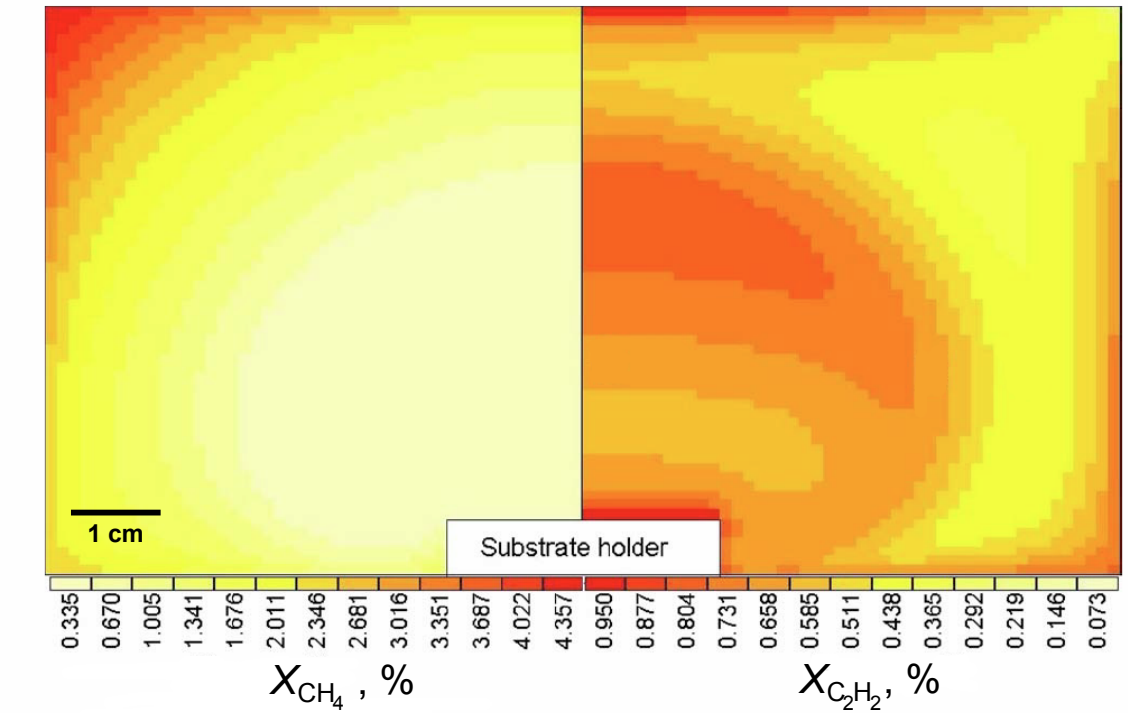

Figure 1.17: 2D(r,z) plots of the calculated C_2H_2 and CH_4 mole fractions, (left and right respectively) from the plasma model. The red colouring highlights regions with the highest mole fractions, whilst the pale yellow region denotes regions with a lower mole fraction . This figure is reproduced from reference 53.

standing the plasma chemistry involved in the CVD of diamond as it can be used to predict various plasma parameters and number densities of gas phase species which would be very difficult to measure experimentally. The number densities from these calculations can consequently be used to guide modelling of gas-surface reactions involved in the growth of diamond and are invaluable in understanding the entire process involved in CVD of diamond.

1.5 Aims

Work presented in this thesis has used optical spectroscopic techniques to investigate the gas phase chemistry within microwave plasmas used to grow diamond via chemical vapour deposition, and computational chemistry techniques to investigate gas-surface reactions involving the addition of gas phase species to the diamond surface and subsequent migration steps which may play a role in determining the morphologies of grown diamond film.

This thesis is organised such that: Chapter 2 includes background on the main computational and experimental techniques used throughout the thesis. Results from cavity ring down spectroscopy

(CRDS) and optical emission spectroscopy (OES) on CH_4/ H_2/ Ar plasmas with high Ar fractions are reported and contrasted with plasma modelling in Chapter 3. Experimental results studying B atoms within B_2H_6/CH_4/H_2/Ar plasmas and how plasma parameters effect their concentration are presented in Chapter 4. Then in Chapter 5 preliminary OES and CRDS work on CO_2/CH_4/H_2 plasmas are presented. Chapters 6-8 describe computational chemistry work. Firstly Chapter 6 details reactions in which hydrocarbon species within the gas phase can directly insert into C-H and C-C bonds on the growing diamond surface. In Chapter 7 the surface migration of CH_2 groups between the $\{100\}$:H 2×1 and $\{111\}$:H surfaces and on the $\{111\}$:H surface of diamond is investigated and calculated energetics for a number of pathways are presented. Finally Chapter 8 details calculated energetics for the insertion of B atoms and BH radicals into C-H and C-C bonds and for a number of pathways via which BH surface groups can migrate on the $\{100\}$:H 2×1 surface, the $\{111\}$:H surface and between the $\{100\}$:H 2×1 and $\{111\}$:H diamond surfaces. These results are compared with the analogous pathways involving CH_2 species. The thesis concludes with a brief summary and suggestions for future work.

References

[1] R. H. Savage and D. L. Schaeffer, *J. Appl. Phys.* **27**, 136 (1956).

[2] K. B. Yen, B. E. Schwickert, and M. F. Toney, *Appl. Phys. Lett.* **84**, 4702 (2004).

[3] R. F. Deacon and J. F. Goodman, *Proc. R. Soc. London, Ser. A* **243**, 464 (1958).

[4] P. W. May, *Phil. Trans. R. Soc. Lond., A* **358**, 473 (2000).

[5] L. Alianelli, K. J. S. Sawhney, A. Malik, O. J. L. Fox, P. W. May, and R. Stevens, *J. Appl. Phys.* **108**, 123107 (2010).

[6] R. P. Mildren and A. Sabella, *Opt. Lett.* **34**, 2811 (2009).

[7] S. Porro, G. De Temmerman, S. Lisgo, P. John, I. Villalpando, J. W. Zimmer, B. Johnson, and J. I. B. Wilson, *Diam. Rel. Mater.* **18**, 740 (2009).

[8] C. E. Nebel, B. Rezek, D. Shin, H. Uetsuka, and N. Yang, *J. Phys. D, Appl. Phys.* **40**, 6443 (2007).

[9] P. Bergonzo, A. Bongrain, E. Scorsone, A. Bendali, L. Rousseau, G. Lissorgues, P. Mailley, Y. Li, T. Kauffmann, F. Goy, B. Yvert, J. A. Sahel, and S. Picaud, *IRBM* **32**, 91 (2011).

[10] H. P. Bovenkerk, F. P. Bundy, H. T. Hall, H. M. Strong, and R. H. Wentorf, *Nature* **184**, 1094 (1959).

[11] F. P. Bundy, *J. Geophys. Res.* **85**, 6390 (1980).

[12] D. G. Goodwin and J. E. Butler, in *Handbook of Industrial Diamond and Diamond Films*, edited by M. A. Prelas, A. Popovici, and L. K. Bigelow, chapter 11, pages 527–581 (Marcel Dekker, Inc., 1998).

[13] T. Tsubota, M. Ohta, K. Kusakabe, S. Morooka, M. Watanabe, and H. Maeda, *Diam. Rel. Mater.* **9**, 1380 (2000).

[14] M. Ece, B. Oral, and J. Patscheider, *Diam. Rel. Mater.* **5**, 211 (1996).

[15] Yu. A. Mankelevich, N. V. Suetin, M. N. R. Ashfold, J. A. Smith, and E. Cameron, *Diamond Relat. Mater.* **10**, 364 (2001).

[16] J. Ma, J. C. Richley, M. N. R. Ashfold, and Yu. A. Mankelevich, *J. Appl. Phys.* **104**, 103305 (2008).

[17] R. Kalish, *Carbon* **37**, 781 (1999).

[18] W. Müller-Sebert, E. Wörner, F. Fuchs, C. Wild, and P. Koidl, *Appl. Phys. Lett.* **68**, 759 (1996).

[19] A. Gicquel, M. Chenevier, Kh. Hassouni, A. Tserepi, and M. Dubus, *J. Appl. Phys.* **83**, 7504 (1998).

[20] D. Zhou, T. G. McCauley, L. C. Qin, A. R. Krauss, and D. M. Gruen, *J. Appl. Phys.* **83**, 540 (1998).

[21] C.-F. Chen, Y. C. Huang, S. Hosomi, and I. Yoshida, *Hyomen Gijutsu* **40**, 305 (1989).

[22] J. R. Petherbridge, P. W. May, S. R. J. Pearce, K. N. Rosser, and M. N. R. Ashfold, *J. Appl. Phys.* **89**, 1484 (2001).

[23] C. F. Chen, S. Chen, H. Ko, and S. E. Hsu, *Diam. Rel. Mater.* **3**, 443 (1994).

[24] P. K. Bachmann, D. Leers, and H. Lydtin, *Diam. Rel. Mater.* **1**, 1 (1991).

[25] J. C. Richley, O. J. L. Fox, M. N. R. Ashfold, and Yu. A. Mankelevich, *J. Appl. Phys.* **109**, 063307 (2011).

[26] J. E. Butler, Yu. A. Mankelevich, A. Cheesman, J. Ma, and M. N. R. Ashfold, *J. Phys.: Condens. Matter* **21**, 364201 (2009).

[27] J. E. Butler and R. L. Woodin, *Phil. Trans. R. Soc. Lond., A* **342**, 209 (1993).

[28] Z. L. Wang, J. Bentley, R. E. Clausing, L. Heatherly, and L. L. Horton, *J. Mater. Res.* **9**, 1552 (1994).

[29] K. Bobrov, A. Mayne, G. Comtet, G. Dujardin, L. Hellner, and A. Hoffman, *Physical Review B* **68**, 195416 (2003).

[30] D. Huang and M. Frenklach, *J. Phys. Chem.* **95**, 3692 (1991).

[31] S. J. Harris, *Appl. Phys. Lett.* **56**, 2298 (1990).

[32] S. J. Harris and D. G. Goodwin, *J. Phys. Chem.* **97**, 23 (1993).

[33] B. Garrison, E. Dawnkaski, D. Srivastava, and D. Brenner, *Science* **255**, 835 (1992).

[34] A. Cheesman, J. N. Harvey, and M. N. R. Ashfold, *J. Phys. Chem. A* **112**, 11436 (2008).

[35] S. Skokov, B. Weiner, and M. Frenklach, *J. Phys. Chem.* **98**, 8 (1994).

[36] L. F. Sutcu, C. J. Chu, M. S. Thompson, R. H. Hauge, J. L. Margrave, and M. P. D'Evelyn, *J. Appl. Phys.* **71**, 5930 (1992).

[37] M. Tsuda, M. Nakajima, and S. Oikawa, *J. Am. Chem. Soc.* **108**, 5780 (1986).

[38] C. C. Battaile, D. J. Srolovitz, and J. E. Butler, *Diam. Rel. Mater.* **6**, 1198 (1997).

[39] J. E. Butler and I. Oleynik, *Phil. Trans. R. Soc. A* **366**, 295 (2008).

[40] C. J. Chu, R. H. Hauge, J. L. Margrave, and M. P. D'Evelyn, *Appl. Phys. Lett.* **61**, 1393 (1992).

[41] D. N. Belton and S. J. Harris, *J. Chem. Phys.* **96**, 2371 (1992).

[42] D. A. Horner, L. A. Curtiss, and D. M. Gruen, *Chem. Phys. Lett.* **233**, 243 (1995).

[43] B. V. Deryagin and D. v. Fedosayev, *Surf. Coating Technol.* **38**, 131 (1989).

[44] M. Frenklach and S. Skokov, *J. Phys. Chem. B* **101**, 3025 (1997).

[45] M. Frenklach, S. Skokov, and B. Weiner, *Nature* **372**, 535 (1994).

[46] K. Larsson and J. O. Carlsson, *Phys. Rev. B: Condens. Matter* **59**, 8315 (1999).

[47] J. E. Field, *The properties of natural and synthetic diamond* (Academic Press Limited, 1992).

[48] A. T. Collins and A. W. S. Williams, *J. Phys. C: Solid St. Phys.* **4**, 1789 (1971).

[49] T. Yokoya, T. Nakamura, T. Matsushita, T. Muro, Y. Takano, M. Nagao, T. Takenouchi, H. Kawarada, and T. Oguchi, *Nature* **438**, 647 (2005).

[50] R. G. Farrer, *Solid State Commun.* **7**, 685 (1969).

[51] K. Hassouni, F. Silva, and A. Gicquel, *J. Phys. D: Appl. Phys.* **43**, 153001 (2010).

[52] D. W. Comerford, J. A. Smith, M. N. R. Ashfold, and Yu. A. Mankelevich, *J. Chem. Phys.* **131**, 0044326 (2009).

[53] Yu. A. Mankelevich, M. N. R. Ashfold, and J. Ma, *J. Appl. Phys.* **104**, 113304 (2008).

[54] Yu. A. Mankelevich, M. N. R. Ashfold, D. W. Comerford, J. Ma, and J. C. Richley, *Thin Solid Films* **519**, 4421 (2011).

[55] J. Ma, J. C. Richley, D. R. W. Davies, A. Cheesman, M. N. R. Ashfold, and Yu. A. Mankelevich, *J. Phys. Chem. A* **114**, 2447 (2010).

2

Computational methods, background spectroscopy, and experimental techniques

2.1 Computational techniques

Computational chemistry allows for the detailed study and mapping of the potential energy surface (PES) associated with different molecules and reactions. The PES is a multidimensional surface where potential energy is related to the geometry of atoms in the system. The larger system and the more degrees of freedom that are available the more complicated the surface becomes. From the PES the global energy minimum of the system can be determined. A reaction coordinate can also be determined from a PES and is the pathway on the PES through which a chemical reaction will occur converting the reactants to products. Along this pathway minima and transition states (first order saddle points) associated with the reaction can be identified. A simplified PES restricted to the reaction coordinate is illustrated in Figure 2.1.

Two main types of calculation have been employed to study a variety of different chemical reactions within this thesis. These are the quantum mechanical (QM) based technique of density functional theory (DFT) and the empirical technique of molecular mechanics (MM). QM calculations model the electronic interactions between atoms within molecules and can be used in the calculation of accurate energetics and various other properties of the species in question. The calculations however, are computationally intensive and take significantly longer the larger the molecule in question is. MM calculations model the interaction of atoms within a molecule using predetermined empirical potentials. This approach is significantly quicker than that used in the QM calculations and enables the study of significantly larger structures. MM calculations do however, suffer from a major drawback, in that they are unable to describe the bond breaking and forming processes which are involved in chemical reactions. QM/MM techniques combine the accuracy of QM techniques and their ability to describe chemical reactions with the ability of MM calculations to handle large systems.

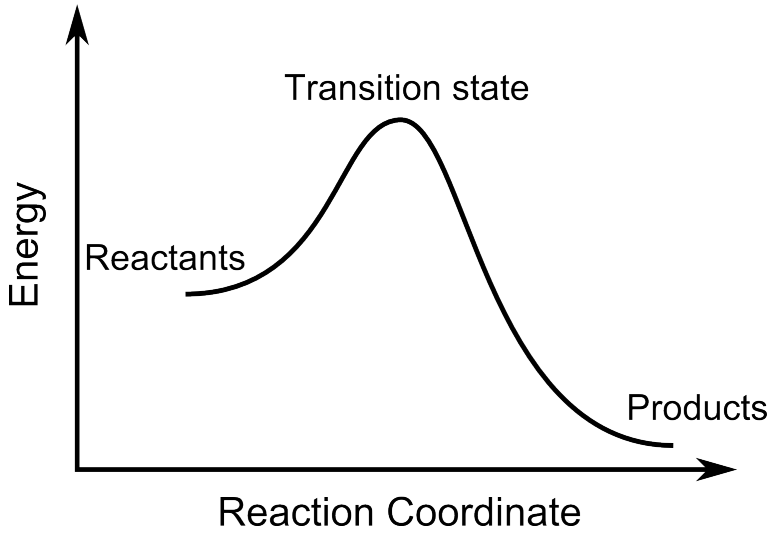

Figure 2.1: A simplified illustration of a potential energy surface along the reaction coordinate.

2.1.1 The Schrödinger equation and the Hartree-Fock approximation

The time-independent Schrödinger equation (2.1) links the wavefunction Ψ of a system via the Hamiltonian operator, $\hat{\mathrm{H}}$ to the total energy, E of the system.

$$\hat{\mathrm{H}}\Psi = \mathrm{E}\Psi \tag{2.1}$$

The solution to the Schrödinger equation would tell us the total energy of the system of interest and the wavefunction would contain all the information that could possibly be known about the state of the system. However, apart from a few simple systems (e.g. a H atom) this equation is unsolvable. Attempts to solve the equation approximately form the basis of most ab initio techniques.

The Hamiltonian operator representing the total energy of a molecular system can be broken down into five different contributions (2.2); the kinetic energy of the electrons and the nuclei $\hat{\mathrm{T}}_e$ and $\hat{\mathrm{T}}_N$ respectively and the potential energy terms resulting from the electrostatic nucleus-electron $\hat{\mathrm{V}}_{Ne}$ (can also termed $\hat{\mathrm{V}}_{\mathrm{ext}}$), electron-electron $\hat{\mathrm{V}}_{ee}$ and nucleus-nucleus $\hat{\mathrm{V}}_{NN}$ interactions.

$$\hat{\mathrm{H}} = \hat{\mathrm{T}}_e + \hat{\mathrm{T}}_N + \hat{\mathrm{V}}_{Ne} + \hat{\mathrm{V}}_{ee} + \hat{\mathrm{V}}_{NN} \tag{2.2}$$

$\hat{\mathrm{H}}$ can be simplified by assuming the Born-Oppenheimer approximation. This states that, due to the large difference between the masses of nuclei and electrons, the nuclei move significantly slower than the electrons, hence it can be assumed that the nuclei are effectively fixed in space. This results

in the removal of the $\hat{T}_N$ term as the kinetic energy of stationary atoms will be equal to zero and the nucleus-nucleus potential energy term $\hat{V}_{NN}$ will become a constant. This results in the electronic Hamiltonian (2.3).

$$\hat{H}_{\text{elec}} = \hat{T}_e + \hat{V}_{Ne} + \hat{V}_{ee} \tag{2.3}$$

The electronic Schrödinger equation with the Hamiltonian $\hat{H}_{\text{elec}}$ thus has the electronic wavefunction Ψ_{elec} as its solution (2.4).

$$\hat{H}_{\text{elec}}\Psi_{\text{elec}} = E_{\text{elec}}\Psi_{\text{elec}} \tag{2.4}$$

The electronic wavefunction is dependent on the coordinates of the electrons at a fixed nucleus arrangement and is unobservable. The square of the wavefunction is equal to the probability density of finding the electrons at locations within the system. The wavefunction is said to be normalized if the integral of the square of the wavefunction over all space is equal to 1 (2.5).

$$\int \cdots \int |\Psi(\vec{x}_1, \vec{x}_2, \ldots, \vec{x}_N)|^2 d\vec{x}_1, d\vec{x}_2, \ldots, d\vec{x}_N = 1 \tag{2.5}$$

where $\vec{x}_i$ represents the position and spin of electron i.

As the true ground state wavefunction of the system is unknown, it is impossible to solve the Schrödinger equation exactly (with a few exceptions as mentioned earlier) and obtain the true ground state energy E_0. The energy of the true ground state however can be approached systematically using the variational principle, (2.6) which states that any value of E derived from a normalized approximate wavefunction Ψ_{trial} will be larger than the true energy of the ground state unless $\Psi_{\text{trial}} = \Psi_0$.[1]

$$\int \Psi^*_{\text{trial}}\hat{H}\Psi_{\text{trial}}\, d\tau = E_{\text{trial}} \geq E_0 = \int \Psi^*_0\hat{H}\Psi_0\, d\tau \tag{2.6}$$

Therefore the true ground state energy and wave function can be ascertained by minimising the energy by searching through all acceptable N-electron wavefunctions. The wavefunction which results in the lowest energy is equal to Ψ_0. An acceptable wavefunction must meet certain requirements so that it makes physical sense, such as it must be normalizable and, in the case of electrons, Ψ must

be anti-symmetric (*i.e.* upon interchanging the spatial and spin coordinates of any two electrons the wavefunction changes sign (2.7)).

$$\Psi(\vec{\mathrm{x}}_1, \vec{\mathrm{x}}_2, \ldots, \vec{\mathrm{x}}_\mathrm{N}) = -\Psi(\vec{\mathrm{x}}_2, \vec{\mathrm{x}}_1, \ldots, \vec{\mathrm{x}}_\mathrm{N}) \tag{2.7}$$

Searching over all acceptable N-electron wavefunctions however is not possible and usually a subset of the possible wavefunctions is used. The variation principle can then be applied within the subset and the energy minimized accordingly. However this will not result in locating the true ground state of the system unless the Ψ_0 lies within the subset.

The Hartree-Fock approximation is an example of this approach whereby the search for the true N-electron wavefunction is restricted to the subset consisting of all Slater determinants (Φ_{SD}) composed of N spin orbitals ($\chi_i(\vec{\mathrm{x}}_j)$) (2.8). This ensures that the wavefunction is antisymmetric and therefore complies with the Pauli exclusion principle that no two electrons of similar spin can occupy the same quantum state simultaneously.

$$\Psi_0 \approx \Phi_{\mathrm{SD}} = \frac{1}{\sqrt{N!}} \begin{vmatrix} \chi_1(\vec{x}_1) & \chi_2(\vec{x}_1) & \cdots & \chi_\mathrm{N}(\vec{x}_1) \\ \chi_1(\vec{x}_2) & \chi_2(\vec{x}_2) & \cdots & \chi_\mathrm{N}(\vec{x}_2) \\ \vdots & \vdots & \ddots & \vdots \\ \chi_1(\vec{x}_\mathrm{N}) & \chi_2(\vec{x}_\mathrm{N}) & \cdots & \chi_\mathrm{N}(\vec{x}_\mathrm{N}) \end{vmatrix} \tag{2.8}$$

The spin orbitals are composed of both a spatial orbital ϕ and a spin function (either α or β) representing the spin of the electron $\pm\frac{1}{2}$. The spin orbitals within the Slater determinant are then varied and the energy minimized to obtain the Hartree-Fock energy E_{HF}.

Hartree-Fock theory however suffers from that fact that it describes a system of N electrons in which the electrons only interact in an averaged sense (*i.e.* it neglects electron correlation). This limits the accuracy of Hartree-Fock theory. This deficiency has led to the development of other approaches to deal with the electron correlation such as Møller-Plesset perturbation theory, configuration interaction and coupled cluster theory.

2.1.2 Density functional theory

Methods such as Hartree-Fock rely on approximating the true wavefunction of the system in an attempt to solve the Schrödinger equation approximately. This approach has the advantage that once

the wavefunction is known all information about the system is available. However, as the system increases in size with the addition of more atoms and electrons the wavefunction becomes very complicated and harder to calculate. Another approach is to use the electron density $\rho(\vec{r})$ and gives rise to the name of the technique: density functional theory (DFT).

Modern density functional theories are based on the two Hohenberg-Kohn theorems[2]. The first theorem states that an applied external potential $\hat{V}_{ext}(\vec{r})$ is a unique functional of $\rho(\vec{r})$. The demonstrated proof is based on *reductio ad absurdum* and is as follows:

Assuming that two external potentials $\hat{V}_{ext}$ and $\hat{V}'_{ext}$ both give rise to the same electron density and are in turn part of two different Hamiltonians which only differ by their external potential (2.9).

$$\hat{H} = \hat{T} + \hat{V}_{ee} + \hat{V}_{ext} \text{ and } \hat{H}' = \hat{T} + \hat{V}_{ee} + \hat{V}'_{ext} \tag{2.9}$$

Each of these Hamiltonians will therefore be associated with a different ground state wavefunction, Ψ and Ψ' and each wavefunction will have a corresponding ground state energy E_0 and E'_0, where $E_0 \neq E'_0$ as they correspond to different wavefunctions and satisfy different Schrödinger equations (unless $\hat{V}_{ext}$ and $\hat{V}'_{ext}$ only differ by a constant).

From the variational principle it can then be seen that

$$E_0 < \int \Psi'^* \hat{H} \Psi' \, d\vec{r} = \int \Psi'^* \hat{H}' \Psi' \, d\vec{r} + \int \Psi'^* (\hat{H} - \hat{H}') \Psi' \, d\vec{r} \tag{2.10}$$

As the Hamiltonian operators only differ by the external potential,

$$E_0 < E'_0 + \int \rho(\vec{r}) [\hat{V}_{ext} - \hat{V}'_{ext}] d\vec{r} \tag{2.11}$$

Then by interchanging the primed and unprimed quantities it is also seen that

$$E'_0 < E_0 + \int \rho(\vec{r}) [\hat{V}'_{ext} - \hat{V}_{ext}] d\vec{r} \tag{2.12}$$

Combining (2.11) and (2.12) together leads to

$$E_0 + E'_0 < E_0 + E'_0 \tag{2.13}$$

This is self-contradictory and demonstrates that there can be no two $\hat{V}_{ext}$ which yield the same ground state electron density, and therefore $\rho(\vec{r})$ uniquely determines $\hat{H}$ and hence Ψ and E.

The ground state energy is thus shown to be a functional of the ground state electron density and its components must be as well.[3]

$$E_0[\rho_0] = T[\rho_0] + E_{ee}[\rho_0] + E_{Ne}[\rho_0] \tag{2.14}$$

This can then be separated into parts which are either dependent or independent of the system. For example, the potential energy, E_{Ne}, representing the nuclei-electron interaction is dependent on the system, whilst the kinetic energy, $T[\rho_0]$ and electron-electron repulsion term, $E_{ee}[\rho_0]$ are independent. The energy can then be expressed as

$$E_0[\rho_0] = E_{Ne}[\rho_0] + F_{HK}[\rho_0] \tag{2.15}$$

where $F_{HK}[\rho_0]$ is the Hohenberg-Kohn functional and contains the system-independent parts of the total energy.

The second Hohenberg-Kohn theorem demonstrates how the variational principle can be applied in density functional theory, *i.e.* any energy obtained from the functional using a trial density $\rho'(\vec{r})$ (satisfying the condition that $\int \rho'(\vec{r})\ d\vec{r} = N$ in a system containing N particles) will be larger than that produced from the true ground state electron density ρ_0.

$$E[\rho'] = E_{Ne}[\rho'] + F_{HK}[\rho'] \geq E_{Ne}[\rho_0] + F_{HK}[\rho_0] = E[\rho_0] \tag{2.16}$$

Unfortunately the exact form of the functional $F_{HK}[\rho]$ and its constituent parts $T[\rho]$ and $E_{ee}[\rho]$ are unknown, it is therefore impossible to solve the equation exactly. The electron-electron interaction term $E_{ee}[\rho]$ can be split into two parts, the classical Coulomb part $J[\rho]$ (the form of which is known) and a non-classical contribution, $E_{ncl}[\rho]$. The Kohn-Sham approach[4] allows the problem of calculating the total kinetic energy $T[\rho]$ to be bypassed by introducing the idea of a system without electron-electron interactions. As in Hartree-Fock theory, the wave function of a non-interacting system is represented as a Slater determinant. The Slater determinant in this case is made up of Kohn-Sham orbitals which are determined by the operation of the one-electron Kohn-Sham operator. This ends up splitting the kinetic energy into two parts, the exact kinetic energy of a non-interacting system, $T_S[\rho]$ that can be

calculated from the Slater determinant plus an unknown non-classical part, $T_C[\rho]$. This leads to the functional:

$$F[\rho] = T_S[\rho] + J[\rho] + E_{XC}[\rho] \tag{2.17}$$

where,

$$E_{XC}[\rho] = T_C[\rho] + E_{ncl}[\rho] \tag{2.18}$$

and is termed the exchange-correlation functional. This represents the remaining unknown parts of the functional $F[\rho]$.

The local density approximation (LDA) is one approach that has been applied to try and approximate the form of the exchange-correlation functional. This approach is based on the model of a uniform electron gas (a system which consists of electrons moving on a positive background charge such that the system is electrically neutral and the electron density has a constant value everywhere). Under this approximation, the form of the exchange and correlation energy functionals are known to a high degree of accuracy and an estimate of the E_{XC} can be calculated. This model is fairly good for systems such as simple metals,[3] but it is unlikely to prove as good a model for molecules and atoms.

In order to address the shortcomings of the LDA method in its treatment of the electron density in molecules and atoms the generalized gradient approximation (GGA) was developed. The GGA not only relies on the density information at a particular point ($\rho(\vec{r})$) as in the LDA, but also includes the density gradient ($\nabla\rho(\vec{r})$) at that particular point (2.19).[5]

$$E_{XC}^{GGA}[\rho(\vec{r})] = E_{XC}^{LDA}[\rho(\vec{r})] + \Delta E_{XC}\left[\frac{|\nabla\rho(\vec{r})|}{\rho^{\frac{4}{3}}(\vec{r})}\right] \tag{2.19}$$

This allows for non-uniform electron density distributions, which are much more realistic for treatment of molecules and atoms.

In both LDA and GGA, E_{XC} can be split into two contributions, exchange E_X and correlation E_C (2.20).

$$E_{XC} = E_X + E_C \tag{2.20}$$

A number of GGA functionals have been developed to describe both the exchange and correlation energies, e.g. the exchange functional B developed by Becke[6] and optimised by fitting to the known exchange energies of rare gas atoms He-Rn and PBE by Perdew, Burke and Ernzerhof.[7] These are used in conjunction with correlation functionals such as P86[8] and LYP[9] (LYP, unlike most other functionals, is not based on the uniform electron gas but, instead, on an expression describing the correlation energy of an helium atom).

The exchange-correlation energy functional can also be expressed as a function of λ, an interelectron coupling strength parameter.[3]

$$E_{XC} = \int_0^1 E_{XC}^{\lambda} \, d\lambda \tag{2.21}$$

The value of λ governs the extent to which the coulombic repulsion between electrons is "turned" on. $\lambda = 0$ is equivalent to the non-interacting system whilst $\lambda = 1$ represents the fully interacting system. This equation thus links the non-interacting and fully interacting systems together and is known as the adiabatic connection.

When $\lambda = 0$, the system is free of electron-electron interaction and E_{XC} is composed only of exchange. This exchange contribution can then be calculated from the Slater determinant of Kohn-Sham orbitals just as happens in Hartree-Fock theory. When $\lambda = 1$, approximations of E_{XC} are available from existing functionals. The dependence of E_{XC}^{λ} as a function of λ between the values of 0 and 1 is however unknown, so approximations must be made. One of the simplest approximations is that E_{XC}^{λ} is linear with respect to λ. This led to the half and half method[10] (2.22).

$$E_{XC}^{HH} = \frac{1}{2}E_{XC}^{\lambda=0} + \frac{1}{2}E_{XC}^{\lambda=1} \tag{2.22}$$

The $\frac{1}{2}E_{XC}^{\lambda=1}$ contribution is calculated using the LDA exchange-correlation functional and the $\frac{1}{2}E_{XC}^{\lambda=0}$ contribution is from the Slater determinant. The incorporation of both Hartree-Fock type exchange and DFT exchange-correlation energies has led to these functionals being termed, hybrid functionals.

One of the next advances in the development of these hybrid functionals was the introduction of semiempirical weightings to determine the contribution of various components of the functional, e.g. the B3PW91 functional[11](2.23):

$$\mathrm{E}_{\mathrm{XC}}^{\mathrm{B3PW91}} = \mathrm{E}_{\mathrm{XC}}^{\mathrm{LDA}} + a(\mathrm{E}_{\mathrm{X}}^{\lambda=0} - \mathrm{E}_{\mathrm{X}}^{\mathrm{LDA}}) + b\Delta\mathrm{E}_{\mathrm{X}}^{\mathrm{B88}} + c\Delta\mathrm{E}_{\mathrm{C}}^{\mathrm{PW91}} \tag{2.23}$$

The semiempirical coefficients are then optimised by comparison with a test set of energies. One of the most popular hybrid functionals is B3LYP[12] (2.24), which is a modified version of the B3PW91 functional where the LYP correlation functional is used in place of PW91.

$$\mathrm{E}_{\mathrm{XC}}^{\mathrm{B3LYP}} = (1-a)\mathrm{E}_{\mathrm{X}}^{\mathrm{LDA}} + a\mathrm{E}_{\mathrm{X}}^{\lambda=0} + b\Delta\mathrm{E}_{\mathrm{X}}^{\mathrm{B88}} + c\Delta\mathrm{E}_{\mathrm{C}}^{\mathrm{LYP}} + (1-c)\Delta\mathrm{E}_{\mathrm{C}}^{\mathrm{LDA}} \tag{2.24}$$

2.1.3 Molecular mechanics

Modelling of the electronic interactions using wavefunction or density functional based methods allows for accurate computation of molecular geometries and the study of chemical reactions. These methods are however computationally intensive making their application to large systems impractical. Molecular mechanics (MM) is one solution to the problem of modelling large systems.

Instead of attempting to solve the electronic Schrödinger equation for the entire system the interactions between atoms within the system are determined by a set of empirical potentials that govern; bond lengths, bond angles, torsion angles and non-bonding interactions. The relative energy of the system can then be approximated by the sum of all the contributions.

A simple approximation for the change in the potential energy caused by a bond stretching is that of the harmonic oscillator (2.25), where r_{AB}, $r_{\mathrm{AB,eq}}$ and k are the bond length, equilibrium bond length and force constant between two atoms respectively.

$$\mathrm{E}_{Bondstretch} = \frac{1}{2}k(r_{\mathrm{AB}} - r_{\mathrm{AB,eq}})^2 \tag{2.25}$$

This simple approximation works well close to the equilibrium bond length but as the difference between the actual bond length and the equilibrium bond length increases the accuracy decreases. A number of solutions are available to solve this problem. One is to use a Morse potential (2.26) and another solution is to include higher cubic or quartic terms each with their own force constants to the harmonic oscillator potential (2.27).

$$\mathrm{E}_{Bondstretch} = D_{\mathrm{AB}}(1 - e^{-\alpha_{\mathrm{AB}}(r_{\mathrm{AB}} - r_{\mathrm{AB,eq}})})^2 \tag{2.26}$$

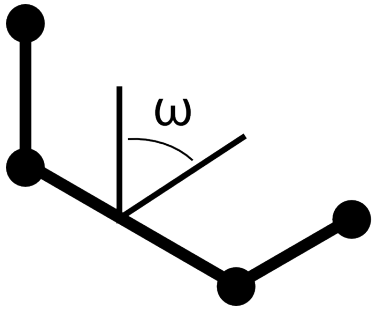

Figure 2.2: An illustration of the torsion (dihedral) angle ω between four atoms.

$$\mathrm{E}_{Bondstretch} = \frac{1}{2}[k + k_3(r_{\mathrm{AB}} - r_{\mathrm{AB,eq}}) + k_4(r_{\mathrm{AB}} - r_{\mathrm{AB,eq}})^2](r_{\mathrm{AB}} - r_{\mathrm{AB,eq}})^2 \ . \tag{2.27}$$

D_{AB} and α_{AB} in the Morse potential are the dissociation energy of the bond and a fitting constant, respectively. The Morse potential provides a better description of the potential energy associated with the change in bond length than inclusion of higher terms to the harmonic potential does, but it is much more computationally intensive to evaluate.[5] As MM methods are designed for use on very large systems, the computationally more efficient method is normally chosen.

A similar function is used to describe the change in potential energy arising from a change in a bond angle, θ (2.28).

$$\mathrm{E}_{Bondangle} = \frac{1}{2}[k + k_3(\theta - \theta_{\mathrm{eq}}) + k_4(\theta - \theta_{\mathrm{eq}})^2 + \ldots](\theta - \theta_{\mathrm{eq}})^2 \tag{2.28}$$

The potential energy of the system can also be influenced by strain induced by torsion. The strain is caused by the repulsion between the electron clouds associated with bonds and groups which are attached to two atoms bonded together. This results in a periodic function dependent on the torsion (dihedral) angle, ω. An illustration of the torsion angle between four atoms is shown in Figure 2.2.

To describe the periodicity of torsional strain a function of the form shown in (2.29) is typically used.[5]

$$\mathrm{E}_{Torsion} = \frac{1}{2}\sum_{\{j\}} V_j[1 + (-1)^{j+1}\cos(j\omega + \psi_j)] \tag{2.29}$$

V_j is the amplitude and $\{j\}$ is a set of periodicities reflecting the torsions environment. ψ_j represents a phase angle which, allows for fine tuning of the torsions.

In a real system bond lengths, angles and torsions are not independent of each other. MM calculations therefore also include coupling terms such as stretch-bend coupling to take account of this[5].

Non-bonding interactions are also calculated and can be split into two different categories, the van der Waals interactions (steric interactions) and the electrostatic interactions (*i.e.* interactions between charges present on atoms).

Van der Waals interactions are typically described with the Lennard-Jones potential (2.30).

$$\mathrm{E}_{vdW} = 4\varepsilon_{\mathrm{AB}} \left[\left(\frac{\sigma_{\mathrm{AB}}}{r_{\mathrm{AB}}} \right)^{12} - \left(\frac{\sigma_{\mathrm{AB}}}{r_{\mathrm{AB}}} \right)^{6} \right] \tag{2.30}$$

The inverse 6th power relationship to the distance between two atoms, r_{AB}, describes the attractive potential between an induced dipole on each atom. While the inverse 12th power term represents the repulsive potential as the atoms become increasingly close together. $\varepsilon_{\mathrm{AB}}$ is the well depth of the attraction and σ_{AB} is the inter-atomic distance where the attractive and repulsive forces balance each other.

The potential energy associated with electrostatic non-bonding interactions originates from the interaction of partial charges on two atoms A and B (q_{A} and q_{B}). The potential energy is related to the distance between the two atoms r_{AB} and a dielectric constant $\varepsilon_{\mathrm{AB}}$ by;

$$\mathrm{E}_{electrostatic} = \frac{q_{\mathrm{A}} q_{\mathrm{B}}}{\varepsilon_{\mathrm{AB}} r_{\mathrm{AB}}} \tag{2.31}$$

The electrostatic interactions can be further extended to include the polarisation of atoms.[5]

To describe the interactions present in a system a number of parameters relating to the atoms and their local environment are required. These parameters are normally contained within so called force fields. The force fields are normally tailored to specific applications and are derived from relevant experimental measurements or quantum chemical calculations. A large number of different force fields exist, e.g. the MM2 force field, used in our current studies which is tailored for organic molecules and includes parameters derived from diamond and a selection of other hydrocarbons,[13] and the CHARMM force field that is parametrized for biomolecules.

2.1.4 QM/MM calculations

QM/MM is a hybrid technique which aims to combine the high accuracy of QM calculations and their ability to describe chemical reactions with the scalability of MM calculations, in an attempt to offset the weaknesses of both approaches when used separately. These calculations are typically approached by selecting a small region of the system where a chemical reaction is taking place and treating it with QM methods, whilst the rest of the system which is not actively involved in the reaction, but may play an important role in determining the geometry, is treated with MM methods.

The overall QM/MM system can be described by the combination of the Hamiltonians representing the QM ($\hat{\mathrm{H}}_{QM}$) and MM ($\hat{\mathrm{H}}_{MM}$) regions plus a third Hamiltonian $\hat{\mathrm{H}}_{QM/MM}$ representing the interactions between the QM and MM regions[14] (2.32).

$$\hat{\mathrm{H}}_{Total} = \hat{\mathrm{H}}_{QM} + \hat{\mathrm{H}}_{MM} + \hat{\mathrm{H}}_{QM/MM} \tag{2.32}$$

The total energy of the system can also be divided into separate parts 2.33.

$$\mathrm{E}_{Total} = \mathrm{E}_{QM} + \mathrm{E}_{MM} + \mathrm{E}_{QM/MM} \tag{2.33}$$

A number of different levels of QM/MM theory exist and therefore different forms of $\hat{\mathrm{H}}_{QM/MM}$. One example of which is shown in (2.34),[15] illustrating the steric and electrostatic contributions.

$$\hat{\mathrm{H}}_{QM/MM} = \underbrace{-\sum_{iM}\frac{q_M}{r_i M} + \sum_{\alpha M}\frac{Z_\alpha q_M}{R_{\alpha M}}}_{\text{Electrostatic}} + \underbrace{\sum_{\alpha M}\left\{\frac{A_{\alpha M}}{R^{12}_{\alpha M}} - \frac{B_{\alpha M}}{R^{6}_{\alpha M}}\right\}}_{\text{Steric}} \tag{2.34}$$

i and α represent electrons and nuclei in the QM region respectively and M represents atoms in the MM region.

A major obstacle in the QM/MM method is how to model the connections between the two regions successfully, as the interconnection will most likely occur via a bond. Separating the QM and MM regions along the interconnecting bonds without any adjustment will result in the QM region possessing an unpaired electron for each broken bond. This would likely result in the introduction of errors into the QM calculations. A number of different solutions have been proposed which aim to remove the problem of unpaired electrons. These include; the local self consistent field (LSCF) approach,[16–18] where a combination of hybrid and atomic orbitals are used to describe the covalent

bonds between the two regions, and the use of link atoms[15], where additional atoms (usually hydrogen atoms) are added to just the QM region in order to satisfy the valencies created by breaking the bonds between the two regions. The work presented in this thesis uses the integrated molecular orbital and molecular mechanics method (IMOMM)[19], which uses link atoms to connect the QM and MM regions, and does not include electrostatic interactions between the two regions (*i.e.* the electrostatic term in equation 2.34 is set to zero).

The IMOMM method has also been extended to allow for the combination of two different levels of QM theory.[20] The entire system can be separated further into increasing numbers of layers each treated using different levels of computational theory with the ONIOM scheme.[21]

The IMOMM version used in presented computational work is based on the QoMMMA program[22,23] and ignores the electrostatic interactions in the QM/MM Hamiltonian (2.34).

2.1.5 Transition state theory

For a reaction to take place between reactants to form a specific product, the reactants must meet each other with enough energy and in a favourable geometry. The reaction then normally proceeds via an activated complex. For example, the bimolecular reaction between A and B to form C (2.35).

$$A + B \rightarrow (AB)‡ \rightarrow C \tag{2.35}$$

The rate of this reaction (the rate at which the product is produced) is dependent on the concentration of A and B and rate constant, k, which can be determined using the Arrhenius equation (1.1).

Transition state theory (TST) is one approach to calculate the rate constant.

The theory behind conventional transition state theory (CTST) was first published in 1935[24,25] and relies on four main assumptions[26]:

- Systems crossing the saddle point cannot turn back and reform reactants.
- The molecules have a Maxwell-Boltzmann energy distribution and the concentration of activated complexes becoming products can be calculated using equilibrium theory.
- The motion over the saddle point is able to be separated from other motions present in the activated complex.
- The reaction can be treated classically, *i.e.* no quantum effects.

A rate equation for the rate constant can then be derived from the partition functions of the reactants and the activated complex. For a bimolecular reaction between A and B the rate constant can be calculated using equation (2.36).[26]

$$k = \frac{k_B T}{h} \frac{q_{\ddagger}}{q_A q_B} e^{-E_0/RT} \,, \tag{2.36}$$

where $q_{\ddagger}$, q_A and q_B are the partition functions of the activated complex, reactant A and reactant B respectively, k_B is the Boltzmann constant, h is Planck's constant, E_0 is the energy change when one mole of A reacts with 1 mole of B to form one mole of $(AB)\ddagger$ at absolute zero, R is the ideal gas constant and T is the temperature.

The total partition functions for each species can be calculated by separating them into their parts related to the electronic q_e, vibrational q_v, rotational q_r and translation q_t contributions (2.37).

$$q = q_e q_v q_r q_t \tag{2.37}$$

Each contribution can then be evaluated separately and the total calculated.

A number of limitations to CTST stemming from the assumptions made lead to inaccuracies in the calculation of the rate constant. A number of extensions to CTST have been proposed to try to resolve these problems. For example, variational transition state theory (VTST) corrects for multiple crossings of the saddle point by evaluating the rate constant at different positions along the reaction coordinate and the minimum rate calculated is taken as the most accurate.

2.2 Spectroscopy background

2.2.1 Atomic and Molecular spectra

Atoms and molecules each exhibit unique spectral features related to their electronic states and, in the case of molecules, also their vibrational and rotational states. These features result from either transitions to an excited state by absorption of a photon equal in energy to the spacing between the upper and lower levels, or emission of a photon from an excited state to a lower state. These features allow for the detection and study of species within many diverse environments e.g. the detection of atmospheric species on distant planets and the study of species within flames. Work presented in this

thesis uses a combination of absorption and emission spectroscopy to observe a number of atoms and molecules present within plasmas used in the chemical vapour deposition of diamond.

2.2.1.1 Atomic Spectra

Spectra observed for atoms are found to exhibit sharp lines at particular wavelengths in emission and absorption. This is due to the energy levels being quantized. The system can be described using quantum mechanics and as seen in Section 2.1.1, the wavefunction of a particular system will contain all the information about the system. For an atom, this wavefunction can be described using four quantum numbers[27]:

- The principal quantum number, n, taking values 1,2,3,..., ∞, determines the energy of the orbital.
- The orbital quantum number, l, taking values $0, 1, 2, 3, \ldots, n-1$ and determines the orbitals shape and the electronic angular momentum.
- The magnetic quantum number, m_l, taking values $l, l-1, \ldots, -l$ and determines the direction of an orbital and the behaviour of the electrons in a magnetic field. This is also the projection of the angular momentum along a specified axis.
- The spin quantum number, s, with a value of $\frac{1}{2}$ only, representing the electrons spin.

The atomic orbitals can then be labelled according to the value of l, e.g. the labels *s,p,d,f* are used for $l = 0, 1, 2, 3$, respectively and with n, resulting in *ns, np, nd* and *nf* orbitals. For a given n and l, a number of each orbital type exist based on the value of m_l, e.g. there are three *p* orbitals np_x, np_y and np_z because m_l has three values $(-1, 0, 1)$ when $l = 1$. Each orbital can be occupied by two electrons however no two electrons may share the same quantum numbers, in a fully occupied orbital each electron will therefore have a different spin (m_s), either $+\frac{1}{2}$ or $-\frac{1}{2}$.

As an electron moves in its orbital around a nucleus it possesses both orbital angular momentum, related to the quantum number l, and spin angular momentum, related to s. These two quantities are combined to find the total angular momentum quantum number of the system, j, which is defined as

$$j = l + s, l + s - 1, \ldots, |l - s|. \tag{2.38}$$

For atoms with more than one electron the total angular momentum includes contributions from all of them. Two methods exist for calculating the sum of the orbital (**L**) and spin angular momentum (**S**) for multiple electrons. One is the Russell-Saunders coupling (or LS-coupling). This involves first summing the orbital angular momentum and spin angular momentum from each electron separately to calculate the total orbital and total spin angular momentum. These are then combined together to find the total angular momentum, **J**.

$$\sum_i l_i = \mathbf{L}, \quad \sum_i s_i = \mathbf{S}, \quad \mathbf{L} + \mathbf{S} = \mathbf{J} \tag{2.39}$$

This method is typically used for small to medium sized atoms. In larger atoms, the spin-orbit interactions become more significant and the other coupling scheme, *j-j* coupling, becomes more appropriate. This scheme involves first working out the total angular momentum *j* for each electron and then adding these together to work out the overall total *i.e.*

$$l_i + s_i = j_i, \quad \sum_i j_i = \mathbf{J} \tag{2.40}$$

The total orbital angular momentum vector (**L**), total spin angular momentum vector (**S**) and total angular momentum vector (**J**) each have associated with them corresponding quantum numbers *S, L* and *J* respectively.

Under the Russell-Saunders coupling regime;

$$L = l_1 + l_2, l_1 + l_2 - 1, \ldots, |l_1 - l_2| \tag{2.41}$$

$$S = s_1 + s_2, s_1 + s_2 - 1, \ldots, |s_1 - s_2| \tag{2.42}$$

$$J = L + S, L + S - 1, \ldots, |L - S| \tag{2.43}$$

These can be used to construct term symbols used to describe the electronic states of the atom. This term symbol takes the form

$$^{2S+1}L_J \tag{2.44}$$

where, for L = 0,1,2,3 . . ., the symbols *S,P,D,F* . . . are used respectively. 2S+1 is the spin multiplicity of the state, the states are referred to as singlets when S=0, doublets when S=$\frac{1}{2}$, triplets when S=1, *etc*.

As an example, the ground state of an hydrogen atom with has a term symbol of $^2S_{1/2}$ whilst the same atom with the electron excited into a 2p orbital will have the term symbol of $^2P_{3/2}$ and $^2P_{1/2}$

Transitions between the various upper and lower energy levels are not always allowed in quantum mechanics and these are governed by a series of selection rules:

$$\Delta S = 0 \tag{2.45}$$

$$\Delta L = 0, \pm 1 \tag{2.46}$$

$$\Delta l = \pm 1 \tag{2.47}$$

$$\Delta J = 0, \pm 1 \tag{2.48}$$

$$J = 0 \not\leftrightarrow J = 0 \tag{2.49}$$

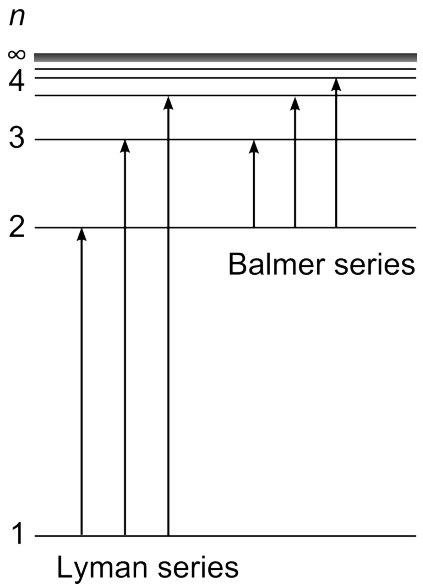

Figure 2.3: Illustration of the hydrogen atoms energy levels and a selection of lines from the Lyman and Balmer series.

An illustration of the effect these selection rules have can be easily demonstrated in the case of an hydrogen atom. The H atom spectrum is made up of a series of lines arising from transitions between various upper (n') and lower (n") energy levels. For example, the Lyman series arising from transitions between n' = $2, \ldots, \infty \rightarrow$ n" = 1 and the Balmer series n' = $3, \ldots, \infty \rightarrow$ n" = 2. An

illustration of these lines in absorption is shown in Figure 2.3.

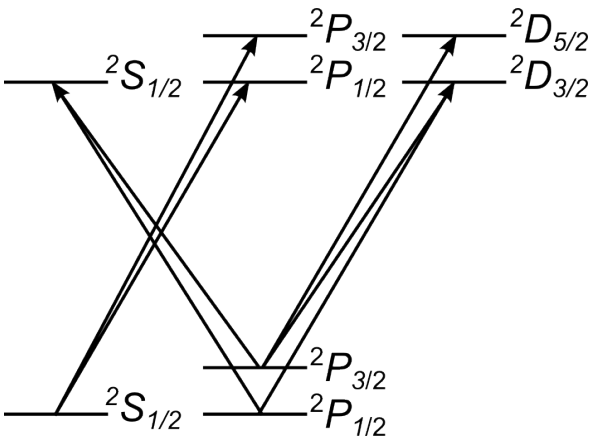

Figure 2.4: The fine structure of the Hydrogen Balmer alpha absorption resulting from spin-orbit coupling and the selection rules.

Each lines is actually made up of a number of very close transitions (fine structure) due to spin-orbit splitting within the energy "levels". The allowed transitions are limited by the selection rules. An example of this is shown in Figure 2.4 for the Balmer alpha line (n'=3 $\rightarrow$n"=2). The upper and lower levels are split into five and three separate levels, respectively. Thus there are fifteen possible energy gaps but, due to the selection rules, only a total of seven transitions are allowed.

2.2.1.2 Molecular Spectra

Molecules are species which include more than one atom. Molecules are free to rotate around an axis and the atoms can change their relative positions producing vibrational motion. Both the rotation and vibration of molecules can be observed spectroscopically and produces additional fine structure associated with electronic transitions. Reflecting the fact that the electronic transitions may also involve a simultaneous change in the vibrational and rotational states.

The energy separation between vibrational levels are smaller than those between electronic levels. Rotational levels are even more closely spaced. An illustration is shown in Figure 2.5. Pure vibrational spectra (*i.e.* changes from one vibrational state to another in the same electronic state) tend to lie in the infrared region of the electromagnetic spectrum and rotational spectra are seen in the microwave region.

A simple approximation to the vibrational energy levels of diatomic molecules is that of the harmonic oscillator (2.50).

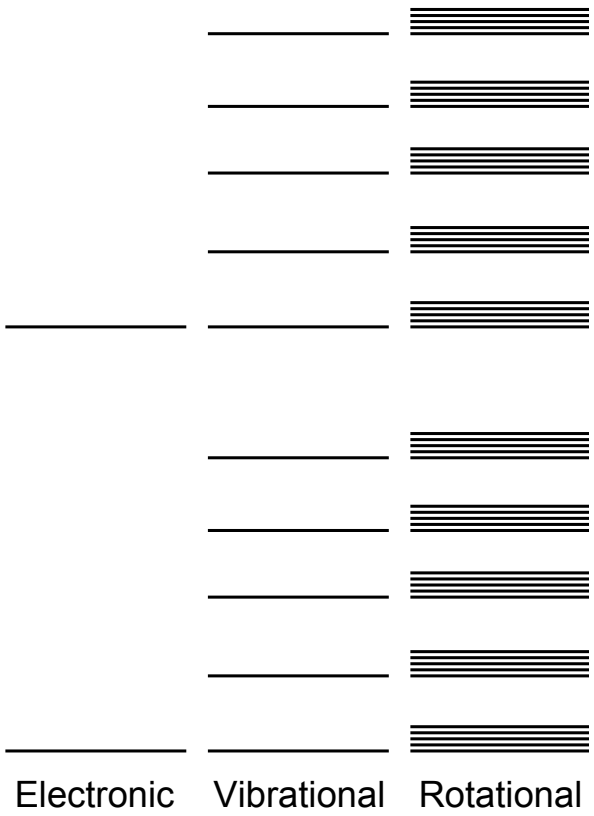

Figure 2.5: Illustration of the spacing of electronic, vibration and rotational levels in a molecule

$$\epsilon_v = (v + \frac{1}{2})\bar{\omega}_0 \qquad \mathrm{cm}^{-1} \tag{2.50}$$

where v is the vibration quantum number, taking integer values running from $0 \rightarrow \infty$, and ω_0 is the oscillation frequency

$$\bar{\omega}_0 = \frac{1}{2\pi c}\sqrt{\frac{k}{\mu}} \qquad \mathrm{cm}^{-1} \tag{2.51}$$

where μ is the reduced mass and k is a force constant. Due to the quantisation of the vibrational energy levels a molecule can never have zero vibrational energy. The minimum energy is found to be equal to $\frac{1}{2}\bar{\omega}_0$. For the harmonic oscillator approximation the selection rule of $\Delta v = \pm 1$, applies and the spacing between all vibrational levels is the same. The harmonic oscillator, whilst a fair approximation to the vibrational energy levels at low v, becomes poor at higher energy levels due to anharmonic effects. These effects can be taken into account by introducing an anharmonicity constant (x_e).

$$\epsilon_v = (v + \frac{1}{2})\bar{\omega}_e - (v + \frac{1}{2})^2\bar{\omega}_e x_e \qquad \mathrm{cm}^{-1} \tag{2.52}$$

where $\bar{\omega}_e$ is related to $\bar{\omega}_0$ by

$$\bar{\omega}_0 = \bar{\omega}_e(1 - \frac{1}{2}x_e) \qquad \mathrm{cm}^{-1}. \tag{2.53}$$

This results in the vibrational levels no longer being evenly spaced, instead become closer together in energy at higher v. The $\Delta v = \pm 1$ selection rule is also lifted meaning that transitions between all vibrational levels are allowed.

A simple approach to calculating the rotational energy levels of diatomic molecules is the rigid rotor approximation. Within the rigid rotor approximation, energy levels are given by

$$\epsilon_J = \frac{h}{8\pi^2 Ic}J(J+1) \qquad \mathrm{cm}^{-1} \tag{2.54}$$

where *J* in this instance is the rotational quantum number and can take the values, *J* = 0,1,2,. . .,∞ , I is the moment of inertia and c is the speed of light. This equation is normally seen written as

$$\epsilon_J = BJ(J+1) \qquad \mathrm{cm}^{-1} \tag{2.55}$$

where B is termed the rotational constant. The spectrum will thus exhibit rotational lines with equal spacing of $2B$. As J increases though centrifugal distortion affects the energy levels and the spacing between lines will change. Fine structure associated with rotational transitions is commonly observed in vibrational and electronic spectroscopy and forms branches associated with the change in J, e.g. ΔJ=-1, 0 and +1, which are termed P, Q and R branches, respectively.

As with atomic species, the electronic states can be described using term symbols but, due to the lack of spherical symmetry (as in atoms), the orbital angular momentum quantum number (L) is no longer a good quantum number as the orbital angular momentum is not conserved. The component of the orbital angular momentum along the internuclear axis in a diatomic (or linear) molecule is still conservative though. The total axial orbital momentum can therefore be defined with a corresponding good quantum number Λ describing the molecular orbitals. The total axial orbital momentum can be calculated from the sum of the axial orbital momentum of each electron $\boldsymbol{\lambda}_i$. The axial orbital quantum number λ_i is defined as:

$$\lambda = |m_l| \tag{2.56}$$

where for $\lambda = 0, 1, 2, 3 \ldots$ the orbitals are called $\sigma, \pi, \delta, \phi$ respectively.

The total axial orbital momentum quantum number Λ is given by:

$$\Lambda = |\sum_i m_{l_i}| \tag{2.57}$$

as m_l can be positive or negative. $\Lambda = 0, 1, 2, 3 \ldots$ corresponds to $\Sigma, \Pi, \Delta, \Phi \ldots$ states.

The total axial momentum of the system, $\mathbf{\Omega}$ is given by:

$$\mathbf{\Omega} = \mathbf{\Lambda} + \mathbf{\Sigma} \tag{2.58}$$

where $\mathbf{\Sigma}$ is the axial component of the total spin angular momentum. This vector will have an associated quantum number Ω.

Molecular term symbols are normally written with the general form:

$$^{2S+1}\Lambda^{+/-}_{\Omega,(g/u)} \tag{2.59}$$

The $+/-$ indicates whether, on reflection through a plane containing the internuclear axis, the molecular orbital is symmetric or antisymmetric. This notation is only used for Σ states as states with $\Lambda > 0$ are doubly degenerate with respect to this symmetry operation, and thus have both states which are symmetric and antisymmetric. A g or u subscript is used if the diatomic molecule consists of two identical nuclei, and indicates whether the wavefunction of the electronic state is unchanged (gerade) or changes sign (ungerade) with respect to reflection through an inversion centre.

The respective energy of various states in a molecule are normally marked with a letter before the term symbol. An X normally indicates the ground state and subsequent excited states of the same multiplicity are labelled A,B,C... respectively. Lower case letters are typically used to indicate excited states with different multiplicity. For example the term symbol of the singlet ground state of C_2 is $X^1\Sigma^+_g$ and the term symbol of its first excited triplet state is $a^3\Pi_u$.

As with atomic spectra, a number of selection rules apply which govern allowed transitions between

different energy levels. For electronic transitions, the selection rules are:

$$\Delta\Lambda = 0, \pm 1 \tag{2.60}$$

$$\Delta S = 0 \tag{2.61}$$

$$\Delta\Omega = 0, \pm 1 \tag{2.62}$$

$$\Sigma^+ \leftrightarrow \Sigma^+ \qquad \Sigma^- \leftrightarrow \Sigma^- \qquad \Sigma^+ \not\leftrightarrow \Sigma^- \tag{2.63}$$

$$g \leftrightarrow u \qquad g \not\leftrightarrow g \qquad u \not\leftrightarrow u \tag{2.64}$$

There are also a number of selection rules relating to the rotational quantum number J governing the observed rotational fine structure. For ${}^1\Sigma \rightarrow {}^1\Sigma$ transitions

$$\Delta J = \pm 1 \tag{2.65}$$

for all other cases

$$\Delta J = 0, \pm 1 \tag{2.66}$$

transitions between $J' = 0$ and $J'' = 0$ are however, forbidden. These rules mean that for ${}^1\Sigma \rightarrow {}^1\Sigma$, only the P and R ($\Delta J = -1$ and $\Delta J = +1$ respectively) rotational branches are observed, whilst for all other transitions a Q branch ($\Delta J = 0$) will also be observed.

2.2.1.3 Line intensity

The intensity of a specific transition depends on the population of the state which is either absorbing or emitting, and the probability of the transition occurring. Assuming that the system is at equilibrium the population in the different energy levels will be determined by the Boltzmann distribution (2.67).

$$\frac{N_j}{N_i} = \frac{g_j}{g_i} e^{-\frac{h\nu}{k_B T}} \tag{2.67}$$

N_j and N_i are the populations of the upper and lower states respectively, g_j and g_i are their degen-

eracies, h is Planck's constant, ν is the frequency of the radiation, k_B is Boltzmann's constant and T is the temperature.

There are three different processes which can result from the interaction of electromagnetic radiation with the energy levels of molecules and atoms. These are:

- Absorption: the photon of radiation is absorbed and excites the absorbing species into a higher energy state.
- Spontaneous Emission: A species already in an excited state emits a photon of radiation as it transitions from an upper state to a lower state of energy.
- Stimulated emission: Interaction between a photon with a particular energy and a atom or molecule causes the species to drop to a lower energy level and emit a photon.

An illustration of these three processes is shown in Figure 2.6

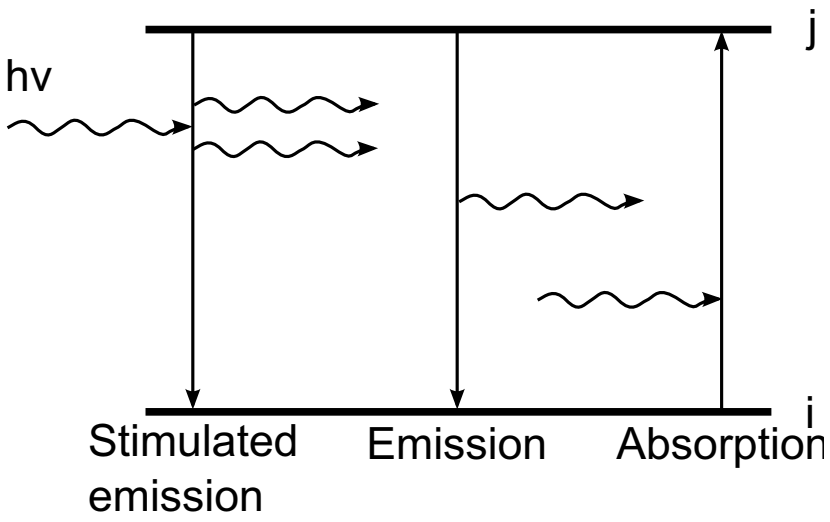

Figure 2.6: The three different ways in which electromagnetic radiation can interact with two different energy levels (i and j)

A measure of the probability of each of these events occurring is given by the three Einstein coefficients, B_{ij}, A_{ji} and B_{ji} which correspond to the processes of absorption, emission and stimulated emission, respectively. The value of each of these coefficients can be linked together by the following relationships:

$$B_{ij} = \frac{g_j}{g_i} B_{ji} \tag{2.68}$$

$$A_{ji} = \frac{8\pi h}{\lambda^3} B_{ji} \tag{2.69}$$

The intensity of vibrational transitions observed in vibrational-electronic spectra are determined by the Franck-Condon principle. This reflects the fact that electronic transitions take place much faster than the nuclei in a molecule can move, the same physics that underpins the Born-Oppenheimer approximation introduced in 2.1.1. The overlap of the vibrational wavefunctions in the upper and lower states thus becomes important in determining the strength of a transition. A molecule in its ground state electronic and vibrational level will have a certain equilibrium bond length (r_{eq}). If this molecule is then excited to a higher energy level with the same r_{eq}, the most favourable vibrational transition will likely be the (v" $= 0 \rightarrow v' = 0$) followed by (v" $= 0 \rightarrow v' = 1$) and so on. However, if the equilibrium bond length is longer in the excited state the overlap with the excited $v' = 0$ level will not be as good. The v"=0 wavefunction will instead overlap better with the wavefunctions of higher v' vibrational states resulting in transitions to higher vibrational levels becoming dominant.

2.3 Experimental Techniques

2.3.1 Lasers

Laser is an abbreviation of the phrase "Light amplification by stimulated emission of radiation". Lasers work by creating a population inversion within a gain medium (e.g. Nd:YAG crystal or Organic dyes). Which when placed within a low loss optical resonator builds up a pulse of light due to the stimulated emission.

The creation of the population inversion (the creation of a significant population in an upper excited state with a low population in a lower energy level) is key to the production of a working laser system. A four level system is one of the most favourable ways to create this population inversion and is illustrated in Figure 2.7.

The four level laser scheme relies on fast relaxation from the excited state [created by pumping (e.g. with a flash lamp or another laser) the gain medium] to the metastable excited state, and that relaxation from this excited state back to the ground state (or lower excited) is slow. This allows the population in the metastable state to increase. Fast relaxation of the lower state of the laser transition also means that no significant population in that level builds up and inhibits the laser action.

Once a population inversion has been obtained, emitted photons originating from the laser transition are then used to amplify the light. This is done by placing the gain medium within an optical resonator. Typically the resonator consists of two highly reflective mirrors with the gain medium placed

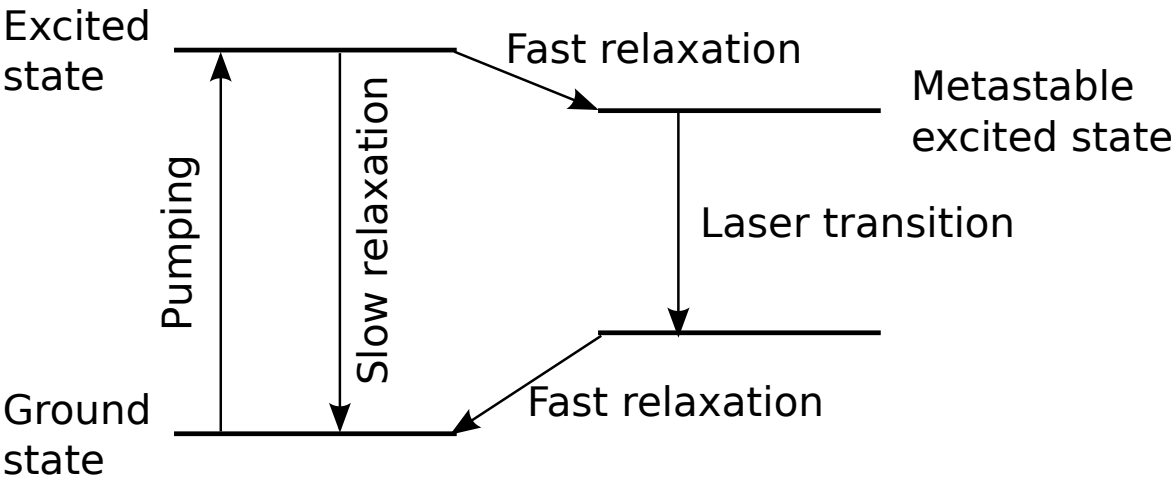

Figure 2.7: Illustration of processes within a four level laser scheme

in between them. As the gain medium is pumped the emitted light from the laser transition passes back and forth between the two mirrors and through the gain medium causing stimulated emission and amplification of the light pulse. This is referred to as loop gain. This setup for a pulsed laser system typically results in a pulse of laser light of about 0.1 - 100 μs.

In certain applications shorter, more intense laser pulses are more desirable. To achieve such laser pulses, one technique often used is that of Q-switching. Q is the quality factor of the optical resonator used to create the laser pulse. A low Q value indicates that there are high losses within the resonator whilst high Q is the opposite.

Q-switching works by lowering the Q-factor of the optical resonator and then pumping the gain medium to create a large population inversion but, due to the high losses of the cavity, no laser action results. The Q-factor is then quickly switched so that the optical resonator is low loss and the laser pulse builds up very quickly, depleting the energy stored within the gain medium. This results in a short (5-50 ns), intense burst of laser output.

2.3.1.1 Nd:YAG laser

The Nd:YAG laser is a solid state laser and one of the most commonly used laser sources. It is a four level laser system based on transitions of Nd^{3+} atoms which are implanted into a crystal of yttrium aluminium garnet ($Y_3Al_5O_{12}$). The laser system is typically pumped using a Xe flash lamp for pulsed laser operation.

The main laser transition of the Nd:YAG laser is at 1064 nm, which can be converted to give light at 532 nm, 355 nm and 266 nm by second, third and fourth-harmonic generation using non-linear

crystals. The second and third harmonics at 532 nm and 355 nm are routinely used to pump dye lasers.

2.3.1.2 Dye Lasers

The main problem with lasers such as the Nd:YAG laser, especially for use in spectroscopy experiments, is that they only output radiation at certain wavelengths, and unless the species you are interested in happens to fall on those wavelengths they are not particularly useful. Dye lasers, however, can produce tuneable laser radiation over a large wavelength range, determined by the dye of choice.

The dye lasers are based on the use of organic dyes in solution as the gain medium. Due to the structure of the organic dyes they typically have very dense and broad energy bands. Upon excitation, a large number of different states can be occupied, resulting in the production of light at a variety of wavelengths. By appropriately tuning the resonator of the dye laser, specific wavelengths can be selected, resulting in a tuneable laser system.

A large variety of organic dyes exist that can be used within dye lasers and, in conjunction with frequency multiplication techniques, the dye laser allows for the production of tuneable laser radiation all the way from the ultra-violet to the near infra-red.

2.3.2 Spectroscopic methods

2.3.2.1 Optical emission spectroscopy

Optical emission spectroscopy (OES) is a passive technique and works simply by monitoring the light emitted from a particular species as it relaxes from an excited state to one of lower energy. The technique is thus sensitive to the population of the excited species and the specific conditions which produce the excited state. It can therefore be useful in providing insight into other processes, for example in the study of plasmas, OES allows for information about factors such as the electron distribution to be ascertained, indirectly.

OES does have a number of drawbacks, it typically provides qualitative (rather than quantitative) information about the system in question and, because it is sensitive to the excited levels rather than the ground state, information gathered may not fully reflect trends in the species studied due to convolution with the processes creating the excited state.

2.3.2.2 Absorption spectroscopy

Absorption spectroscopy (AS) is sensitive to the lower state of a system and works by monitoring the absorption of incident radiation that promotes a species from a lower to a higher energy state. This allows the study of species present in environments where there is no emission of radiation.

The absorbance (A), of a species can be directly related to its concentration by the Beer-Lambert law (2.70)

$$A = \ln\frac{I_0}{I} = \sigma n L \tag{2.70}$$

where I_0 is the initial intensity of the light, I is the intensity of the light after passing through the sample, n is the number density of the absorbing species, σ is the absorption cross-section and L is the path length of the light passing through the medium. σ and n are commonly combined to form α, the absorption coefficient.

AS is therefore a quantitative technique and concentrations of species can be directly calculated from observed spectra.

Whilst AS is a quantitative technique and can be used to study the behaviour of species within their ground states, the experiments are typically more difficult to set up (when compared to techniques such as OES). The reliance of AS on knowledge of the initial intensity of the radiation and its resultant intensity makes measuring species at low concentrations difficult. Any fluctuations in the initial intensity of the light source will cause spurious results and the detection of small changes between the initial and final light intensities will become increasingly difficult as the quantity of light absorbed decreases.

2.3.2.3 Cavity ring-down spectroscopy

Cavity ring down spectroscopy (CRDS) is a highly sensitive multi-pass laser absorption technique and overcomes many of the problems inherently associated with simple absorption spectroscopy.

CRDS relies on the construction of an optical cavity consisting of two highly reflective mirrors ($R > 99\%$). The system of interest is contained within this cavity. A laser pulse is then passed into this cavity and is reflected back and forth between the mirrors thousands of times. This results in a path length that can be many kilometres long. As the two mirrors are not perfectly reflective, a small

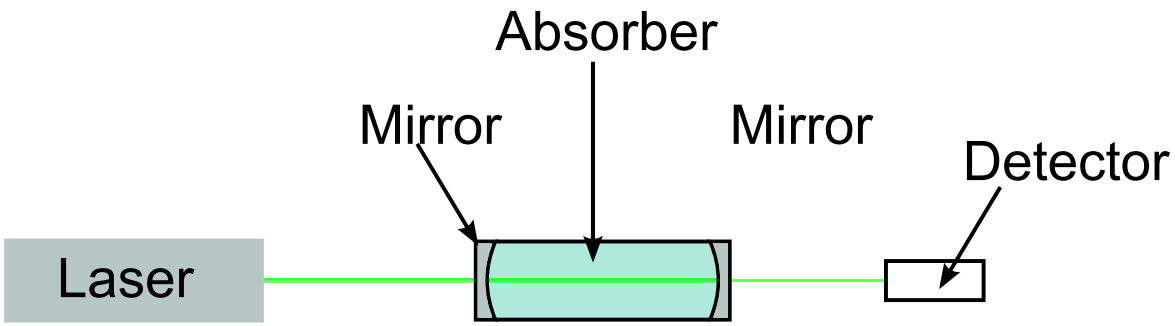

Figure 2.8: A diagram of a typical CRDS experimental setup

amount of light escapes with each round trip that the light makes. The intensity of the light in the cavity decays exponentially. A simple CRDS experimental setup is illustrated in Figure 2.8.

The transmitted light, I_{T} is related to the time, t and the initial intensity, I_0 by

$$I_{\mathrm{T}} = I_0 e^{-\frac{t}{\tau}} \tag{2.71}$$

where τ is the ring down time (the decay rate of the light). For an empty cavity, the ring-down time τ_0 is determined by the reflectivity of the mirrors, the distance between the mirrors, L and the speed of light, c.

$$\tau = \frac{L}{c(1-R)} \quad \text{when} \quad R \approx 1 \tag{2.72}$$

If, at a particular wavelength, a species within the cavity absorbs the light the ring down time will decrease. When an absorbing species is in the plasma τ is given by,

$$\tau = \frac{L}{c(1-R+n\sigma l)} \tag{2.73}$$

where l is the effective path length (the length of the absorbing volume which may not be equal to L), n is the number density of the absorber and σ is its absorption cross section. The decay rate k is equal to τ^{-1}.

By measuring the change in decay rate, Δk, between no absorption (*i.e.* an empty cavity) and with the absorbing species present the number density of specific species can be calculated.

$$\Delta k = \frac{1}{\tau} - \frac{1}{\tau_0} = \frac{c(1-R+n\sigma l)}{L} - \frac{c(1-R)}{L} = \frac{cn\sigma l}{L} \tag{2.74}$$

therefore

$$n = \frac{L\Delta k}{c\sigma l} \tag{2.75}$$

Unless the effective path length is known absolute column densities (D) for the absorbing species are deduced, where

$$D = nl \tag{2.76}$$

CRDS offers advantages over traditional absorption spectroscopy due to its sensitivity, and the fact that it is insensitive to variations in the initial light intensity (the decay rate is the important factor).

References

[1] P. W. Atkins and R. S. Friedman, *Molecular Quantum Mechanics* (Oxford University Press, third edition, 2001).

[2] P. Hohenberg and W. Kohn, *Phys. Rev.* **136**, 864 (1964).

[3] K. Wolfram and M. C. Holthausen, *A Chemist's Guide To Density Functional Theory* (Wiley-VCH, second edition, 2001).

[4] W. Kohn and L. J. Sham, *Phys. Rev.* **140**, A1133 (1965).

[5] C. J. Cramer, *Essentials of Computation Chemistry : Theories and Models* (Wiley, second edition, 2004).

[6] A. D. Becke, *Phys. Rev. A* **38**, 3098 (1988).

[7] J. P. Perdew, B. Kieron, and M. Ernzerhof, *Phys. Rev. Lett.* **77**, 3865 (1996).

[8] J. P. Perdew, *Phys. Rev. B* **33**, 8822 (1986).

[9] C. Lee, W. Yang, and R. G. Parr, *Phys. Rev. B* **37**, 785 (1988).

[10] A. D. Becke, *J. Chem. Phys.* **98**, 1372 (1993).

[11] A. D. Becke, *J. Chem. Phys.* **98**, 5648 (1993).

[12] P. J. Stephens, F. J. Devlin, C. F. Chabalowski, and M. J. Frisch, *J. Phys. Chem.* **98**, 11623 (1994).

[13] N. L. Allinger, *J. Am. Chem. Soc.* **99**, 8127 (1977).

[14] G. Monard and K. M. Merz Jr., *Acc. Chem. Res.* **32**, 904 (1999).

[15] M. J. Field, P. A. Bash, and M. Karplus, *J. Comput. Chem.* **11**, 700 (1990).

[16] V. Théry, D. Rinaldi, J.-L. Rivail, B. Maigret, and G. G. Ferenczy, *J. Comput. Chem.* **15**, 269 (1994).

[17] G. Monard, M. Loos, V. Théry, K. Baka, and J.-L. Rivail, *Int. J. Quantum Chem.* **58**, 153 (1996).

[18] X. Assfeld and J.-L. Rivail, *Chem. Phys. Lett.* **263**, 100 (1996).

[19] F. Maseras and K. Morokuma, *J. Comput. Chem.* **16**, 1170 (1995).

[20] S. Humbel, S. Sieber, and K. Morokuma, *J. Chem. Phys.* **150**, 1959 (1996).

[21] M. Svensson, S. Humbel, R. D. J. Froese, T. Matsubara, S. Sieber, and K. Morokuma, *J. Phys. Chem.* **100**, 19357 (1996).

[22] J. N. Harvey, *Faraday Discuss.* **127**, 165 (2004).

[23] A. C. Tsipis, A. G. Orpen, and J. N. Harvey, *Dalton Trans.* (2005).

[24] H. Eyring, *J. Chem. Phys.* **3**, 107 (1935).

[25] M. G. Evans and M. Polanyi, *Trans. Faraday Soc.* **31**, 875 (1935).

[26] K. J. Laidler, *Chemical Kinetics* (HarperCollins Publishers, third edition, 1987).

[27] C. N. Banwell, *Fundamentals of Molecular Spectroscopy* (McGraw-Hill Book Company, third edition, 1983).

3

Diagnostics of Ar-rich $CH_4/H_2/Ar$ plasmas

The results in this section have been previously published as part of a paper in the Journal of Applied Physics.[1]

3.1 Introduction

The use of H_2/Hydrocarbon gas mixtures to grow diamond via chemical vapour deposition is now a routine process.[2] Activation of this input gas mixture (which can be achieved by a number of different techniques) produces a wide variety of radical species which, upon reaction with the substrate form diamond (see Chapter 1). Variation of the input gas mixture, such as the C/H ratio, has been shown to have an effect on the morphology of the diamond grown. Increasing the C/H ratio is typically found to reduce the average grain size within the diamond films from microcrystalline diamond (MCD) to nanocrystalline diamond (NCD).[3]

Conventionally the C/H ratio is adjusted by increasing the hydrocarbon fraction within the input gas mixture. An alternative method for increasing the C/H ratio within the gas mixture was developed by Gruen and co-workers[4–6] and involved progressively substituting the H_2 in the input gas mixture with Ar. Increasing the amount of Ar substituted for H_2 to very high levels (e.g. plasmas with an input gas mixture of 1% CH_4, 1% H_2, 98% Ar) leads to growth of polycrystalline diamond films with grain sizes of just a few nanometres[7,8]. These films have been termed ultra-nanocrystalline diamond (UNCD).

There have been a number of previous experimental studies on the effect Ar addition has on the growth and morphology of CVD diamond[9,10] and also on species within the gas phase as the input argon mole fraction (X_0(Ar)) is varied (85-99%[11] and 0-53.1%[12]). A number of modelling studies have also investigated microwave plasmas with high Ar mole fractions.[9,13,14] The work presented in this chapter uses CRDS to obtain column densities of C_2(a), CH(X) radicals and H atoms (in their

n=2 excited state) as a function of height above the substrate (z), Power (P) and pressure (p) at our base conditions (14.7% H_2/ 0.5% CH_4/ 84.8% Ar) and as a function of the mole fractions of CH_4, $X_0(CH_4)$ and H_2, $X_0(H_2)$ within the input gas mixture. Similar measurements are also performed using OES to study electronically excited H atoms and CH, C_2 and C_3 radicals. These results are then compared with 2D(r, z) modelling of the gas phase chemistry and composition within the reactor (see Chapter 1.4.1) by Yuri Mankelevich (Moscow State University).

3.2 Experimental

The microwave CVD reactor used in the current experiments is a custom built reactor, designed by Element Six Ltd. The reactor is cylindrical in nature with a diameter of 6 cm. Two 25 mm vertical slits are cut into the reactor on opposite sides to allow for a laser beam to pass through the chamber. The reactor is split into two regions by a quartz window separating the lower high vacuum region from the upper region that is at atmospheric pressure. A cross-section view of the microwave reactor and CRDS experimental set up is shown in Figure 3.1.

Microwaves (from a 2 kW Muegge 2.45 GHz microwave generator) are coupled into the reactor via a rectangular wave guide and antenna at the top of the reactor. The walls of the reactor are water cooled and the quartz window is air cooled by a blower through the upper portion of the reactor. The input gas mixture is controlled using a number of mass flow controllers (MFCs) and is mixed before entering the chamber. The gas enters the chamber via two ports located just below the quartz window. The chamber is exhausted to an Edwards rotary pump through the base. Pressures are measured with a Baratron (MKS type 622) and are controlled using a negative feedback loop that adjusts a butterfly valve on the exhaust. A molybdenum substrate is placed in the centre of the reactor on top of a Mo wire (0.35 mm thick) to separate it from the water cooled base. The temperature of the substrate is measured using a single colour optical pyrometer.

The CRDS setup consists of two highly reflective mirrors (R $>$ 0.99) placed in adjustable mounts at either end of an 84 cm long cavity. The cavity is constructed of two stainless steel arms (each of which contains a flexible bellow section) that are attached to the sides of the reactor over the two 25 mm slits (see Figure 3.1). The optics are set-up so that the height of the laser beam can be adjusted with submillimeter precision relative to that of the main chamber containing the plasma ball, allowing for the vertical profiling of species within the plasma. A photomultiplier tube (PMT) is placed at the opposite end of the cavity to detect the transmitted light. A filter of appropriate wavelength is placed in front of the PMT to reduce excess light from the plasma.

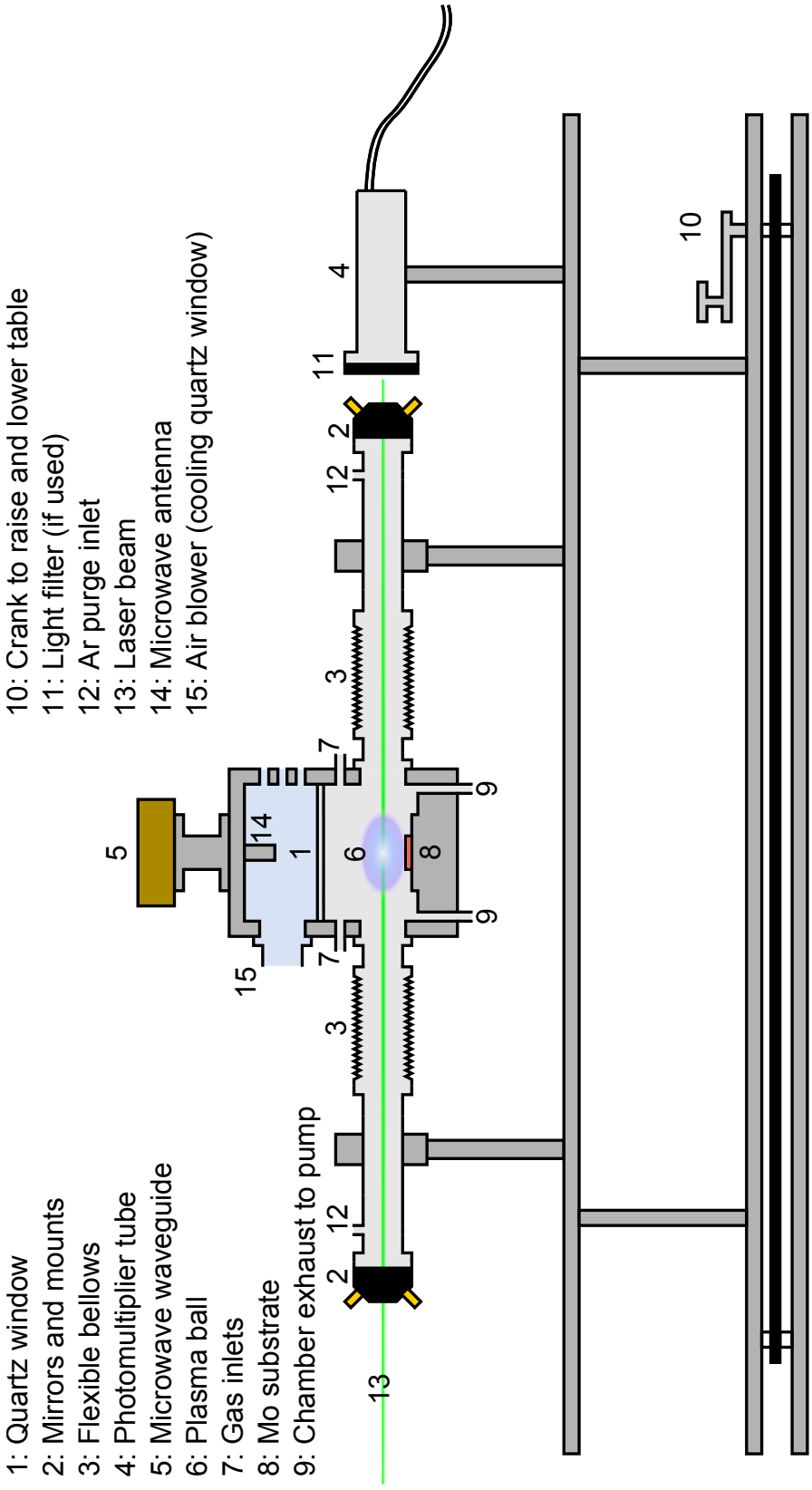

Figure 3.1: Cross section of the microwave CVD reactor and CRDS set-up used in the current investigations.

The laser light is generated by a Nd:YAG (Continuum Surelite III) pumped dye laser (Spectra Physics PDL-3) and is directed into the CRDS cavity via a spatial filter, a series of beam steering optics and a periscope built of two 90° prisms (the upper of which is mounted on the translatable platform) used to raise the laser beam to the height of the microwave chamber. The laser was operated at a repetition rate of 10 Hz and at a number of different wavelengths ≈ 652.2, ≈ 515 and ≈ 431 nm for the detection of H(n=2) atoms, C_2(a, v=0) and CH (X, v=0) radicals, respectively. The dyes used to generate the laser light for the detection of C_2(a, v=0), CH (X, v=0) and H(n=2) are Coumarin 503 (in methanol), Exalite 428 (in 1,4-dioxane) and DCM (in methanol) respectively. The wavelength was calibrated by directing a portion of the laser output through an etalon with a free spectral range of $\approx$0.85 cm^{-1}.

CRDS data was acquired using a custom-written LABVIEW program in conjunction with a digital oscilloscope (LeCroy WaveRunner 64Xi, 4 channel, 600 MHz, 10 Gs/s) connected via an ethernet connection.

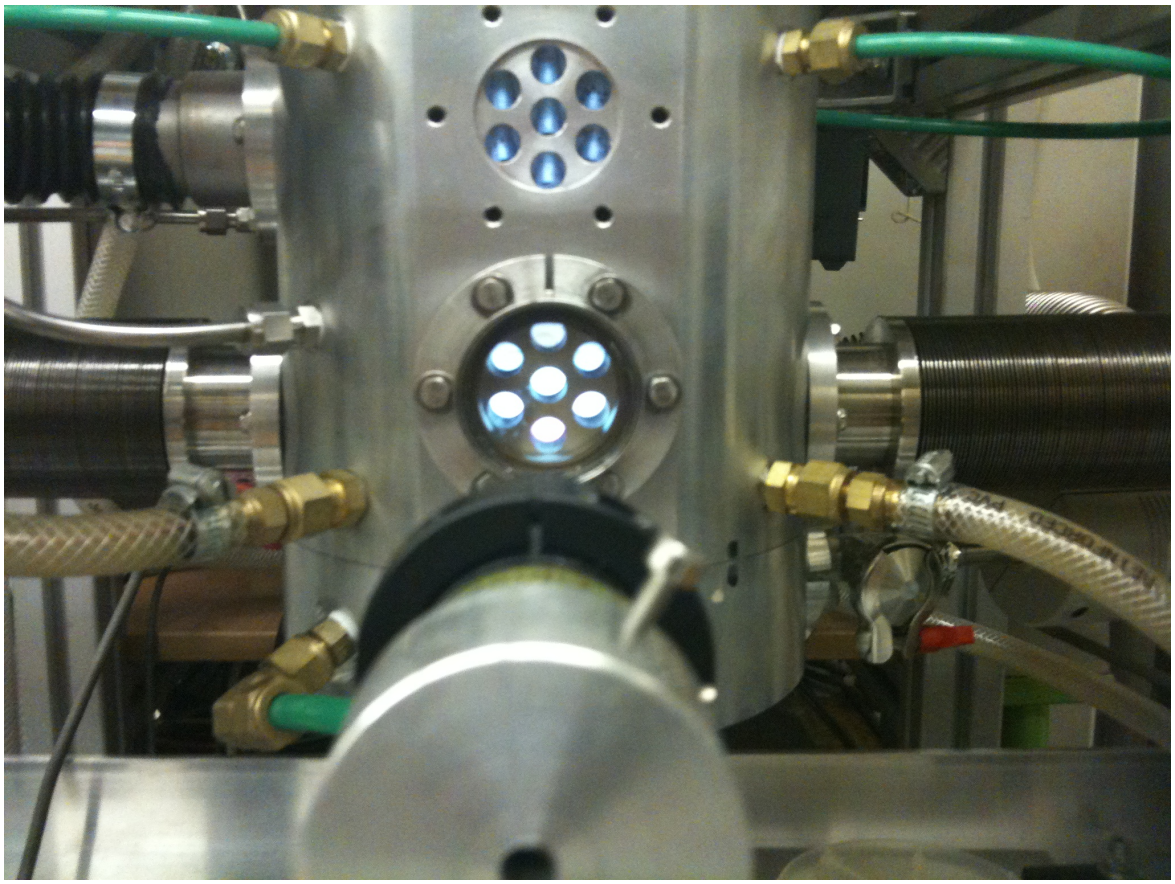

Figure 3.2: Photograph of the MWPECVD reactor used for cavity ring-down spectroscopy. The aperture used for OES can be seen in the foreground.

Optical emission spectra were captured from a volume just below the centre of the luminous plasma

ball through the lower ≈ 9 mm aperture in the front window of the reactor (see Figure 3.2). The emission from this aperture was focused on to the end of a quartz multi-core optical fibre and dispersed through a monochromator and onto a cooled charge coupled device (CCD) strip detector (Oriel Instaspec IV, 600 lines mm^{-1} ruled grating). The resulting spectra have a resolution of better than 1 nm over a 300 nm portion of the emission spectrum. Spectra were recorded with a 20 ms exposure time and the data averaged 1000 times. Background spectra were recorded with the plasma off. A spatial profile of the plasma emission was also obtained by removing the CRDS cavity and placing diamond windows on each side of the reactor. One ≈1 mm aperture was then placed next to the diamond window and a second aperture at the end of a steel tube was placed ≈20 cm from the first. The light was then captured with an optical fibre and dispersed through the monochromator and onto the CCD detector. The entire setup was able to move up and down relative to the reactor chamber allowing a spatial profile to be obtained with an approximate resolution of better than 1 mm.

Base conditions for all work presented within the current chapter were defined as total pressure $p = 150$ Torr, input power $P = 1.0$ kW and a total gas flow rate, $F_{\text{Total}} = 525$ standard cm^3 per minute (sccm). The initial gas mixture into the reactor is defined as a mole fraction X_0 of F_{Total}, with the base mixture as follows: $X_0(CH_4)$ = 0.5 % [F_{CH_4} = 2.7 sccm], $X_0(H_2)$ = 14.7 % [F_{H_2} = 77 sccm] and X_0(Ar) = 84.8 % [F_{Ar} = 445 sccm]. During investigations on the effect of $X_0(H_2)$ and/or $X_0(CH_4)$, variations from the base conditions were compensated by a corresponding adjustment in X_0(Ar) such that F_{Total} remains constant. A fraction of the total Ar flow (50 sccm) into the gas mixture was directed into the reactor via the inlets at either end of the cavity arms so as to avoid excessive build up of particulates within the arms of the cavity reducing the ring down time. Apart from the variation of X_0(Ar) to maintain F_{Total} all parameters other than the one of interest were maintained at the base conditions (unless specified in the results).

3.3 Results and discussion

The effect of decreasing $X_0(H_2)$ can be seen clearly in Figure 3.3: where a) shows the plasma under MCD type growth conditions (0.5 % CH_4 / 92% H_2 / 7.5 % Ar, p = 150 Torr, P = 1.0 kW) and it has a purple/white colour and quite a small luminous volume above the substrate. Reduction of $X_0(H_2)$ to 36.9 % and 9.2 %, b) and c) respectively, shows both a significant increase in the luminous volume of the plasma and a change in colour from purple to pale green and then a intense white/green colour.

A change is also observed in the substrate temperature (T_{sub}) which initially increases as $X_0(H_2)$

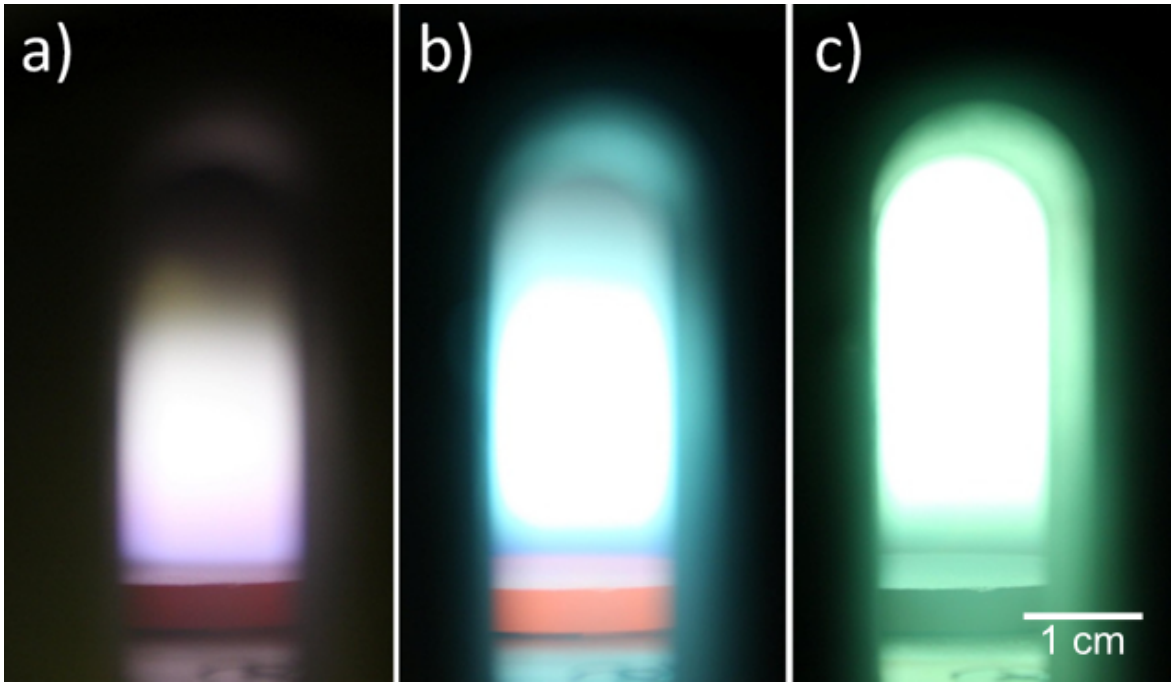

Figure 3.3: Images of the plasma ball seen through the front port of a MWPECVD reactor with differing $X_0(H_2)$, a) 92%, b) 36.9% and c) 9.2%. Other reactor conditions are kept constant, p=150 Torr, P=1.0 kW, $X_0(CH_4)$=0.5% and the balance in the gas mixture is made up using Ar. Pictures taken by O.J.L Fox.

is reduced but, once $X_0(H_2)$ falls below ≈20%, T_{sub} also starts to decrease (Figure 3.4). A similar decrease in the cooling water temperature through the base of the reactor (ΔT_{base}) when $X_0(H_2) <$ 20% was observed, though the temperature of the water flowing through the side walls increased. These changes are all consistent with the plasma volume becoming larger and its centre moving further away from the substrate as $X_0(H_2)$ is decreased.

In this chapter, we use a combination of emission and absorption spectroscopy to investigate the effect on a number of species within CH_4/H_2/Ar plasmas (with high Ar fractions) as a number of process parameters are varied. This data is then compared with computational modelling performed by Yuri Mankelevich (Moscow State University) in an attempt to provide a detailed description of these plasmas and the experimental trends.

3.3.1 Cavity ring down spectra of C_2(a), CH(X) and H(n=2)

Typical spectra obtained by cavity ring down spectroscopy for the $C_2(d^3\Pi_g \leftarrow a^3\Pi_u$, v'= 0←v"=0), CH ($A^2\Delta \leftarrow X^2\Pi$, v'=0←v"=0) and the H(n=3←n=2) transitions are shown in Figure 3.5.

The portion of the C_2(d←a) (0,0) transition acquired using CRDS consists of five resolved lines

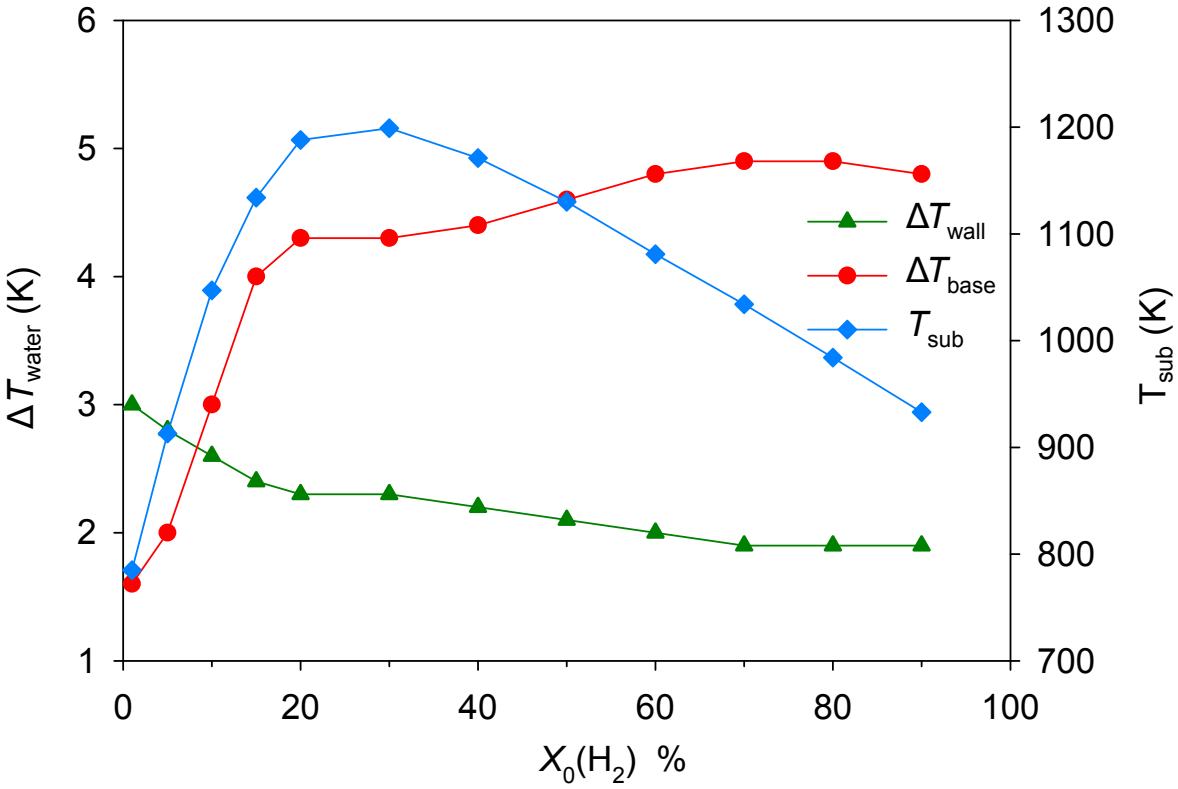

Figure 3.4: Measured substrate temperatures and the temperature change (between input and output) of the cooling water flowing (at 1 l min^{-1}) through the base (ΔT_{base}) and side walls (ΔT_{wall}) of the MWPECVD reactor as a function of $X_0(H_2)$, other reactor parameters are; P=1.0 kW, p=150 Torr, $X_0(CH_4)$ = 0.5% and Ar as balance.

originating from the rotational fine structure associated with the transition. Three of the lines are from the R branch and are transitions originating from low J (8, 9 and 10) levels whilst two of the lines are from the P branch and involve transitions between high J levels (37, 38 and 39). The largest peak in the spectrum actually consists of two lines. The ratio of peak heights between the low and high J transitions provides an indication of the average rotational temperature (T_{rot}) of the C_2(a) radicals along the path of the laser. Values obtained for T_{rot} provide a reasonable approximation of the gas temperature T_{gas}, as at the pressures involved (≈100-200 Torr) collisions between species within the gas phase should allow for efficient transfer between rotational and translational energy levels.

C_2(a, v=0) absorption spectra obtained at three values of $X_0(H_2)$ (1 %, 14.7 % and 88.6 %) are shown in Figure 3.6 along with two simulations of the C_2(d←a) (0,0) spectrum when T_{gas} = 2000 and 3000 K (produced using PGOPHER [15]). All three experimental spectra show features very similar to the T_{rot}=3000 K simulation, suggesting that the gas temperature of the region of the plasma within which C_2(a) is located is ≈3000 K. The gas temperature along the column probed by the laser is far from homogeneous, with the gas temperature reaching a maximum in the centre of the plasma and

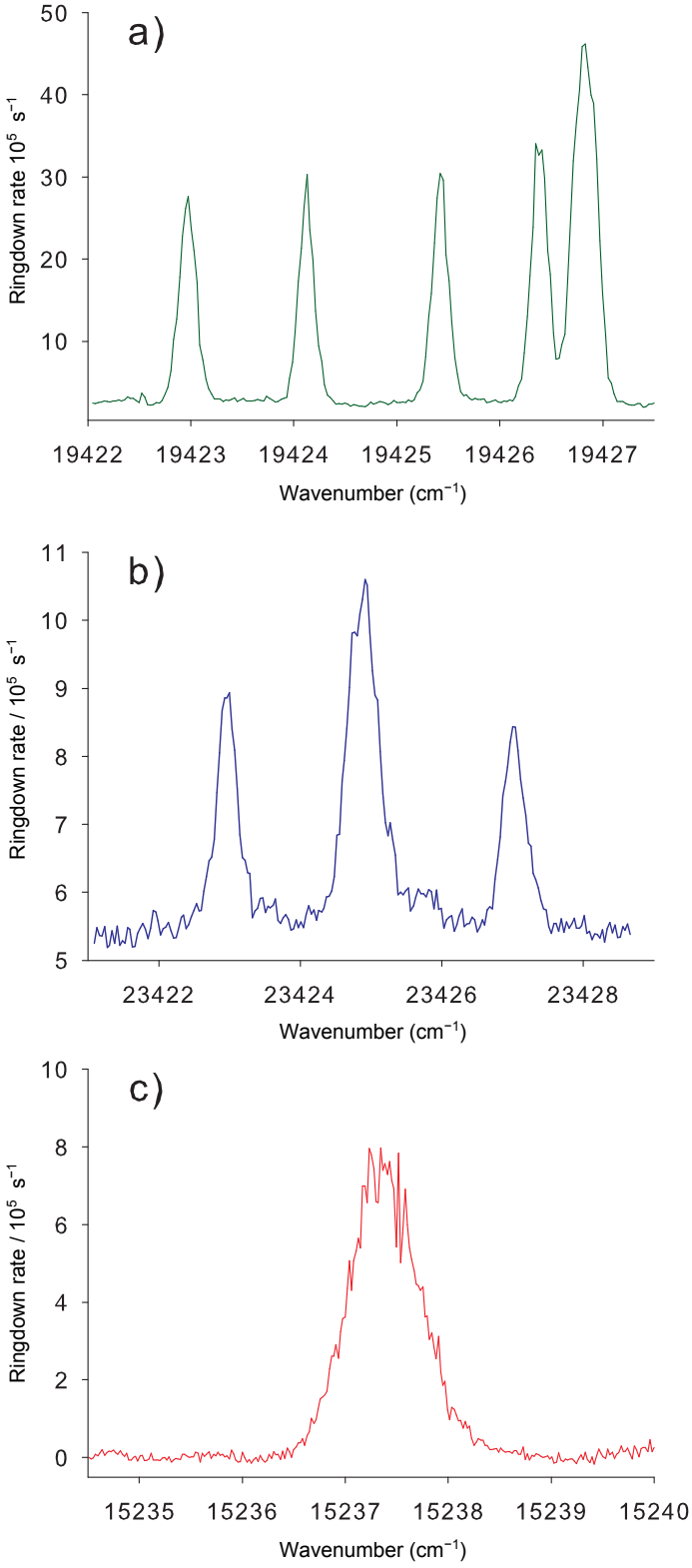

Figure 3.5: Typical spectra obtained for a) a portion of the C_2 ($d^3\Pi_g \leftarrow a^3\Pi_u$) (0,0) transition, b) a portion of the CH ($A^2\Delta \leftarrow X^2\Pi$) (0,0) transition and c) the H ($n = 3 \leftarrow n = 2$) transition.

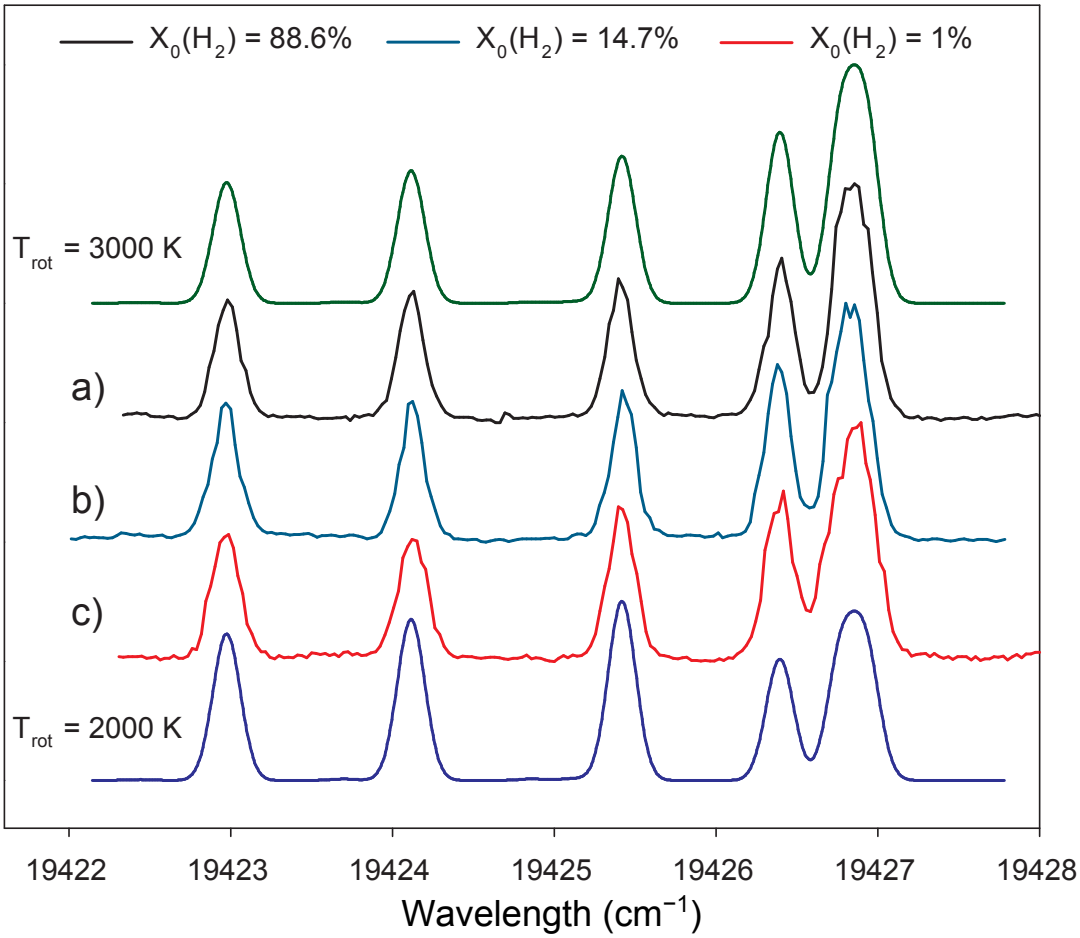

Figure 3.6: CRDS spectra of a portion of the $C_2(d^3\pi_g \leftarrow a^3\Pi_u)$ (0,0) band measured for a) typical MCD growth conditions (H_2-rich, 4.4% CH_4 / 88.6% H_2 / 7% Ar, p = 150 Torr, P= 1.5 kW), b) base conditions in our present experiments (0.5%CH_4 /14.7%H_2 / 84.8%Ar, p = 150 Torr, P= 1.0 kW) and c) UNCD type growth conditions (0.5%CH_4 / 1%H_2 / 98.5%Ar, p = 150 Torr, P= 0.5 kW). The upper and low traces are PGOPHER simulations of the relevant portion of the transition assuming $T_{\rm rot}$ = 3000 and 2000 K, respectively.

decaying to room temperature near to the water cooled walls. The $T_{\rm rot}$ value of ≈3000 K obtained for C_2(a) radicals thus implies that these radicals are located close to the centre of the plasma. This was also observed in earlier studies of 4.4% CH_4/88.6% H_2/7% Ar plasmas by Ma *et al.*[12] Figure 3.6 also suggests that $T_{\rm rot}$ and therefore $T_{\rm gas}$ are relatively insensitive to adjustment of the H_2/Ar ratio.

A number of groups have previously published $T_{\rm rot}$ values which can be compared to the value obtained in the current work. One study reported significantly lower $T_{\rm rot}$ values of 1150-1350 K in early broadband absorption studies of C_2(a) radicals in 1% CH_4 / 2% H_2 / 97% Ar, $0.5 \leq p \leq 100$ Torr, $0.5 \leq P \leq 1.5$ kW plasmas.[16] However re-analysis of the published emission and absorption spectra in this paper with PGOPHER suggests that the $T_{\rm rot}$ values were closer to 3000 K. CRD spectra reported by Rabeau *et al.*[11] in plasmas containing 1% CH_4, 0% - 14% H_2 and 99% - 86% Ar, at p

= 90 Torr and P = 2.1 kW also measured T_{rot} values of ≈ 3000 K. Lombardi *et al.*[17] recorded T_{rot} values in the range of 3000-4200 K from analysis of broadband absorption and emission spectra and, as with our current CRDS measurements, in addition no clear changes were observed as the H_2/Ar ratio or P were varied.

3.3.2 Column density calculations

The intensity of the lines recorded in the CRDS spectra can be directly related to the number density of the absorbing species by;

$$\int \alpha \, \mathrm{d}\bar{v} = \frac{\lambda^2 g_j}{8\pi c g_i}[\mathrm{X}]Ap \quad . \tag{3.1}$$

where, α is the absorption coefficient, $\bar{v}$ is the wavenumber, λ is the wavelength of the specific line, g_j and g_i are the electronic degeneracies of the upper and lower states, respectively, c is the speed of light, [X] is the number density of species X, A is the Einstein A coefficient for the specific band being measured (for example A_{00} is used in the conversion of the line strengths of the v'=0←v"=0 transition in the C_2 d←a spectra to column densities) and p is a constant relating the fraction of the spectrum represented in the measured lines to the total transition strength of the entire band. The constant p is temperature dependent and its value is calculated from PGOPHER simulations and is henceforth referred to as a PGOPHER coefficient. As observed above, T_{rot} calculated from measured C_2 spectra return a value of ≈3000 K, consequently this value was used in the calculation of the PGOPHER coefficients.

The absorption coefficient can be directly related to the measured ring down time by;

$$\alpha = \frac{L\Delta k}{c l_{\mathrm{eff}}} \quad , \tag{3.2}$$

where L is the length of the cavity (i.e the distance between the two mirrors, which in the case of our current experiments is ≈84 cm), Δk is the change in the ring down rate and l_{eff} is the effective path length through the absorber.

Combining equations 3.1 and 3.2 leads to;

$$\int \frac{L\Delta k}{c l_{\mathrm{eff}}} \, \mathrm{d}\bar{v} = \frac{\lambda^2 g_j}{8\pi c g_i}[\mathrm{X}]Ap \quad . \tag{3.3}$$

Subsequent rearrangement of equation 3.3 and cancellation results in;

$$\int \Delta k \, \mathrm{d}\bar{v} = \frac{\lambda^2 l_{\text{eff}} g_j}{8\pi L g_i}[\mathrm{X}] A p \ . \tag{3.4}$$

This equation relates the number density of species X to the area under the recorded line ($\int \Delta k \, \mathrm{d}\bar{v}$). This depends on knowing the the effective path length (l_{eff}) of the laser through the absorbing species X, however. Due to the nature of the plasma and its inherent inhomogeneity, l_{eff} is difficult to define. Instead column densities (D_{X}) are recorded, where

$$D_{\mathrm{X}} = l_{\text{eff}}.[X]. \tag{3.5}$$

Consequently, column densities for species X are calculated using

$$D = \frac{8\pi L g_i}{\lambda^2 A p g_j} \int \Delta k \, \mathrm{d}\bar{v} \ . \tag{3.6}$$

A slightly different approach was however required for the conversion of measured H(n=2) absorptions into column densities, as the measured absorption peak is a convolution of seven different transitions. The absorption measured is therefore related to the population of the lower levels (N_i) and the absorption cross sections for each of the transitions(σ_{ij});

$$\int \alpha \, \mathrm{d}v = \sum_{i,j} N_i \sigma_{ij} \ . \tag{3.7}$$

The lower (n=2) levels ($^2S_{\frac{1}{2}}$, $^2P_{\frac{1}{2}}$, $^2P_{\frac{3}{2}}$) all lie very close in energy and their populations can be considered to be proportional to their electronic degeneracy *i.e.* ,

$$N_i = N_{\mathrm{H}(n=2)} \frac{g_i}{\sum\limits_i g_i} \ . \tag{3.8}$$

In the case of H(n=2) $\sum\limits_i g_i$ = 8.

The absorption cross section σ_{ij} can be directly related to the Einstein A coefficient for each of the transitions by

$$\sigma_{ij} = \frac{g_j A_{ji} \lambda^3 v_{ij}}{g_i 8\pi c} = \frac{g_j A_{ji} \lambda_{ij}^2}{g_i 8\pi} \, . \tag{3.9}$$

Combining equations 3.7, 3.8 and 3.9 leads to the following equation

$$\int \alpha \, \mathrm{d}v = \sum_{i,j} N_{\mathrm{H}(n=2)} \frac{g_i}{8} \cdot \frac{g_j A_{ji} \lambda_{ij}^2}{g_i 8\pi} \tag{3.10}$$

$$= \frac{N_{\mathrm{H}(n=2)}}{64\pi} \sum_{i,j} g_j A_{ji} \lambda_{ij}^2 \, . \tag{3.11}$$

The measured absorption is also related to the ring down rate by,

$$\int \alpha \, \mathrm{d}v = \frac{L}{c l_{\mathrm{eff}}} \int \Delta k \, \mathrm{d}v \tag{3.12}$$

Combining equations 3.11 and 3.12,

$$\frac{L}{c l_{\mathrm{eff}}} \int \Delta k \, \mathrm{d}v = \frac{N_{\mathrm{H}(n=2)}}{64\pi} \sum_{i,j} g_j A_{ij} \lambda_{ij}^2 \tag{3.13}$$

$$N_{\mathrm{H}(n=2)} . l_{\mathrm{eff}} = \frac{64\pi L}{c \sum_{i,j} g_j A_{ij} \lambda_{ij}^2} \int \Delta k \, \mathrm{d}v \tag{3.14}$$

$$D_{\mathrm{H}(n=2)} = \frac{64\pi L}{\sum_{i,j} g_j A_{ij} \lambda_{ij}^2} \int \Delta k \, \mathrm{d}\bar{v} \tag{3.15}$$

The Einstein A coefficients, PGOPHER coefficients, degeneracies and wavelengths used to convert the measured absorptions of C_2(a), CH(X) and H(n=2) to column densities are listed in Appendix B.

3.3.3 Column density measurements

Column densities of C_2(a, $v = 0$), CH(X, $v = 0$) radicals and H(n=2) atoms (represented as {C_2(a, v=0)}, {CH(X, v=0)} and {H(n=2)} from now on) have been measured as a function of height above the substrate (z) under our current experimental base conditions using CRDS and are shown in Figure 3.7. For comparison column density measurements from the earlier work of Ma *et al.*[12] under H_2-

rich (MCD) plasma conditions (4.4% CH_4/ 88.6% H_2/ 7% Ar, p= 150 Torr, P = 1.5 kW) and column densities returned from the Bristol-Moscow plasma model under the current base conditions are also included.

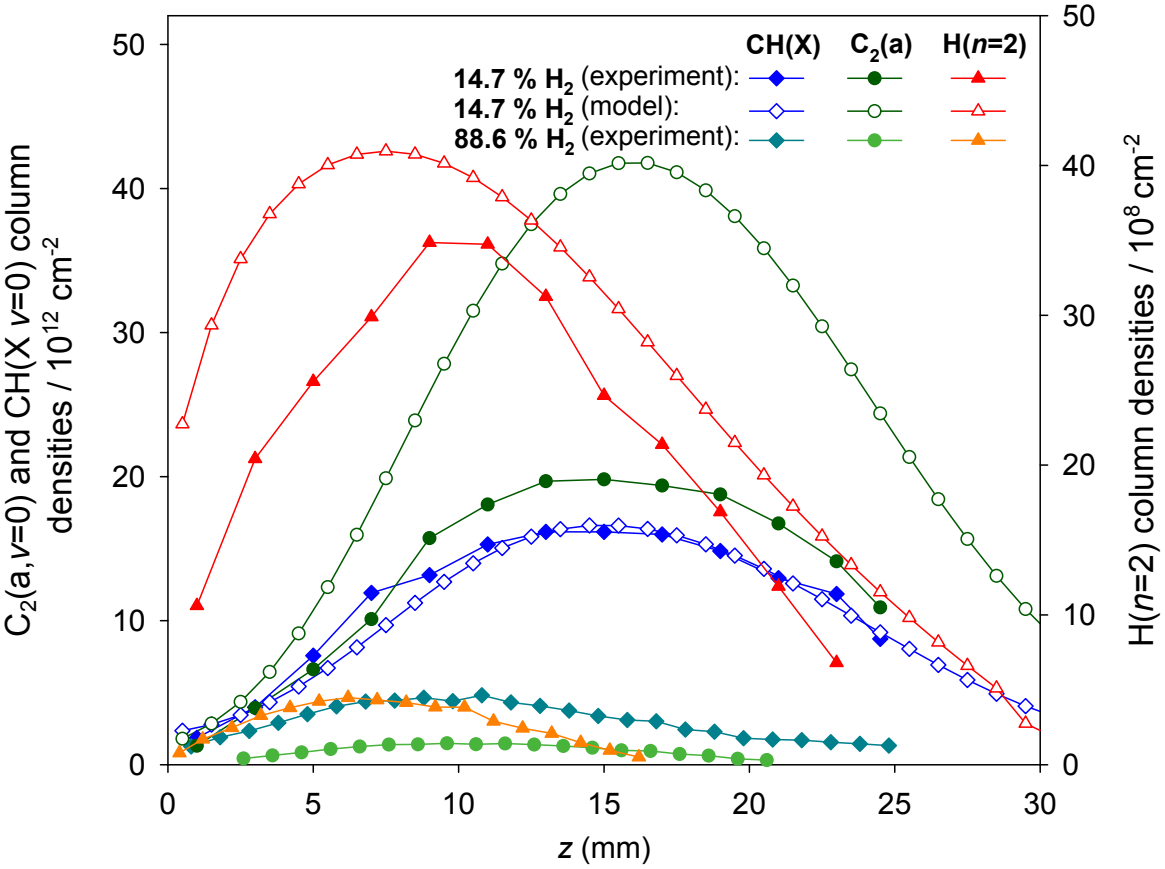

Figure 3.7: Measured and calculated (filled and open symbols respectively) C_2(a, v=0), CH(X, v=0) and H(n=2) column densities as a function of z for the base conditions (0.5% CH_4/ 14.7% H_2/ 84.8% Ar p=150 Torr, P=1.0 kW). Also included for comparison are column densities of C_2(a, v=0), CH(X, v=0) and H(n=2) measured for typical MCD type growth conditions (4.4% CH_4/ 88.6% H_2/ 7% Ar, p=150 Torr, P=1.5 kW, from ref 12)

One major difference between the current base conditions and the previous work on H_2-rich plasmas is that the measured column densities under the current base conditions peak at a greater height above the substrate and show a much more extensive spatial distribution. This is consistent with the visible expansion of the plasma ball seen when $X_0(H_2)$ is reduced. Another difference between the two plasmas is that the peak column densities of all three species under the current base conditions in comparison to those under the MCD conditions are significantly higher, even though the present base conditions contain only a fraction of the input CH_4 (0.5 % *vs.* 4.4 %) and employ a lower power (P = 1.0 *vs.* 1.5 kW). {H(n=2)} is shown to peak closer to the substrate than either {CH(X v=0)} or {C_2(X v=0)}. This phenomenon was also observed in the previous CRDS study on H_2-rich plasmas[12], and

arises because the production of H(n=2) atoms relies on both the concentration of H(n=1) atoms and of suitably energetic electrons or other excited species. The distribution is thus a convolution of the thermal H(n=1) distributions (which is expected to peak near the centre of the plasma) and the distribution of suitably energetic electrons or excited species (with the electron density expected to reach a maximum closer towards the substrate). The good agreement between the calculated results from the plasma model and the experimental measurements is also shown in this figure; the respective column densities agree to within a factor of 2, with the largest discrepancy being the model's over estimation of $\{C_2(a, v=0)\}$. This effect may be a result of a the model lacking a number of additional pathways which would lead to the conversion of C_2 to higher hydrocarbon species.

$\{C_2(a, v=0)\}$, $\{CH(X, v=0)\}$ and $\{H(n=2)\}$ have also been measured as a function of $X_0(H_2)$, $X_0(CH_4)$, p and P at a fixed height, z=9.5 mm above the substrate. Previous work by Ma *et al.*[12] showed that the column densities of all three species increased as $X_0(H_2)$ was reduced from 95.6% to 42.5%. $C_2(a, v=0)$ was found to increase the most across this range, with the $\{C_2(a, v=0)\}/\{CH(X, v=0)\}$ ratio increasing by a factor of 3. In Figure 3.8a it can be seen that as $X_0(H_2)$ is further reduced this trend continues, with $\{C_2(a, v=0)\}$ and $\{CH(X, v=0)\}$ becoming comparable at our base conditions (*i.e.* $X_0(H_2)$=14.7%) and z=9.5 mm. Further reduction of $X_0(H_2)$ sees $\{CH(X, v=0)\}$ first plateau and then start to decrease; in contrast $\{C_2(a, v=0)\}$ continues to steeply increase. $\{H(n=2)\}$ is also seen to increase by approximately a factor of 4 as $X_0(H_2)$ is reduced from 50% to 10%. At the base power and pressure (1 kW and 150 Torr respectively), when $X_0(H_2)$ was reduced to below 10% it became unsafe to operate the reactor for significant lengths of time due to the large increase in size of the plasma ball. Reduction of P to 0.5 kW allowed investigation of plasmas with lower H_2 fractions. Data points for $\{C_2(a, v=0)\}$ at z=9.5 mm, $X_0(H_2)$=1, 5, 10 and 15% and P=0.5 kW are also included in Figure 3.8a. $\{C_2(a, v=0)\}$ in these points showed a continued rise with further reduction of $X_0(H_2)$, in contrast to earlier results of Rabeau *et al.*[11] who found $\{C_2(a, v=0)\}$ to reach a maximum at $\approx X_0(H_2)$=95% before declining. Due to the sooty nature of these very low $X_0(H_2)$ plasmas trends observed are likely to be sensitive to the reactor configuration and changes in the plasma volume as well as the choice of z.

The effect of varying $X_0(CH_4)$ from 0% (hydrocarbon free), to 2% (Once again, $X_0(Ar)$ is adjusted to keep F_{Total} constant) is shown in Figure 3.8b. $\{C_2(a, v=0)\}$ was found to show an approximately linear relationship with increasing $X_0(CH_4)$, whereas $\{CH(X, v=0)\}$ increases less steeply. These trends are similar to those observed in previous work on MCD plasmas,[12] albeit with the column densities measured in the MCD plasmas being around an order of magnitude lower. Upon the introduction of a trace amounts of CH_4 (0.25%) a large increase ($\times 8$) in $\{H(n=2)\}$ is observed. This has

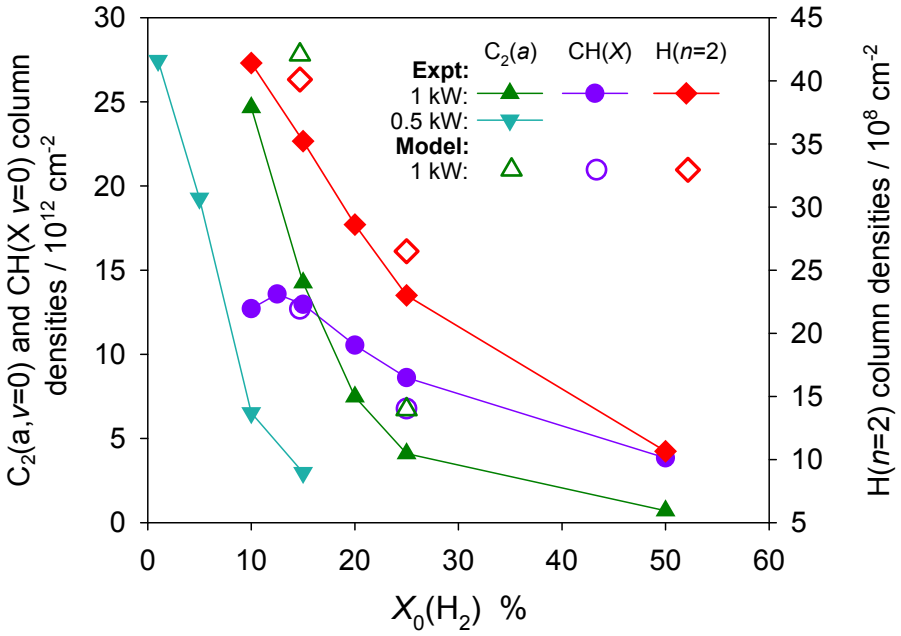

(a)

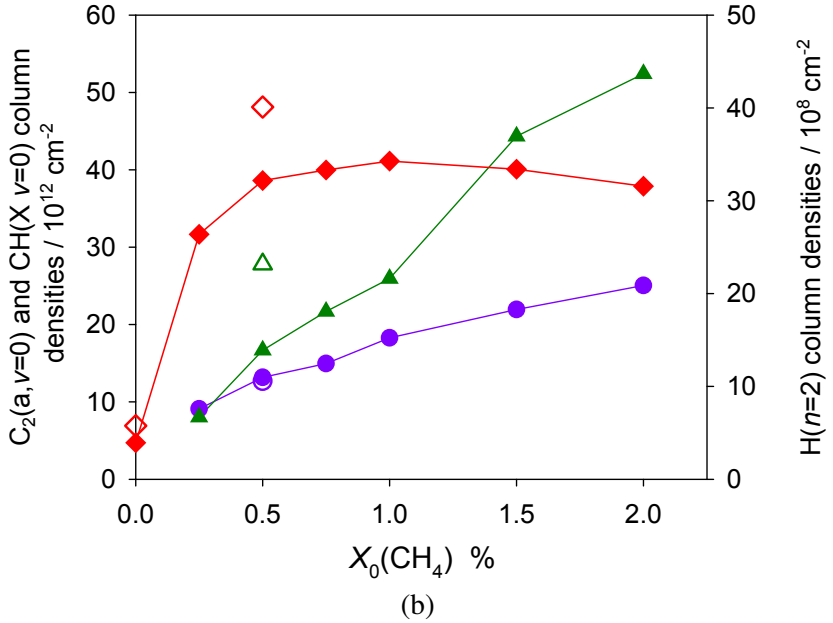

(b)

Figure 3.8: Measured and calculated (filled and open symbols, respectively) column densities of C_2(a, v=0), CH(X, v=0) and H(n=2) as a function of a) $X_0(H_2)$ and b) $X_0(CH_4)$ at a fixed height (z=9.5 mm) above the substrate. F_{Total} is kept at a constant by adjusting X_0(Ar) to compensate for adjustments in $X_0(H_2)$ and $X_0(CH_4)$.

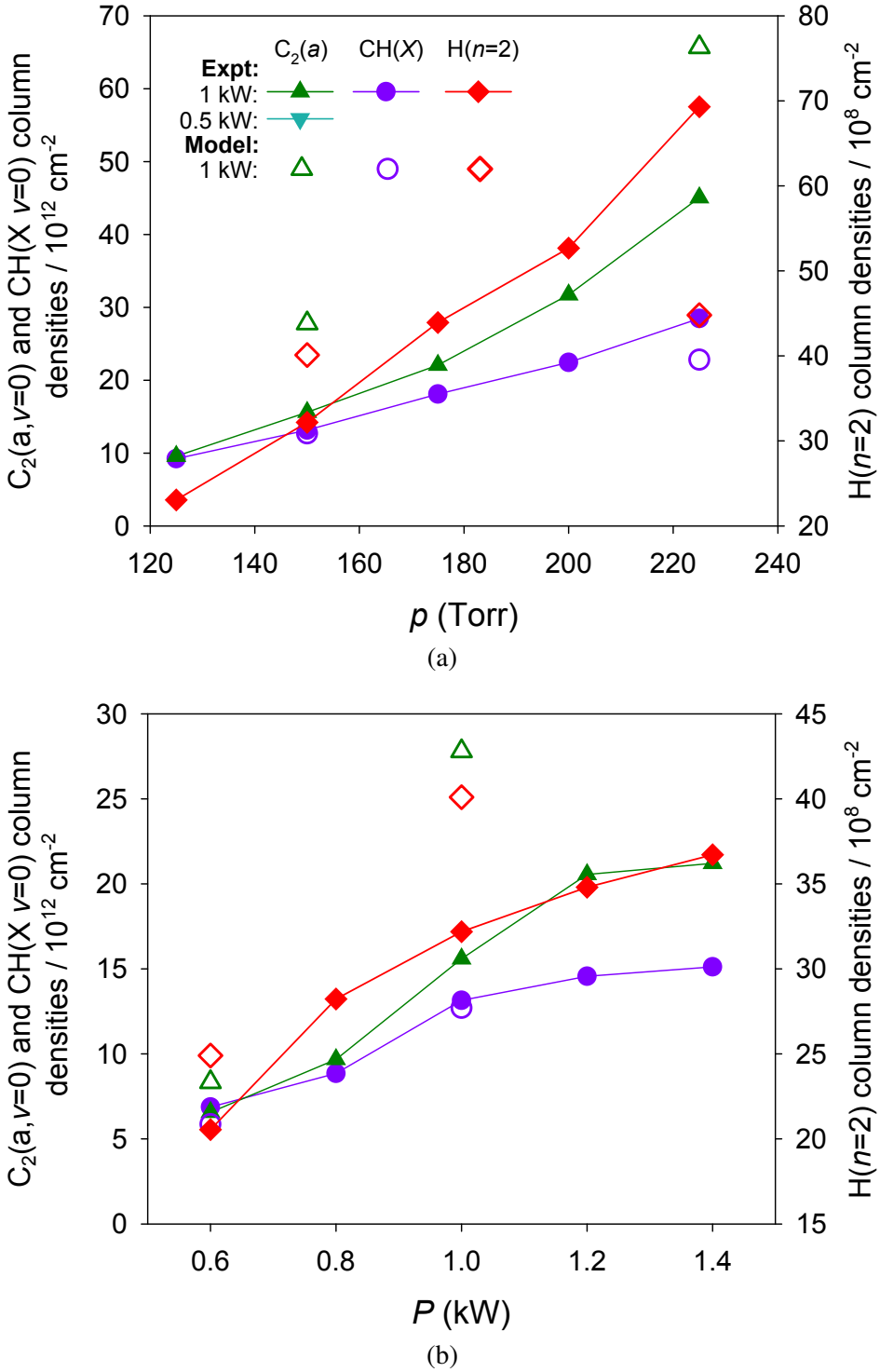

Figure 3.9: Measured and calculated (filled and open symbols, respectively) column densities of C_2(a, v=0), CH(X, v=0) and H(n=2) as a function of a) pressure and b) applied microwave power at a fixed height (z=9.5 mm) above the substrate.

been previously attributed[12] to a change in the dominant ion from H_3^+ and ArH^+ in H_2/Ar plasmas to $C_yH_x^+$ in CH_4/H_2/Ar plasmas and an increase in T_e from 1.28 eV (0% CH_4) to 1.74eV (0.5% CH_4).

Figures 3.9a and 3.9b show the effects of varying both pressure and power, respectively under otherwise base conditions. $\{C_2(a, v=0)\}$, $\{CH(X, v=0)\}$ and $\{H(n=2)\}$ are all seen to increase with increasing p (125-225 Torr), with a greater increase in $\{C_2(a, v=0)\}$ compared to $\{CH(X, v=0)\}$. The increase in column densities measured as pressure is increased may result from a combination of a number of different factors. The main one is likely to be simply the increased number density of all the input gases, though factors such as the plasma volume and shape, as well as changes in the temperature distribution will also contribute. Similarly, as P is increased (from 0.6 to 1.4 kW), all three species' column densities increase with the change in $\{C_2(a, v=0)\}$ once again being greater than $\{CH(X, v=0)\}$.

3.3.4 Optical emission measurements

In conjunction with the CRDS measurements, optical emission spectra were recorded monitoring the emission of $C_2(d\rightarrow a)$, $C_3(A\rightarrow X)$, $CH(A\rightarrow X)$ radicals at 516.5, ≈405 and 431.4 nm, respectively, and the Balmer α (H_α) and Balmer β (H_β) emission of $H(n=3\rightarrow 2)$ and $H(n=4\rightarrow 2)$ atoms at 656.3 and 486.1 nm, respectively. A typical emission spectrum with the various spectral features highlighted is shown in Figure 3.10.

The dependence of the emission intensity of each of the species mentioned above was measured as a function of process conditions. Figure 3.11a shows the effect of varying $X_0(H_2)$ between 50% and 5%. The measured trends were similar to those recorded using CRDS (Figure 3.8a). The intensity of $CH(A\rightarrow X)$ emission firstly increased to a maximum at $X_0(H_2)$≈10% and then decreased upon further reduction of $X_0(H_2)$. Emission from $C_2(d\rightarrow a)$ and $C_3(A\rightarrow X)$ in contrast continued to increase in intensity as $X_0(H_2)$ was reduced to 5%. The intensity of H_α and H_β emission qualitatively showed similar behaviour, with both reaching a peak in emission intensity at $X_0(H_2)$≈10% (similar to $CH(A\rightarrow X)$). The ratio between their emission intensities $I(H_\beta)/I(H_\alpha)$ was also found to change little as the $X_0(H_2)$ is varied. The behaviour of $I(H_\beta)/I(H_\alpha)$ might suggest that T_e is insensitive to $X_0(H_2)$, but the companion modelling shows this is not the case. The calculated ratio of H(n=3) to H(n=2) number densities within in the plasma model remains similar for $X_0(H_2)$=1, 14.7 and 25% even though T_e decreases, T_e = 2.45, 1.74 and 1.67 eV.

The effect of varying $X_0(CH_4)$ from 0% to 2% on the emission intensity of the five transitions is

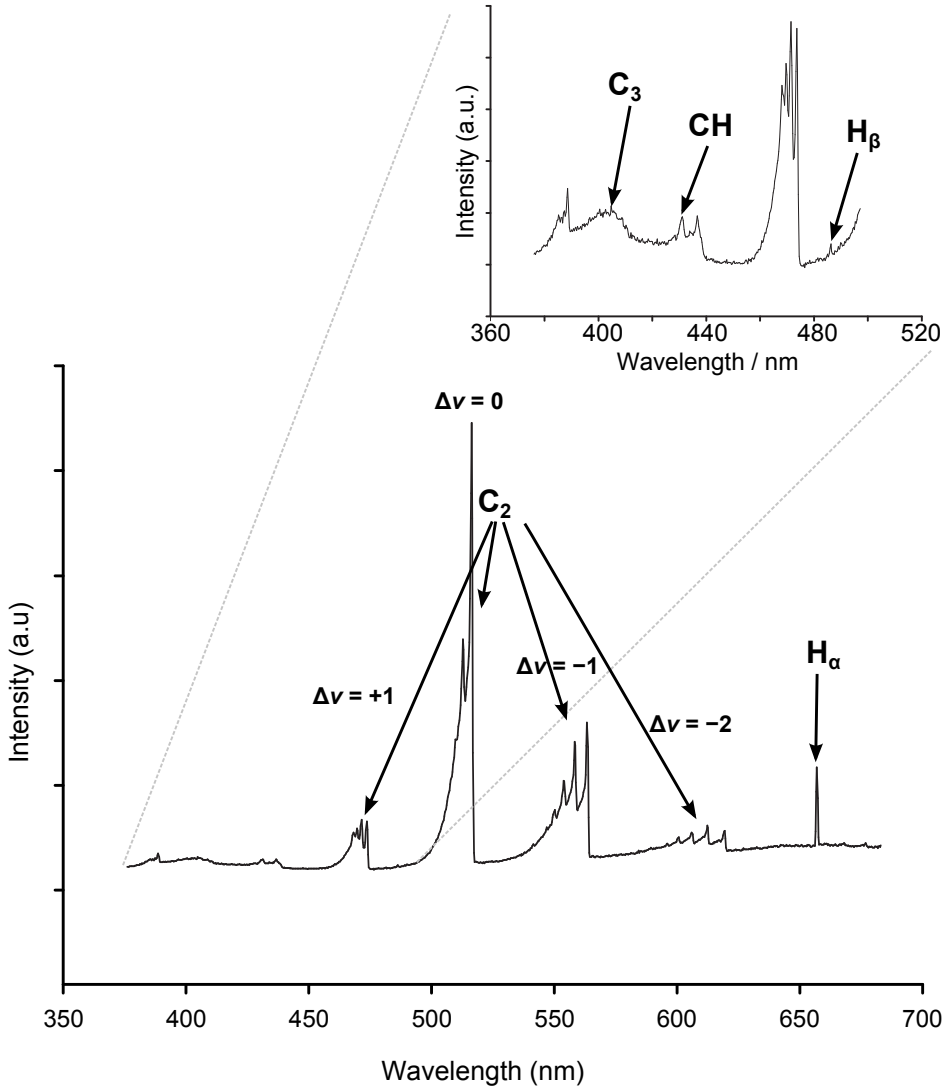

Figure 3.10: A typical emission spectra recorded at base conditions. Emissions associated with C_2(d→a), C_3(A→X) and CH(A→X) radicals as well as those of H(n=3→2) and H(n=4→2) atoms are highlighted.

shown in Figure 3.11b. Once again the behaviour followed that observed in the CRDS measurements (Fig. 3.8b); CH(A) emission increased initially before levelling off, emissions from C_2(d) and C_3(A) both increased quickly with increasing $X_0(CH_4)$ and, finally, H_α and H_β intensities both showed a similar stepped increase as a trace amount of CH_4 ($X_0(CH_4)$=0.25%) were added to the plasma, before slowly declining as $X_0(CH_4)$ was increased further. The initial sharp increase in the intensity of H_α and H_β emission upon addition of 0.25% CH_4 is thought to be a consequence of an increase in T_e (as stated above for the CRDS measurements). The change in T_e might however be expected to manifest itself in a change in the $I(H_\beta)/I(H_\alpha)$ ratio as well. In contrast though, little change is observed in the $I(H_\beta)/I(H_\alpha)$ ratio. Modelling of the plasma however, offers an explanation for this observation, as not only does T_e vary but a numerous of other factors such as; the electron density

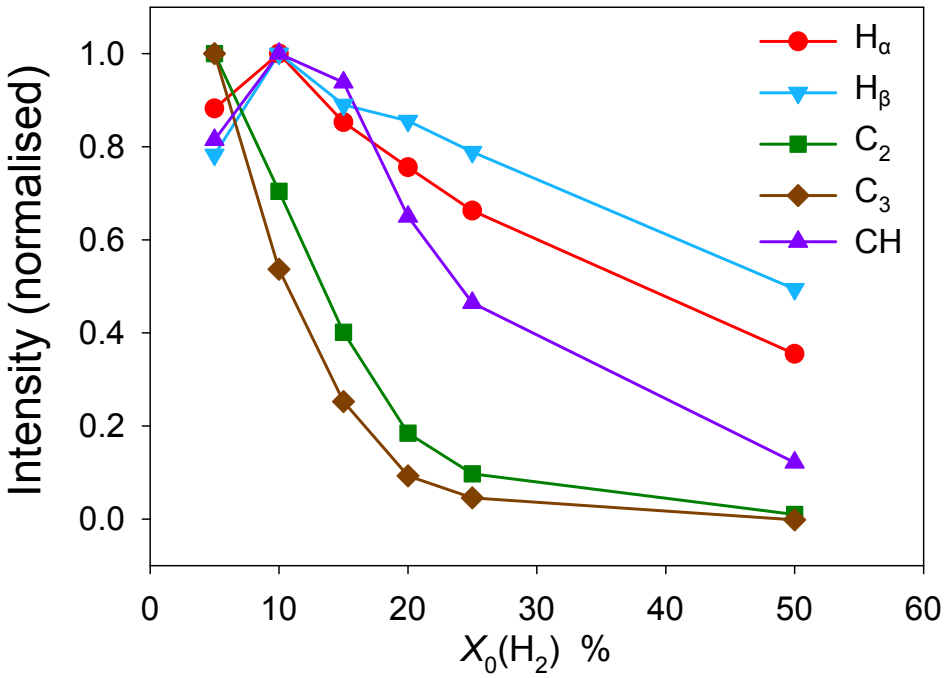

(a)

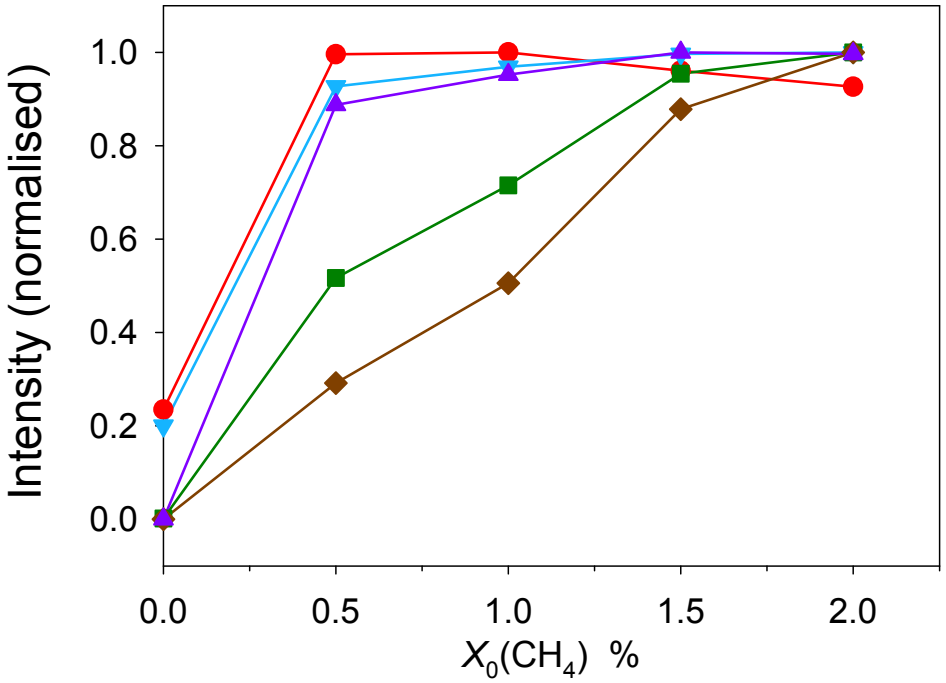

(b)

Figure 3.11: Normalized relative H_α, H_β, C_2(d→a), CH(A→X) and C_3(A→X) emission intensities plotted as a function of a) $X_0(H_2)$ and b) $X_0(CH_4)$. As with CRDS measurements F_{Total} was kept constant by compensating any change in $X_0(H_2)$ or $X_0(CH_4)$ with Ar.

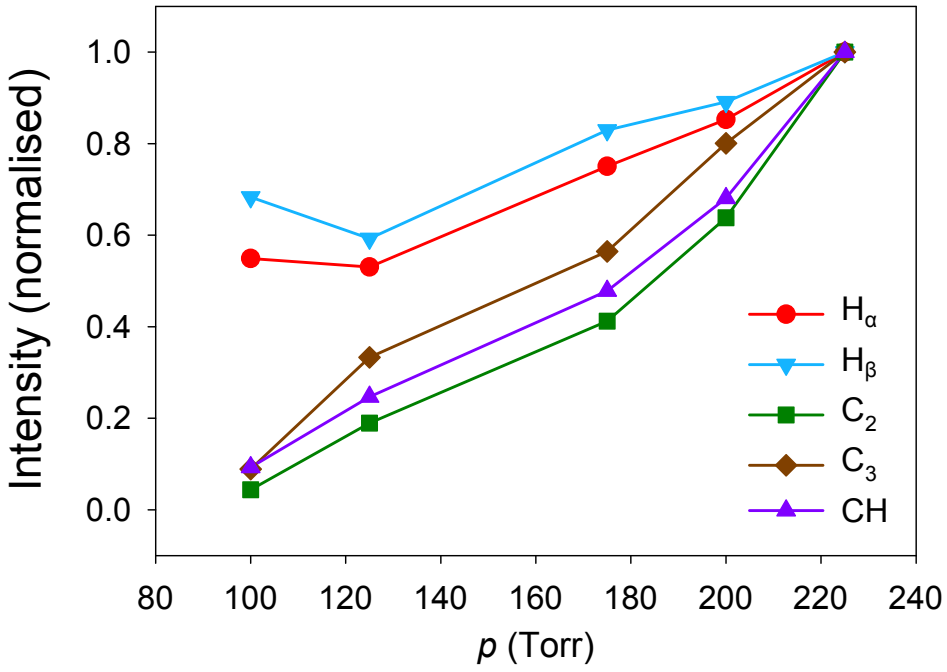

(a)

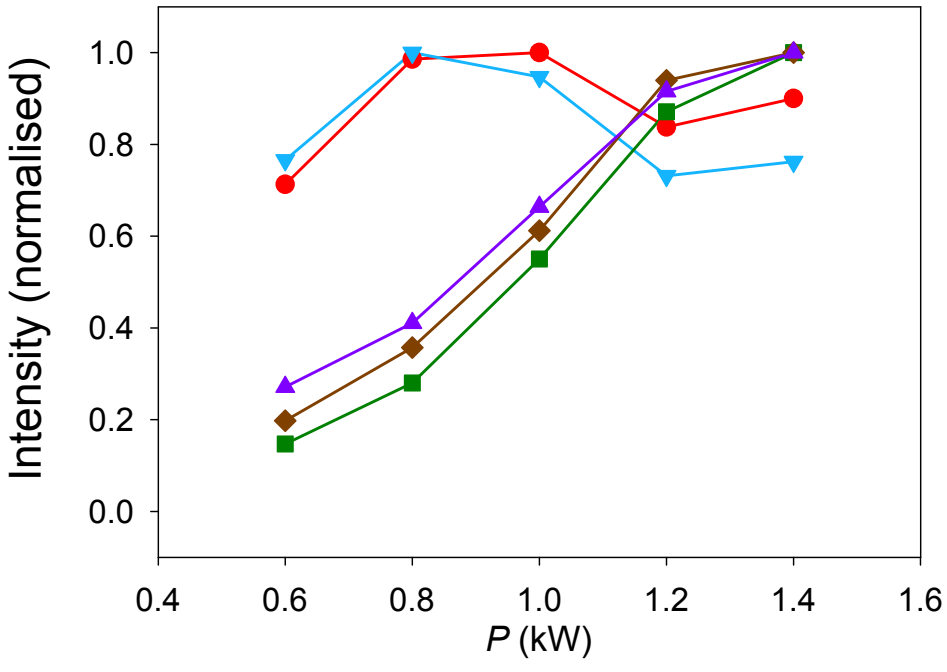

(b)

Figure 3.12: Normalized relative H_α, H_β, C_2(d→a), CH(A→X) and C_3(A→X) emission intensities plotted as a function of a) total pressure and b) applied microwave power.

(n_e), Ar* and H atom concentrations and their respective distributions and the plasma volume also do. Because of the simultaneous variations of these other factors the plasma model is able to replicate both the increase in $I(H_\beta)$ and $I(H_\alpha)$ as trace amounts of CH_4 are added, but also the invariability of the $I(H_\beta)/I(H_\alpha)$ ratio.

The effect of varying the total pressure and applied microwave power is shown in Figures 3.12a and 3.12b, respectively. Varying pressure between 100 and 225 Torr resulted in an increase in emission of all species, reflecting the increased number density of all species within the plasma. Increasing the applied MW power from 0.6 kW to 1.4 kW also gave rise to an increase in emission intensity of CH(X), C_2(d) and C_3(A). The intensity of H_α and H_β, varied little with increasing P, first increasing slightly (0.8 to 1.0 kW) before falling back to initial levels.

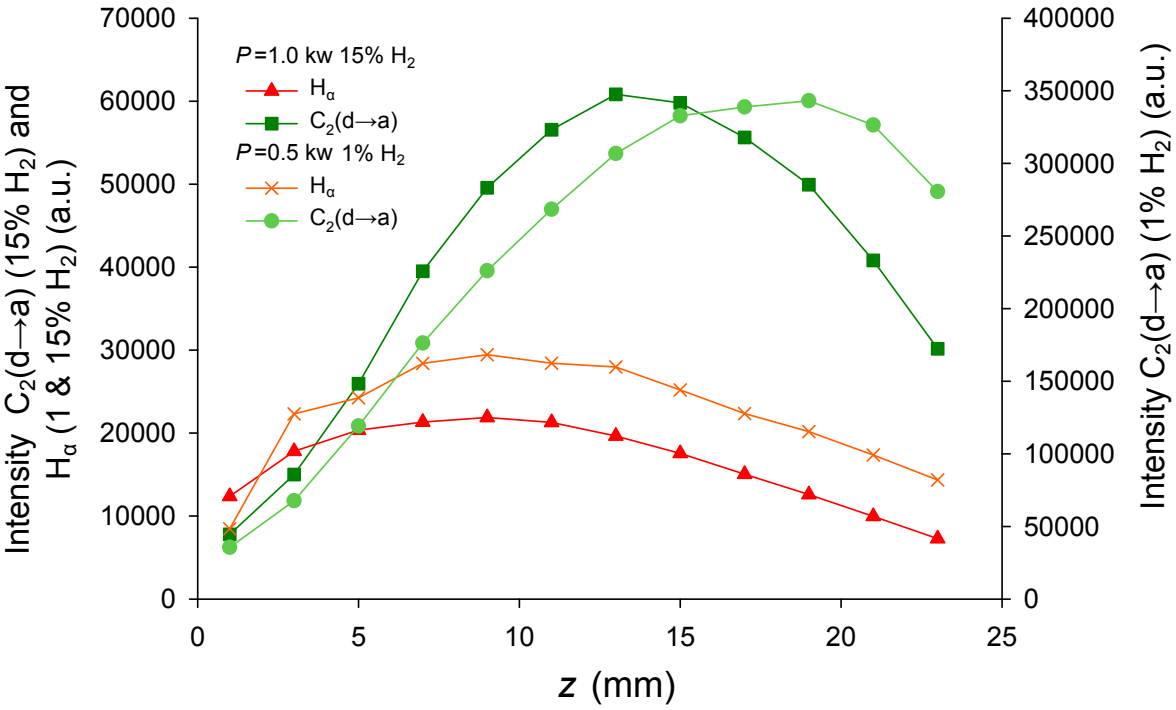

Figure 3.13: Spatial profiles of the emission intensities of the C_2(d→a) and H_α transitions, when $X_0(H_2)$ is 1% and 15%, with P=0.5 kW and 1.0 kW, respectively, p=150 Torr and $X_0(CH_4)$=0.5%.

In Figure 3.13 the emission intensities of both C_2(d) and H_α are shown as a function of z at two different values of $X_0(H_2)$ (1 and 15%). The change in plasma size between $X_0(H_2)$=1 and 15% is clearly seen with the emission intensity of C_2(d) peaking significantly further away from the substrate (z=0) when $X_0(H_2)$=1%. This difference is even more dramatic when it is noted that $X_0(H_2)$ = 1% data were obtained using only half the input power (P = 0.5 kW). H_α however does not exhibit this behaviour with the peak remaining in a similar region. A possible explanation for this is that excitation of H atoms from the ground state H(n=1) to H(n=3) requires higher energy electrons than

C_2(a) to C_2(d) and therefore the H_α emission is more dependant on the EEDF than the C_2(d→a) transition is, offering explaination as to why its emission is constrained closer to the substrate.

3.3.5 Results from plasma modelling

As seen above (figs. 3.8 and 3.9) the 2D(r, z) modelling of the MW plasma by Yuri Mankelevich shows markedly good agreement with the experimentally measured column densities, whilst, also offering insights into how numerous plasma parameters effect the emission of species. In this section some of notable results returned by the 2D(r, z) model regarding the effect of increasing the argon content within the plasma are presented.

Figure 3.14 shows some of the key changes in; the average power density (Q), the average electron temperature (T_e), the proportion of H_2 that is dissociated ([H]/[H_2]) and the plasma volume (V), as $X_0(H_2)$ is decreased. It can be seen clearly that as $X_0(H_2)$ is reduced from 88.6% to 1% the average power density decreased whilst T_e and [H]/[H_2] increased. In fact as $X_0(H_2)$ is increased from 1% to 14.7% the H atom fraction only increases by a factor of ≈2 whilst the H_2 fraction increases by a factor of 14.7.

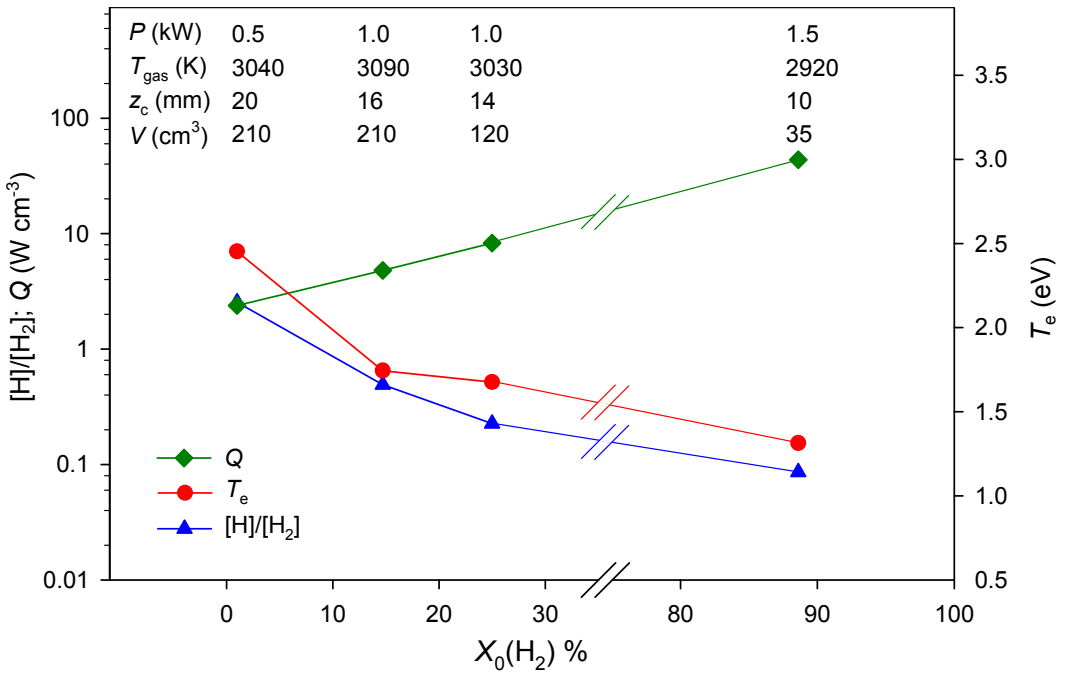

Figure 3.14: Variation of the average power density, Q, average electron temperature, T_e and [H]/[H_2] ratio as a function of $X_0(H_2)$ within the central hot region of the plasma (r=0, $z = z_C$ where z_C is the central region of the plasma, and z=0 is the location of the substrate). The points at 1, 14.7 and 25% $X_0(H_2)$ are all calculated with $X_0(CH_4)$=0.5%, a value of 4.4% is used when $X_0(H_2)$=88.6%. Q was estimated from the relationship $Q = \frac{P}{V}$, where V is the plasma volume.

The model also reveals that as $X_0(H_2)$ is decreased, the volume of the plasma increases. Supporting the explanation for the observed changes in the cooling water temperature as it passes through the walls (increased ΔT_{walls}) and the base of the reactor (decreased ΔT_{base}) offered for the results in Figure 3.4. As the plasma expands the walls get hotter as the edges of the plasma move closer, but the base cools as the plasma's hot centre moves further away. This increase in volume is due to the inability of Ar-rich plasmas to absorb the input power as efficiently as H_2 dominated plasmas (as shown in Figure 3.14). Under conditions when $X_0(H_2)$>85%, most of the absorbed MW energy is expended in rotational and vibrational excitation of H_2 (this leads to a small tight plasma above the substrate). Under UNCD type conditions (low $X_0(H_2)$) the energy is expended on rotational and vibration excitation of H_2 and C_yH_x species[9], but the density of low energy excited states however, is smaller in these Ar-rich plasmas, leading to a lower absorbance capacity. As the absorbance capacity of these plasmas is lower, the volume of the plasma is required to expand in order to accommodate the same input power. The total absorbance capacity, P_{max} for the MWPECVD reactor parameters used in the model with an average H_2 mole fraction ($X(H_2)$) of ≈1% is calculated to be ≈1.1 kW. This reduced absorbance capacity may explain why the measured column densities and emission intensities start to plateau as P was increased.

Another key point highlighted in the model is that T_{gas} in the centre of the plasma shows little variation with $X_0(H_2)$, always staying close to 3000 K. The thermal conductivity of the Ar-rich plasmas is lower than H_2-rich plasmas and, therefore might be expected to result in an increase in the gas temperature, but this effect is offset by the increase in plasma volume as the Ar fraction is increased.

Figure 3.15 shows a false colour plot of the calculated number densities of CH_3 and C_2(a) radicals as a function of r and z within the reactor volume when operating under the current base conditions. As with the previous work of Ma *et al.*[12], it can be seen that the CH_3 is located in the cooler regions of the plasma whilst C_2 is concentrated in the hotter region.

3.3.6 Conclusions

In this chapter a combination of cavity ring down and optical emission spectroscopy has been applied to explore the effect of large variations in the H_2/Ar ratio within the input gas mixture. Column densities of C_2(a, v=0), CH(X, v=0) radicals and H(n=2) atoms were measured and a spatial profile of all three species at the base conditions (0.5% CH_4/ 14.7% H_2/ 84.8% Ar, p=150 Torr, P=1.0 kW, F_{Total}=525 sccm) was produced. This showed a significant increase in the measured number densities as well as more extensive spatial distributions when compared to results for H_2-rich plasmas (4.4%

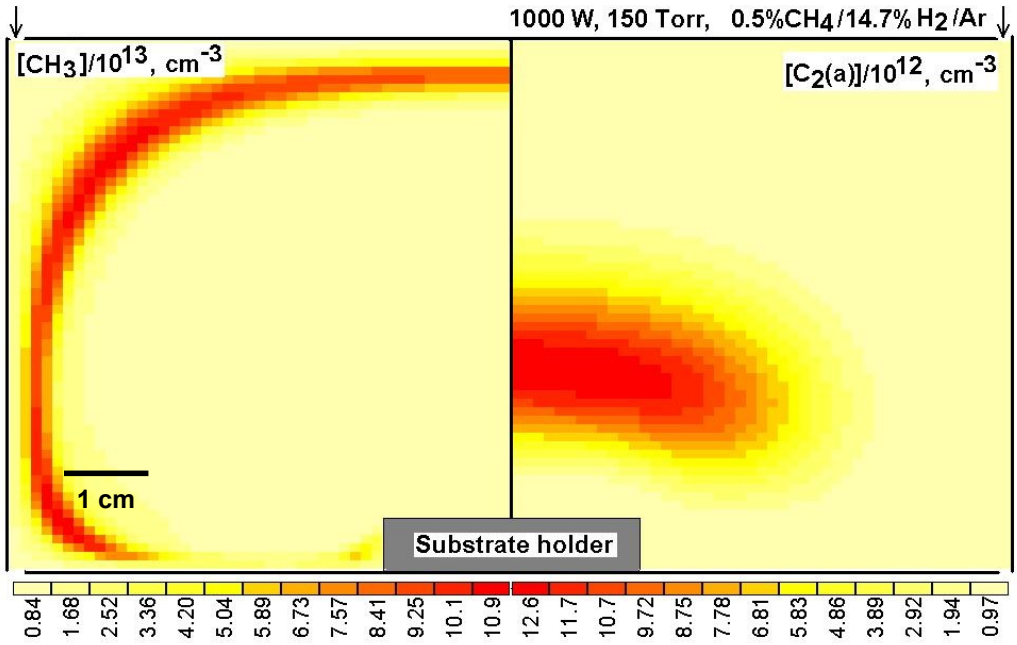

Figure 3.15: 2D(r, z) model distributions of CH_3 (left) and C_2(a) (right) number densities for the present base conditions. The vertical z and radial r dimension used when simulating the reactor were both 6 cm.

CH_4/ 88.6% H_2/ 7% Ar) explored previously by Ma *et al.*[12] Column densities as a function of process conditions $X_0(H_2)$, $X_0(CH_4)$, P and p were also obtained at a fixed height above the substrate. OES measurements were also used qualitatively to explore the effects of these same process conditions on excited C_2(d), C_3(A), CH(A) radicals and H(n=3 and n=4) atoms. Measurements of temperature changes in the cooling water flowing through the reactor walls and base as well as the change in the substrate temperature as a function of $X_0(H_2)$ were also recorded and have highlighted changes in the dissipation of the applied MW power upon substituting H_2 by Ar in the process gas mixture.

Results from 2D(r, z) modelling of the Ar-rich plasmas have been shown to capture, and offer explanations for many of the trends observed in the CRDS and OES experiments. The effect of increasing X_0(Ar) was found to result in a reduction in the plasma's capacity to absorb the microwave input power. This is the primary reason why the Ar-rich plasmas have significantly larger volume compared with H_2-rich ones.

The qualitative agreement between the trends observed in both OES and CRDS experiments shows that, as in previous studies,[18] OES offers a quick way to qualitatively capture many trends seen within plasmas used for CVD of diamond.

The addition of argon into the process gas mixture offers a number of advantages over H_2 dominated plasmas of similar microwave powers. Firstly an increased production of C_xH_y radicals and atomic

hydrogen. A recent study by Tallaire *et al.*[19] found that upon addition of Argon to the gas phase the growth rate increased. The increased production of atomic hydrogen was suggested as a reason for this. Secondly the increase in the size of the plasma ball as the Ar mole fraction is raised, will in turn increase the area over which deposition will occur. As the microwave power does not need to be raised and in some cases (very high Ar fraction) may even need to be lowered as the Ar fraction is increased, Ar addition could therefore be an efficient method to both increase growth rates and deposition area.

References

[1] J. C. Richley, O. J. L. Fox, M. N. R. Ashfold, and Yu. A. Mankelevich, *J. Appl. Phys.* **109**, 063307 (2011).

[2] D. G. Goodwin and J. E. Butler, in *Handbook of Industrial Diamond and Diamond Films*, edited by M. A. Prelas, A. Popovici, and L. K. Bigelow, chapter 11, pages 527–581 (Marcel Dekker, Inc., 1998).

[3] P. W. May, *Phil. Trans. R. Soc. Lond., A* **358**, 473 (2000).

[4] D. Zhou, T. G. McCauley, L. C. Qin, A. R. Krauss, and D. M. Gruen, *J. Appl. Phys.* **83**, 540 (1998).

[5] D. Zhou, D. M. Gruen, L. C. Qin, T. G. McCauley, and A. R. Krauss, *J. Appl. Phys.* **84**, 1981 (1998).

[6] J. Birrel, J. E. Gerbi, O. A. Auciello, J. Gibson, J. Johnson, and J. A. Carlisle, *Diam. Rel. Mater.* **14**, 86 (2005).

[7] D. M. Gruen, *Annu. Rev. Mater. Sci.* **29**, 211 (1999).

[8] D. M. Gruen, O. A. Shenderova, and Y. A. Vul', editors, *Synthesis, Properties and Applications of Ultrananocrystalline Diamond*, volume 192 of NATO Science Series Part II (Springer, New York, 2005).

[9] O. J. L. Fox, J. Ma, P. W. May, M. N. R. Ashfold, and Yu. A. Mankelevich, *Diamond Relat. Mater.* **18**, 750 (2009).

[10] W. Zhu, A. Inspektor, A. Badzian, T. Mckenna, and R. Messier, *J. Appl. Phys.* **68**, 1490 (1990).

[11] J. R. Rabeau, P. John, J. I. B. Wilson, and Y. Fan, *J. Appl. Phys.* **96**, 6724 (2004).

[12] J. Ma, J. C. Richley, M. N. R. Ashfold, and Yu. A. Mankelevich, *J. Appl. Phys.* **104**, 103305 (2008).

[13] F. Mohasseb, K. Hassouni, F. Bénédic, G. Lombardi, and A. Gicquel, *Synthesis, Properties and Applications of Ultrananocrystalline Diamond*, volume 192 of NATO Science Series Part II (Springer, New York, 2005).

[14] J. M. Albella and F. J. Gordillo-Vázquez, *Plasma Sources Sci. Technol.* **11**, 498 (2002).

[15] C. M. Western, PGOPHER http://pgopher.chm.bris.ac.uk/.

[16] A. N. Goyette, J. E. Lawler, L. W. Anderson, D. Gruen, T. G. McCauley, D. Zhou, and A. R. Krauss, *J. Phys. D, Appl. Phys.* **31**, 1975 (1998).

[17] G. Lombardi, K. Hassouni, F. Bénédic, F. Mohasseb, J. Röpcke, and A. Gicquel, *J. Appl. Phys.* **96**, 6739 (2004).

[18] J. Ma, M. N. R. Ashfold, and Yu. A. Mankelevich, *J. Appl. Phys.* **105**, 043302 (2009).

[19] A. Tallaire, C. Rond, F. Bénédic, O. Brinza, J. Achard, F. Silva, and A. Gicquel, *Phys. Status Solidi A* **208**, 2028 (2011).

4

CRDS study of B atoms within $B_2H_6/CH_4/H_2/Ar$ plasmas used for the deposition of boron doped diamond

The work in this chapter has previously been published as part of two papers on the diagnostics of $B_2H_6/H_2/Ar$[1] and $B_2H_6/CH_4/H_2/Ar$[2] plasmas. Also included in this chapter for comparison are column densities obtained for BH radicals as a function of various process conditions performed by Jie Ma[3].

4.1 Introduction

As previously mentioned in Chapter 1.3 the doping of diamond with boron leads to the production of p-type semiconducting diamond, which has a number of potential uses. One of the most frequently used methods to introduce boron into the grown diamond is to add boron containing species into the gas phase during the CVD process. A commonly used source gas is diborane (B_2H_6) which is normally diluted in H_2. A number of previous studies have attempted to correlate properties of the grown diamond such as their growth rates, quality and dopant concentrations with variations in the growth conditions (e.g. plasma parameters, gas flow rates and substrate temperature).[4–6] Few studies in contrast have focused on diagnostics of boron containing plasmas. Microwave activated $B_2H_6/H_2/Ar$ gas mixtures have been previously studied using OES and infrared tunable diode laser absorption spectroscopy.[7,8] These have allowed for the determination of the rotational temperature (T_{rot}) of BH* and H_2* within these plasmas as well as monitoring of B containing species as a function of MW power. Similar studies of $B_2H_6/CH_4/H_2/Ar$ microwave plasmas have also led to the determination of T_{rot} [9] and the determination of relative number densities of B atoms and BH radicals as a function of the B/C ratio.[10] Previous experimental diagnostics and modelling of $B_2H_6/CH_4/H_2$

and B_2H_6/H_2 gas mixtures within HF activated reactors[11] has suggested that the densities of BH_x species are determined by the thermal break down of B_2H_6 to BH_3 (Reaction 4.1) and subsequent H-shifting reactions (Reactions 4.2-4.4). Coupling between boron and carbon within the gas phase has also been suggested as an important process and offered as an explanation for differences between experimental measurements and preliminary model outputs.[11]

$$B_2H_6 + M \rightarrow BH_3 + BH_3 + M \tag{4.1}$$

$$BH_3 + H \rightleftharpoons BH_2 + H_2 \tag{4.2}$$

$$BH_2 + H \rightleftharpoons BH + H_2 \tag{4.3}$$

$$BH + H \rightleftharpoons B + H_2 \tag{4.4}$$

The addition of oxygen has been previously shown[12,13] to result in a significant reduction in the amount of boron that is incorporated into diamond films. In previous[3] and the work presented here, a number of notable effects are thought to be caused by trace air impurities (mainly O_2) within the reactor chamber.

To fully understand the complicated chemistry within $B_2H_6/CH_4/H_2/Ar$ MW plasmas it is important to also understand the chemistry of boron within $B_2H_6/H_2/Ar$ plasmas. The aim of this chapter is therefore to use CRDS to provide information on the spatial distribution of B atoms within the gas phase and the effect of discharge conditions (pressure, applied MW power and gas flow rates) on the column density of B atoms within both $B_2H_6/H_2/Ar$ and $B_2H_6/CH_4/H_2/Ar$ plasmas. Also included are calculations on reactions between H_2BO and CH_3 within the gas phase that may lead to the liberation of BH_x and explain phenomena that are observed in CRDS.

4.2 Experimental

The current work involves the use of CRDS to monitor B atoms in their low lying $2^2P_{3/2}$ excited state within both $B_2H_6/H_2/Ar$ and $B_2H_6/CH_4/H_2/Ar$ plasmas. Base conditions for the $B_2H_6/H_2/Ar$ plasmas

were defined as follows: pressure, p = 150 Torr, Applied MW power, P=1.5 kW, H_2 flow rate F_{H_2}= 525 sccm (standard cubic centimetres), B_2H_6 flow rate $F_{B_2H_6}$ = 0.003 sccm and Ar flow rate F_{Ar} = 40 sccm. Base conditions for $B_2H_6/CH_4/H_2$/Ar plasmas are largely the same as those above but with addition of CH_4, F_{CH_4}= 25 sccm and F_{H_2} = 500 sccm is adjusted so as to keep the total flow rate, F_{Total} = 565 sccm, the same. The B_2H_6 gas was diluted in H_2 (200 ppm in H_2) prior to mixing. To achieve flow rates $F_{B_2H_6}$ = 0.003 sccm into the reactor a flow rate, $F_{B_2H_6/H_2}$ = 15 sccm is used. The low $F_{B_2H_6}$ was required as once $F_{B_2H_6} > 0.005$ sccm the absorption by B atoms became too strong (i.e. the ring down time was too short) to measure reliably with the current experimental setup.

The CRDS experimental setup used for measurement of B atoms is largely the same as that detailed in Chapter 3. A few small details are however different. The dye used to generate laser light was LD489. The output of the dye laser was frequency doubled using a β-Barium borate (BBO) crystal to generate light at a wavelength of ≈250 nm. The frequency doubled light was then separated from the fundamental using a Pellin-Broca prism before being directed into the ring down cavity. The mirrors used to form the ring down cavity were manufactured by LayerTec Inc. and had a reflectivitiy, R=0.991. The wavelength of the laser was monitored by directing the fundamental beam through an etalon (free spectral range ≈0.85 cm^{-1}).

Additional computational calculations presented in this chapter were performed using Gaussian03[14]. Geometries of potential energy minima and transition states were fully optimised with B3LYP density functional theory (DFT) and the 6-31G(d) basis set. Vibrational frequencies were also computed to confirm the nature of all stationary points. Single point energies were then calculated using B3LYP and the larger 6-311+G(2df,p) basis set. Reported transition state energies and reaction enthalpies ($\Delta_r H$) are based on the single point B3LYP/6-311G+(2df,p) energies and are in kJ mol^{-1}.

4.3 Results and discussion

Measured B atom column densities presented below are compared with ^{11}BH(X, v=0) column densities (measured by Jie Ma[1,2]) as well as with plasma modelling performed by Yuri Mankelevich to help explain the observed experimental trends.

4.3.1 Typical B atom spectrum

Figure 4.1a shows a typical absorption spectrum obtained by CRDS of B atoms within the plasma. One peak arises from the ground $2^2P_{1/2}$ state and the other from the low lying $2^2P_{3/2}$ level (only

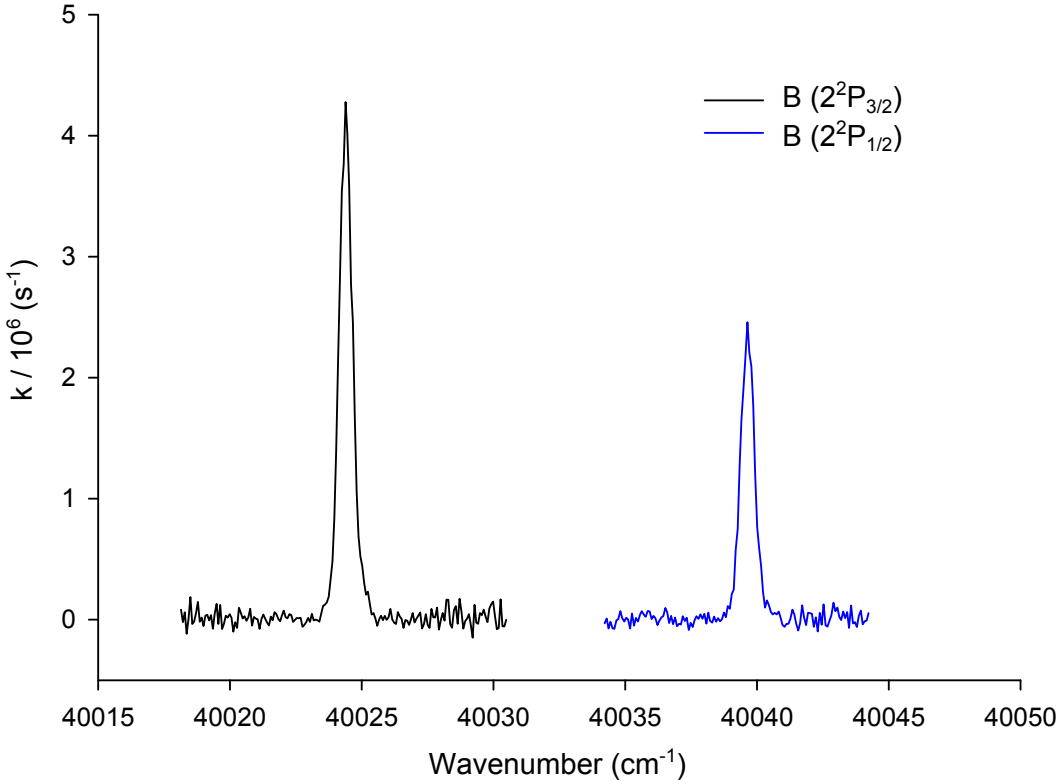

(a)

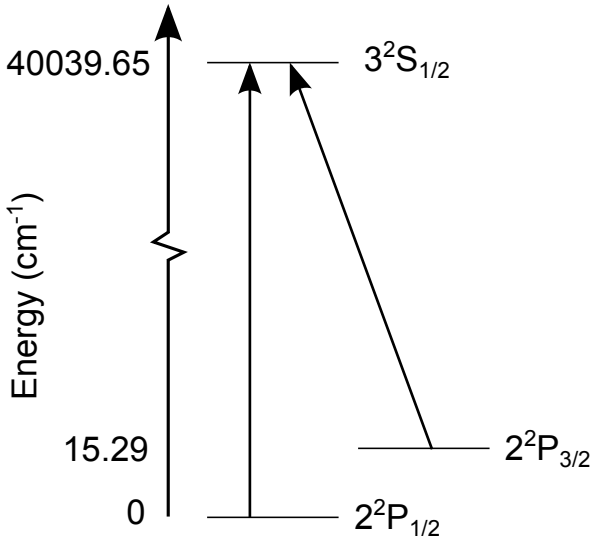

(b)

Figure 4.1: a) Typical CRD spectrum of the B($3^2S_{1/2}$←$2^2P_{1/2}$) and B($3^2S_{1/2}$←$2^2P_{3/2}$) transitions. b) Grotrian diagram illustrating the relevant energy levels of B atoms, and the two transitions.

15.29 cm^{-1} above the ground state see Figure 4.1b). Previous measurements of the BH absorption lines by CRDS [1,2] have provided T_{rot} and consequently T_{gas} (due to the efficient rotational-translation energy transfer of these high pressure plasmas) values for both B_2H_6/ H_2/ Ar and B_2H_6/ CH_4/ H_2/ Ar of ≈2300 K and ≈2600 K respectively. These high temperatures, combined with the low energy of the $2^2P_{3/2}$ level, ensures that the relative intensities of these two species will be determined by their degeneracies, i.e. 2:1 for the $2^2P_{3/2}$ and $2^2P_{1/2}$ levels respectively.

Column densities of B($2^2P_{1/2}$) and B($2^2P_{3/2}$) (henceforth $\{B_{3/2}\}$) atoms can be calculated in a similar fashion to those of C_2(a), CH(X) and H(n=2) shown the previous chapter with equation 4.5.

$$D_{B_i} = \frac{g_i 8\pi L \bar{v}_{ij}^2}{g_j A_{ij}} \int \Delta k \, \mathrm{d}\bar{v} \tag{4.5}$$

where, D_{B_i} is the B atom column density in state i, g_i and g_j are the degeneracies of the lower and upper levels respectively, $\bar{v}$ is the wavenumber of the transition, A_{ji} is the Einstein A coefficient of the relevant transition and $\int \Delta k \, \mathrm{d}\bar{v}$ is the area covered by the line.

4.3.2 B atom profile

Figure 4.2 shows the spatial profiles of both B($2^2P_{3/2}$) atoms and ^{11}BH(X, v=0) radicals within B_2H_6/H_2/Ar and B_2H_6/CH_4/H_2/Ar plasmas. Note that B exists as two isotopes with atomic weights of 10 and 11 and relative abundances of 1:4. These are not resolved in the spectrum of atomic B but (because of the different reduced masses) are separated in the spectrum of BH. Without CH_4 in the gas mixture both B and BH show extensive profiles with their column densities still increasing when $z > 20$ mm. Upon introduction of 25 sccm of CH_4, the spatial distribution of B atom is reduced, plasma modelling has also shown that the BH spatial distribution contracts slightly [2], but, due to the restricted height (maximum of 20-25 mm above the substrate) at which experimental measurements can be recorded this effect is not obvious. The change in the spatial distribution of $\{B_{3/2}\}$ upon addition of CH_4 can be accounted for by the depletion of [H] in the cooler regions of the plasma by reactions with CH_4. This causes reaction 4.4 to shift in favour of the reactants and thus reduces [B] in the cooler regions. It must be noted though that even after addition of CH_4 both ^{11}BH(X, v=0) radicals and B($2^2P_{3/2}$) atoms have much more extensive spatial distributions than C_2(a), CH(X) and H(n=2) seen under typical conditions used for growth of microcrystalline diamond [15] (shown in Figure 3.7).

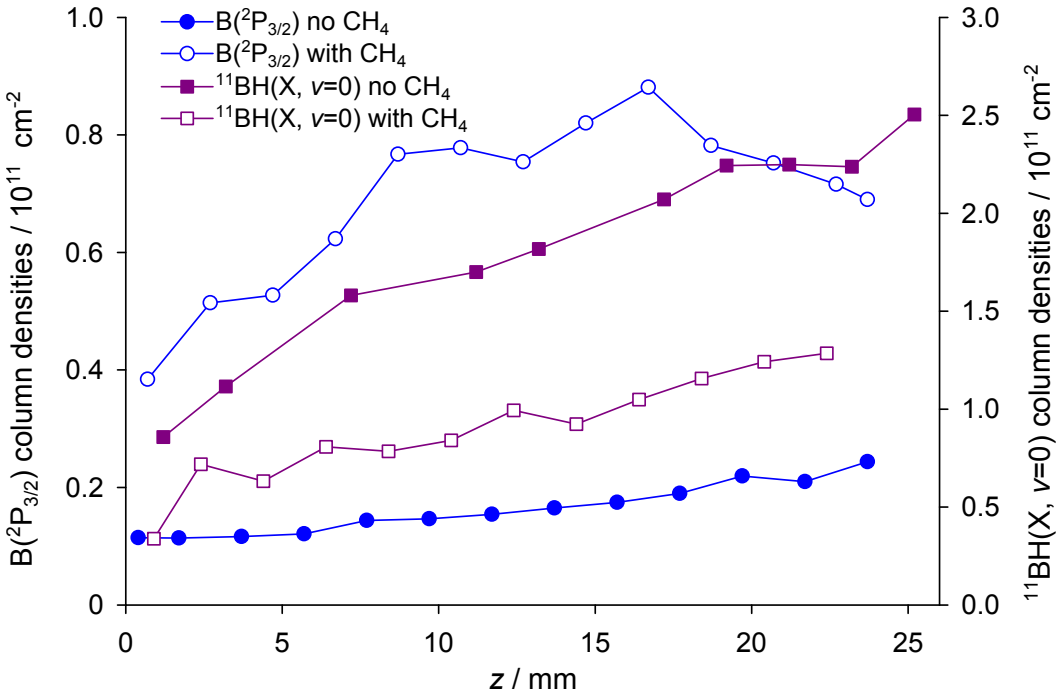

Figure 4.2: Measured B($2^2P_{3/2}$) and ^{11}BH(X, v=0) column densities (blue circles and purple squares respectively) under base conditions for B_2H_6/H_2/Ar and $B_2H_6/CH_4/H_2$/Ar plasmas (filled and open symbols respectively) as a function of z.

4.3.3 Effect of process conditions

Comparison of measured B($2^2P_{3/2}$) and BH(X, v=0) column densities at a fixed height above the substrate (z = 10 mm) are shown below as a function of B_2H_6 flow rate (Fig. 4.3a), Ar flow rate (Fig. 4.3b), P (Fig. 4.4a), p (Fig. 4.4b) and CH_4 flow rate (Fig. 4.5). The base B_2H_6 flow rate used for the measurement of $\{B_{3/2}\}$ was 0.003 sccm whilst for $\{BH\}$, 0.009 sccm was used. This difference was due to the BH absorption being too weak at 0.003 sccm whilst the absorption of B atoms became too great at higher B_2H_6 flow rates (the absorption was saturated), the ring down time thus became too short to accurately measure with the current experimental setup. The effect of saturation on the measured $\{B_{3/2}\}$ can clearly be seen in Figure 4.3a (measurements on $B_2H_6/CH_4/H_2$/Ar plasmas), when a kink appears in the initially linear relationship with $F_{B_2H_6}$, once $F_{B_2H_6} > 0.005$ sccm. Measurement of column densities from the weaker B($3^2S_{1/2} \leftarrow 2^2P_{1/2}$) line (scaled by a factor of 2) as a function of $F_{B_2H_6}$ shows that the relationship between B atoms and $F_{B_2H_6}$ is still linear and column densities calculated from the B($3^2S_{1/2} \leftarrow 2^2P_{3/2}$) line are underestimating $\{B_{3/2}\}$ once $F_{B_2H_6} > 0.005$ sccm.

Figure 4.3a shows the effect of varying the $F_{B_2H_6}$ on both measured BH(X) and B($2^2P_{3/2}$) column densities in B_2H_6/H_2/Ar and $B_2H_6/CH_4/H_2$/Ar plasmas. With no CH_4 in the plasma, the trends in both

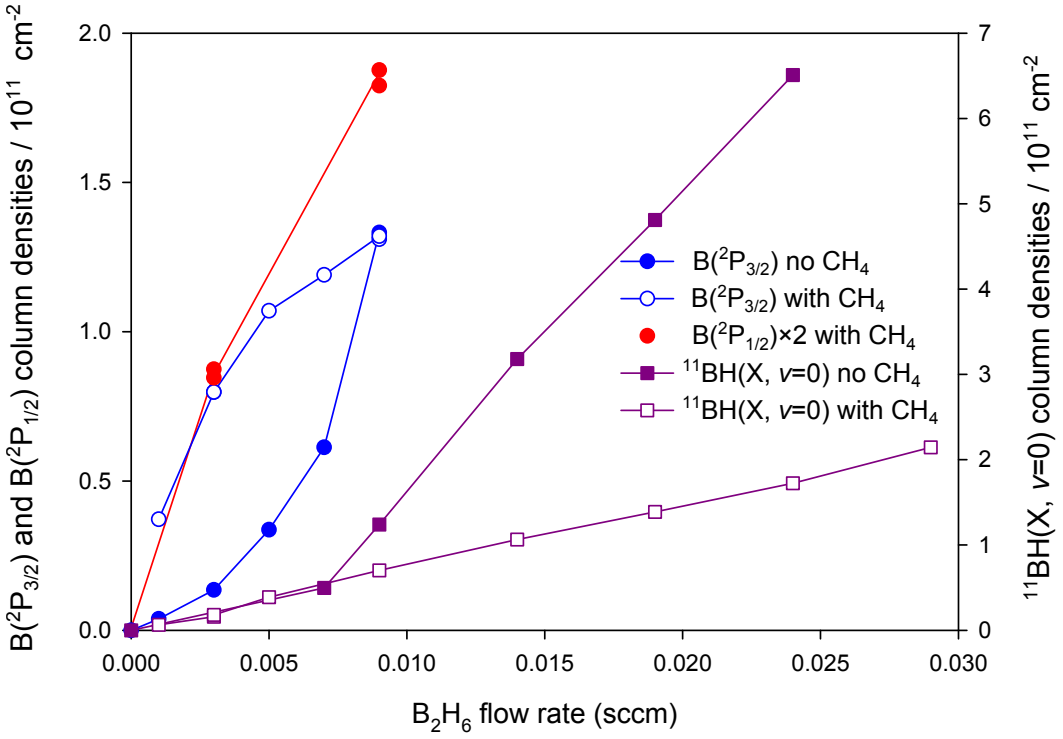

(a)

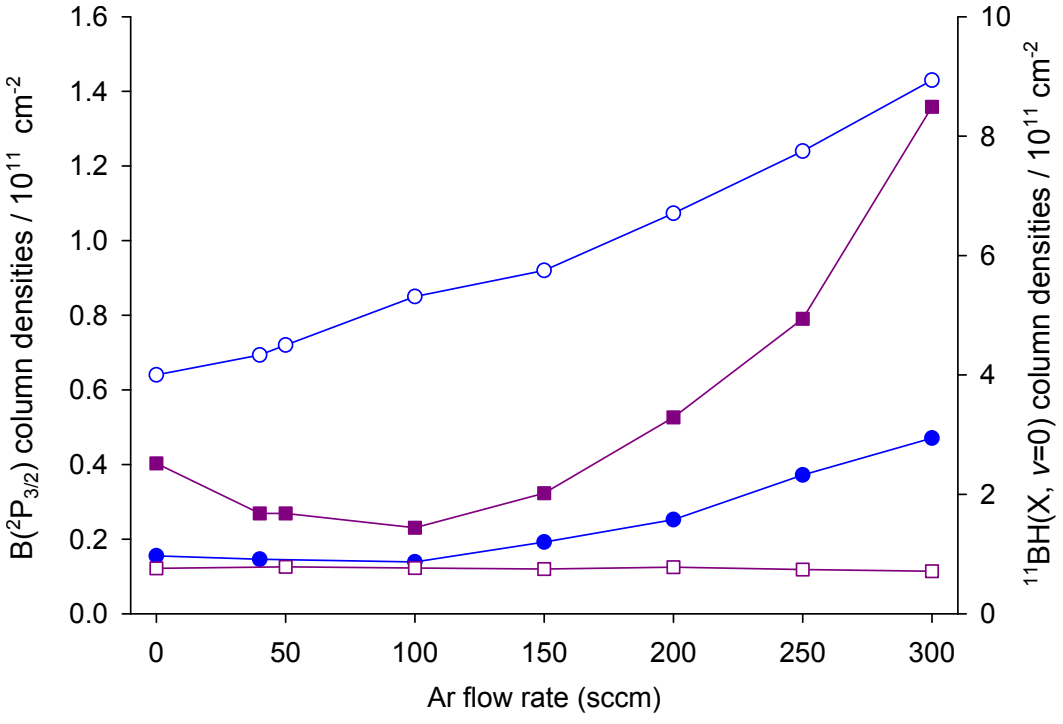

(b)

Figure 4.3: Measured B($2^2P_{3/2}$) and ^{11}BH(X, v=0) column densities (blue circles and purple squares respectively) under base conditions for $B_2H_6/H_2/Ar$ and $B_2H_6/CH_4/H_2/Ar$ plasmas (filled and open symbols respectively) as a function of a) B_2H_6 flow rate and b) Ar flow rate. Red circles are measured B($2^2P_{1/2}$) column densities multiplied by a factor of two.

$\{B_{3/2}\}$ and $\{BH\}$ appear to be non-linear at low $F_{B_2H_6}$ but, once $F_{B_2H_6} > 0.006$ sccm, the relationship becomes linear. Upon addition of 25 sccm of CH_4 to the plasma the relationship between $\{B_{3/2}\}$, $\{BH\}$ and $F_{B_2H_6}$ is found to scale linearly for the entire range investigated ($\{B_{3/2}\}$ deviates from the linear relationship due to the absorption becoming saturate). The initial non-linearity observed in $B_2H_6/H_2/Ar$ plasmas has been attributed to trace air impurities within the plasma that react with the BH_x species within the gas phase. Once $F_{B_2H_6}$ is increased sufficiently that its concentration exceeds that of the impurity the trend becomes linear. Addition of CH_4 into the gas phase acts to "getter" the trace gas impurity and the trend becomes linear.

The effect of F_{Ar} is shown in Figure 4.3b. In $B_2H_6/H_2/Ar$ plasmas increasing F_{Ar} was found to have little effect on $\{B_{3/2}\}$, whilst $\{BH\}$ decreased as F_{Ar} was increased to 100 sccm. Further increase in F_{Ar} (up to 300 sccm) resulted in both $\{B_{3/2}\}$ and $\{BH\}$ increasing. As in Chapter 3, this change is attributable to reduced power density of plasmas with large Ar fractions. This leads to an increase in the hot volume of the plasma and hence increased thermal dissociation of B_2H_6. The ratio between B atoms and BH radicals will also be affected by this change, as both [H] and the rate of reaction 4.4 will change. Reaction 4.4 is exothermic and thus its rate ($k_{4.4}$) will decrease in the hot plasma region. In contrast, increased production of H atoms within the hot region will shift the reaction towards the products. Modelling shows that the competition between these two factors is important in controlling the ratio of B to BH. Within $B_2H_6/CH_4/H_2/Ar$ plasmas, increased F_{Ar} results in a linear increase in $\{B_{3/2}\}$ and no change in $\{BH\}$. As with $B_2H_6/H_2/Ar$ plasmas, the changes observed are largely because of changes in the H atom density and the expansion of the plasma.

In Figure 4.4a changes in both $\{B_{3/2}\}$ and $\{BH\}$ are shown as a function of the applied microwave power. When no CH_4 is present within the gas mixture and the applied MW power is low ($P < 0.75$ kW) measured values of $\{B_{3/2}\}$ decreased as P increased, $\{BH\}$ in contrast increased. At powers > 0.75 kW the opposite trend was observed with $\{B_{3/2}\}$ slowly increasing, whilst $\{BH\}$ declined. When CH_4 is added to the gas mixture the sharp decrease in $\{B_{3/2}\}$ at lower powers was no longer observed, instead $\{B_{3/2}\}$ shows a steady increase with P. $\{BH\}$ showed a similar trend to that seen in $B_2H_6/H_2/Ar$ plasmas. As above with changes in the Ar flow rate, the trends between B atoms and BH radicals are thought to be largely dependent on reaction 4.4. As power is increased T_{gas} also increases, resulting in a reduction in $k_{4.4}$, but also increases [H] and $[BH_3]$ as a consequence of increased H_2 and B_2H_6 dissociation. Changes in; the plasma volume, distribution of species and the portion of the plasma that is probed caused by increasing P will also effect the measured column densities.

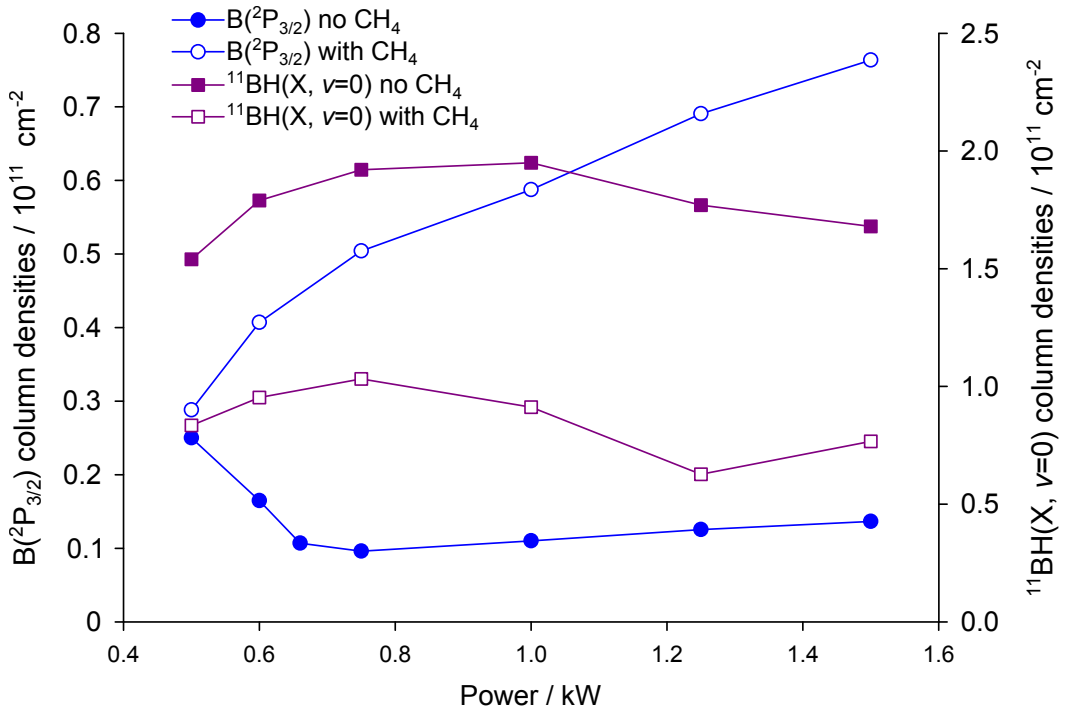

(a)

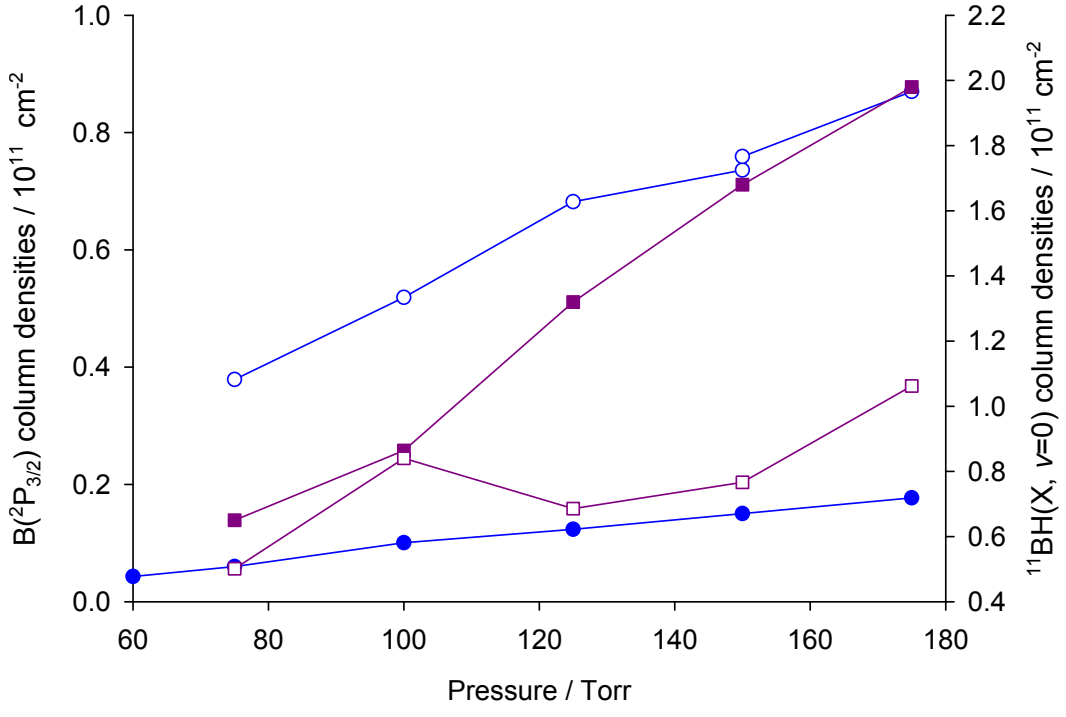

(b)

Figure 4.4: Measured B($2^2P_{3/2}$) and ^{11}BH(X, v=0) column densities (blue circles and purple squares respectively) under base conditions for $B_2H_6/H_2/Ar$ and $B_2H_6/CH_4/H_2/Ar$ plasmas (filled and open symbols respectively) as a function of a) applied microwave power and b) total pressure.

Increasing the total pressure was found to result in linear increases in both $\{B_{3/2}\}$ and $\{BH\}$ (Figure 4.4b). As p is increased a number of changes will occur to various plasma parameters, such as increased power densities, higher T_{gas}, increased electron density and a reduced volume. All of these changes will impact processes generating both B and BH and their conversion and loss mechanisms to different extents. Primarily though, the trend observed will be a consequence of the increase in the total gas concentration, brought about by the increased pressure.

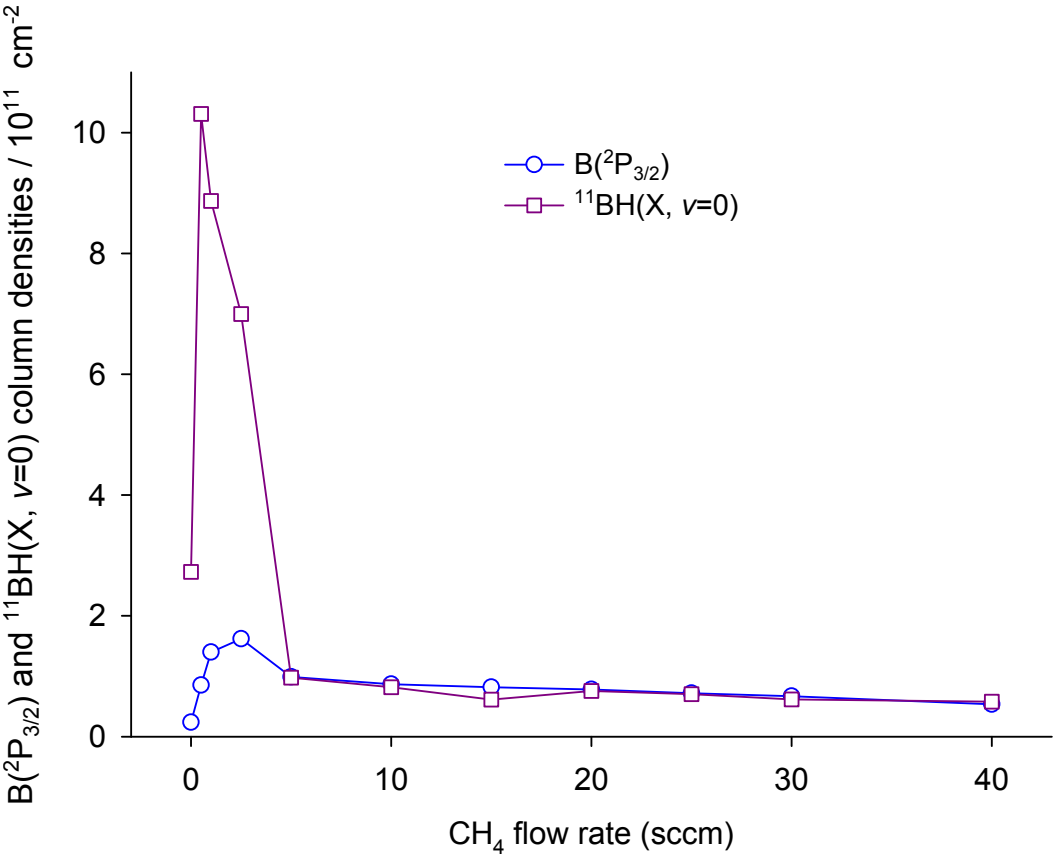

Figure 4.5: Measured B($2^2P_{3/2}$) and ^{11}BH(X, v=0) column densities (blue circles and purple squares respectively) under base conditions for $B_2H_6/CH_4/H_2$/Ar plasmas as a function of CH_4 flow rate.

Figure 4.5 shows the measured B($2^2P_{3/2}$) and BH(X, $v = 0$) column densities as F_{CH_4} is adjusted. Upon the introduction of low flow rates of CH_4 ($0 < F_{CH_4} < 5$ sccm) both the column densities of B($2^2P_{3/2}$) and BH(X, $v = 0$) were seen to rise steeply and before falling. Once F_{CH_4}>5 sccm both measured B($2^2P_{3/2}$) and BH(X, $v = 0$) exhibit a linear decrease with increasing F_{CH_4}. This latter decrease in both species is attributed to the B-C coupling reactions in the gas phase, removing B atoms and BH radicals from the gas phase.

2D plasma modelling was initially unable to reproduce the local maximum observed at low CH_4 flow rates using a simplified reaction scheme which involved the H-shifting reactions (4.2-4.4), B-C

coupling reactions and B-O reactions (to model the trace air impurity). Instead, modelling predicted that a steady decline would be observed similar to that seen at higher $F_{\mathrm{CH_4}}$. A number of possible explanations for this phenomenon were tested within the model, such as reduced B atom loss by reaction with oxygen on addition of CH_4 (due to hydrocarbon species reducing the concentration O_2 within the gas phase) , NH_x species formed from dissociation of trace N_2 within the gas phase and reacting with boron containing species, and enhanced B_2H_6 dissociation rates for M=C_xH_y. None of these, however, were able to reproduce the local maximum that was observed.

In the simplified reaction scheme HBO (formed by the reaction of B containing species with trace air impurities) was just treated as a B-containing sink species. One possible explanation for the local maximum is that reactions between CH_x species and HBO will result in the liberation of BH_x species.

HBO is also just one of many $H_xB_yO_z$ species that may exist within the gas phase produced via H-shifting type reactions such as;

$$\mathrm{HBO + H + M \rightleftharpoons H_2BO + M} \tag{4.6}$$

and

$$\mathrm{H_2BO + H \rightleftharpoons HBO + H_2.} \tag{4.7}$$

DFT calculations were performed to study a number of possible reaction schemes which could result in the conversion of $H_xB_yO_z$ + C_xH_y to BH_x + $H_XC_yO_z$. Modelling suggested that the most abundant CH_x and $H_XB_yO_z$ species would be CH_3 and HBO respectively. The dominant reaction between these two species involves the formation of a B-C bond and is exothermic,

$$\mathrm{CH_3 + HBO + M \rightarrow H_3CB(O)H + M.} \quad \Delta_r H = -65\,\mathrm{kJmol^{-1}} \tag{4.8}$$

However, no obvious subsequent reactions transfering the oxygen from the boron atom can be envisioned. The alternative reaction forming a C-O bond and yielding the product, H_3COBH was calculated to be ≈52 kJ mol^{-1} endothermic and involve an activation barrier of ≈111 kJ mol^{-1}, ruling this out as a feasible gas phase reaction.

As an alternative, the radical-radical reaction of CH_3 with H_2BO was investigated. The initial addition

process,

$$CH_3 + H_2BO + M \rightarrow H_3COBH_2 + M, \quad \Delta_r H = -318\,\mathrm{kJmol^{-1}} \tag{4.9}$$

was found to be highly exothermic and barrier-less. Upon further reaction with gaseous H atoms,

$$H_3COBH_2 + H + M \rightarrow H_3COBH_3 + M \quad \Delta_r H = -43\,\mathrm{kJmol^{-1}} \tag{4.10}$$

and

$$H_3COBH_3 + H + M \rightarrow H_3COHBH_3 + M \quad \Delta_r H = -333\,\mathrm{kJmol^{-1}} \tag{4.11}$$

$$H_3COHBH_3 \rightarrow CH_3OH + BH_3 \quad \Delta_r H = +54\,\mathrm{kJmol^{-1}} \tag{4.12}$$

results in the liberation of BH_3. The steps 4.9-4.10 were all found to be exothermic and calculated to be essentially barrierless. The final step (4.12) is found to be slightly endothermic by 54 kJ mol^{-1}. It should also be noted, however, that another exothermic pathway is able to compete with reaction 4.10,

$$H_3COBH_2 + H \rightarrow CH_3 + HOBH_2, \tag{4.13}$$

however this pathway represents an essentially a null cycle with respect to transferring O from B.

The inclusion of these additional reaction pathways coupled with the assumption that H_2BO is in steady state with HBO and the ratio [H_2BO]/([H_2BO]+ [HBO]) is constant at 0.1, has resulted in the model accurately reproducing the observed experimental trends, including the local maximum observed at low F_{CH_4}.

4.4 Conclusions

Column densities of $B(2^2P_{3/2})$ atoms were successfully measured within $B_2H_6/H_2/Ar$ plasmas as well as $B_2H_6/CH_4/H_2/Ar$ plasmas as a function of the height above the substrate, CH_4 flow rate, Ar flow rate, B_2H_6 flow rate, applied microwave power and pressure. $B(2^2P_{3/2})$ atoms were found to exhibit extensive spatial distributions though not as extensive as the previously measured distributions of BH radicals. The measured $B(2^2P_{3/2})$ column densities combined with those previously determined for BH radicals have been used for comparison with 2D plasma modelling which has provided explanations for many of the observed experimental trends. In addition, DFT calculations are presented on mechanisms for the liberation of BH_x species from $H_xB_yO_z$. Once included in the 2D plasma model these reactions allowed for the reproduction of the local maxima observed in both B and BH column densities when low CH_4 flow rates are added to a pre-existing $B_2H_6/H_2/Ar$ plasma.

References

[1] J. Ma, J. C. Richley, D. R. W. Davies, A. Cheesman, M. N. R. Ashfold, and Yu. A. Mankelevich, *J. Phys. Chem. A* **114**, 2447 (2010).

[2] J. Ma, J. C. Richley, D. R. W. Davies, M. N. R. Ashfold, and Yu. A. Mankelevich, *J. Phys. Chem. A* **114**, 10076 (2010).

[3] J. Ma, Exploration of the gas phase chemistry in microwave activated plasmas used for diamond chemical vapour deposition., PhD thesis, University of Bristol, 2008.

[4] E. Gheeraert, A. Deneuville, and J. Mambou, *Carbon* **73**, 107 (1999).

[5] B.-J. Lee, B.-T. Ahn, and Y.-J. Baik, *Diam. Rel. Mater.* **8**, 251 (1999).

[6] R. Ramamurti, M. Becker, T. Schuelke, G. T, D. Reinhard, and J. Asmussen, *Diam. Rel. Mater.* **17**, 1320 (2008).

[7] M. Osiac, B. P. Lavrov, and J. Röpcke, *J. Quant. Spec. Radiat. Transfer* **74**, 471 (2002).

[8] B. P. Lavrov, M. Osiac, A. V. Pipa, and J. Röpcke, *Plasma Sources Sci. Technol.* **12**, 576 (2003).

[9] M. Rayar, P. Veis, C. Foissac, P. Supiot, and A. Gicquel, *J. Phys. D, Appl. Phys.* **39**, 2151 (2006).

[10] M. Rayar, P. Supiot, P. Veis, and A. Gicquel, *J. Appl. Phys.* **104**, 033304 (2008).

[11] D. W. Comerford, A. Cheesman, T. P. F. Carpenter, D. M. E. Davies, N. A. Fox, R. S. Sage, J. A. Smith, M. N. R. Ashfold, and Yu. A. Mankelevich, *J. Phys. Chem. A* **110**, 2868 (2006).

[12] J. Ruan, K. Kobashi, and W. J. Choyke, *Appl. Phys. Lett.* **60**, 1884 (1992).

[13] I. Sakaguchi, M. Nishitani-Gamo, K. P. Loh, K. Yamamoto, H. Haneda, and T. Ando, *Diam. Rel. Mater.* **7**, 1144 (1998).

[14] M. J. Frisch, G. W. Trucks, H. B. Schlegel, G. E. Scuseria, M. A. Robb, J. R. Cheeseman, J. A. Montgomery Jr., T. Vreven, K. N. Kudin, J. C. Burant, J. M. Millam, S. S. Iyengar, J. Tomasi, V. Barone, B. Mennucci, M. Cossi, G. Scalmani, N. Rega, G. A. Petersson, H. Nakatsuji, M. Hada, M. Ehara, K. Toyota, R. Fukuda, J. Hasegawa, M. Ishida, T. Nakajima, Y. Honda, O. Kitao, H. Nakai, M. Klene, X. Li, J. E. Knox, H. P. Hratchian, J. B. Cross, V. Bakken, C. Adamo, J. Jaramillo, R. Gomperts, R. E. Stratmann, O. Yazyev, A. J. Austin, R. Cammi, C. Pomelli, J. W. Ochterski, P. Y. Ayala, K. Morokuma, G. A. Voth, P. Salvador, J. J. Dannenberg, V. G. Zakrzewski, S. Dapprich, A. D. Daniels, M. C. Strain, O. Farkas, D. K. Malick, A. D. Rabuck, K. Raghavachari, J. B. Foresman, J. V. Ortiz, Q. Cui, A. G. Baboul, S. Clifford, J. Cioslowski, B. B. Stefanov, G. Liu, A. Liashenko, P. Piskorz, I. Komaromi, R. L. Martin, D. J. Fox, T. Keith, M. A. Al-Laham, C. Y. Peng, A. Nanayakkara, M. Challacombe, P. M. W. Gill, B. Johnson, W. Chen, M. W. Wong, C. Gonzalez, and J. A. Pople, Gaussian 03, Revision B.04, Gaussian, Inc., Wallingford, CT, 2004.

[15] J. Ma, J. C. Richley, M. N. R. Ashfold, and Yu. A. Mankelevich, *J. Appl. Phys.* **104**, 103305 (2008).

5

OES and CRDS diagnostics of $CO_2/CH_4/H_2$ plasmas.

5.1 Introduction

Chemical vapour deposition of diamond usually involves the use of activated gas mixtures containing 1-5% CH_4 in H_2 (or a mixture of H_2 and Ar). Numerous investigations have also looked at the addition of other species into the gas mixture and their effect on diamond growth. One such species is oxygen, which has been shown to have a number of effects on CVD of diamond such as increased deposition rates[1] and the ability to grow diamond at lower substrate temperatures[2,3]. Oxygen can be added to the gas mixture in a number of different ways, with the most commonly encountered methods being the use of CO_2[4], CO[5] or O_2[6] gases. Previous studies have attempted to rationalise the effect of varying the C:O, O:H and C:H ratios within the gas mixture and their effect on growth of diamond, and have been summarised in the so called Bachmann triangle[7] (Figure 5.1).

From the Bachmann triangle it can be noted that diamond growth occurs predominately in a region where the C/O ratio ≈ 1, with non-diamond carbon increasingly formed when C/O > 1 and growth ceasing as C/O falls below 1. $CO_2/CH_4/H_2$ gas mixtures used in the current work tend to involve significantly more CH_4 when compared to typical CH_4/H_2 plasmas (with some just using a 1:1 mixture of CH_4 and CO_2). A number of previous studies have attempted to study oxygen containing plasmas using a variety of techniques including OES[4,8–10], mass spectrometry[2,9,11] and computational modelling[2,9,12].

The work presented in this section uses a combination of OES and CRDS to study $CO_2/CH_4/H_2$ plasmas, the distribution of a number of species within them, and the effect of varying CVD process parameters (applied microwave power, total pressure, H_2 fraction and CH_4 to CO_2 ratio). Previous work[13] has shown that trends seen in OES are qualitatively consistent with those from quantitative

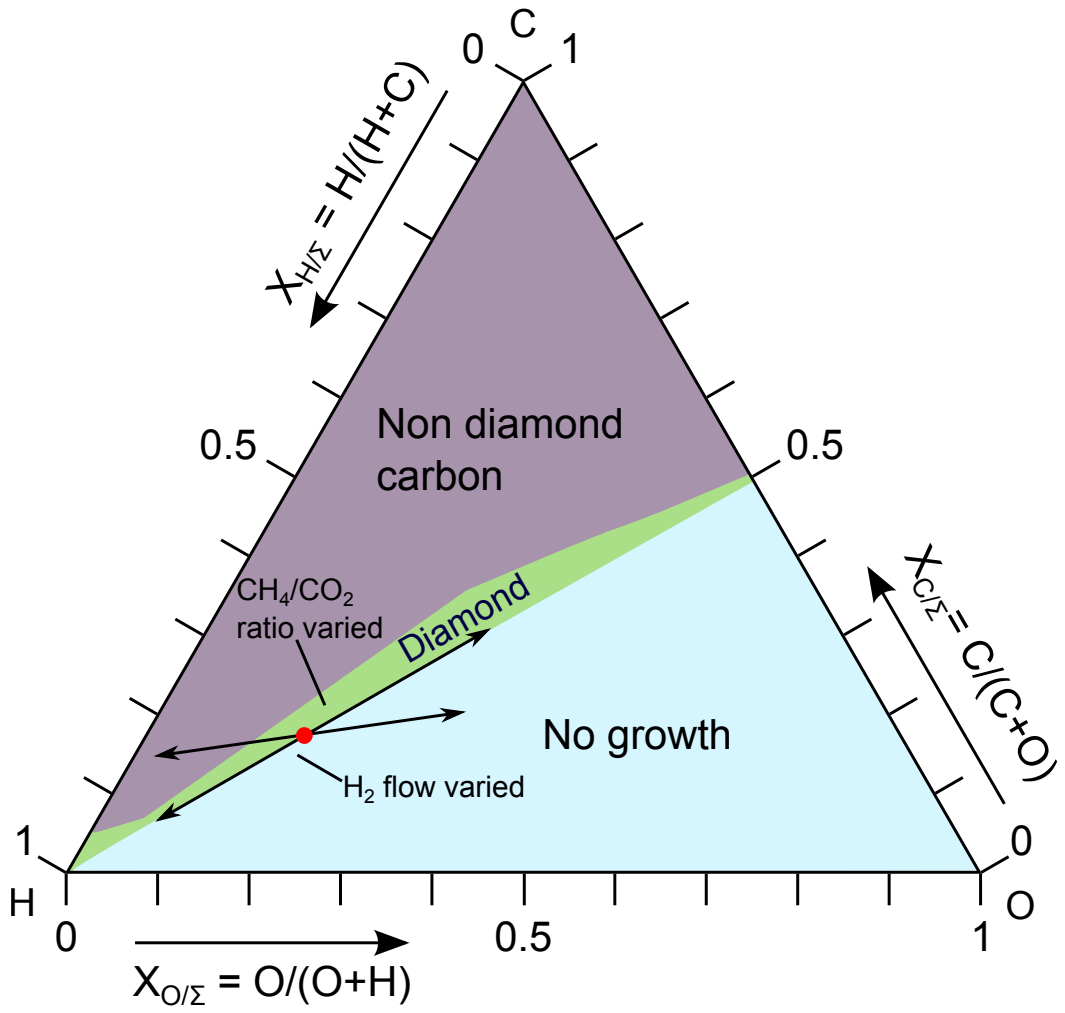

Figure 5.1: A simplified version of the Bachmann triangle,[7] showing the diamond growth region, as well as the areas where no growth and non-carbon growth occurs. Also shown are the location of the current base conditions (red dot) and the direction traversed by varying the H_2 fraction or CO_2/CH_4 ratio.

CRDS measurements of species within $H_2/CH_4/Ar$ plasmas. OES would therefore appear to be a good method to gain a quick overall impression of $CO_2/CH_4/H_2$ plasmas and the effect of various changes in process parameters. CRDS can then be used to obtain quantitative measurements of column densities as well as estimates of the average rotational temperature of species such as $C_2(a)$ within the plasma.

5.2 Experimental

The base conditions used in the current experiments were defined as follows; CO_2 flow rate F_{CO_2} = 175 sccm, CH_4 flow rate F_{CH_4} = 175 sccm, H_2 flow rate F_{H_2} = 150 sccm, total gas flow rate F_{Total} = 500 sccm, microwave power P = 1.0 kW and pressure p = 150 Torr. The total gas flow was

kept constant when adjusting the H_2 fraction ($X_0(H_2)$) by adjusting both the $X_0(CO_2)$ and $X_0(CH_4)$ fractions to keep the $X_0(CH_4)$:$X_0(CO_2)$ ratio the same (e.g. when $X_0(H_2)$ = 90%, $X_0(CH_4)$ and $X_0(CO_2)$ = 5%). All other conditions are otherwise fixed whilst the chosen parameter is varied. Base conditions for measurement of the C_2(d←a)(0,0) transition were carried out with a slightly different ratio of CH_4 to CO_2 ($X_0(CH_4)/(X_0(CO_2)+X_0(CH_4)$ = 0.51) as the weak C_2 absorption at $X_0(CH_4)$ = $X_0(CO_2)$ made measuring column densities difficult in the current experiment.

The MWPECVD reactor used for the OES and CRDS measurements was the same as that described in Chapter 3. Measurement of both CH(X, v=0) and C_2(a, v=0) column densities (henceforth referred to as {CH(X)} and {C_2(a)}, respectively) was carried out using the same procedure as described in Chapter 3. Emission spectra were captured through the vertical slits in the side of the reactor. The side arms used for CRDS were removed and replaced with two diamond windows. Emitted light from the plasma was directed via a series of lenses in to the front end of an optical fibre attached to a monochromator and onto a cooled charge coupled device (CCD) strip detector (Oriel Instaspec IV, 600 lines mm^{-1} ruled grating). The first lens (with a focal length of 12 cm) was placed at ≈20.5 cm from the centre of the reactor. The second lens was then placed at the point at which the plasma image is in focus (≈24 cm from the first lens). This lens was largely redundant and was in place for historical reasons, although, adjustment of this lens did allow for some fine tuning of the setup. Finally, a third lens was placed 12 cm from the second lens to focus the light through an aperture (diameter of ≈2 mm) and on to the optical fibre. Spatial profiles were then acquired in a similar manner to the CRDS experiments by either raising or lowering the table relative to the reactor. A schematic of the experimental set-up is shown in Figure 5.2. The experiment was aligned and the height was calibrated using a laser beam (aligned so that it passed centrally through the reactor via the vertical slits). The position of the substrate was defined as z = 0 mm. Spectra were recorded with a 0.5 s exposure time and averaged over 64 scans with a resolution of better than 1 nm over a 300 nm portion of the emission spectrum. Single point measurements of the effect of the various discharge parameters on both the emission intensity and column densities were recorded z = 10 mm above the substrate.

5.3 Results and discussion

In order to gain an impression of overall trends within CO_2/CH_4/H_2 plasmas as a function of height above the substrate (z) and discharge parameters, OES was used to monitor the emission from excited H(n=3) (H_α) and H(n=4) (H_β) atoms at 656.2 and 486.1 nm, respectively and excited CH(A), C_2(d),

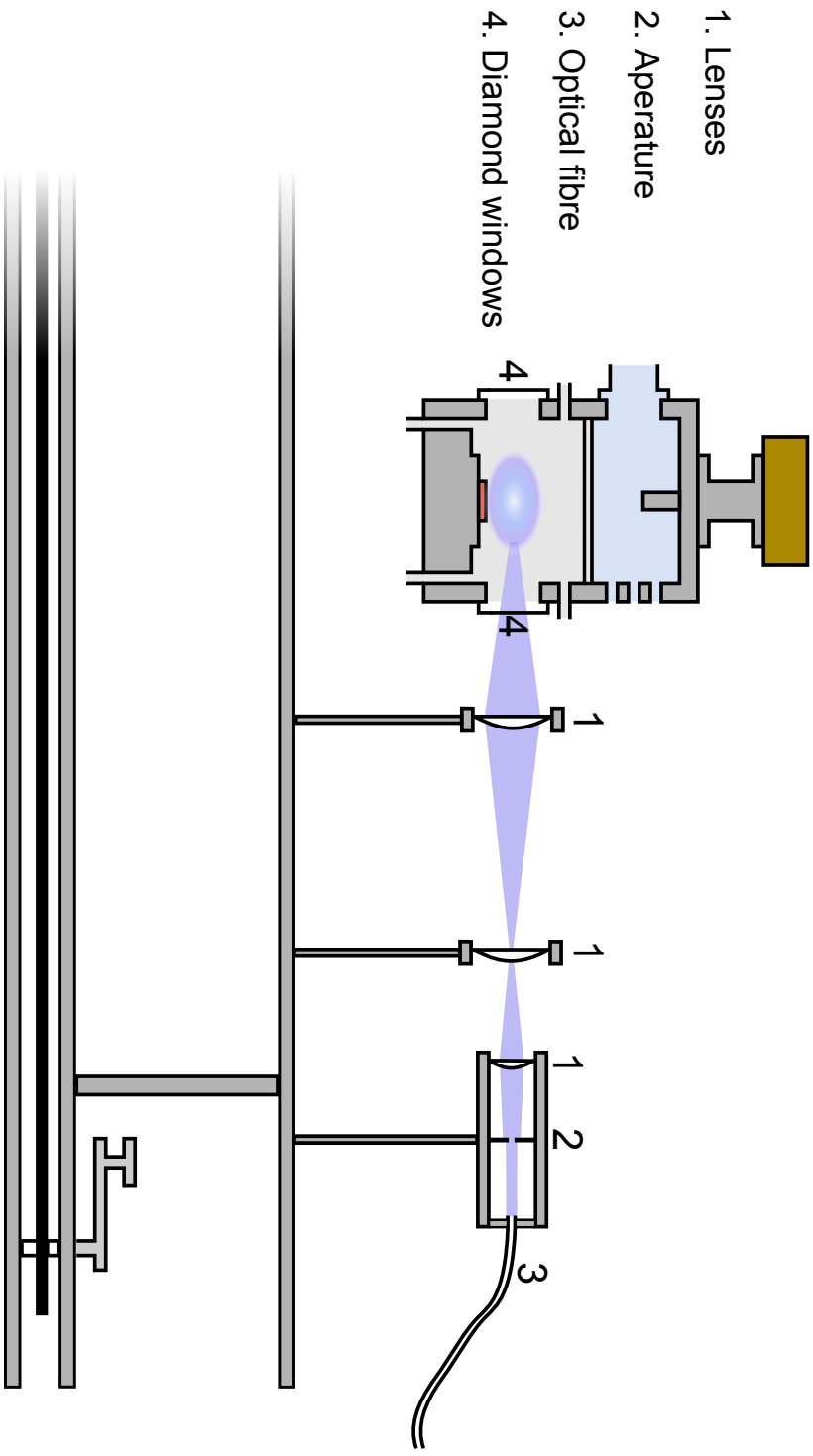

Figure 5.2: Cross section of the MWPECVD reactor and the OES setup used in the current investigations.

C_3(A), OH(A) and CO(B) molecules at 434.1, 516.5, ≈405, 309 and 483 nm, respectively (also referred to as H*, CH*, C_2*, C_3* and CO* and OH*). An OES spectrum showing the commonly observed spectral features is shown in Figure 5.3. Typical CRDS spectra for C_2(a, v=0) and CH(X, v=0) were shown in Chapter 3, which also contained a description of the method used for calculating column densities. CRD spectra of the C_2(a, v=0) can be used in conjunction with simulations of the C_2(a←d,) (0,0) transition in PGOPHER[14] to provide information on the rotational temperature, T_{rot}, of C_2(a) within the plasma and consequently the average gas temperature T_{gas} of the region in which C_2(a) is present. At z = 10 mm, the T_{rot} obtained for C_2(a) at the base conditions is ≈3200 K. This value is slightly, but reproducibly, higher than the typical values of ≈3000 K obtained in CH_4/H_2/Ar plasmas.

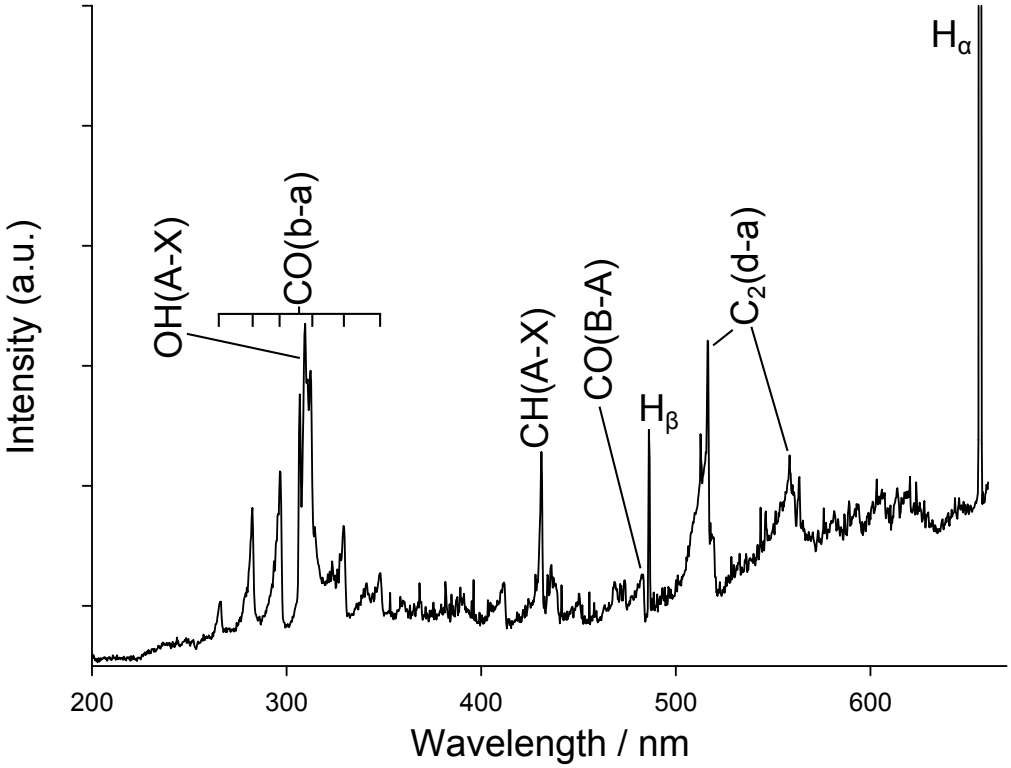

Figure 5.3: OES spectrum showing the spectral features observed in a $CO_2/CH_4/H_2$ plasma operating at base conditions (this is constructed by combining two separate spectra due to the limited wavelength range (≈ 300 nm) which can be captured before the grating requires adjustment). Emission from excited C_3(A) is not observed at base conditions but the feature becomes increasingly evident when CH_4 is in excess of CO_2.

Figure 5.4a shows the emission intensities of different species under base conditions as a function of height above the substrate. Emission from CO(B) is seen to peak closest to the substrate, followed by

H_α and H_β, C_2(d) and CH(A) and, lastly, OH(A) which peaks furthest away. The distribution of C_2(d) and CH(A) both peak slightly closer (8 mm *vs.* 10 mm) to the substrate than seen in previous work on typical MCD-depositing CH_4/H_2/Ar plasmas[13], suggesting that the plasma ball may be smaller and more localised than CH_4/H_2/Ar plasmas. Preliminary 0D and 2D modelling of $CO_2/CH_4/H_2$ plasmas[15] suggests that CO is one of the main products of reactions within these plasmas. It is therefore present throughout the reactor and not just the hot regions. From the ideal gas equation it is clear that the gas will be denser in cooler regions, *i.e.* the number density of CO will peak in the cooler regions, and not in the centre of the plasma ball where species such as C_2 and CH peak (see Chapter 3). As OES measures emission from excited states the profile seen for CO may therefore be described as a combination of the CO number density, peaking in the cool regions, and the distribution of electrons and excited species with sufficient energy to promote CO to its excited state. This offers an explanation for the observation of CO emissions peaking closer to the substrate: the observed emissions reflect the spatial distribution of sufficiently excited collision species, primarily electrons.

Spatial profiles of both $\{C_2(a)\}$ and $\{CH(X)\}$ determined by CRDS are shown in Figure 5.4b. $\{C_2(a)\}$ and $\{CH(X)\}$ were both found to peak at $z \approx 10$ mm and their maximal values at base conditions are similar to those measured for typical CH_4/H_2/Ar plasmas used for the growth of MCD.[16] The C_2* and CH* emission intensities fall faster at large z, compared to $\{C_2(a)\}$ and $\{CH(X)\}$ determined by CRDS, reiterating the fact that OES signals reflect a convolution of the spatial distributions of the species of interest and the electrons which promote it to the emitting state.

The relationship between the proportion of CH_4 to CO_2 in the input gas mixture, defined as a mole fraction ratio, $R = X_0(CH_4)/(X_0(CO_2) + X_0(CH_4))$, and the emission intensity is shown in Figure 5.5a. Spatial profiles obtained by OES are shown in Figures 5.6a and 5.6b where $R = 0.43$ and 0.57, respectively.

As the mole fraction ratio of CH_4 to CO_2 is raised from 0.43 to 0.50 little or no emission is observed from excited C_2(d) or C_3(A). Emission from CH(A) also remains low initially but starts to increase once $R \approx 0.47$. Similar trends are also observed in the emission from CO(B) and excited H atoms.

Once $R > 0.5$ the emission from the CH(A→X), H_α and H_β transitions increased sharply before reaching a maximum when $R \approx 0.52$ followed by a slight decline as R is increased further. Emission from excited CO(B) molecules increased steeply at first, but showed signs of levelling out as R is raised. Increases were initially observed in emission from C_2(d→a) and C_3(A→X) until $R \approx 0.515$,

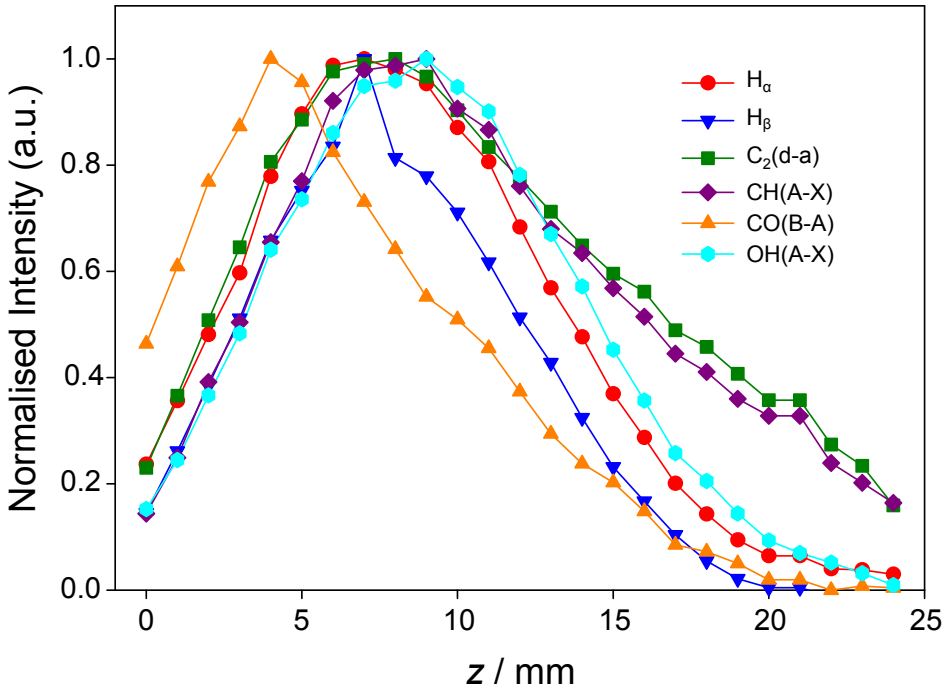

(a)

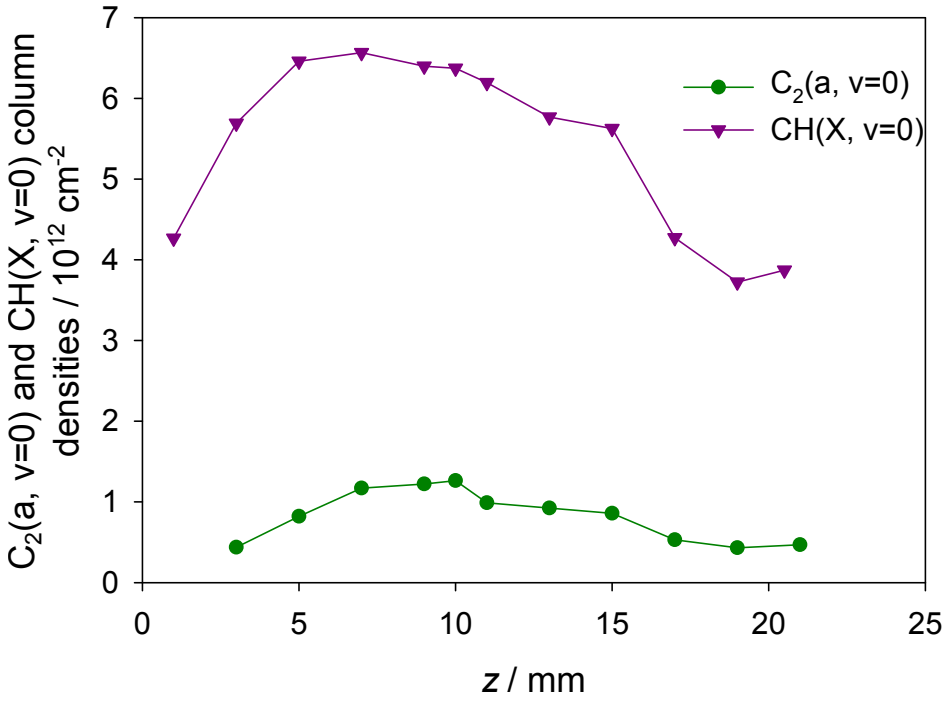

(b)

Figure 5.4: a) Normalised emission intensities of the H_α, H_β, C_2(d-a), CH(A-X), C_3(A-X), CO(B-A) and OH(A-X) transitions and b) Column densities of C_2(a, v=0) and CH(X, v=0) at base conditions, as a function of height above the substrate, z.

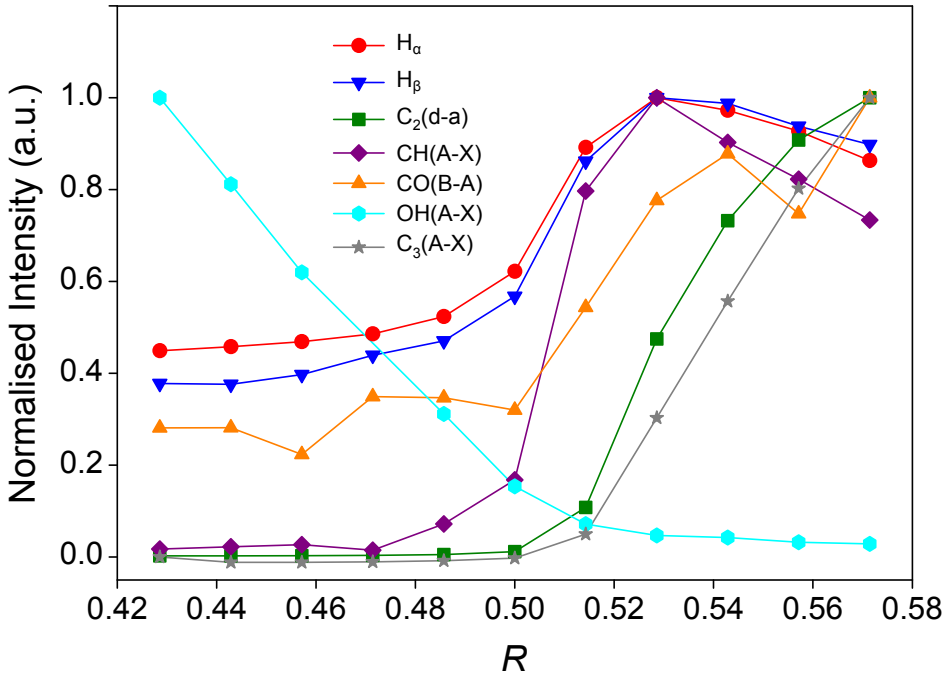

(a)

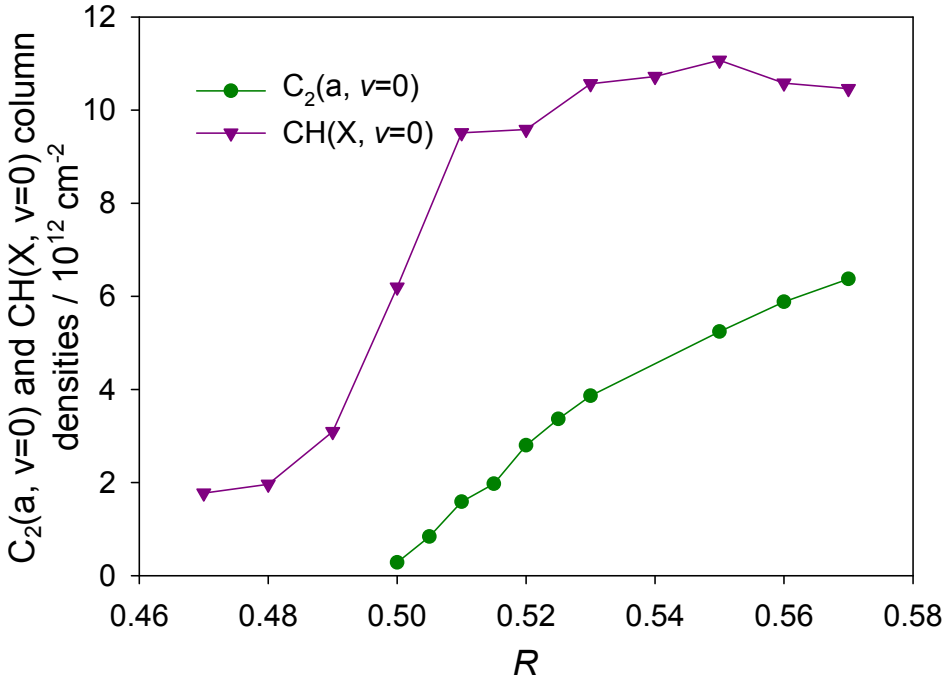

(b)

Figure 5.5: a) Normalised emission intensities of the H_α, H_β, C_2(d→a), CH(A→X), C_3(A→X), CO(B→A) and OH(A→X) transitions and b) C_2(a, v=0) and CH(X, v=0) column densities, z=10 mm, at a function of R, where R = $X_0(CH_4)/(X_0(CO_2)$ + $X_0(CH_4))$. Other discharge parameters were kept fixed as their base values as R was varied.

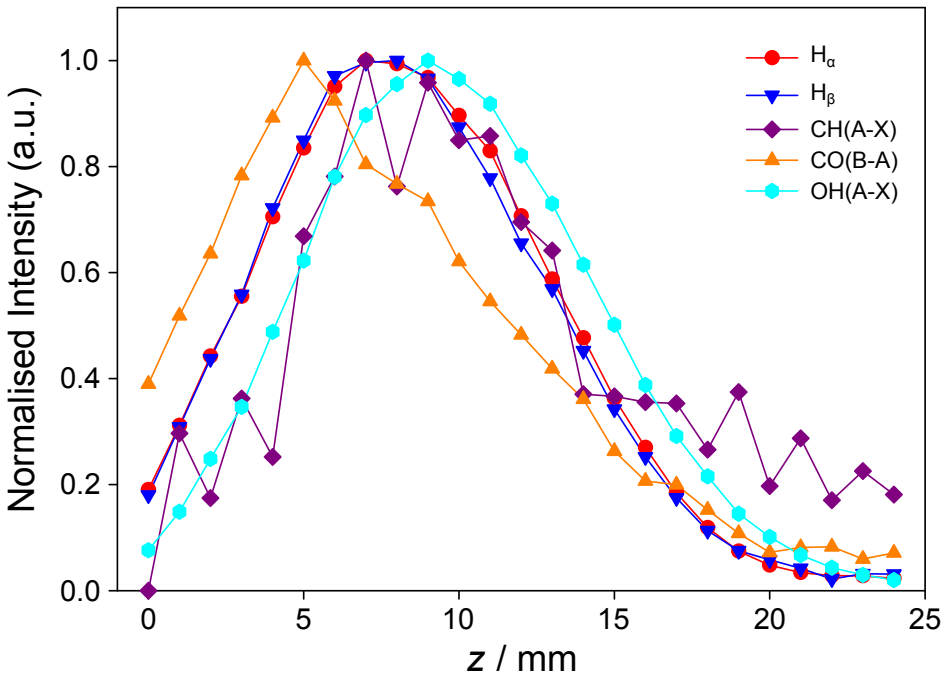

(a)

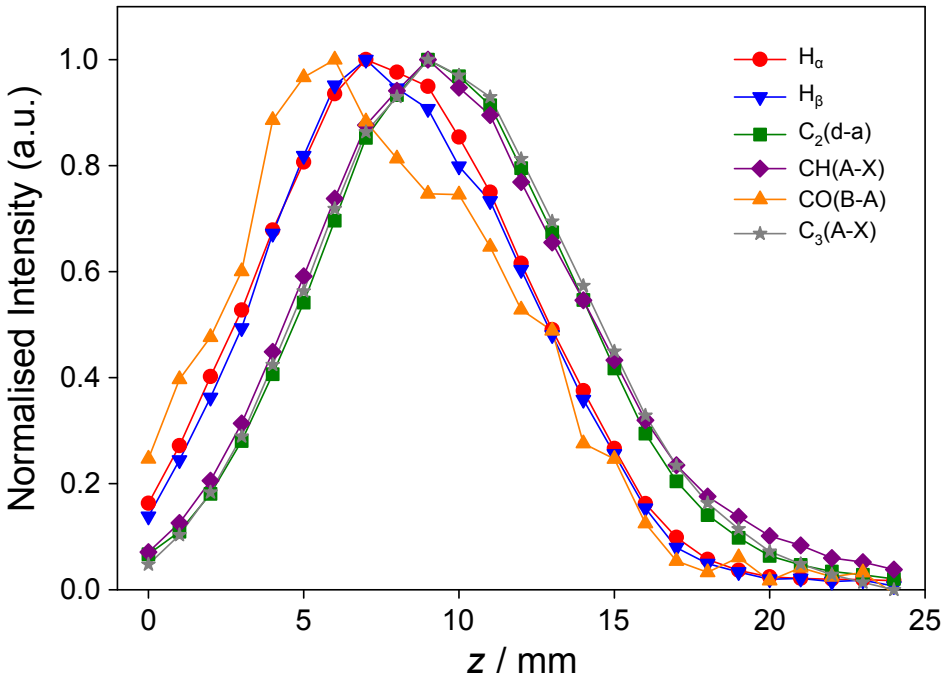

(b)

Figure 5.6: Normalised emission intensities of the C_2(d→a), CH(A→X), C_3(A→X), CO(B→A), H_α, H_β, and OH(A→X) transitions as a function of height above the substrate when: a) $R \approx 0.43$ and b) $R \approx 0.57$. Emission from OH(A) is not observed when $R \approx 0.57$ and C_3(A) is not observed when $R \approx 0.43$.

after this point the emission intensity of both species increased sharply. Emission from OH(A), in contrast to all the other species, showed a steady decline as R is increased. Varying R was seen to have little effect on the spatial distribution of excited OH(A), CO(B) radicals and H(n=3) and H(n=4) atoms, whilst the distribution of C_2(d) and CH(A) radicals reached a maximum further away from the substrate at higher R. The change in the C_2(d) and CH(A) distributions may be indicative of a larger plasma ball once $X_0(CH_4)$ is higher than $X_0(CO_2)$, and a possible decrease in the absorbed power density of the plasma causing an increase in its volume. Emission from C_2(d) and CH(A) is likely to be more sensitive to the thermal distribution of the ground state species than emission from CO(B), H(n=3), H(n=4) and OH(A), due to their excited states lying lower in energy (2.48 eV and 2.87 eV *vs.* 10.78, 12.1, 12.7 and 4.05 eV, respectively) and as a consequence less tied to the electron density n_e and the electron energy distribution function (EEDF). In addition, it is important to note that although the peak in emission appears to be further away from the substrate when $R \approx 0.57$, emission from both CH(A) and C_2(d) exhibits a steeper decline above the maximum, which may suggest that when R = 0.5 CH(A) and C_2(d) are both distributed over a slightly larger volume.

Measured column densities of C_2(a, v=0) and CH(X, v=0) as a function of R are shown in Figure 5.5b. The observed trends agree well with the OES results: {CH(X)} rapidly rises once $R > 0.5$ before reaching a plateau and {C_2(a)} shows a near-linear increase. Both of these trends are similar to those seen within CH_4/H_2/Ar plasmas as $X_0(CH_4)$ is increased[16].

When CO_2 is in excess, oxygen containing species (e.g. OH, O_2, etc.) within the plasma would react with C_xH_y species explaining the reduced emission of CH*, C_2* and C_3*, as well as the low C_2(a, v=0) and CH(X, v=0) column densities recorded. Once $R > 0.5$, a sharp rise is observed in CH*, C_2* and C_3* emission, as well as in the column densities of C_2(a, v=0) and CH(X, v=0).

Figure 5.7 shows the effect of varying $X_0(H_2)$ on a) emission from C_2(d), CH(A), CO(B), OH(A), H(n=3) and H(n=4) and b) the column densities of C_2(a, v=0) and CH(X, v=0). OES showed an initial increase in both the emission from C_2(d) and CH(A) as $X_0(H_2)$ is decreased from 95% to 70%, followed by a slow decline as $X_0(H_2)$ is decreased further. H_α and H_β emission both showed a gradual decline, whilst emission of both CO(B→A) and OH(A→X) increased as $X_0(H_2)$ is reduced. Column densities of C_2(a, v=0) and CH(X, v=0) were both found to increase as $X_0(H_2)$ was decreased (fig. 5.7b). Figure 5.8 shows spatial distributions of emission from a) C_2(d), b) H(n=3) and H(n=4), c) CH(A), d) CO(B) and e) OH(A). Generally the measured emission intensities were observed to reach their maximum values closer to the substrate as $X_0(H_2)$ was decreased. The largest changes were once again observed in the distribution of C_2(d→a) and CH(A→X) emissions which, as mentioned

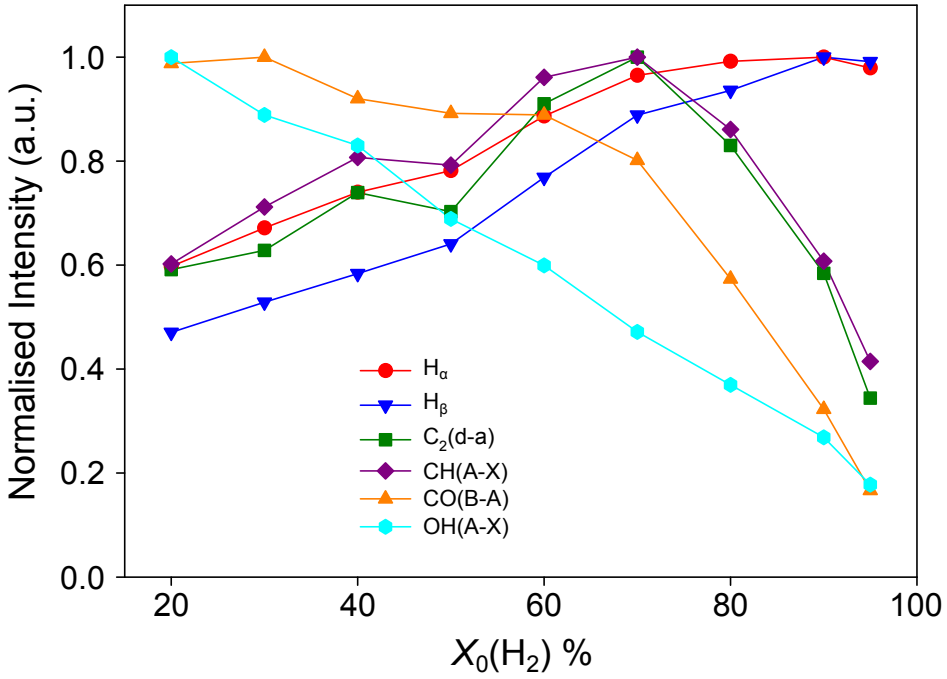

(a)

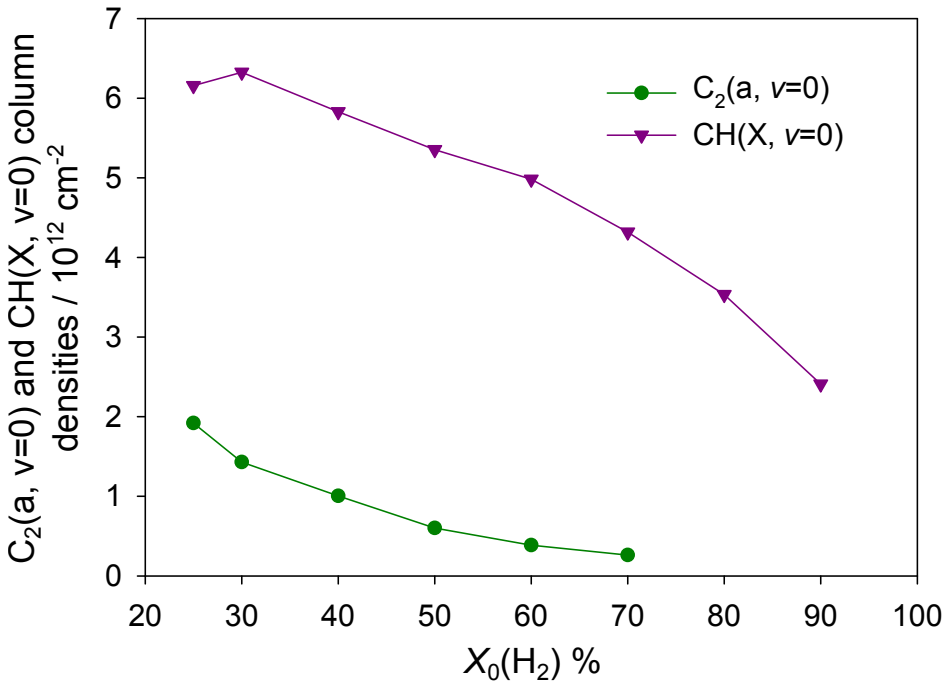

(b)

Figure 5.7: Effect of varying $X_0(H_2)$ on a) emission from C_2(d), CH(A), CO(B), OH(A), H(n=3) and H(n=4) species and b) column densities of C_2(a, v=0) and CH(X, v=0) at z=10 mm. C_2(a, v=0) column densities were obtained at R = 0.51. F_{CH_4} and F_{CO_2} are varied to keep F_{Total} and the $X_0(CH_4)$:$X_0(CO_2)$ ratio constant.

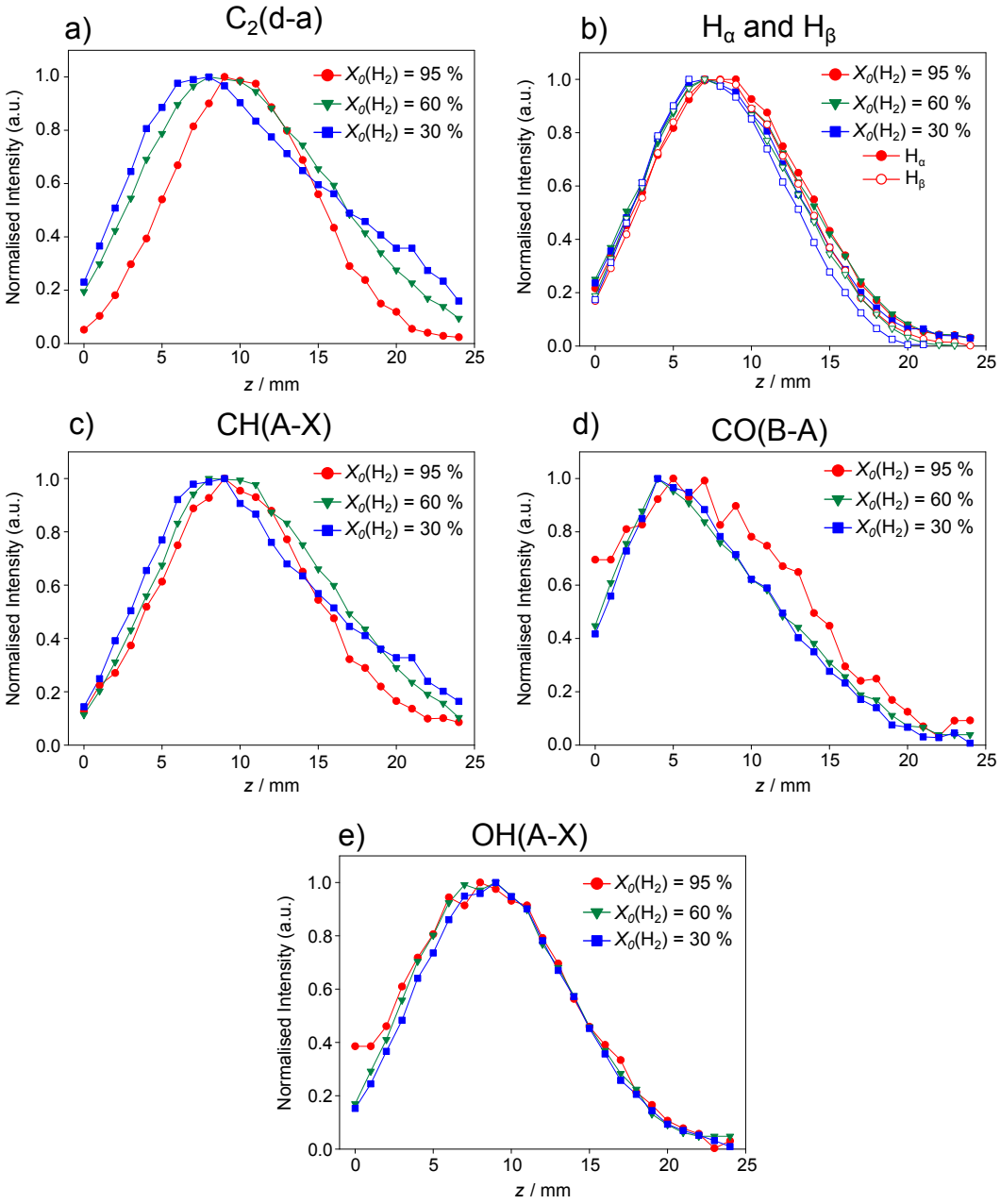

Figure 5.8: Normalised emission intensities of a) C_2(d→a), b) H_α and H_β, c) CH(A→X), d) CO(B→A) and e) OH(A→X) as a function of z when $X_0(H_2)$ = 95, 60 and 30% (red, green and blue points, respectively). F_{CH_4} and F_{CO_2} are varied to keep F_{Total} and the $X_0(CH_4)$:$X_0(CO_2)$ ratio constant.

above, are not as closely tied to the EEDF as the other monitored transitions. Another trend to be noted is the increased emission of C_2(d→a) and CH(A→X) in the periphery of the plasma (z >15 mm) at low $X_0(H_2)$, possibly indicating that they are more widely distributed.

The difference between the trends observed in CRDS and OES for both C_2 and CH (Fig. 5.7) suggests that a number of other plasma parameters may be changing as CH_4 and CO_2 is substituted for H_2, such as the electron temperature, T_e, and the electron density, n_e. A decrease in T_e as $X_0(H_2)$ would offer an explanation for the decrease in the H_α/H_β ratio seen in Figure 5.7a. The trends shown in OES are likely to be a combination of these and many other factors, and changes in the dominant gas phase reactions will require careful computational modelling for detailed explanation.

Figure 5.9a shows the emission intensities of C_2(d→a), CH(A→X), CO(B→A), OH(A→X), H_α and H_β as a function of P. Column densities of C_2(a, v=0) and CH(X, v=0) as a function of P are shown in Figure 5.9b. The measured intensities of CH(A→X), CO(B→A) and OH(A→X) showed little change as P was varied from 0.6 to 1.4 kW. H_α and H_β emission both increased linearly with increased power, whilst emission of C_2(d→a) showed a slight decrease. CRDS measurements however show that $\{C_2(a)\}$ and $\{CH(X)\}$ increase by a factor of ≈6 and ≈2 between P = 0.6 and P = 1.4 kW, respectively. The different trends between emission and absorption measurements as P is varied may again be due to a number of factors, such as changes in various reaction rates, n_e, T_e, T_{gas} and the plasma volume.

Finally, the effect of varying the pressure on emission intensities and column densities are shown in Figure 5.10a and 5.10b, respectively. Figure 5.11 shows the changes in emission intensities as a function of z at three different pressures (100, 150 and 200 Torr). The emission intensities of all the investigated transitions were found to decrease as p was raised from 100 to 200 Torr, apart from OH(A→X) which increased. Once again column densities from CRDS do not entirely agree with the OES measurements. Although $\{CH(X)\}$ shows a similar trend, decreasing with pressure, $\{C_2(a)\}$ does not, and instead increases with pressure. In Figure 5.11 we see that increasing the pressure results in the shift of maximum emission intensities of each species closer towards the substrate, indicating an overall reduction in the plasma's size which is clearly seen in the spatial distributions of C_2(d→a) and CH(A→X) emission. The relative invariability in the spatial distributions of H_α, H_β and CO(B→A) emissions with pressure also suggests that pressure changes have little effect on the EEDF. A number of factors may account for the observed discrepancy between CRDS and OES measurements, with various plasma processes scaling differently as the pressure is changed and further modelling and experimentation will be needed to fully explain the trends.

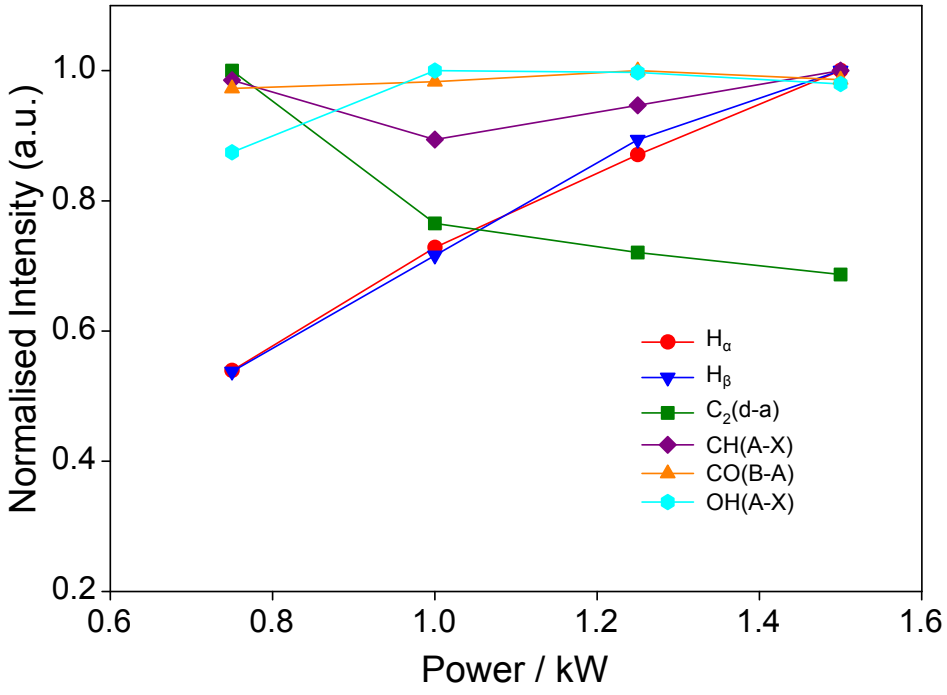

(a)

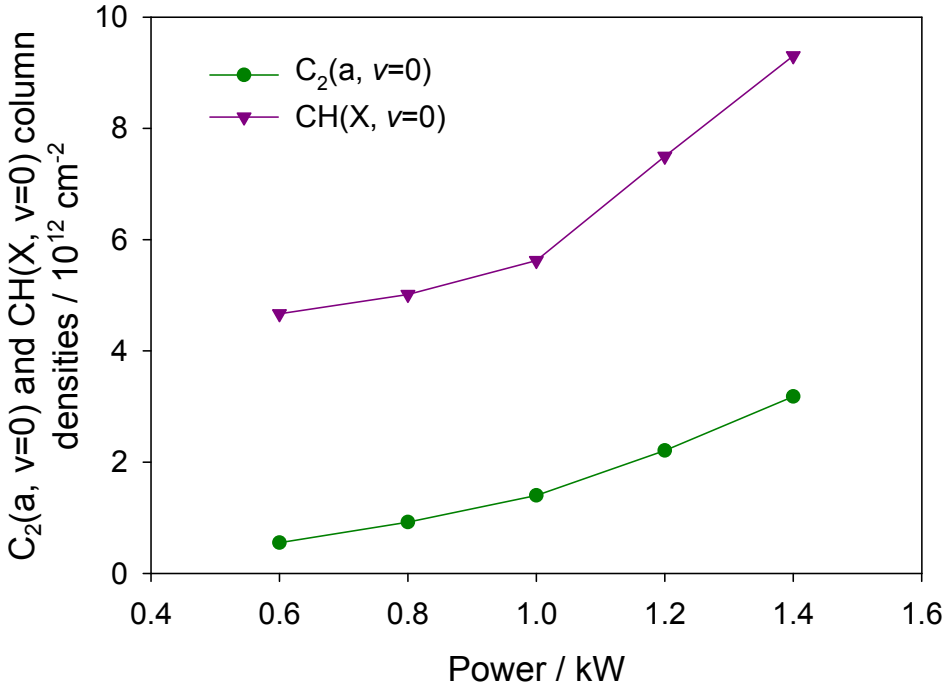

(b)

Figure 5.9: Effect of varying P on a) emission from C_2(d), CH(A), CO(B), OH(A), H(n=3) and H(n=4) and b) column densities of C_2(a, v=0) and CH(X, v=0) at z = 10 mm. Emission intensities and CH(X, v=0) column densities were obtained with R = 0.5, C_2(a, v=0) column densities were obtained with R = 0.51. All other parameters were kept at base conditions.

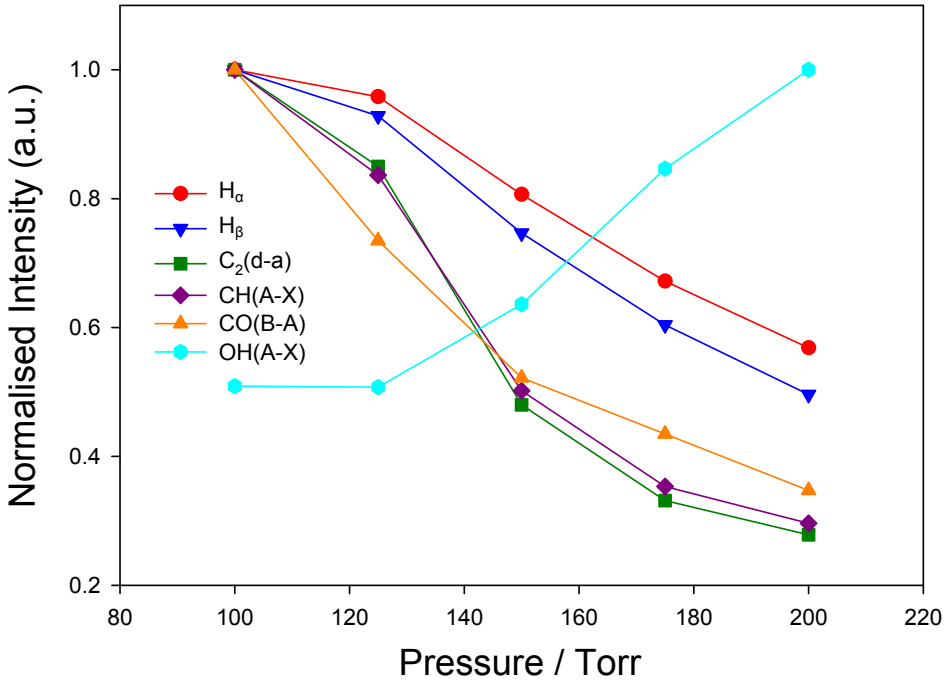

(a)

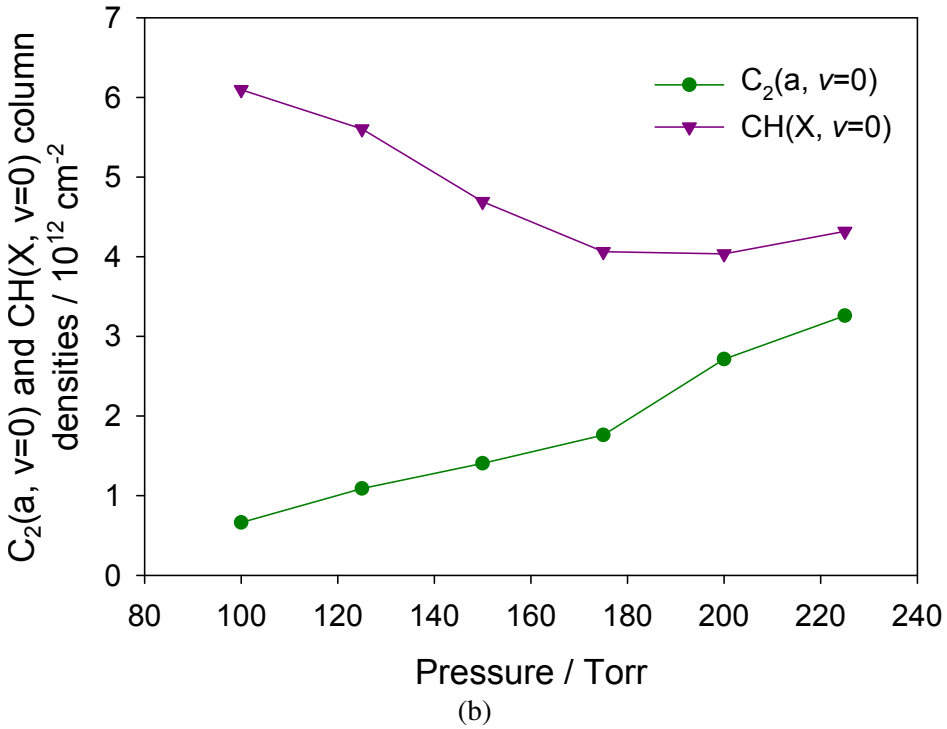

(b)

Figure 5.10: Effect of varying p on a) emission from C_2(d), CH(A), CO(B), OH(A), H(n=3) and H(n=4) and b) column densities of C_2(a, v=0) and CH(X, v=0) at z = 10 mm. Emission intensities and CH(X, v=0) column densities were obtained with R = 0.5, C_2(a, v=0) column densities were obtained with R = 0.51. All other parameters were kept at base conditions.

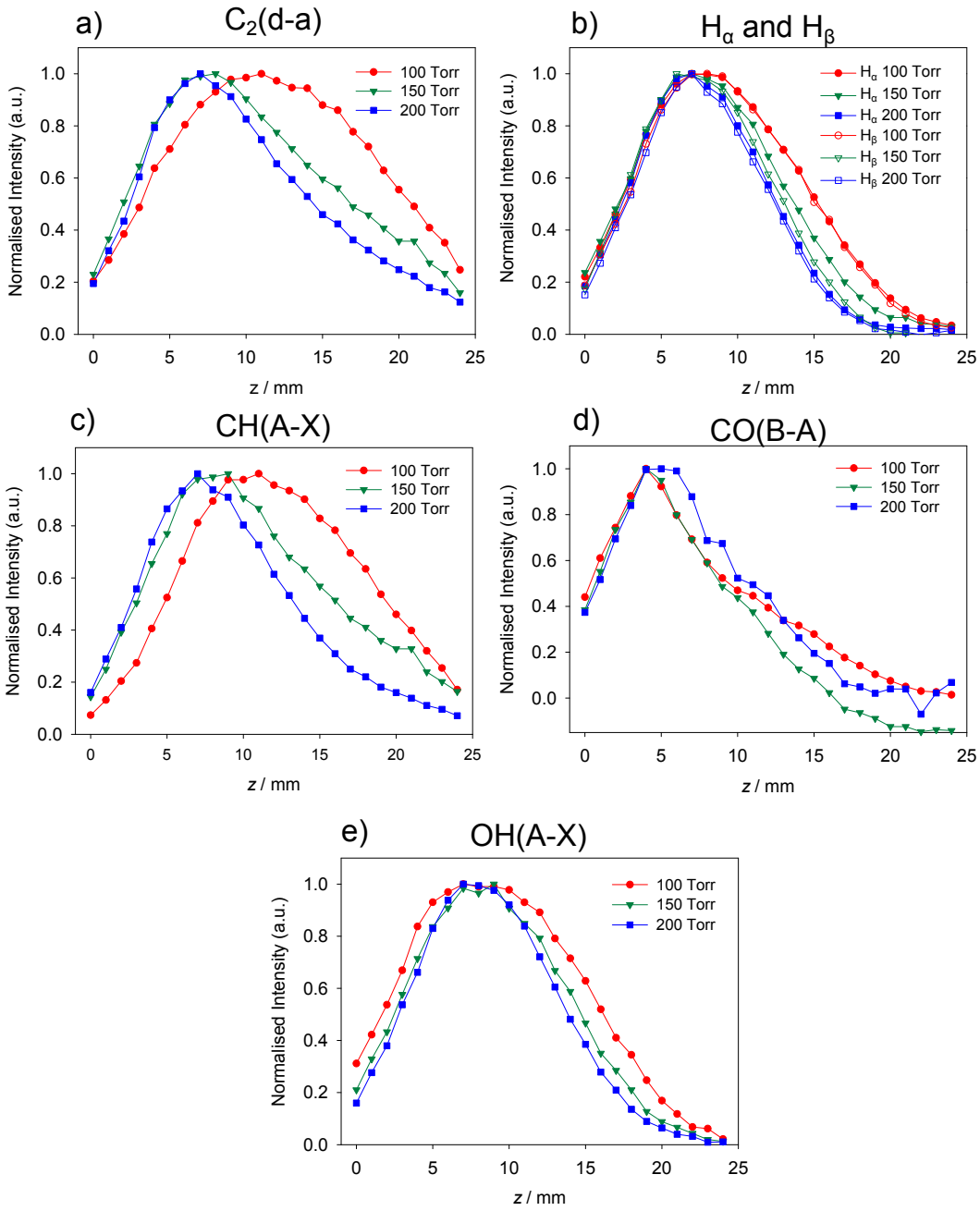

Figure 5.11: Normalised emission intensities of a) C_2(d→a), b) H_α and H_β, c) CH(A→X), d) CO(B→A) and e) OH(A→X) as a function of z when p = 100, 150 and 200 Torr (red, green and blue points, respectively). All other parameters were kept at base conditions.

5.4 Conclusion

OES spectroscopy was successfully applied to investigate the trends of several excited species in MW activated CO_2/CH_4/H_2 plasmas as a function of height above the substrate and a number of process conditions (p, P, $X_0(H_2)$ and $X_0(CH_4)$:$X_0(CO_2)$). Column densities of C_2(a, v=0) and CH(X, v=0) were also obtained using CRDS. Spatial profiles of species obtained by OES and CRDS showed good agreement under base conditions. CH(X, v=0) column densities were found to be slightly higher under the current base conditions than in previous work on H_2 dominated CH_4/H_2/Ar plasmas[16] whereas C_2(a, v=0) column densities were slightly lower. Rotational temperatures obtained from simulations of the C_2(d←a)(0,0) band yielded a $T_{\mathrm{rot}} \approx 3200$ K suggesting that peak temperature within these plasmas may be higher than CH_4H_2/Ar plasmas.

OES and CRDS also showed good agreement as $X_0(CH_4)$:$X_0(CO_2)$ was varied. However, decreasing $X_0(H_2)$ from 95% led to an initial increase in the emission intensity of C_2* and CH* before emissions declined, whereas the measured column densities of both C_2(a, v=0) and CH(X, v=0) showed a steady increase. Discrepancies between OES and CRDS were also observed as pressure and power were varied. These differences between the behaviour of electronically excited species and the ground state species (or low-lying excited state in the case of C_2(a)) possibly indicate that changes in n_e, T_e, the EEDF and the reactions which generate the excited states are occurring as $X_0(H_2)$, p and P are varied. Therefore it is important to be careful in the use of OES spectroscopy in the analysis of trends within these CO_2/CH_4/H_2 plasmas as the observed trends of excited species do not necessarily correlate with those of the ground states.

For more a detailed analysis of the observed trends from both OES and CRDS measurements a combination of computational plasma modelling as well as additional column density measurements of species such as OH, H(n=2) and HCO are required. Such work is ongoing.

References

[1] C.-F. Chen, Y. C. Huang, S. Hosomi, and I. Yoshida, *Hyomen Gijutsu* **40**, 305 (1989).

[2] J. R. Petherbridge, P. W. May, S. R. J. Pearce, K. N. Rosser, and M. N. R. Ashfold, *J. Appl. Phys.* **89**, 1484 (2001).

[3] C. F. Chen, S. Chen, H. Ko, and S. E. Hsu, *Diam. Rel. Mater.* **3**, 443 (1994).

[4] G. Balestrino, M. Marinelli, E. Milani, A. Paoletti, I. Pinter, and A. Tebano, *Appl. Phys. Lett.* **62**, 879 (1993).

[5] Y. Muranaka, H. Yamashita, K. Sato, and H. Miyadera, *J. Appl. Phys.* **67**, 6247 (1990).

[6] T. Kawato and K. Kondo, *Jpn. J. App. Phys.* **26**, 1429 (1987).

[7] P. K. Bachmann, D. Leers, and H. Lydtin, *Diam. Rel. Mater.* **1**, 1 (1991).

[8] T. P. Mollart and K. L. Lewis, *Diam. Rel. Mater.* **8**, 236 (1999).

[9] M. A. Elliott, P. W. May, J. R. Petherbridge, S. M. Leeds, M. N. R. Ashfold, and W. N. Wang, *Diam. Rel. Mater.* **9**, 311 (2000).

[10] C. Met, S. de Persis, L. Vandenbulcke, O. Aubry, J. L. Delfau, C. Vovelle, and V. Lago, *J. Electrochem. Soc.* **153**, F127 (2006).

[11] T. Gries, L. Vandenbulcke, J. N. Rouzaud, and S. de Persis, *Plasma Sources Sci. Technol.* **19**, 025015 (2010).

[12] J. R. Petherbridge, P. W. May, and M. N. R. Ashfold, *J. Appl. Phys.* **89**, 5219 (2001).

[13] J. Ma, M. N. R. Ashfold, and Yu. A. Mankelevich, *J. Appl. Phys.* **105**, 043302 (2009).

[14] C. M. Western, PGOPHER http://pgopher.chm.bris.ac.uk/.

[15] Yu. A. Mankelevich, personal communication.

[16] J. Ma, J. C. Richley, M. N. R. Ashfold, and Yu. A. Mankelevich, *J. Appl. Phys.* **104**, 103305 (2008).

6

Computational studies on the insertion of C_xH_y species into bonds of the diamond surface.

This work looks at possible ways in which various minor radical species such as CH_x (x=0-2) may contribute to the growth of CVD diamond films. This work has been published in J. Phys. Chem. A[1].

6.1 Introduction

Due to the nature of the gas phase chemistry present within CVD reactors used for the deposition of diamond films (see Chapter 1.2.3) a large variety of different stable and radical hydrocarbon species are present. Predicted number densities of a selection of species present above the substrate for typical microcrystalline diamond (MCD) and ultra-nanocrystalline (UNCD) CVD conditions are shown in Table 6.1 and also illustrated in Figure 6.1. Under typical MCD growth conditions the CH_3 radical is the most abundant of the C_1H_x hydrocarbon radicals near the growing surface, by one or more orders of magnitude. Most contemporary growth mechanisms have therefore focused on the growth of diamond from CH_3 radicals, though other species such as C_2 and C_2H_2 have also been proposed (see Chapter 1.2.4). As can be seen in Figure 6.1, the concentration of species such as atomic carbon are closer to that of CH_3 for the UNCD conditions and, consequently, may start contributing to the growth process.

The addition of CH_3, to the growing diamond surface, first requires a free surface radical site for the gas phase species to bond to. However, under typical MCD growth conditions (1-5% CH_4 in H_2) the growing diamond surface is largely hydrogen terminated, only $\approx$ 10% of the surface sites are not terminated and in the form of radicals sites at which CH_3 radicals can add. Species such as $^1CH_2$ are known to directly insert into C-H[4–6] and C-C[7,8] bonds in various gas-phase hydrocarbon species. In the case of diamond, this type of direct insertion reaction would allow gas phase species

Table 6.1: Predicted number densities of a variety of gas phase species 0.5 mm above the growing diamond surface from calculations presented in Ma *et al.*[2] (MCD) and Richley *et al.*[3] MCD process conditions: 4.4% CH_4, 7.1% Ar, 88.5% H_2, Pressure (p) = 150 Torr, Power (P) = 1.5 kW. UNCD process conditions: 0.5% CH_4, 1% H_2, 98.5% Ar, p = 170 Torr, P = 0.7 kW.

	Number density/cm^{-3}	
Species	MCD	UNCD
H	8.2×10^{15}	1.99×10^{15}
CH_4	1.4×10^{15}	9.92×10^{12}
CH_3	1.1×10^{14}	1.51×10^{12}
$^3CH_2$	4.6×10^{11}	4.61×10^{9}
$^1CH_2$	1.1×10^{10}	1.32×10^{8}
CH	1.7×10^{10}	1.29×10^{9}
C	5.1×10^{10}	7.48×10^{10}
C_2H_6	1.0×10^{12}	
C_2H_5	2.7×10^{11}	
C_2H_4	4.8×10^{14}	
C_2H_3	1.9×10^{13}	
C_2H_2	1.1×10^{16}	2.43×10^{15}
C_2H	3.1×10^{10}	3.00×10^{11}
C_2(X)	1.5×10^{7}	3.37×10^{9}
C_2(a)	6.3×10^{7}	8.82×10^{9}
C_3	1.3×10^{13}	1.83×10^{14}
C_3H_2	2.1×10^{14}	1.43×10^{14}

to add to the other 90% of the surface carbon atoms that are still H-terminated. If the C-H bond insertion pathway is available to gas phase species present at the diamond surface then growth might no longer be limited to ≈10% of the surface that is not H-terminated, and could offer an alternative (or complementary) mechanism to the classic CH_3 addition at a radical site.

In this chapter quantum mechanical (QM) and quantum mechanical/molecular mechanical (QM/MM) approaches are used to investigate the insertion of CH_2, CH, C, C_2 and C_3 into C-H and C-C bonds on the H-terminated 2×1 reconstructed {100} (2×1{100}:H) surface and the possible contribution of these reactions to CVD diamond growth. The 2×1{100}:H surface was chosen in this study as it is an important and frequently observed surface in CVD grown diamond. Many of the reactions investigated will also be relevant to other crystal faces present on the growing diamond.

6.2 Computational Method

A combination of QM and QM/MM calculations were performed to investigate the insertion reactions presented in this chapter. The QM calculations used density functional theory (DFT) to model

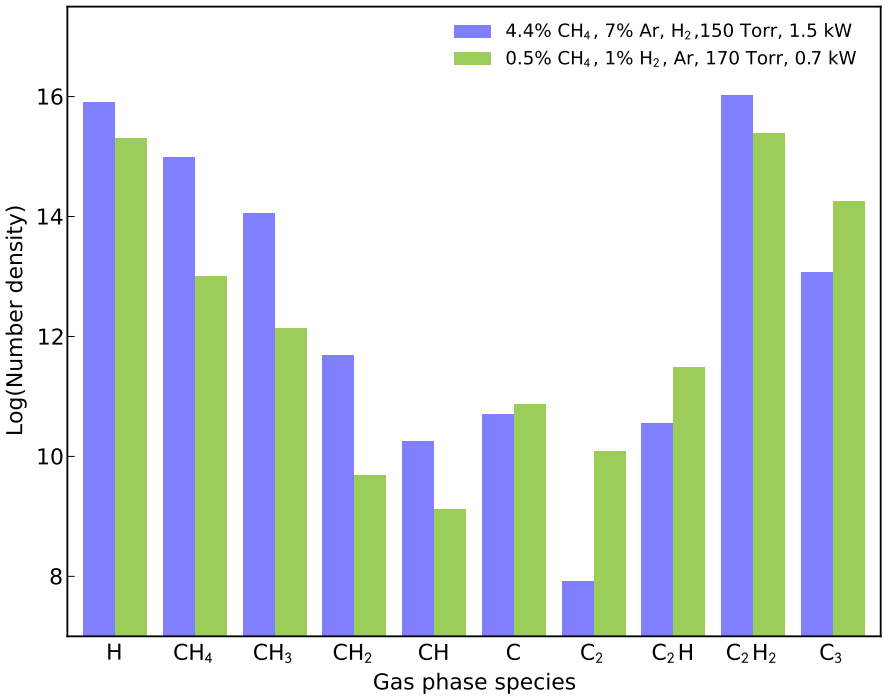

Figure 6.1: Bar chart showing the difference in the predicted number density of a number of species 0.5 mm above the growing substrate, from simulations of the plasma under MCD and UNCD conditions. Based on the data presented in Table 6.1.

a C_9H_{14} cluster (which has previously been employed in modelling studies of carbon addition and incorporation into the diamond lattice[9]) and two additional structures representing CH_3 surface groups and an incorporated CH_2 group. These variants were created by adjusting the initial C_9H_{14} cluster by either replacing one of the surface H atoms with a CH_3 group or inserting a CH_2 group into a C-C bond. Figure 6.2 illustrates the three different clusters as well as the five distinguishable C-H bonds (HC1-HC5) and the four distinguishable C-C bonds (CC1-CC4) which would be located on the diamond surface.

Optimized geometries of potential energy minima and transition states (TSs) associated with the insertion of the different C_xH_y radical species into each of the C-H and the C-C bonds were computed using the Gaussian03 program[10] with the B3LYP density functional and the 6-31G(d) basis set. The nature of the stationary points was confirmed by calculating the vibrational frequencies associated with each optimized geometry. These vibrational frequencies were also used to obtain an estimate of the zero-point correction (ZPC) and the entropy of the system. Single-point energies for each of the B3LYP/6-31G(d) optimized geometries were then calculated using the larger 6-311G(d,p) basis set. The QM energies reported for the insertion reactions presented are based on the B3LYP/6-

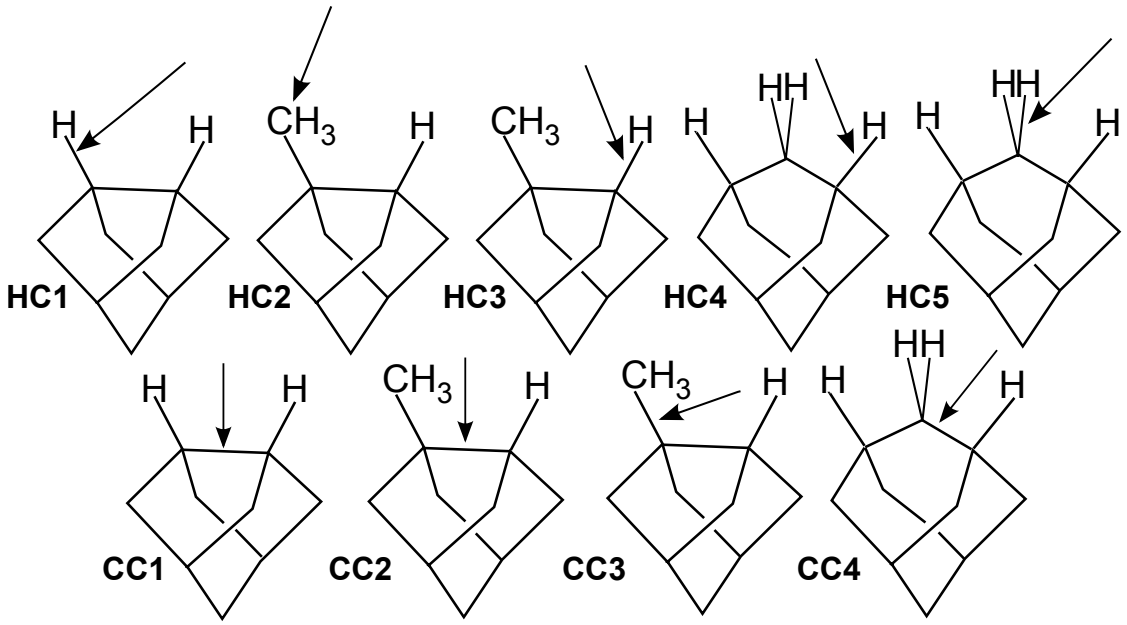

Figure 6.2: Illustration showing the basic C_9H_{14} cluster and the two variants used in the QM calculations, as well as the five distinguishable C-H (HC1-HC5) and the four C-C (CC1-CC4) bonds on the diamond surface.

311G(d,p)//B3LYP/6-31G(d) single point energies and include zero-point energy corrections (ZPC) from calculations at the B3LYP/6-31G(d) level of theory. Energies are in kJ mol^{-1}.

Differing approach angles of the incoming C_xH_y fragment towards the insertion site can lead to several isomeric TSs and energy minima. An example of this can be seen in the minimum energy structure found in the entrance channel of the C atom insertion into HC1 (shown in Figure 6.4) where the carbon atom approaches the C-H bond from different angles. In these cases the lowest energy pathway calculated is included in the results below.

Also employed in the present study was a QM/MM approach whereby a small QM region is embedded within a larger MM network to complement the QM investigations of the various C_xH_y species insertions into surface C-H bonds (HC1) or C-C bonds (CC1). The calculations were preformed using the QoMMMa program[11,12]. Calculations on the QM region were performed using Jaguar 5[13] whilst the MM region was modelled using TINKER[14]. The QM region was based on a small C_9 cluster similar to that used in the QM calculations and the MM network used was a $5 \times 9 \times 4$ slab (defined in terms of the number of C-C dimer bonds), with the initial geometry defined by the bulk diamond lattice points as used in previous work by Cheesman *et al.*[9] The base QM/MM model is shown in Figure 6.3a. The B3LYP density functional with the 6-31G(d) basis set was used for optimization of the QM region's geometry, whilst the MM2 molecular mechanics protocol was used for that of the MM region. Single point energies for the QM region were then calculated at the B3LYP/6-

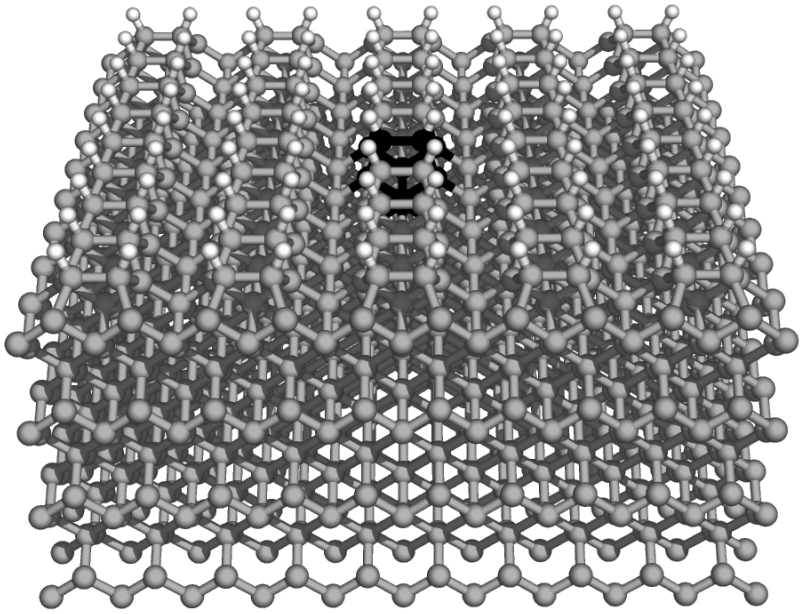

(a)

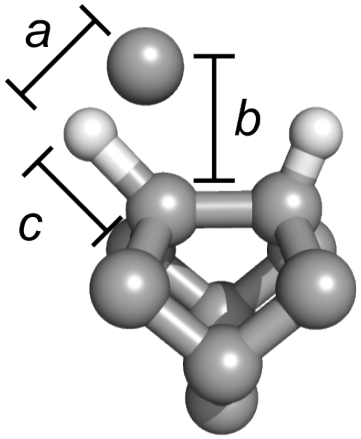

(b)

Figure 6.3: (a) shows an example of the QM/MM structure used in the current calculations. The MM network is shown in grey whilst the black central region is the structure treated with QM. (b) shows the QM region for the insertion of atomic carbon into a C-H bond on the diamond. The bond lengths highlighted are used to restrict q such that $q = a + b - c$.

311g(d,p) level of theory. These energies were combined with the corresponding MM energy and the ZPC determined from the corresponding QM calculation. Identification of approximate TSs for each of the investigated reactions was achieved by calculating the energy of the system of interest along a chosen reaction coordinate (q). This reaction coordinate was chosen to be either a key bond length, or combination of bond lengths, representing the insertion of the gas phase radical of choice into the surface bond. An example of a reaction coordinate used is shown in Figure 6.3b where $q = a + b - c$. The system is then held close to the desired value of q with a harmonic constraint. The energies of the QM region and MM region are then combined for each calculation at different q and the transition state is taken as the point of maximum energy along the curve. The step sizes used for the value q were chosen such that the estimated error in locating the approximate transition states was $\leq$ 5 kJ mol^{-1}. The reported energies are given in kJ mol^{-1} and include the ZPC from the corresponding QM calculation.

6.3 Results

Calculated energies for the insertion of C atoms and CH, CH_2, C_2 and C_3 radicals into C-H and C-C bonds designed to mimic the diamond C{100}:H 2×1 surface are presented in the following section.

6.3.1 C(^{3}P) Atoms

Atomic carbon has previously been proposed as a species that may play an important role in the growth of diamond films[15,16]. Under the gas temperatures typically observed in diamond CVD environments the gas phase C atoms close to the growing diamond will be in their ^{3}P ground state. The present calculations have consequently focused on the insertion of C(^{3}P) into the various bonds portrayed in Figure 6.2.

The reliability of the current DFT calculations were assessed by studying the insertion of C(^{3}P) into one of the C-H bonds of methane. A previous study of this reaction by Kim *et al.*[17] at the CCSD(T)/6-311+G(3df,2p) level of theory obtained a reaction exothermicity, ΔE = −268 kJ mol^{-1}, and identified a TS (E_{TS} = 51 kJ mol^{-1}) and a shallow minimum in the entrance channel ($E_{complex}$= −3.3 kJ mol^{-1}), where the quoted energies are defined relative to the reactants. The B3LYP/6-311g(d,p)//B3LYP/6-31g(d) calculations used in the present calculations return a virtually identical TS geometry and energies that are in good agreement with those of Kim *et al.* : ΔE = −285 kJ mol^{-1},

Table 6.2: B3LYP/6-311g(d,p)//B3LYP/6-31g(d) energies including the ZPC calculated at the B3LYP/6-31g(d) level for the entrance channel complex ($E_{complex}$), transition states (E_{TS}) and the overall change in energy (ΔE) associated with insertion of C(^{3}P) into the C-H and C-C bonds shown in Figure 6.2. All energies are defined relative to those of the reactants.

Insertion site	$E_{complex}$/kJ mol^{-1}	E_{TS}/kJ mol^{-1}	ΔE/kJ mol^{-1}
CC1	−21.2	90.5	−305.1
CC2	−21.0	115.9	−352.1
CC3	−14.6	166.3	−321.1
CC4	−29.2	156.8	−304.5
HC1	−21.1	−1.8	−305.3
HC2	−14.7	14.2	−289.6
HC3	−21.9	−0.2	−302.3
HC4	−29.4	−6.0	−300.6
HC5	−23.9	0.9	−294.2

E_{TS} = 34.7 kJ mol^{-1} and $E_{complex}$ = −4.6 kJ mol^{-1}.

The insertion of C(^{3}P) into the various C-H and C-C bonds was found in all cases to be highly exothermic and to proceed via a shallow minimum energy complex in the entrance channel leading to the TS. Table 6.2 shows the calculated energies of the TSs, the entrance channel complexes and the overall energy change associated with each of the C-H and C-C bond insertions. Energy barriers related to the insertion of C(^{3}P) atoms into C-H bonds were found to be small. In contrast, insertion into C-C bonds involved substantial energy barriers.

The insertion of a C(^{3}P) atom into a surface C-H bond (equivalent to HC1) has also been investigated with QM/MM methods. The structures and energies obtained for the various stages of this reaction were found to be in close agreement with those of the QM model ($E_{complex}$, E_{TS} and ΔE = −23.0, −0.2 and −302.5 kJ mol^{-1}, respectively). However the QM and QM/MM methods return rather different structures for the entrance channel complex and the transition states, as the neighbouring surface groups present in the QM/MM calculations serve to constrain the approach angle of the gas phase C(^{3}P) atom. The preferred approach angle towards the C-H bond in the QM calculations was found to be from the side (as shown in Figure 6.4 HC1) whilst in the QM/MM calculations the C(^{3}P) atom approached from above. This reflects the lack of steric hindrance from the rest of the diamond surface when using the small C_9H_{14} QM cluster. Insertion into C-C bonds was also investigated using QM/MM methods. However an approximate TS could not be located in this case, due to problems optimizing the geometry at values of q close to the location of the transition state. The portion of the potential energy surface (PES) that was able to be determined along q is shown in Figure 6.5. Again, $q = a + b - c$ where in this case a = the distance between the gas phase C atom and one of the surface

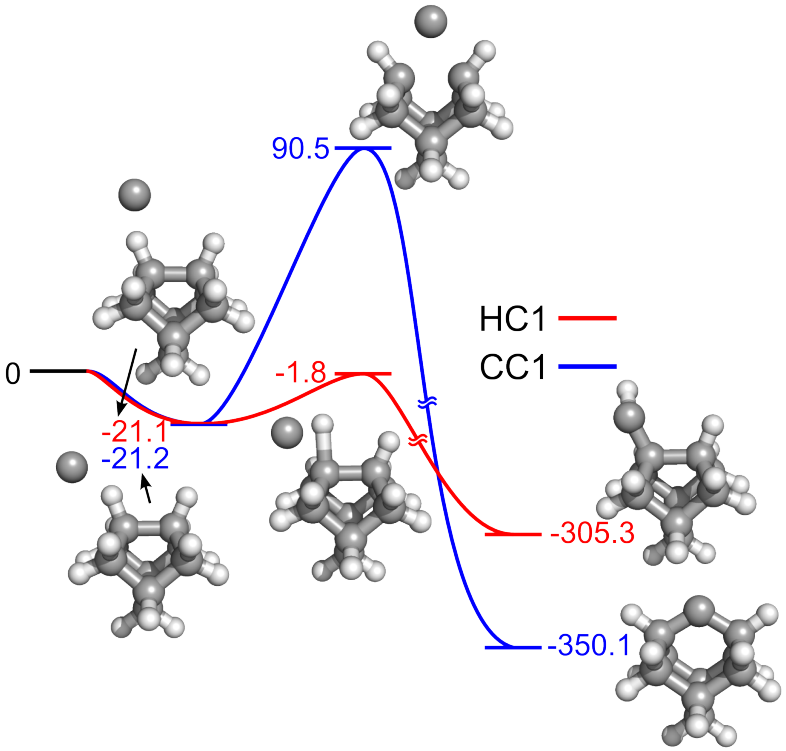

Figure 6.4: Minimum energy pathways for the insertion of C(^{3}P) atoms into a C-H (HC1) and a C-C (CC1) bond, including B3LYP/6-31g(d) optimized structures for the entrance channel complex, transition state and final product. Energies are in kJ mol^{-1} and are from B3LYP/6-311g(d,p)//B3LYP/6-31g(d) calculations with zero point corrections caculated at the B3LYP/6-31g(d) level.

C atoms, b = the distance between the gas phase C atom and the other surface C atom (*i.e.* not the one used to define a) and c = C-C bond length as shown in Figure 6.5. These calculations confirm that the insertion of C(^{3}P) into the C-C bond will involve a significantly higher barrier ($>$ 54 kJ mol^{-1}) than insertion into a C-H bond, which is in good agreement with the QM cluster calculations.

6.3.2 CH ($X^2\Pi$) radicals

The insertion of ground state ($X^2\Pi$) CH radicals into C-H bonds of methane and ethylene has been previously studied using QM modelling[18–20] and experimental rate constants have also been measured at a range of temperatures for the reaction of CH(X) with CH_4 and larger hydrocarbons[20–23]. These studies all lead to the notion that the insertion of a CH radical into a C-H bond of an alkane should be a barrier-less process.

As with the insertion of atomic carbon insertion, calculations on a number of different C-H and C-C bonds were investigated for the insertion of CH, the results of which are presented in Table 6.3. Each

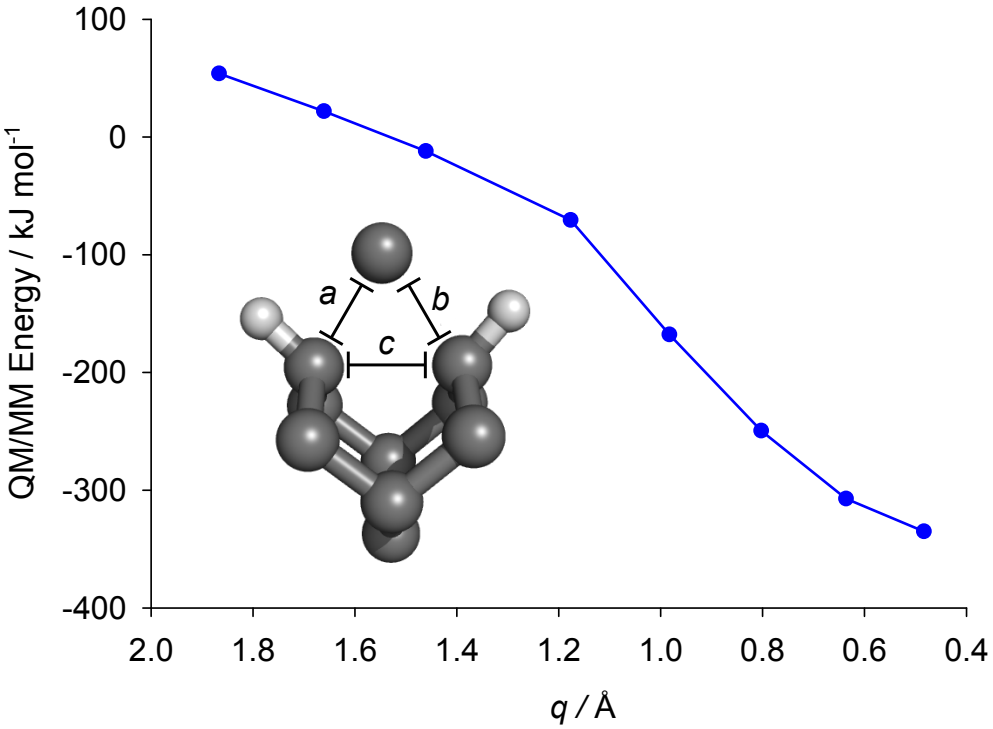

Figure 6.5: PES along reaction coordinate q, where $q = a + b - c$; a = the distance between the gas phase C atom and one of the surface C atoms, b = the distance between the gas phase C atom and the other surface C atom (*i.e.* not the one used to define a) and c = C-C bond length. A q value of ≈0.5 Å corresponds to the fully inserted product. Plotted energies are from B3LYP/6-311g(d,p) single point energies on B3LYP/6-31g(d):MM2 geometries.

of these insertion reactions were found to proceed via an entrance channel complex which, in all cases, lies lower than the reactant energy. The C-H insertions (HC1-HC5) were then found to involve passage over a TS also lying well below the reactants energy. TSs associated with insertion into a C-C bond were, on the other hand, found to be considerably higher than the reactant energy. After the single-point energies calculated with the larger 6-311G(d,p) basis set and zero point corrections were included, the energies of the TSs for insertion into the various C-H bonds were found actually to be lower in energy than that of the corresponding entrance channel complex, casting doubt on whether there is any real barrier to these reactions.

QM/MM calculations used to investigate CH radical insertion into both C-H and C-C bonds failed to reveal any obvious energy barrier for insertion into a C-H bond. Instead the potential energy surface plotted along q was found to be relatively flat and any barrier that may be present is likely to be small and comparable to the errors associated with the calculations performed at each value of q. Insertion into the C-C dimer bond on the C{100}:H 2×1 surface was found to involve a significant energy barrier of ≈77 kJ mol^{-1}, slightly lower than that calculated in the corresponding QM calculations,

conceivably due to the stretching of the dimer bond caused by the surrounding MM matrix.

Table 6.3: B3LYP/6-311g(d,p)//B3LYP/6-31g(d) energies including the ZPC calculated at the B3LYP/6-31g(d) level for the entrance channel complex ($E_{complex}$), transition states (E_{TS}) and the overall change in energy (ΔE) associated with insertion of CH($X^2\Pi$) into the C-H and C-C bonds shown in Figure 6.2. All energies are defined relative to those of the reactants.

Insertion site	$E_{complex}$/kJ mol^{-1}	E_{TS}/kJ mol^{-1}	ΔE/kJ mol^{-1}
CC1	−32.1	82.7	−454.6
CC2	−28.7	110.7	−457.1
CC3	−28.7	171.2	−411.5
CC4	−40.7	157.0	−397.5
HC1	−36.3	−40.1	−413.2
HC2	−27.1	−28.6	−391.1
HC3	−36.2	−39.1	−409.1
HC4	−41.7	−42.4	−408.2
HC5	−36.2	−38.3	−403.8

6.3.3 CH_2

Carbenes are well known to have different reactivities depending on their electronic configuration[24] (either singlet or triplet). Triplet carbenes are likely to abstract an H atom when reacting with a hydrocarbon species, whereas the singlet species can insert directly into C-H bonds. Methylene (CH_2) is the simplest carbene species and has a triplet (X^3B_1) ground state, and its first excited singlet state (a^1A_1) lies ≈0.4 eV higher in energy. These states are henceforth referred to as $^3CH_2$ and $^1CH_2$, respectively. Many theoretical studies of $^1CH_2$ radical insertion into C-H[4–6] and C-C[7,8] bonds of isolated hydrocarbon molecules have been published, and show that insertion into C-H bonds typically involves low energy barriers, while insertion into C-C bonds involves large energy barriers. Experimental studies also confirm this difference as the relative rate of insertion into C-H bonds is significantly faster compared with C-C bonds.[25]

Transition states for the insertion of $^1CH_2$ radicals into various C-H and C-C bonds on the diamond surface have been identified in the present QM calculations and their energies are reported in Table 6.4. All the identified transition states for insertion of $^1CH_2$ into C-H bonds are found to lie lower in energy than the reactants and consequently the insertion should be a rapid process. However, insertion should be even more facile than suggested by the energies of the identified transition states, because if the $^1CH_2$ radical approaches the C-H bond in an alternative orientation to the one identified in the TS no barrier to insertion is found. This barrierless route to insertion also explains our inability to locate a local minimum associated with the TSs listed in Table 6.4. This is due to the fact that,

Table 6.4: B3LYP/6-311g(d,p)//B3LYP/6-31g(d) energies including the ZPC calculated at the B3LYP/6-31g(d) level for transition states (E_{TS}) and the overall change in energy (ΔE) associated with insertion of $^1CH_2$ into the C-H and C-C bonds shown in Figure 6.2. All energies are defined relative to those of the reactants.

Insertion site	E_{TS}/kJ mol^{-1}	ΔE/kJ mol^{-1}
CC1	122.2	−487.5
CC2	149.6	−476.6
CC3	200.2	−433.4
CC4	195.9	−408.1
HC1	−15.3	−449.6
HC2	−5.8	−433.4
HC3	−9.3	−443.7
HC4	−22.0	−438.7
HC5	−15.8	−437.7

as the geometry is relaxed away from that of the TS towards that of the of the suspected entrance channel complex, the CH_2 moiety is able to reorient itself such that subsequent optimisation leads to the barrierless insertion into either the same or a different C-H bond. This agrees well with the work of Bach *et al.*[4], where two transition states for $^1CH_2$ insertion into C-H bonds were located using Hartree-Fock theory. However, at higher levels of theory the lower of the two barriers disappeared, suggesting that one pathway is barrierless. Our QM/MM calculations also support this conclusion as optimisation of the structure along the chosen reaction coordinate with the $^1CH_2$ in the more favourable orientation shows no barrier.

Insertion into C-C bonds has also been investigated by QM and QM/MM techniques. Table 6.4 shows the calculated QM energies of the transition states identified for insertion into a variety of C-C bonds (CC1-CC4). These all involve high barriers. The QM/MM calculations for $^1CH_2$ insertion into CC1 return a slightly smaller barrier to insertion of ≈106 kJ mol^{-1}, possibly due to increased strain in the dimer bond due to surrounding diamond lattice.

In contrast to the insertion mechanisms of $^1CH_2$, $^3CH_2$ can add to surface radical sites in reactions analogous to those involving CH_3 radicals. They can also abstract H atoms from surface C-H bonds. QM calculations at the B3LYP/6-311G(d,p)//B3LYP/6-31G(d) level of theory including zero point corrections calculated at the B3LYP/6-31G(d) level, show that the energy barrier for abstraction of a H atom from a surface C-H bond on a HC1-type structure is only 14.3 kJ mol^{-1}. The product of this abstraction process would be a surface radical and a gas phase CH_3 radical. In principle, these species could then recombine to form a surface bound CH_3 group.

6.3.4 C_2

The C_2 radical possesses a $X^1\Sigma_g^+$ ground state and several previous computational studies have reported singlet C_2 radical insertions into the C-H bonds of methane[26] and a C_9H_{14} cluster[27], at several different levels of theory. A low lying triplet state ($a^3\Pi_u$) also exists only 0.089 eV above the ground state. The singlet and triplet states of C_2 are henceforth referred to as $^1C_2$ and $^3C_2$, respectively.

Previous studies on the insertion of $^1C_2$ into C-H bonds of methane have suggested a negligible energy barrier.[26,27] The present QM calculations also lend support to this view, as we were unable to locate a TS for $^1C_2$ insertion into a C-H bond such as HC1. The reaction was found to be highly exothermic ($\Delta E = -477.7$ kJ mol^{-1}) which is in good agreement with the previous work of Gruen *et al.*[27] who found $\Delta E = -480.6$ kJ mol^{-1} at the B3LYP/6-31G(d) level of theory. The resulting vinylidene-like product of this insertion reaction can then rearrange to form an acetylene group on the diamond surface. This rearrangement was found to be an exothermic process with $\Delta E = -198$ kJ mol^{-1}. A TS for this rearrangement was located and, after inclusion of higher level single-point energies and zero point correction, was found to lie -4.9 kJ mol^{-1} below that of the vinylidene-like group, indicating that the barrier to rearrangement must be very small.

Similar energies are also returned by the equivalent QM/MM studies, which found no activation barrier to $^1C_2$ radical insertion into a C-H bond on the C{100}:H 2×1 surface (the potential energy along the chosen reaction coordinate is shown in Figure 6.6). The formation of the vinylidene-like appendage was found to be exothermic by 468 kJ mol^{-1}, in good agreement with the previous QM calculations, and its subsequent rearrangement to form the surface bound acetylene group was deduced to involve a small barrier ($E_{TS} \approx 1$ kJ mol^{-1}, calculated at the B3LYP/6-31g(d):MM2 level) and be exothermic by 201.7 kJ mol^{-1}. As with the QM calculations, single point calculations with the larger basis set found the TS lying lower in energy than the vinylidene-like structure.

In contrast, $^3C_2$ radicals do not participate in insertion reactions but will add to surface radical sites and can contribute to H atom abstraction from surface C-H bonds.

6.3.5 C_3

The insertion of a C_3 radical, in its $X^1\Sigma_g^+$ ground state, into a surface C-H bond was found from QM calculations (on the HC1 structure) to be an exothermic process ($\Delta E = -231$ kJ mol^{-1}) but involve a significant energy barrier ($E_{TS} \approx 105$ kJ mol^{-1} at the B3LYP/6-31g(d) level).

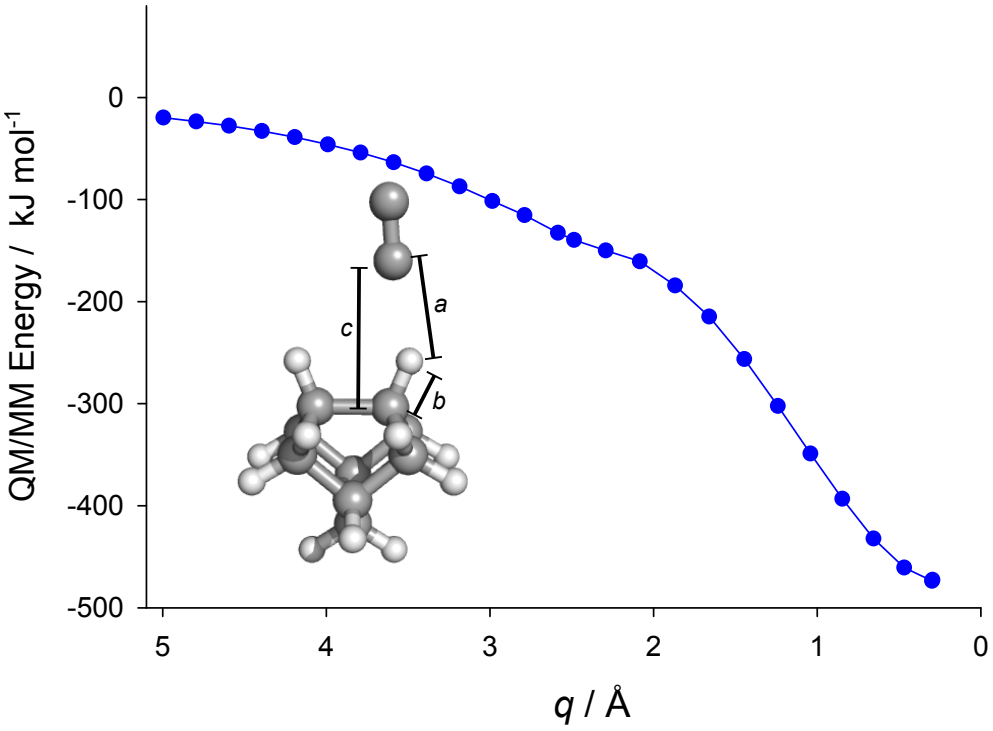

Figure 6.6: PES along reaction coordinate q, where $q = a + b - c$; a = distance between gas phase $^1C_2$ species and the H atom of the C-H bond, b = the distance between the C and H atoms of the C-H bond and c = distance between gas phase $^1C_2$ species and the C atom of the C-H bond. A q value of ≈0.3 Å indicates the fully inserted product. Plotted energies are from B3LYP/6-311g(d,p) single point energies on B3LYP/6-31g(d):MM2 geometries.

6.3.6 Discussion

Insertion mechanism

The interaction of the orbitals of the gas phase species and the surface C-H and C-C bonds are key to whether the species in question will be able to insert directly into the surface C-H and C-C bonds. The mechanism is well known for singlet carbenes, such as $^1CH_2$, which possess a doubly occupied donor orbital and a low-lying empty acceptor orbital[4]. The doubly occupied donor orbital of the carbene is able to interact with the empty σ^* orbital of the bond into which insertion is to occur and the empty p orbital of the carbene is able to accept electron density from the σ orbital of the surface C-H bond (illustrated in Figure 6.7).

Similar interactions between the orbitals of CH, $^1C_2$ radicals and C(^{3}P) atoms with the surface bonds can then be invoked to describe their respective insertion processes.

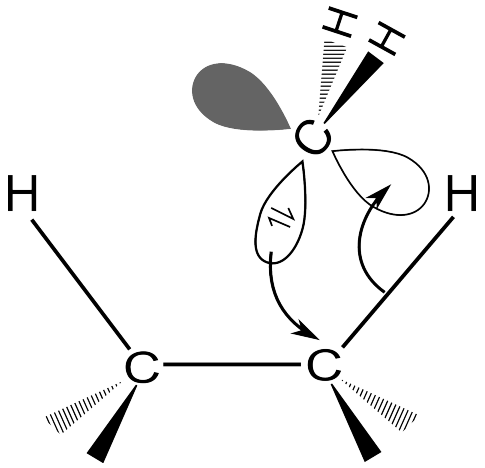

Figure 6.7: Cartoon illustrating the insertion mechanism of $^1CH_2$ into a C-H bond.

Impact on diamond growth

During diamond CVD the growing surface will experience a large flux of species towards the surface. The flux rate of a particular species i, can be estimated using[28],

$$F_i = N_i \times V_i \tag{6.1}$$

where N_i is the number density of species i and V_i is the thermal velocity of species i which can be calculated using,

$$V_i = 1.455 \times 10^4 \left(\frac{m_i}{T_{\text{sub}}} \right) . \tag{6.2}$$

m_i is the mass of species i (e.g. m_i = 1 for H atoms and 15 for CH_3 radicals), T_{sub} is the substrate temperature. Utilising the calculated H atom density under MCD growth conditions presented in Table 6.1, and assuming that T_{sub} = 1000 K, the flux of atomic hydrogen to the surface is calculated to be $\approx 3 \times 10^{22}$ cm^{-2} s^{-1}. As a result of the high flux of atomic hydrogen to the surface, the diamond will be predominantly H-terminated. However, at any one point in time a fraction of the surface atoms will be radicals. During CVD of diamond the surface is in a state of constant fluctuation where surface carbon atoms frequently exchange terminating H atoms with the gas phase species directly above the surface. Each surface atom will experience $\approx 10^7$ collisions per second with incident gaseous H atoms (assuming a surface density of $\approx 2 \times 10^{15}$ C atoms per cm^{-2}). As seen in Table 6.1 the number density of $C_1H_x (x \leq 3)$ radicals in the gas phase is typically two or more orders of magnitude lower than that of H atoms. The rate at which incident hydrocarbon radicals such as CH_3 encounter reactive

radical sites (assuming that at any one time 10% of the surface carbon atoms will be radicals) on the diamond surface is consequently only on the order of ≈1000 s^{-1} and represents the rate limiting step for the incorporation of new carbon species into the diamond lattice[9,29].

The results outlined above indicate that CH, $^1CH_2$, $^1C_2$ radicals and C(^{3}P) atoms all exhibit essentially barrierless insertion pathways into C-H bonds based on the energies returned by the QM and QM/MM calculations. Nevertheless the rate of these reactions will be determined by the change in Gibbs energy ($\Delta_r G$). At the substrate temperatures (≈1000 K) involved in diamond CVD the contribution of entropy to $\Delta_r G$ can become significant, especially, when the reaction involves loss of a gas phase species. For example, from the QM calculations for insertion of C(^{3}P) into a surface C-H bond the entropy change can be calculated as $\Delta_r S \approx -116$ J K^{-1} mol^{-1}. At 1000 K, this reduces the overall change in energy by ≈116 kJ mol^{-1} and raises the energy of the transition state by ≈ 107 kJ mol^{-1} relative to that of the reactants. Given the high entropic contributions and the already large potential energy barriers calculated for C-C bond insertion, it is concluded that C-C bond insertion is not an important process in diamond CVD.

C-H bonds on the growing diamond surface outnumber the fraction of radical sites by a factor of ten or more in most diamond CVD environments. Insertion of CH, $^1CH_2$, $^1C_2$ radicals and C(^{3}P) atoms into C-H bonds on the diamond surface offers an alternative route to introduce C atoms onto the growing surface. Under MCD conditions, all these species are in low abundance relative to that of CH_3 (Table 6.1). In particular, the singlet states of CH_2 and C_2 radicals make up only ≈ 1% and 27% of their total radical density near the surface, respectively (assuming the gas mixture is at local thermodynamic equilibrium). This is a result of the energy differences and degeneracies of the two states of each species. Thus C-H insertion reactions under typical MCD conditions are expected to make, at most, a small contribution to the overall incorporation of carbon into the growing film.

However, under UNCD conditions the predicted CH_3 number density (Table 6.1) differs greatly from that under MCD conditions. The CH_3 radical density is two orders of magnitude lower, whilst the number density of C(^{3}P) atoms has increased by ≈50%. Coupled with the fact that most of the growing diamond surface will be C-H terminated, the insertion of C(^{3}P) atoms into C-H bonds may well play a significant role in the nucleation and growth of UNCD films. A C(^{3}P) atom may also add to a surface radical site. Such additions, together with the C-H insertion mechanism, means that an incident C atom is able to react at any surface site, and may offer a partial explanation for the high nucleation density and small grain sizes that characterise UNCD films.

From Table 6.1 it can be seen that the $^1C_2$ radical number density near the surface under UNCD

growth conditions is predicted to be an order of magnitude lower than that of C(^{3}P) atoms. As seen above, these radicals can also insert into surface C-H bonds without a potential barrier. This process will result in the addition of two carbon atoms onto the surface. However, hydrogenation of the pendant vinylidene or acetylene group (after rearrangement) will leave them vulnerable to subsequent loss by β-scission[30].

Insertion rates

The reaction rate constants of C(^{3}P) atoms and CH radicals inserting into C-H bonds have been calculated from vibrational frequencies computed in the QM calculations using transition state theory. These rate constants are listed in Appendix C.

6.3.7 Conclusions

Most current growth mechanisms for diamond CVD have focused on the CH_3 radical as the main growth species, and the addition of this species on to the surface from the gas phase is normally regarded as the rate limiting step. In this chapter a combination of QM and QM/MM computational methods have been utilised to explore other potential gas-surface interactions that may allow other carbon containing species (C atoms and CH, CH_2, C_2 and C_3 radicals) in the gas phase to play a role in the growth process. This work mostly centred on insertion of radicals into bonds on the C$\{100\}$:H 2×1 surface, although the various reactions investigated will also be valid on other diamond surfaces. The QM calculations used a small C_9H_{14} cluster to mimic the surface. The QM/MM calculations involved a similar QM cluster which was then embedded in an extensive network of carbon atoms treated using molecular mechanics methods (see Figure 6.3a). Minimum energy pathways for the insertion of C atoms or CH, $^1CH_2$ or $^1C_2$ radicals into C-H bonds were shown to be essentially barrierless, while insertion into a C-C bond on the diamond surface was found to involve significant barriers, which likely precludes such reactions from being relevant to the growth mechanism of diamond. Under typically MCD growth conditions the impact of the studied insertion mechanisms on diamond growth is thought to be small due to the low relative concentrations of the relevant gas phase species. However, under certain gas phase conditions, such as those prevalent when growing UNCD films, insertion reactions may start to play a greater role in diamond growth (particularly the insertion reactions of C(^{3}P) atoms).

References

[1] J. C. Richley, J. N. Harvey, and M. N. R. Ashfold, *J. Phys. Chem. A* **113**, 11416 (2009).

[2] J. Ma, J. C. Richley, M. N. R. Ashfold, and Yu. A. Mankelevich, *J. Appl. Phys.* **104**, 103305 (2008).

[3] J. C. Richley, O. J. L. Fox, M. N. R. Ashfold, and Yu. A. Mankelevich, *J. Appl. Phys.* **109**, 063307 (2011).

[4] R. D. Bach, M. D. Su, E. Aldabbagh, J. L. Andres, and H. B. Schlegel, *J. Am. Chem. Soc.* **115**, 10237 (1993).

[5] M. S. Gordon and D. R. Gano, *J. Am. Chem. Soc.* **106**, 5421 (1984).

[6] M. Ramalingam, K. Ramasami, P. Venuvanalingam, and V. Sethuraman, *J. Mol Struc-Theochem* **755**, 169 (2005).

[7] M. S. Gordon, J. A. Boatz, D. R. Gano, and M. G. Friederichs, *J. Am. Chem. Soc.* **109**, 1323 (1987).

[8] D. R. Gano, M. S. Gordon, and J. A. Boatz, *J. Am. Chem. Soc.* **113**, 6711 (1991).

[9] A. Cheesman, J. N. Harvey, and M. N. R. Ashfold, *J. Phys. Chem. A* **112**, 11436 (2008).

[10] M. J. Frisch, G. W. Trucks, H. B. Schlegel, G. E. Scuseria, M. A. Robb, J. R. Cheeseman, J. A. Montgomery Jr., T. Vreven, K. N. Kudin, J. C. Burant, J. M. Millam, S. S. Iyengar, J. Tomasi, V. Barone, B. Mennucci, M. Cossi, G. Scalmani, N. Rega, G. A. Petersson, H. Nakatsuji, M. Hada, M. Ehara, K. Toyota, R. Fukuda, J. Hasegawa, M. Ishida, T. Nakajima, Y. Honda, O. Kitao, H. Nakai, M. Klene, X. Li, J. E. Knox, H. P. Hratchian, J. B. Cross, V. Bakken, C. Adamo, J. Jaramillo, R. Gomperts, R. E. Stratmann, O. Yazyev, A. J. Austin, R. Cammi, C. Pomelli, J. W. Ochterski, P. Y. Ayala, K. Morokuma, G. A. Voth, P. Salvador, J. J. Dannenberg, V. G. Zakrzewski, S. Dapprich, A. D. Daniels, M. C. Strain, O. Farkas, D. K. Malick, A. D. Rabuck, K. Raghavachari, J. B. Foresman, J. V. Ortiz, Q. Cui, A. G. Baboul, S. Clifford, J. Cioslowski, B. B. Stefanov, G. Liu, A. Liashenko, P. Piskorz, I. Komaromi, R. L. Martin, D. J. Fox, T. Keith, M. A. Al-Laham, C. Y. Peng, A. Nanayakkara, M. Challacombe, P. M. W. Gill, B. Johnson, W. Chen, M. W. Wong, C. Gonzalez, and J. A. Pople, Gaussian 03, Revision B.04, Gaussian, Inc., Wallingford, CT, 2004.

[11] J. N. Harvey, *Faraday Discuss.* **127**, 165 (2004).

[12] A. C. Tsipis, A. G. Orpen, and J. N. Harvey, *Dalton Trans.* (2005).

[13] Jaguar, Schrödinger Inc., Portland, OR, 2000.

[14] J. W. Ponder, Tinker: Software Tools for Molecular Design, v4.0; Saint Louis, MO, 2003.

[15] R. Joe, T. A. Badgwell, and R. H. Hauge, *Diamond Relat. Mater.* **7**, 1364 (1998).

[16] B. W. Yu and S. L. Girshick, *J. Appl. Phys.* **75**, 3914 (1994).

[17] G. S. Kim, T. L. Nguyen, A. M. Mebel, S. H. Lin, and M. T. Nguyen, *J. Phys. Chem. A* **107**, 1788 (2003).

[18] Z. X. Wang and M. B. Huang, *Chem. Phys. Lett.* **291**, 381 (1998).

[19] Z. X. Wang and M. B. Huang, *J. Chem. Soc., Faraday Trans.* **94**, 635 (1998).

[20] N. Galland, F. Caralp, Y. Hannachi, A. Bergeat, and J. C. Loison, *J. Phys. Chem. A* **107**, 5419 (2003).

[21] J. E. Butler, J. W. Fleming, L. P. Goss, and M. C. Lin, *Chem. Phys.* **56**, 355 (1981).

[22] M. R. Berman and M. C. Lin, *Chem. Phys.* **82**, 435 (1983).

[23] J. C. Loison, A. Bergeat, F. Caralp, and Y. Hannachi, *J. Phys. Chem. A* **110**, 13500 (2006).

[24] W. Kirmse, *Carbene chemistry* (Academic; New York, 2nd edition, 1971).

[25] R. Becerra and H. M. Frey, *Chem. Phys. Lett.* **138**, 330 (1987).

[26] D. A. Horner, L. A. Curtiss, and D. M. Gruen, *Chem. Phys. Lett.* **233**, 243 (1995).

[27] D. M. Gruen, P. C. Redfern, D. A. Horner, P. Zapol, and L. A. Curtiss, *J. Phys. Chem. B* **103**, 5459 (1999).

[28] Yu. A. Mankelevich, personal communication.

[29] B. Garrison, E. Dawnkaski, D. Srivastava, and D. Brenner, *Science* **255**, 835 (1992).

[30] D. G. Goodwin and J. E. Butler, in *Handbook of Industrial Diamond and Diamond Films*, edited by M. A. Prelas, A. Popovici, and L. K. Bigelow, chapter 11, pages 527–581 (Marcel Dekker, Inc., 1998).

7

Migration of surface CH_2 groups on the H-terminated $\{111\}$ and between 2×1 $\{100\}$ and $\{111\}$ surfaces of diamond.

This chapter addresses the migration of pendant CH_2 groups on the H-terminated $\{111\}$ surface and between 2×1 $\{100\}$ and $\{111\}$ surfaces of diamond. This work has been previously published.[1]

7.1 Introduction

The diamond $\{100\}$ surface has been the subject of many theoretical studies due to its frequent appearance in CVD grown diamonds. Due to steric constraints, the fully H-terminated $\{100\}$ surface forms a 2×1 reconstruction,[2] resulting in a surface structure consisting of rows of carbon atoms paired up as dimers. Another commonly observed surface in CVD diamond samples is the H-terminated $\{111\}$ surface.[3] Both these surfaces are illustrated in Figure 7.1. The addition and incorporation of gaseous hydrocarbon species at the growing diamond surface during CVD has been studied in detail (see Chapter 1.2.4), with CH_3 now generally regarded as the primary growth species in most CVD environments. The addition of CH_3 to the growing diamond crystal during CVD is dependent on the location of the surface radical site, which are distributed randomly over the surface. Experimentally observed surfaces are, however, smooth.[4] To account for this phenomena it has been suggested that carbon species on the surface are able to migrate.[5]

A number of previous studies have centred on the migration of surface CH_2 groups (*i.e.* groups formed by the abstraction of an H atom from an adsorbed CH_3 species) both on the $\{100\}$:H 2×1[5–7] surface and the $\{111\}$ surface[8]. Migration of CH_2 groups on both surfaces requires the presence of a surface radical site adjacent to the pendant CH_2 group. A ring closing reaction and subsequent

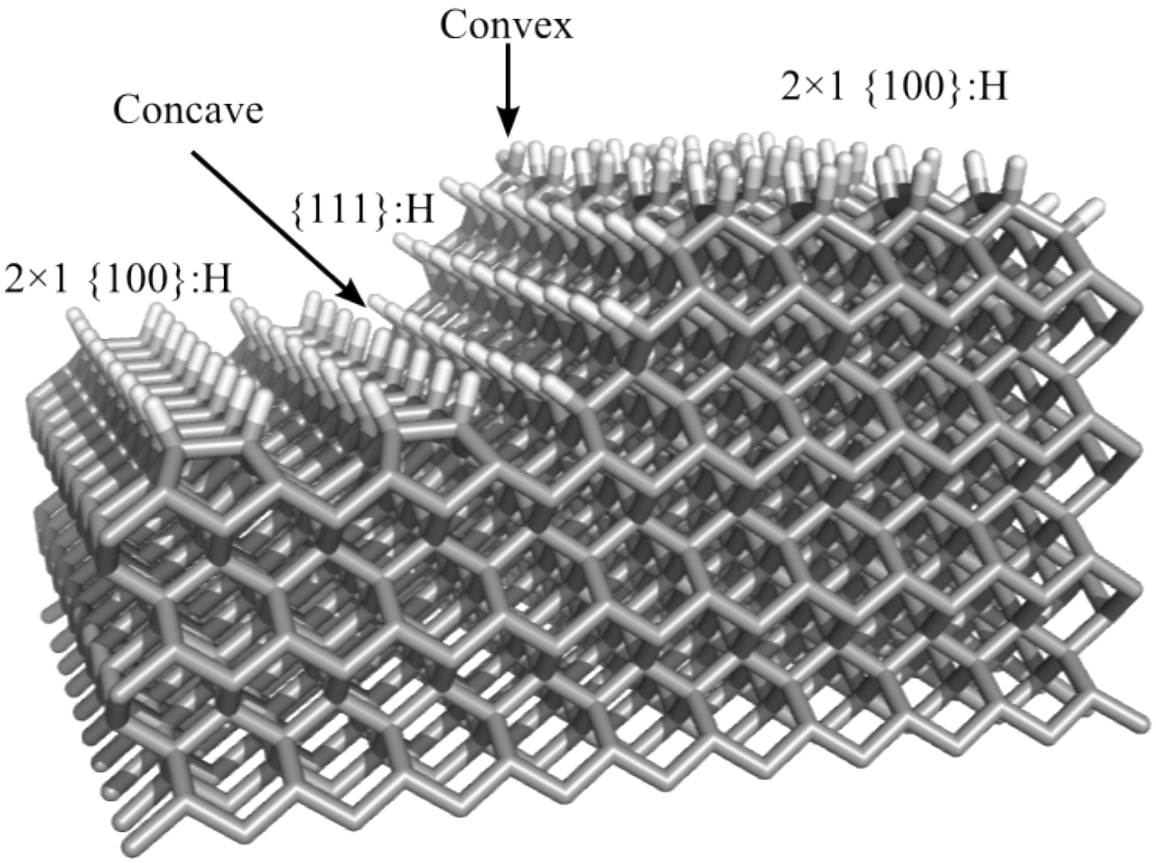

Figure 7.1: An example of a base model used in the current set of calculations. The two C{100}:H 2×1 surfaces and the C{111}:H surface are highlighted. Also shown are the two different step edges which we identify as convex and concave. The orientation of the dimer bonds on the upper and lower surfaces is also illustrated where they lie parallel and perpendicular to the step edges, respectively. A number of similar models are used in this study with varying orientations of the dimer bonds.

opening between the two radicals results in either the migration of the group along the surface by one carbon atom or return to its original position.

Rather than exhibiting a simple flat surface, CVD grown crystals often comprise a set of terraces separated by steps.[4] Each step consists of an upper and lower surface, with another surface in between. The point at which the different surfaces intersect is termed a step edge. The migration of CH_2 groups towards the step edges and subsequent incorporation into the crystal lattice has been suggested as a possible explanation for this stepped texture observed in CVD diamond.[6] Recent work by May *et al.*[9] utilising a simple kinetic Monte Carlo (KMC) model has highlighted how the migration over a step edge might be important in determining the morphology of CVD grown films. A recent study by Eckert *et al.*[10] has used Metropolis Monte Carlo based methods to study the interactions of various C_xH_y species at step edges and whether they enhance, or inhibit, the extension of diamond terraces during growth.

Work presented in this chapter utilises hybrid quantum mechanical/molecular mechanical (QM/MM) cluster based calculations to both re-investigate the energetics associated with the migration of CH_2 on the H-terminated $\{111\}$ surface and explore the energetics associated with the possible routes for migration of surface bound CH_2 between the 2×1 reconstructed $\{100\}$ H-terminated surface and the $\{111\}$ H-terminated surfaces.

7.2 Computational Methods

The computational work described in this chapter involves using a hybrid QM/MM approach and is performed with the QoMMMa program.[11,12] The approach is similar to that outlined in Chapter 6 where a small QM region treated with DFT, is embedded into a larger MM region described with the MM2 molecular mechanics protocol. The base model begins the same as the one described in the previous chapter (Figure 6.3a). Part of this slab is then removed to produce a stepped surface with upper and lower C$\{100\}$:H 2×1 terraces and a central H-terminated $\{111\}$ surface (C$\{111\}$:H). An example of one of the base models used in the current calculations is shown in Figure 7.1. The region at which the C$\{100\}$:H 2×1 and the C$\{111\}$:H surfaces meet are termed step edges and can be either convex (where the upper surface meets the middle surface) or concave (where the middle surface meets the lower surface). The structure of the step edges formed between the two C$\{100\}$:H 2×1 surfaces and the C$\{111\}$:H is also dependent on the orientation of the dimer bonds on the C$\{100\}$:H 2×1 surfaces. These dimer reconstructions can run across the surfaces either perpendicularly or parallel to the step edge of interest.

Migration pathways for CH_2 groups from one surface to the next will be dependent on the type of step edge and the orientation of the dimer bonds. There are a total of five possible routes for the migration of CH_2 between the three surfaces, two on the convex step edge and three on the concave step edge. The greater number in the latter case is because when the dimer bonds are parallel to the step edge, a migrating CH_2 on the C$\{111\}$:H surface can lie in one of two positions, facing a trough between dimer bonds or facing the centre of the dimer bond. Each of these pathways requires slightly modified QM and MM regions, and therefore a total of five different base models are used to investigate the step edge migrations.

A sixth model was used when investigating migration of CH_2 solely on the C$\{111\}$:H surface. The structure was modified so that the central C$\{111\}$:H surface was extended to ensure that the energies calculated are not influenced by groups on the adjacent surfaces.

The initial and final species for each migration pathway investigated include both a surface radical site and a pendant CH_2 group. These species will contain two unpaired electrons, while the intermediate species formed by a ring-closing reaction will be a closed-shell system. Thus the initial and final structures can be expected to have a triplet electronic configuration, whilst the intermediate structure will have a singlet electronic configuration. The open shell singlet and triplet states were described using unrestricted DFT, whilst the closed shell singlets were described using restricted DFT. Open shell singlets states were found in most cases to lie within 10 kJ mol^{-1} of the corresponding triplet states. The crossings between the singlet and triplet states are highlighted in Figure 7.2.

As in Chapter 6 approximate transition states (TSs) were identified by calculating the total energy of the system along a chosen reaction coordinate. The reaction coordinate (q) used to describe the migration pathways of interest was defined as $q = R_1 - R_2$ where R_1 is the separation of the pendant CH_2 group from the surface carbon and R_2 is the distance between the pendant CH_2 group and the adjacent surface radical site. This reaction coordinate is also illustrated in Figure 7.2.

Geometries for the initial, intermediate and final species and points along q were first optimized at the B3LYP/6-31g(d):MM2 level of theory. Single point energy calculations were then carried out on just the QM region at the B3LYP/6-311g(d,p) level of theory. Energies reported in this chapter for the initial, intermediate, final and approximate TSs are the combination of the single point QM calculations and the MM energies, in kJ mol^{-1} and are defined relative to the energy of the triplet state of the initial species.

7.3 Results and discussion

As seen in previous studies[5–8] of CH_2 migration on H-terminated diamond surfaces, the migration requires that a surface radical site is adjacent to the migrating group. The migration then proceeds via a ring closing reaction, subsequent ring opening will either result in the migrating CH_2 group moving along the surface by one carbon or returning to its original position. The work presented in this chapter focuses on the ring opening and closing process which allow the migration to occur. Hence, the current calculations begin with the adjacent radical site is already present in the calculations reported here (*i.e.* no hydrogen abstraction required).

7.3.1 Migration on the $\{111\}$ surface

The migration of CH_2 groups on the diamond C$\{111\}$:H surface has been previously investigated by Larsson *et al.*[8] using a cluster approach with MP2 perturbation theory, as well as DFT calculations using a periodic slab model. In this section we report energetics calculated using our QM/MM based method for comparison.

Figure 7.2 shows the optimised initial, intermediate and final structures of the QM region returned by the current calculations as well as their relative energies calculated at the B3LYP 6-311g(d,p):MM2 level in kJ mol^{-1}. Migration was found to proceed via a strained 4-membered ring closed state that lies 28 kJ mol^{-1} lower in energy than the initial ring open state. The approximate transition state was calculated to be 22 kJ mol^{-1} higher in energy than the initial structure, somewhat lower than the 52 kJ mol^{-1} predicted in the calculations by Larsson *et al.*[8]

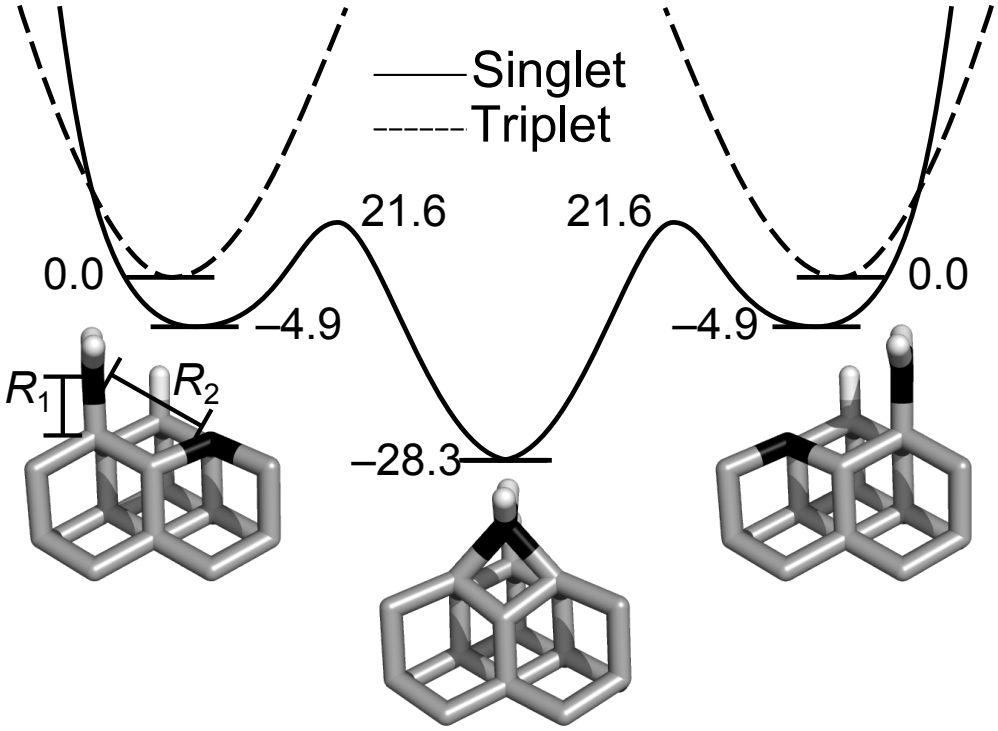

Figure 7.2: Optimised initial, intermediate and final QM structures for the migration of CH_2 on the C$\{111\}$:H surface from the QM/MM calculations. The relative QM/MM B3LYP/6-311G(d,p):MM2 energies (kJ mol^{-1}) are defined relative to that of the initial structure. R_1 and R_2 shown on the initial structure are the bond lengths used to define the reaction coordinate, q. The crossing between the triplet and singlet potential energy surfaces is also highlighted.

Compared to the barrier to migration along the dimer rows or chains on the C$\{100\}$:H 2×1 surface

(104.5 and 145 kJ mol^{-1}, respectively[7]), migration on the C{111}:H surface is likely to be a much more facile process due to its low energy barriers and the relatively unstable intermediate ring closed structure.

The initial and final biradical species in this migration pathway are both triplets, whilst the intermediate 4-membered ring is a closed shell singlet. The migration process will hence involve two changes between triplet and singlet spin-states. The optimized singlet and triplet structures at the initial geometries lie very close in energy. As the intermediate 4-membered ring will only form on the singlet potential energy surface (PES), the rate at which the spin states are able to interchange will be important in determining the migration rate. For similar types of reaction involving changes between singlet and triplet spin states Cheesman *et al.*[7] have argued that, due to the near degeneracy of the triplet and singlet states (which results in a minimum energy crossing point (MECP) lying close to the triplet minimum), the spin-state changes should occur on the nanosecond time scale.

Separate calculations performed by Prof. J. N. Harvey on a cluster corresponding to the QM region utilised in the QM/MM calculations (with capping H atoms included) have explored the spin state changes involved in this migration in greater detail. Optimised structures with energies very similar to those of the QM/MM approach were obtained. The open-shell singlet was found to lie 10.5 kJ mol^{-1} lower in energy than the triplet diradical. The MECP between the singlet and triplet PESs was found to lie $\approx$2 kJ mol^{-1} above the triplet diradical minimum. At the substrate temperatures involved in CVD diamond growth (around 1000 K) the interconversion between the two spin states is expected to be rapid. This rapid interchange of spins states will allow the reaction to proceed quickly on whichever PES has the lowest energy barrier, and it is assumed that this effect is in operation on all the pathways discussed subsequently in this chapter.

7.3.2 Migration between different surfaces

As illustrated in Figure 7.1, two types of step edge exist at the intersection of C{111}:H and C{100}:H 2×1 surfaces, these are referred to as convex and concave. Each of these surfaces can be subdivided further by the orientation of the dimer bonds on the C{100}:H 2×1 surface (perpendicular or parallel to the step edge).

7.3.2.1 Convex step edge

As stated above, migration from the C{100}:H 2×1 to the C{111}:H surfaces via the convex step can occur via two separate pathways dependent on the orientation of the dimer bonds. First consider the case where the dimer bonds lie perpendicular to the convex step edge. The minimum energy pathway for this process is illustrated in Figure 7.3 a). The migration proceeds via a 4-membered ring intermediate which lies 150 kJ mol^{-1} in energy above the initial ring open structure. The high energy of the intermediate is possibly a result of the induced strain causing a distortion of the dimer bond on the upper C{100}:H 2×1 terrace away from its optimum position. This can be observed in the QM regions shown in Figure 7.3 a). The final structure, with the CH_2 group fully migrated on to the C{111}:H surface was calculated to lie 28 kJ mol^{-1} in energy above the initial structure. Energies have also been calculated for approximate TSs states associated with the ring closing and opening steps, these were found to be at $E = +167$ kJ mol^{-1} and $+153$ kJ mol^{-1}, respectively.

Figure 7.3b shows the minimum energy pathway for migration of a pendant CH_2 group from the C{100}:H 2×1 to the C{111}:H surface when the dimer bonds on the former surface are parallel to the convex step edge. The migration pathway was found to involve movement through a 3-membered ring intermediate structure. The intermediate structure was found to be 139 kJ mol^{-1} lower in energy than the initial diradical structure. The final diradical structure with the CH_2 group located on the C{111}:H surface was found to lie 30 kJ mol^{-1} above the initial diradical structure. The 3-membered ring intermediate structure is thus significantly more favourable than the equivalent 4-membered ring structure observed when the dimer bonds are perpendicular to the convex step edge. The exothermicity is still, nevertheless, small compared to the energy normally associated with the formation of a C-C bond, highlighting the strained nature of the intermediate ring structure. Approximate TSs associated with the ring closing and ring opening steps were found for this case to be located at $E = +26$ and $+31$ kJ mol^{-1}, respectively.

In the first migration pathway (Figure 7.3a) the rate limiting step is the formation of the strained 4-membered ring whereas, in the second pathway (Figure 7.3b) it is likely to be the ring opening step. The relative rates of the two pathways will depend upon how efficiently energy associated with the formation of the 3-membered ring-closed structure in the second pathway is dissipated into the bulk. If the energy is efficiently dissipated (the least favourable circumstance) the barrier to forming the full migrated structure will be comparable to that of the first pathway.

For both pathways the barriers involved were found to be larger than those associated with migration on the C{100}:H 2×1 surface and much higher than migration on the C{111}:H surface. Yet

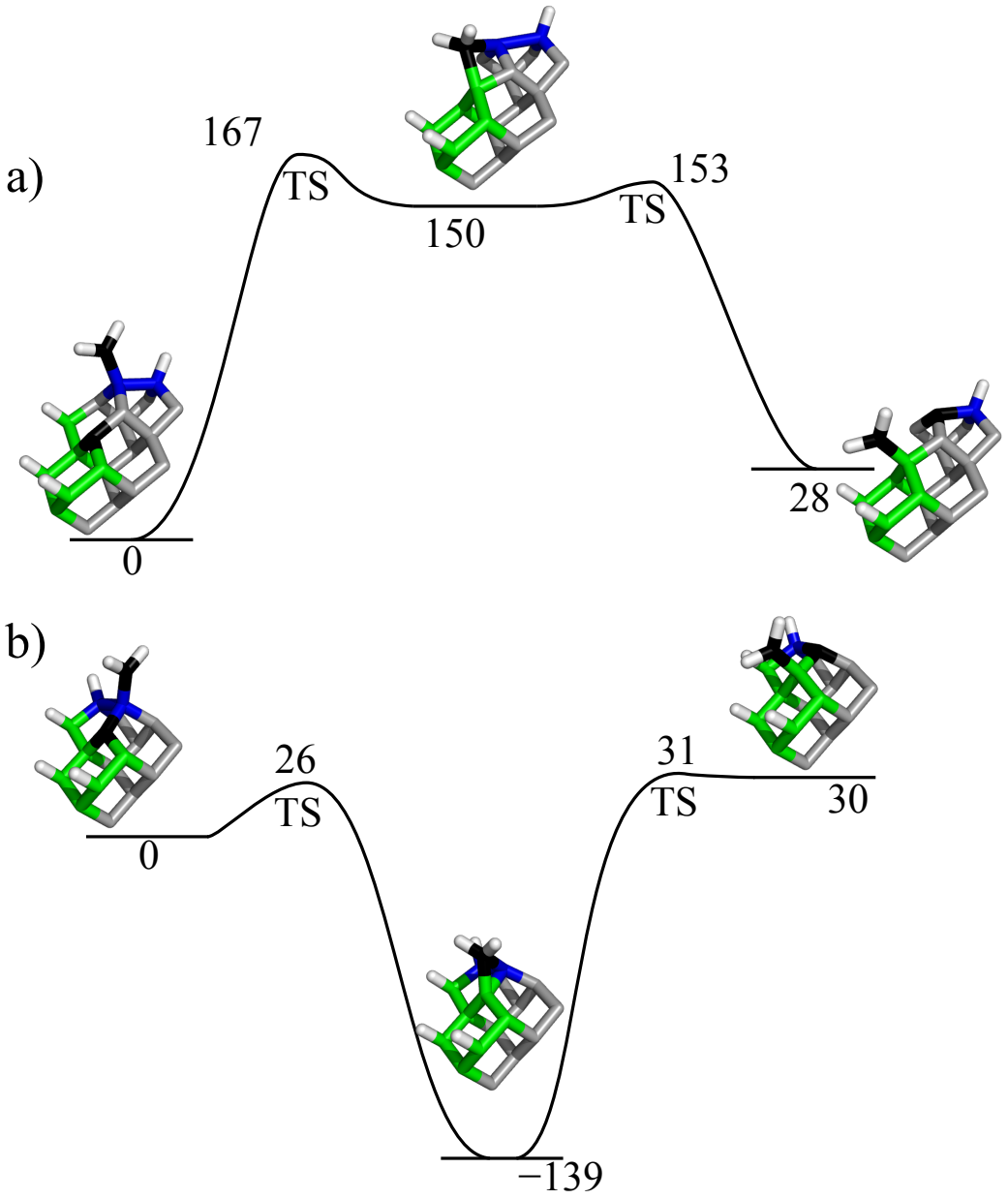

Figure 7.3: Calculated minimum energy profiles for the migration of a surface CH_2 group from the C{100}:H 2×1 surface to the C{111}:H surface via a convex step edge where the dimer bonds are oriented either: a) perpendicular or b) parallel to the step edge. Depictions of the optimised QM regions returned by the QM/MM calculations for the initial, intermediate and final structures are included. Carbon atoms on the C{100}:H 2×1 surface are highlighted in blue whilst those on the C{111}:H are in green. The migrating group and the adjacent surface radical are shown in black. The energies (in kJ mol^{-1}) are from B3LYP/6-311g(d,p):MM2 calculations and defined relative to the initial structure.

at the substrate temperatures involved in most diamond CVD neither of these barriers will be prohibitive.

7.3.2.2 Concave step edge

As already observed for migration over the convex step edge, a number of different migration pathways can be identified depending on the alignment of the dimer bonds on the C{100}:H 2×1 surface. On the concave step edge this results in three different pathways. One migration pathway (P1) from the C{111}:H to the C{100}:H 2×1 is identified when the dimer bonds are perpendicular to the step edge. When the dimer bonds are parallel to the concave step edge, two migration pathways from the C{111}:H to the C{100}:H 2×1 surface can be identified. These are characterized by the initial location of the CH_2 group on the C{111}:H surface, which as discussed previously can either be facing a trough between the dimers or facing directly towards the middle of a dimer bond the C{100}:H 2×1 surface. These two pathways are termed P2 and P3, respectively.

Optimized geometries and energies for the initial structures (migrating CH_2 group on the C{111}:H surface), intermediate ring closed structure and final structure (CH_2 group on the C{100}:H 2×1 surface) for each of the three pathways (P1-P3) have been calculated. All were found to be exothermic with the final ring-open structures lying at $E = -99$, -34 and -60 kJ mol^{-1} for P1, P2 and P3, respectively. The intermediates for pathways P2 and P3 were found to be 5-membered rings with energies of $E = -116$ and -165 kJ mol^{-1}, respectively, relative to their starting structures. Pathway P1 proceeds via a 6-membered ring intermediate with an relative energy of $E = -356$ kJ mol^{-1}. Minimum energy profiles for pathways P1-P3 are shown in Figure 7.4. Approximate TSs could not be located for any of the ring-closing or ring opening steps. However, the pathways are relatively similar to the case seen above (Section 7.3.2.1) for the convex step edge when the dimer bonds are parallel to the step edge, it is consequently predicted that there will be little or no energy barrier to forming the intermediate structures.

From these energetic profiles, it can be assumed that migration of a pendant CH_2 group from the C{111}:H surface to the C{100}:H 2×1 surface of diamond and vice versa, via either pathway P2 or P3 will likely be a relatively facile process under standard CVD conditions, with the ring opening step being rate limiting. The deep well associated with the minimum energy profile for pathway P1, however, indicates that once this 6-membered ring bridging structure is formed during the migration process the CH_2 is likely to be 'trapped' in place (*i.e.* incorporated into the diamond lattice at the step edge). This reinforces the earlier conclusions of Frenklach *et al.*[6]

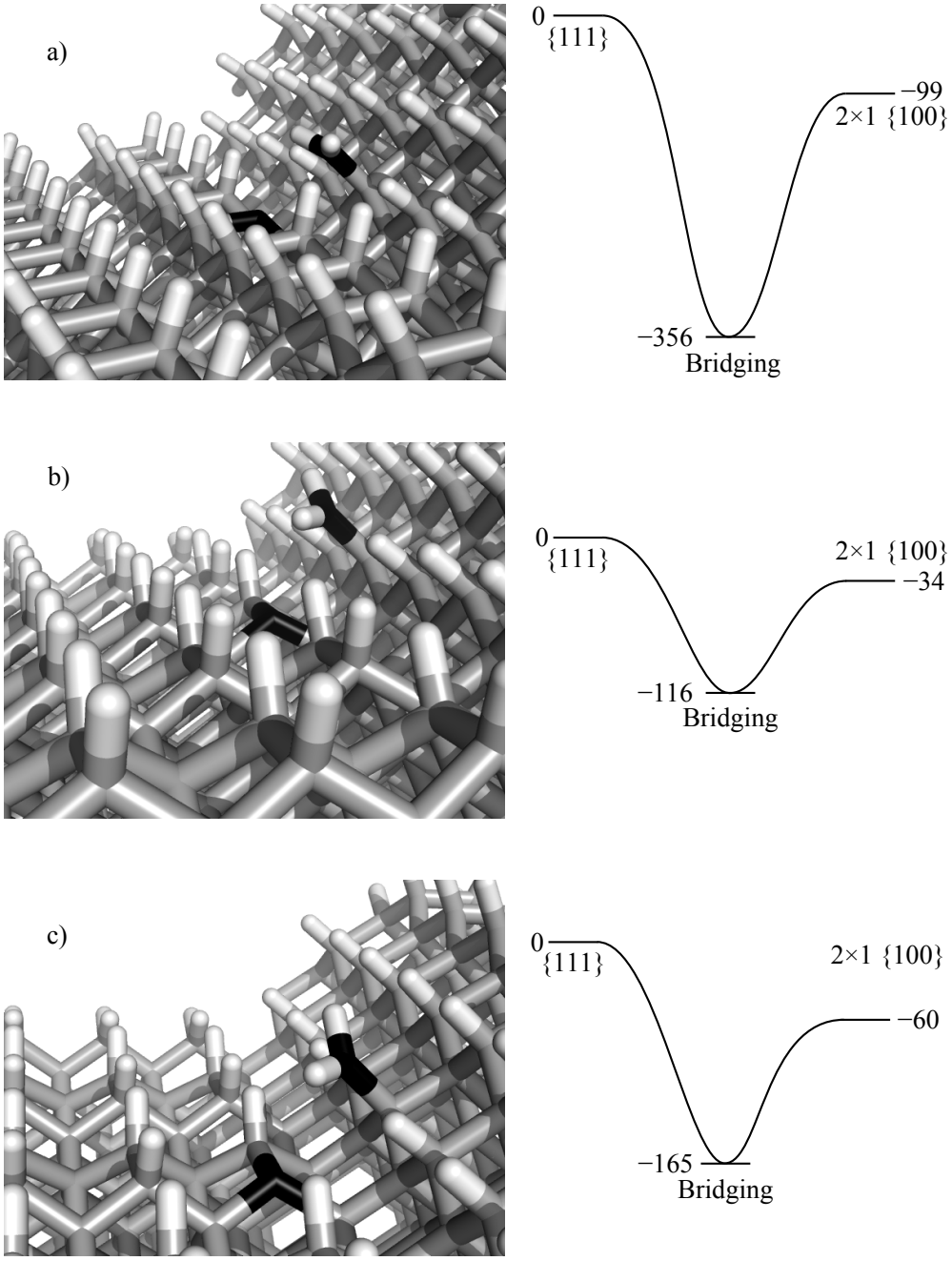

Figure 7.4: Calculated minimum energy profiles for CH_2 migration from the C{111}:H surface to the C{100}:H 2×1 surface via a concave step edge. P1: dimer bonds on the C{100}:H 2×1 surface are perpendicular to the step edge (a); P2 and P3: dimer bonds are parallel to the step edge, starting structures with the CH_2 group facing the trough in between two dimer bonds and the centre of a dimer bond, are shown in b) and c), respectively. The migrating CH_2 group and the adjacent surface radical are highlighted in black. The energies (in kJ mol^{-1}) reported are from B3LYP/6-311g(d,p):MM2 calculations, defined relative to the initial structure in its triplet electronic state.

7.3.3 Conclusions

A number of previous studies have concentrated on the migration of a pendant CH_2 group on the C{100}:H 2×1[5–7] and the C{111}:H[8] diamond surface. In this chapter we reinvestigated the migration on the C{111}:H surface using our QM/MM computational method, and extended the study of surface migrations to include migrations between the C{100}:H 2×1 and the C{111}:H surface. A total of five different pathways for migration were identified between the two surfaces at two different types of step edge (convex and concave, see Figure 7.1); two for the convex step edge and three for the concave step edge. Barriers associated with migration were generally small. The rate of the migration process will thus most likely be limited by the activation of the migrating group and the creation of an adjacent radical site, governed by the H atom flux to the surface from the gas phase. An exception to this is the pathway identified as P1 on the concave step edge. Assuming that the exogercitiy of the ring-closing process is dissipated to the bulk diamond lattice efficiently, once the 6-membered ring structure is formed the CH_2 group will likely be "locked" in place *i.e.* it forms part of the diamond crystal lattice. This result agrees well with earlier work of Frenklach *et al.*[6] and leads to the growth of a new diamond monolayer from the step edge.

References

[1] J. C. Richley, J. N. Harvey, and M. N. R. Ashfold, *Mater. Res. Soc. Symp. Proc.* **1203**, 1203 (2010).

[2] K. Bobrov, A. Mayne, G. Comtet, G. Dujardin, L. Hellner, and A. Hoffman, *Physical Review B* **68**, 195416 (2003).

[3] B. B. Pate, *Surf. Sci.* **165**, 83 (1986).

[4] W. J. P. van Enckevort, G. Janssen, W. Vollenberg, J. J. Schermer, and L. J. Giling, *Diamond Relat. Mater.* **2**, 997 (1993).

[5] M. Frenklach and S. Skokov, *J. Phys. Chem. B* **101**, 3025 (1997).

[6] M. Frenklach, S. Skokov, and B. Weiner, *Nature* **372**, 535 (1994).

[7] A. Cheesman, J. N. Harvey, and M. N. R. Ashfold, *J. Phys. Chem. A* **112**, 11436 (2008).

[8] K. Larsson and J. O. Carlsson, *Phys. Rev. B: Condens. Matter* **59**, 8315 (1999).

[9] P. W. May, J. N. Harvey, N. L. Allan, J. C. Richley, and Yu. A. Mankelevich, in *Diamond Electronics and Bioelectronics - Fundamentals to Applications III*, edited by P. Bergonzo, J. E. Butler, and R. B. Jackman, volume 1203, pages J16–02 (Mater. Res. Soc. Symp. Proc., Warrendale, PA, 2010).

[10] M. Eckert, E. Neyts, and A. Bogaerts, *Cryst. Growth Des.* **10**, 4123 (2010).

[11] J. N. Harvey, *Faraday Discuss.* **127**, 165 (2004).

[12] A. C. Tsipis, A. G. Orpen, and J. N. Harvey, *Dalton Trans.* (2005).

8

Computational study on the insertion of BH radicals and B atoms into bonds on the diamond surface and the migration of surface BH groups on and between the {100} and {111} diamond surfaces

8.1 Introduction

The addition of boron containing species (such as B_2H_6) to the gas phase during CVD of diamond, followed by subsequent incorporation into the diamond lattice, is the most common method for the creation of p-type semiconducting diamond. Modelling of the gas phase chemistry of boron containing plasmas in both HF[1] and MWPE[2] CVD reactors used for the deposition of diamond films has shown that B atoms are the most abundant of the BH_x species near the substrate, followed by BH_3, BH and finally BH_2.

Recent work by Cheesman *et al.*[3] has studied the addition of various gaseous BH_x radical species to the H-terminated 2×1 reconstructed {100} surface (C{100}:H 2×1) and their subsequent incorporation via a mechanism (Figure 8.1) similar to that suggested for the incorporation of CH_3 from the gas phase (see Chapter 1.2.4). As with the addition of CH_3 to the diamond surface, a surface radical site is first needed for the addition of any of the BH_x species. This addition is followed by a series of hydrogen abstraction reactions and rearrangement results in the boron atom being incorporated into a C-C dimer bond on the C{100}:H 2×1 surface and hence the diamond crystal lattice.

In Chapter 6 the insertion of a selection of C_xH_y species directly into C-H and C-C bonds on the diamond surface were investigated. Both B(^{2}P) atoms and BH($X^1\Sigma^+$) radicals exhibit similar orbital configurations to the carbon containing species which were found to insert directly into C-H bonds *i.e.* they both have an occupied donor orbital and an empty acceptor orbital. The insertion of B

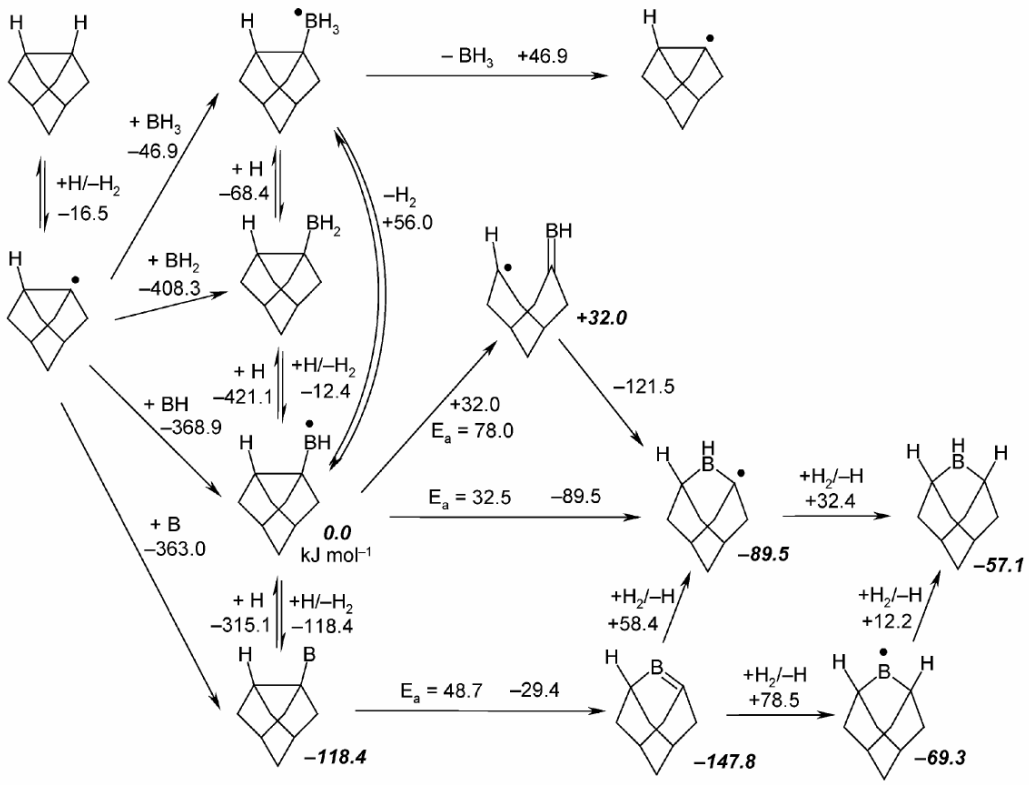

Figure 8.1: Reaction pathways for both the addition of various BH_x species and their incorporation into the diamond C{100}:H 2×1 surface. Calculated energetics are in kJ mol^{-1}. Figure reproduced from Cheesman *et al.* [3]

atoms into methane has previously been studied using ab initio techniques[4,5] and by a number of experiments summarised in Balucani *et al.*[6]. A number of experiments have also looked at the possibility of BH insertion[7,8].

Migration of surface CH_2 groups across C{100}:H 2×1[9–11], C{111}:H[12] and at the intersection of C{111} and C{100}:H 2×1 surfaces (see Chapter 7) have been previously studied in detail. In contrast, the possibility of boron containing species migrating on the growing diamond surface has hitherto, not received any attention.

The first half of this chapter thus focuses on calculating the energetics associated with B atom and BH radical insertion directly into C-H and C-C bonds on the C{100}:H 2×1 surface and how they may impact on the incorporation of B atoms into the surface. The second half of this chapter looks at the possibility of a BH surface group migrating along the diamond surface, and how the migration compares with that of CH_2 groups.

8.2 Computational detail

As with the work in previous chapters studying C_xH_y insertion and CH_2 migration, a combination of QM and QM/MM calculations have been used. For calculations on the insertion of B atoms and BH radicals into the C-C and C-H bonds of the C$\{100\}$:H 2×1 surface a small C_9H_{14} cluster was used to simulate the surface bond in the QM calculations. The QM/MM calculations used a similar C_9 based cluster within a large MM region, the structure of the QM/MM cluster is shown in Chapter 6 (Figure 6.3a). Further detail on the QM and QM/MM calculations involved can be found in Chapter 6. Reaction coordinates used in the QM/MM calculations for the insertion of B and BH were of the same form as those used in the QM/MM calculations on insertion of CH_x species, and the approximate transition states generated are the point of highest energy recorded as the value of the reaction coordinate is varied.

Calculations on the migration of BH surface groups on the C$\{100\}$:H 2×1 surface were carried out using a QM/MM cluster similar to that used to study the insertion reactions, though the QM region was extended so that it also included the next dimer bond along either the dimer chain (Figure 8.2a) or the dimer row (Figure 8.2b).

Details of the calculations studying the migration of BH on the C$\{111\}$:H surface and between the C$\{100\}$:H 2×1 and the C$\{111\}$:H surfaces are identical to those described in Chapter 7, albeit with the CH_2 group replaced by BH.

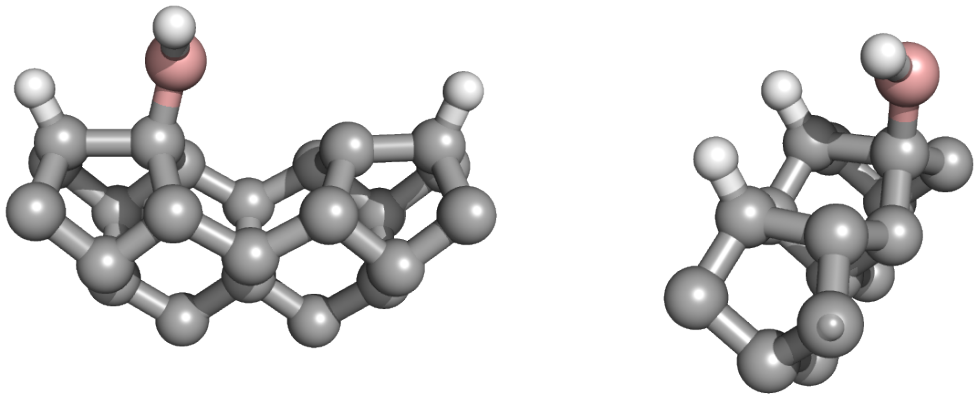

(a) (b)

Figure 8.2: QM regions (with link atoms removed) used within the QM/MM calculations to study migration of pendant BH groups along the dimer chains (a) or dimer rows (b) present on the C$\{100\}$:H 2×1 surface.

For these migration pathways also, approximate transition states were located by plotting the calcu-

lated QM/MM energy at points along a given reaction coordinate, with the maximal value taken to be that of the transition state. Example reaction coordinates for both the insertion reactions and surface migration are shown in Chapters 6 and 7, respectively.

QM calculations on the insertion of B(^{2}P) atoms and BH($X^1\Sigma^+$) radicals into C-H and C-C bonds are performed at the B3LYP/6-311g(d,p)//B3LYP/6-31g(d) level of theory and include zero point correction (ZPC) calculated at the B3LYP/6-31g(d) level unless otherwise stated. Analogous QM/MM calculations are comprised of B3LYP/6-311g(d,p) single point energies calculated on the QM region optimised at the B3LYP/6-31g(d) level with MM2 energies from the molecular mechanics region. A zero-point correction is also included and derived from the QM calculations. QM/MM calculations for the migration of BH radicals are at the same level of theory as those detailed for the insertion calculations, but lack the zero point correction. All energies presented are in kJ mol^{-1}.

8.3 Results and discussion

8.3.1 B and BH insertion

The insertion of both B(^{2}P) atoms and BH($X^1\Sigma^+$) radicals into both C-H and C-C bonds on the diamond C$\{100\}$:H 2×1 surface were investigated using QM calculations on a small C_9H_{14} cluster and by QM/MM calculations. Insertion of BH radicals and B atoms directly into one of the surface C-H bonds and the C-C dimer bond were investigated on the C$\{100\}$:H 2×1 surface, in contrast to the calculations reported in Chapter 6 on C_yH_x insertion where a number of different C-H and C-C bonds were investigated. This strategy was chosen since, in the case of the CH_x ($x = 0 - 2$) insertion, the type of surface C-H or C-C bond being attacked made little difference to the energy barriers involved. The calculations on atomic boron and BH radical insertion thus focus on just the C-H surface bond (shown in Figure 8.3a) and the C-C dimer bond (Figure 8.3b) which will be the most common surface bonds observed during typical H_2-rich diamond CVD on the C$\{100\}$:H 2×1 surface. Energetics presented in this section are defined relative to the reactants, *i.e.* the energy of the C_9H_{14} cluster combined with that of either a B atom or BH radical.

8.3.1.1 C-H bonds

The insertion of B(^{2}P) atoms directly into a C-H bond of methane has previously been investigated by Fang *et al.*[5]. It was found that the insertion proceeded via a transition state 87.4 kJ mol^{-1} higher in

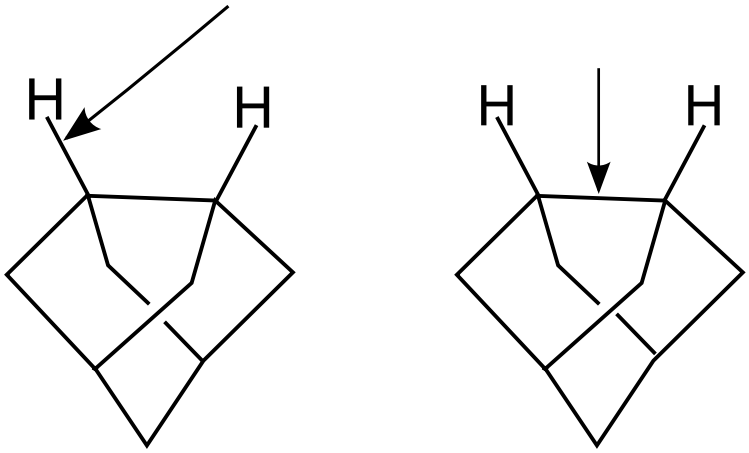

(a) (b)

Figure 8.3: (a) The C-H bond and (b) the C-C bond investigated for insertion of B and BH.

energy than the reactants (calculated at the QCISD(T)/cc-pVTZ//QCISD/6-311G(d,p) level of theory with ZPC at the QCISD/6-311g(d,p) level). The overall reaction was found to be exothermic by 220 kJ mol^{-1}. This compares well with calibration QM calculations performed in the current study, where a transition state for the insertion of B atoms into a C-H bond of methane was located 85 kJ mol^{-1} in energy above that of the reactants with the overall reaction calculated to be exothermic by 197 kJ mol^{-1}. Upon inclusion of ZPC (calculated at the B3LYP/6-31g(d) level) the energy of the transition state falls by 13 kJ mol^{-1} to 72 kJ mol^{-1} and the exothermicity is found to change by 3 kJ mol^{-1} to become 200 kJ mol^{-1}.

Insertion of B atoms into a C-H bond on the C_9H_{14} cluster was calculated to be exothermic by 257 kJ mol^{-1} and involve an activation barrier of 54 kJ mol^{-1}. The geometries of the transition state and final product of the insertion reaction are illustrated in Figure 8.4.

QM/MM calculations of this same insertion reaction at the B3LYP/6-311g(d,p):MM2 level of theory (with zero point correction derived from the analogous QM calculations on the C_9H_{14} cluster at the B3LYP/6-31g(d) level of theory) also return similar energies to those calculated in QM calculations on the small cluster. The reaction in this case was found to be exothermic by 254 kJ mol^{-1} and an approximate transition state was located 66 kJ mol^{-1} above that of the reactants.

For the case of BH ($X^1\Sigma^+$) radical insertion into a C-H bond surface bond we again start with the simpler BH + CH_4 reaction. This reaction was found to proceed via a transition state with energy E_{TS} = +40 kJ mol^{-1} relative to that of the reactants and the overall energy change, $\Delta E = -363$ kJ mol^{-1} (calculated at the B3LYP/6-311g(d,p)//B3LYP/6-31g(d) level). QM calculations on the C_9H_{14} cluster found a very similar energy profile: E_{TS} = 27 kJ mol^{-1} and $\Delta E = -347$ kJ mol^{-1}. The calculated

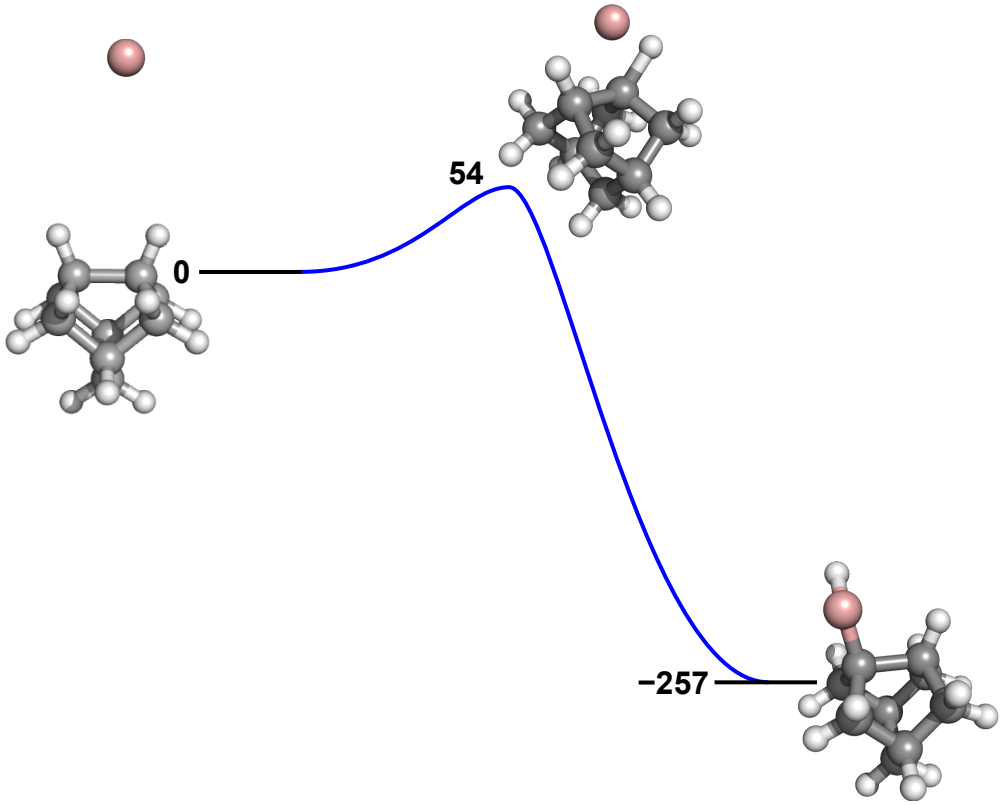

Figure 8.4: An illustration of the potential energy surface involved in the insertion of B(^{2}P) atoms into a C-H bond on the C_9H_{14} cluster. Geometries of the transition state and products shown are from calculations at the B3LYP/6-31g(d) level of theory. Energetics are from calculations at the B3LYP/6-311g(d,p)//B3LYP/6-31g(d) level and include ZPC calculated at the B3LYP/6-31g(d) level. The energies are in kJ mol^{-1} and defined relative to that of the reactants.

geometries of the transition state and product of BH insertion into a C-H bond on the C_9H_{14} cluster are shown in Figure 8.5 with an illustrated energy profile.

Analogous QM/MM calculations on the insertion of BH radicals into a surface C-H bond returned a slightly higher barrier, E_{TS} = 43 kJ mol^{-1} and and overall reaction exothermicty of $\Delta E = -330$ kJ mol^{-1}.

Values calculated by both the QM method and the QM/MM method for E_{TS} and ΔE are found to be in close agreement, though the QM/MM calculations were found to return slightly higher barriers and the reactions were typically slightly less exothermic. This is probably due to the inclusion of steric hindrance from the surrounding surface atoms restricting the orientation at which the B atoms and BH radicals can approach the surface.

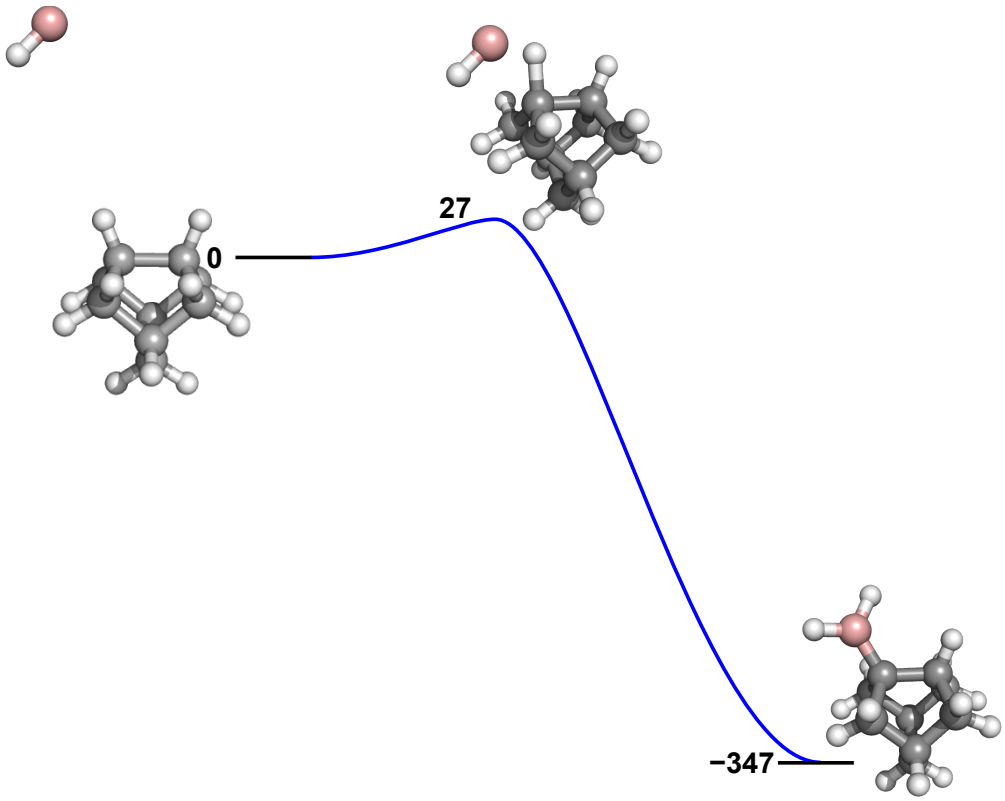

Figure 8.5: An illustration of the potential energy surface involved in the insertion of BH($X^1\Sigma^+$) radicals into a C-H bond on the C_9H_{14} cluster. Geometries of the transition state and products shown are from calculations at the B3LYP/6-31g(d) level of theory. Energetics are from calculations at the B3LYP/6-311g(d,p)//B3LYP/6-31g(d) level of theory and include ZPC calculated at the B3LYP/6-31g(d) level. The energies are in kJ mol^{-1} defined relative to the reactants.

8.3.1.2 C-C bonds

QM calculations on the insertion of B(^{2}P) atoms into a C-C bond (show in Figure 8.3b) on the C_9H_{14} cluster found, E_{TS} = 122 kJ mol^{-1} and $\Delta E = -329$ kJ mol^{-1} relative to the reactants. Structures of the TS and product are shown in Figure 8.6.

QM/MM calculations also found the reaction to be exothermic, $\Delta E = -285$ kJ mol^{-1}. An approximate transition state for the insertion reaction was not successfully located. Nevertheless the energies calculated along the reaction coordinate used to study the reaction indicate that, at the B3LYP/6-311g(d,p):MM2 level, the barrier is at least 119 kJ mol^{-1} higher in energy than the reactants.

Both QM and QM/MM calculations failed to locate transition states for the insertion of BH($X^1\Sigma^+$) radicals into the C-C dimer bond. Despite being unable to locate the TS energies calculated along the reaction coordinate in the QM/MM calculations suggest that the barrier would be at least 350 kJ mol^{-1}.

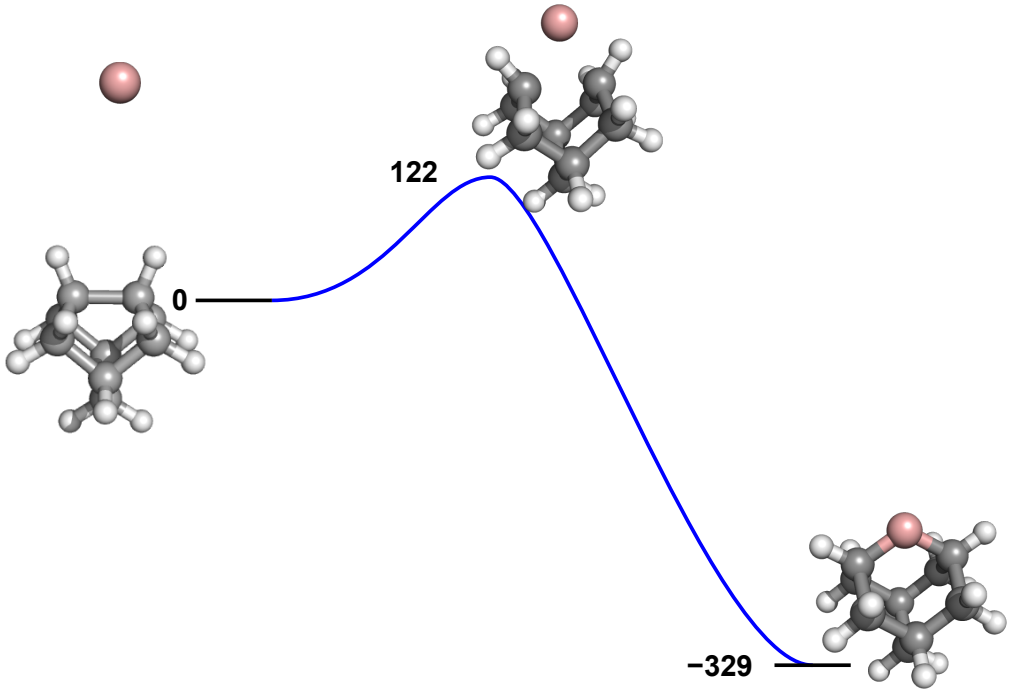

Figure 8.6: An illustration of the potential energy surface involved in the insertion of B (^{2}P) atoms into a C-C dimer bonds on the C_9H_{14} cluster. Geometries of the transition state and products shown are from calculations at the B3LYP/6-31g(d) level of theory. Energetics are at the B3LYP/6-311g(d,p)//B3LYP/6-31g(d) level of theory and include ZPC calculated at the B3LYP/6-31g(d) level. Energies are in kJ mol^{-1} and are defined relative to the reactants.

8.3.1.3 Implications for CVD growth of boron doped diamonds

The energetics calculated for both the insertion of B (^{2}P) atoms and BH ($X^1\Sigma^+$) radicals showed a similar trend to that seen for the insertion reactions of CH_x (x = 0-2) radicals in Chapter 6. As in that case, insertion into a C-H bond was found to be much more energetically favourable than insertion into a C-C bond. This leads us to a similar conclusion as for CH_x insertion: insertion of B atoms and BH radicals into C-C bonds is not likely to play a significant role in diamond CVD.

Insertion of both B atoms and BH radicals into C-H bonds, however, are much more probable processes with activation barriers of 66 and 43 kJ mol^{-1}, respectively. Whilst not as favourable as the insertion of CH_x (x = 0-2) species, B atoms and BH radicals make up a large proportion of the BH_x species[2] present within the plasma and are widely distributed across the plasma volume (see Chapter 4). This is in contrast to those CH_x species found to directly insert into C-H bonds, which are largely located in the hotter plasma regions and make up only $\approx 0.9\%$ of the total C_1 species just above the growing diamond surface (under typical MCD conditions, see table 6.1). This insertion route for B atoms and BH radicals may therefore serve as an important route contributing to the addition of

B atoms onto the growing diamond surface, since it enables addition to all surface C atoms rather than just the surface radical sites (which only make up $\approx 10\%$ of the surface under standard CVD conditions).

8.3.2 BH surface migration

The migration of CH_2 groups on diamond has been studied in a large amount of detail. A surface bound BH group is likely to react in a similar way to a surface bound CH_2 group, as they both have a single unpaired electron which is able to react with an adjacent surface radical. In contrast to CH_2 migration, the possibility of BH groups migrating has not received any attention. This half of the chapter focuses on the computational study of surface bound BH groups migrating on the C$\{100\}$:H 2×1 and C$\{111\}$:H surfaces and between these two surfaces at step edges. As with migration of CH_2 groups on the diamond surface, an adjacent surface radical site is required for the process to proceed. This site would typically be created by the removal of surface H atoms by a gas phase species (usually H atoms). In the current study this process is already assumed to have occurred and the adjacent surface radical is already present. The calculations presented are hence focused just on the steps (ring opening and closing) that result in movement of BH groups along the surface. As seen previously for CH_2 migration (Chapter 7), the initial and final structures in the migration pathways investigated will contain two unpaired electrons, whilst the intermediate ring-closed structure will be closed-shell systems. Thus the initial and final structures will be expected to possess a triplet electronic configuration, while the intermediate ring-closed structure will be expected to have a singlet electronic configuration. The presented energetics associated with BH migration are defined relative to the initial structure in its triplet electronic configuration.

8.3.2.1 C$\{100\}$:H 2×1 surface

As in the case of CH_2 migration,[11] migration of BH groups on the C$\{100\}$:H 2×1 surface can occur via two processes, migration along the chains of dimer bonds or along the rows of dimer bonds. The current QM/MM calculations start with a BH group pre-incorporated into a dimer bond (see the initial QM structures shown in Figures 8.7 and 8.8). Both migration along the dimer chains and the rows in the current calculations start with creation of a surface BH group and reformation of the C-C dimer bond (transition from structures 1-2 in Figures 8.7 and 8.8). This step was found to occur in a single reaction involving the concerted breaking of a B-C bond and reformation of the dimer bond. This is in marked contrast to the migration of CH_2, where the equivalent process occurs in two steps:

First the breaking of a C-C bond to the incorporated CH_2 and formation of a doubly bonded C=CH_2 group and, secondly, the recreation of the dimer bond and formation of the surface CH_2 group, with both processes involving an activation barrier (see Chapter 1.2.4.5).

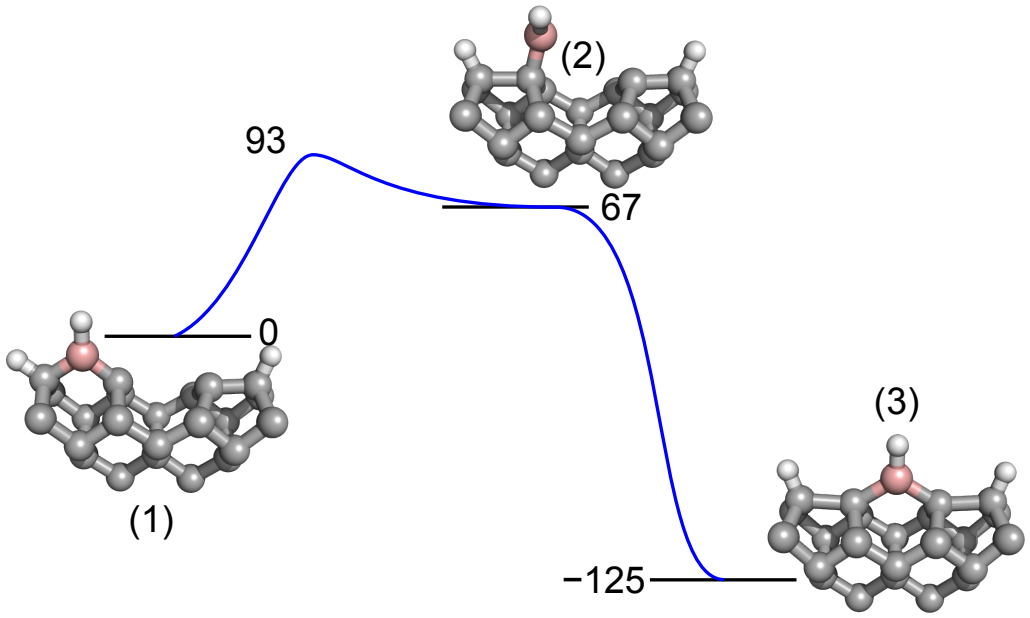

Figure 8.7: BH migration profiles along the dimer chains on the C{100}:H 2×1 surface, with optimised geometries of the QM region within the QM/MM calculations shown. Energies are in kJ mol^{-1} and are defined relative to the initial pre-incorporated structure in its triplet electronic state.

For migration along dimer chains and dimer rows the initial step of forming a pendant BH group was found to be endothermic by 67 and 70 kJ mol^{-1}, and involve barriers of +93 and +104 kJ mol^{-1}, respectively. This is essentially the same process for both pathways and the difference in calculated energies will likely be due to the slightly different clusters used within the calculations. The energies calculated here also compare well with the earlier QM cluster calculations of Cheesman *et al.* [3] on the incorporation of BH radicals into the diamond surface, where ΔE and E_{TS} for the same reaction were found to be +89.5 and +122 kJ mol^{-1}, respectively, at the B3LYP/6-311+g(2df,p)//B3LYP/6-31(g) level of theory.

After the initial step, a ring-closing reaction between the newly formed pendant BH group and the adjacent surface radical, followed by a subsequent ring-opening results in either the migration of the BH group one additional atom along the surface or its reversion to the original geometry. The ring-closing was found to be an exothermic process for both migration along the dimer chains and dimer rows, $\Delta E = -192$ and -214 kJ mol^{-1}, respectively. The ring-closing reaction was found to be a barrierless process for migration along the dimer chains whilst a small barrier of only +4 kJ mol^{-1}

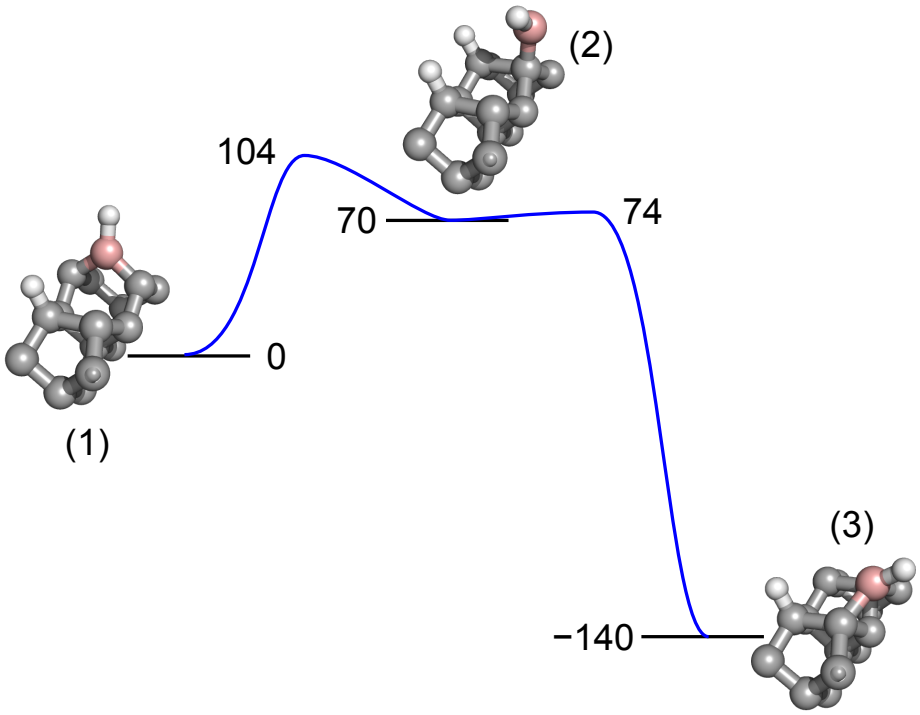

Figure 8.8: BH migration profiles along the dimer rows on the C{100}:H 2×1 surface, with the optimised geometries of the QM region within in the QM/MM calculations shown. Energies are in kJ mol^{-1} and are defined relative to the initial pre-incorporated structure in its triplet electronic state.

was calculated for migration along the dimer rows. This small barrier likely reflects the need for the BH group to rotate in order for the reaction to proceed. Energy profiles for both migration along the dimer chains and dimer rows are shown in Figures 8.7 and 8.8, respectively, along with the optimised minimum energy geometries of the QM region (without link atoms) within the QM/MM calculations along the migration pathway.

8.3.2.2 C{111}:H surface

The migration of pendant BH radicals on the C{111}:H surface used the same base QM/MM cluster as the calculations used to investigate the migration of CH_2 in Chapter 7, albeit with the CH_2 group replaced by BH.

The ring-closing process involved in the migration of BH on the C{111}:H surface was found to be barrierless with an associated exothermicity, $\Delta E = -165$ kJ mol^{-1}, defined relative to the initial ring-open structure in its triplet electronic state. An illustrated energy profile including the optimised geometries of the initial and ring-closed states is shown in Figure 8.9. Due to the symmetry of the

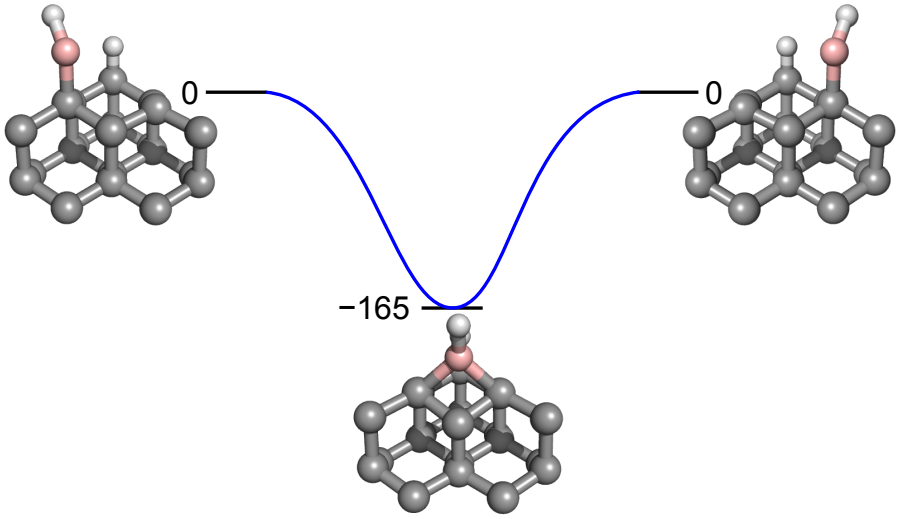

Figure 8.9: Optimised initial, intermediate and final structures of the QM region for the migration of BH on the C{111}:H surface from the QM/MM calculations. The relative QM/MM B3LYP/6-311g(d,p):MM2 energies (in kJ mol^{-1}) are defined relative to that of the initial structure.

{111} surface the initial and final geometries are mirror images of each other.

The migration of a BH group on the {111} surface compared to the equivalent migration of a CH_2 group was found to involve a significantly higher barrier (assuming that all the energy released in the reaction is quickly dissipated into the diamond bulk): 165 *vs.* 50 kJ mol^{-1}.

8.3.2.3 Migration at the step edge

In Chapter 7 it was discussed how migration of a pendant CH_2 group between the C{100}:H 2 × 1 and C{111}:H surfaces at step edges may play an important role in determining surface morphology. The ability of BH radicals to migrate between the different surfaces may be an important factor in determining the positions at which boron atoms are incorporated into the diamond crystal structure. As shown in the previous chapter on CH_2 migration, two step edges are formed by the intersection of two C{100}:H 2 × 1 terraces and a C{111}:H. These step edges were termed the convex and concave step edges, and are illustrated in Figure 7.1. As observed in the previous chapter, a number of different pathways for migration exist on both the convex and concave step edge, due to the orientation of the dimer bonds on the C{100}:H 2 × 1 surface. These can either be parallel or perpendicular to the step edge, leading to two possible pathways for migration across the convex step edge and three pathways for migration across the concave step edge. All energies in this section are defined relative to the initial triplet electronic state when the BH radical group is either located on

the C{100}:H 2×1 surface (for calculations at the convex step edge) or on the C{111}:H surface (for calculations on the at the concave step edge).

Convex step edge

When the dimer bonds are perpendicular to the step edge, the migration proceeds via a 4-membered ring intermediate whereas, when the dimer bonds are parallel to the step edge, the migration proceeds via a 3-membered ring intermediate.

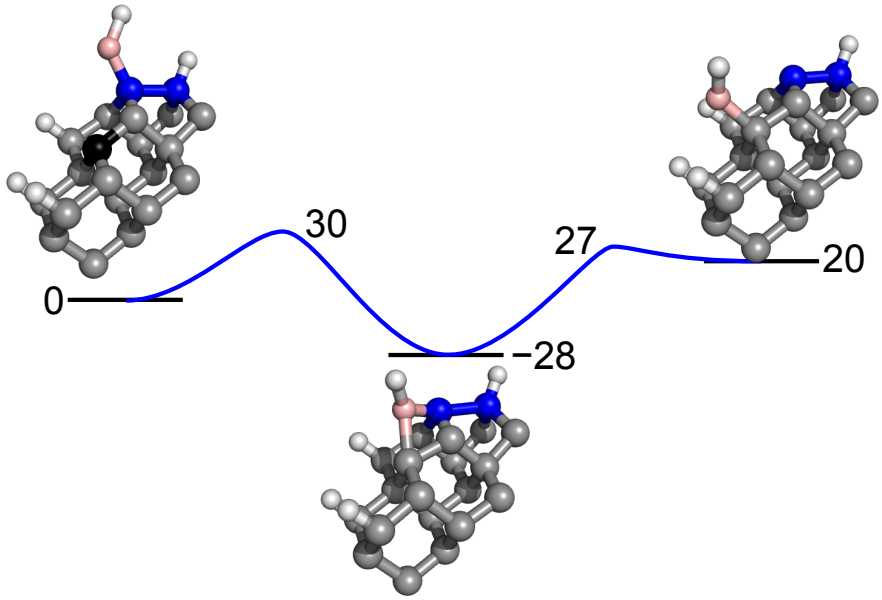

Figure 8.10: Calculated minimum energy profiles for the migration of a pendant BH group from the upper C{100}:H 2×1 surface to the C{111}:H surface via the convex step edge, when the dimer bonds are oriented perpendicular to the step edge. Depictions of the optimised QM regions returned by the QM/MM calculations for the initial, intermediate and final structures are included. Carbon atoms in a dimer bond on the C{100}:H 2×1 surface are highlighted in blue, the migrating group BH group is shown in pink and the adjacent surface radical is shown in black (on the initial structure). The energies (in kJ mol^{-1}) are from B3LYP/6-311g(d,p):MM2 calculations and defined relative to the initial structure.

With the dimer bonds perpendicular to the step edge, the formation of the 4-membered ring intermediate was found to be exothermic (ΔE = -28 kJ mol^{-1}). Formation of this ring-closed state was found to involve a small energy barrier, E_{TS} = 30 kJ mol^{-1}, defined relative to the energy of the initial structure. The final structure, formed once the BH radical has fully migrated to the {111} surface was found to be 20 kJ mol^{-1} higher in energy than that of the initial structure. A barrier associated with the ring-opening step was also located 27 kJ mol^{-1} in energy above the starting structure. A minimum energy profile for this pathway is shown in Figure 8.10, along with depictions of the optimised

initial, intermediate and final geometries of the QM region.

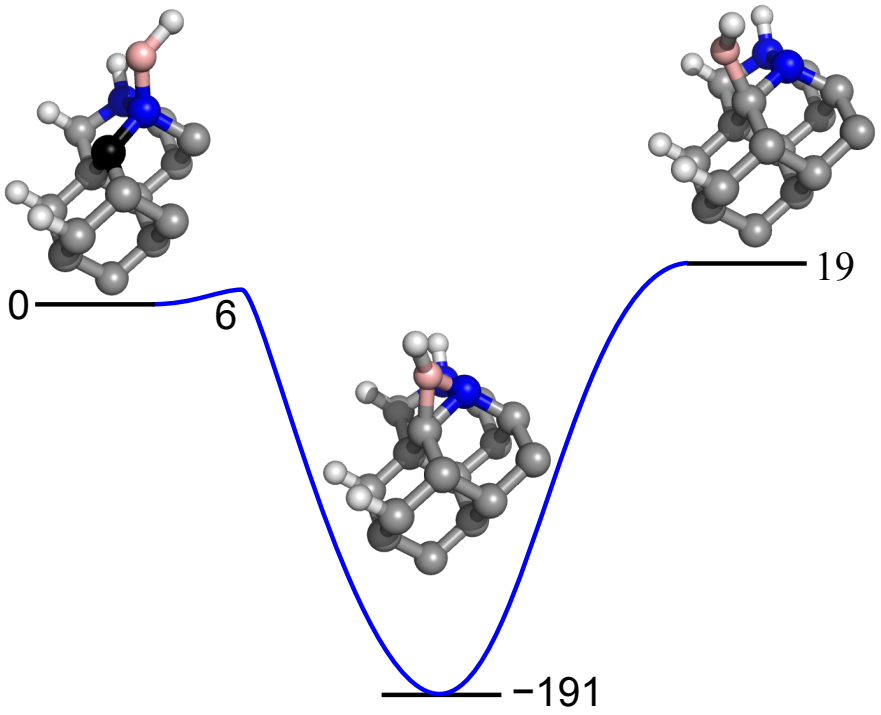

Figure 8.11: Calculated minimum energy profiles for the migration of a pendant BH group from the upper C{100}:H 2 × 1 surface to the C{111}:H surface via a convex step edge where the dimer bonds are oriented parallel to the step edge. Depictions of the optimised QM regions returned by the QM/MM calculations for the initial, intermediate and final structures are included. Carbon atoms in a dimer bond on the C{100}:H 2 × 1 surface are highlighted in blue, the migrating group BH group is shown in pink and the adjacent surface radical is shown in black (on the initial structure). The energies (in kJ mol^{-1}) are from B3LYP/6-311g(d,p):MM2 calculations and defined relative to the initial structure.

When the dimer bonds are parallel to the step edge, the 3-membered ring-closed intermediate structure was found to lie 191 kJ mol^{-1} in energy below that of the initial structure. The overall migration process was calculated to be endothermic, ΔE = +19 kJ mol^{-1}, indicating that the BH radical is slightly less stable on the C{111}:H surface. A small barrier associated with the ring-closing step was located 6 kJ mol^{-1} higher in energy than the initial structure. The subsequent ring-opening step was found not to involve any additional energetic barrier on top of the energy needed to escape from the well associated with the ring-closed state (210 kJ mol^{-1}). The minimum energy pathway for migration from the upper C{100}:H 2 × 1 to the C{111}:H surface along with optimised geometries of the QM region for the initial, intermediate and final structures is shown in Figure 8.11.

There is a stark difference between the energetics associated with the 4-membered ring intermediate when the dimer bonds are perpendicular to the step edge and the 3-membered ring intermediate

when they are parallel. A similar phenomenon is seen for CH_2 migration over this step edge. The 4-membered ring intermediate involving BH is, however, significantly lower in energy than the equivalent structure involving CH_2, $\Delta E = -28$ kJ mol^{-1} for BH *vs.* $+150$ kJ mol^{-1} for CH_2.

In both pathways for BH migration on the convex step edge the rate determining step is likely to be the ring-opening reaction. Assuming that all the energy produced from the ring-closing reaction is quickly dissipated into the bulk of the crystal. This leads to barriers for the ring-opening reaction of 55 and 210 kJ mol^{-1} for the perpendicular and parallel pathways respectively. An idea of the rate constants (k) of the two pathways can be gathered using the Arrhenius equation (1.1).

Assuming that the pre-exponential factor, A, is of the order of a vibrational motion (1×10^{13} s^{-1}) and the temperature is 1000 K, the difference in activation energies between the two pathways results in a difference in rate constants of $\approx 10^8$, *i.e.* migration when the dimer bonds are perpendicular to the step edge is much more facile than when they are parallel to the step edge.

Concave step edge

Migration on the concave step edge can occur via one of three different pathways depending on the orientation of the dimer bonds relative to the step edge. A single pathway (P1) exists when the dimer bonds are perpendicular to the step edge and two when the dimer bonds are parallel to the step edge, where the BH group can either be facing a trough between dimer bonds (P2) or the centre of a dimer bond (P3). Optimized geometries and energies for the initial (BH group on the C$\{111\}$:H surface), and final (BH group on the C$\{100\}$:H 2×1 surface) structures and the intermediate ring-closed states for each of the three pathways were calculated (minimum energy profiles and illustrations of the initial structure used in each pathway are shown in Figure 8.12). The intermediate ring-closed structures calculated for pathways P2 and P3 were both 5-membered rings whilst the intermediate structure for pathway P1 was a 6-membered ring.

For each migration pathway, the overall reaction was found to be slightly exothermic, with the energy of the final structure relative to the initial structure calculated to be -24, -31 and -27 kJ mol^{-1} for pathways P1, P2 and P3 respectively. The formation of the intermediate ring-closed states were found to be highly exothermic with $\Delta E = -325$, -261 and -310 kJ mol^{-1} for pathways P1, P2 and P3 respectively. Approximate transition states were unable to be located for either the ring-closing or ring-opening reactions, but the present calculations indicate though that if any barriers exist they are likely to be small. Minimum energy profiles for each pathway (P1-P3) are shown in Figure 8.12 as well as an image illustrating the initial geometry used in each pathway with the migrating BH group

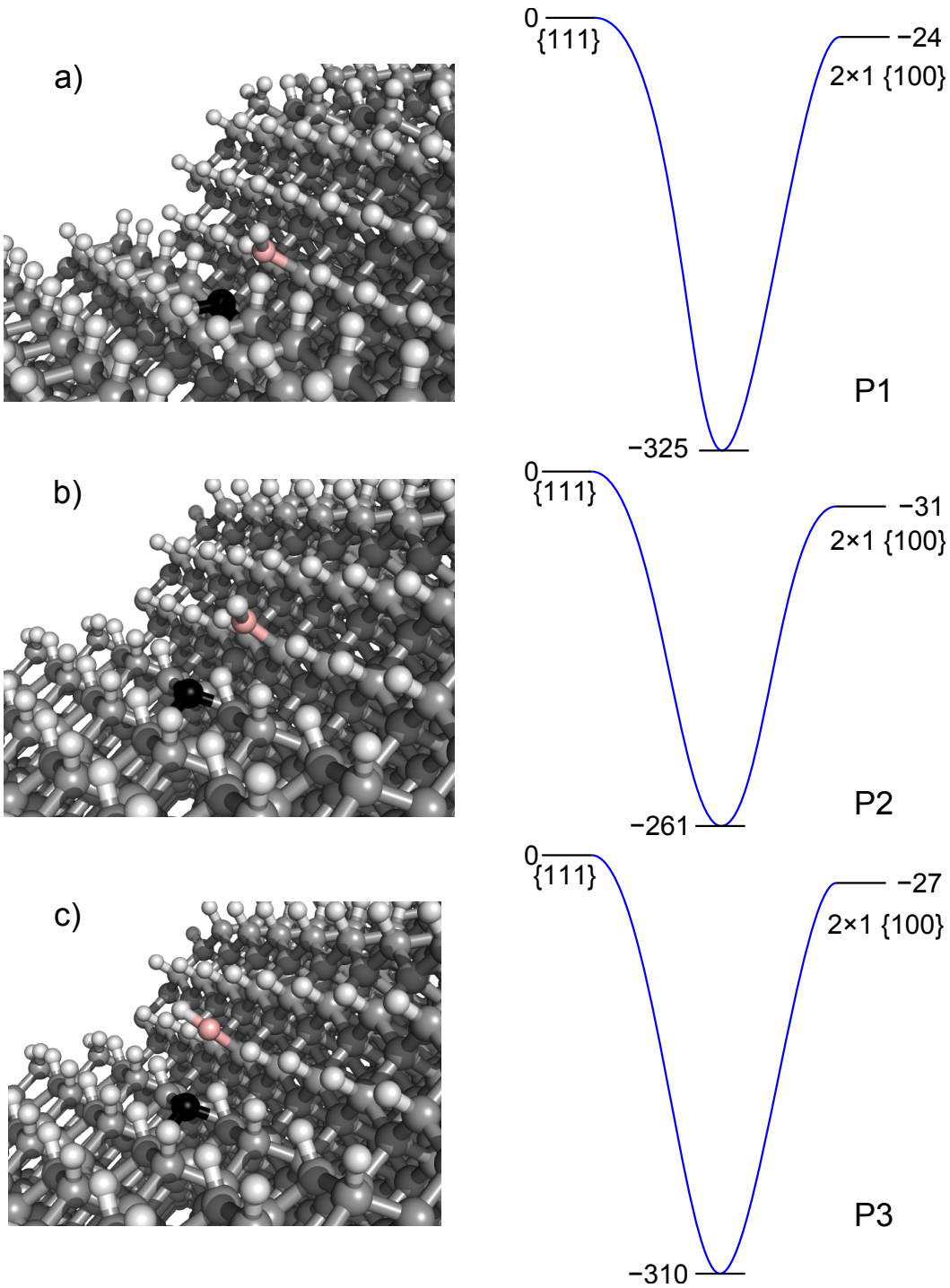

Figure 8.12: Calculated minimum energy profiles for BH migration from the C{111}:H surface to the C{100}:H 2×1 surface via a concave step edge. (a) P1: dimer bonds on the C{100}:H 2×1 surface are perpendicular to the step edge ; P2 and P3: dimer bonds are parallel to the step edge. Starting structures with the BH group facing the trough in between two dimer bonds or the centre of a dimer bond are shown in b) and c) respectively. The migrating BH group and adjacent surface radical are highlighted in pink and black, respectively. The energies (in kJ mol^{-1}) reported are from B3LYP/6-311g(d,p):MM2 calculations, defined relative to the initial structure.

and surface radical highlighted.

8.3.2.4 BH *vs.* CH_2 migration

The ring-closed intermediates involved in the migration of a pendant BH group were found to be in almost all cases more stable than the equivalent structures during CH_2 migration. If, as above, it is assumed that any reaction exoergicity is quickly dissipated into the bulk, the barriers involved in the ring-opening reactions will therefore be larger. Once these ring-closed structures are formed, BH groups will therefore be less likely than CH_2 groups to migrate any further.

These calculations also demonstrate that BH surface groups can more readily form stable structures at non-lattice positions than migrating CH_2 groups. For example, on the concave step edge, the 5-membered ring-closed states seen for pathways P2 and P3 are calculated to be much more stable (ΔE = -263 and -311 kJ mol^{-1}) than the analogous structures involved in CH_2 migration (ΔE = -116 and -165 kJ mol^{-1}).

Due to the deep energy minima in most BH migration pathways, BH incorporation into the diamond lattice, may therefore be expected to occur relatively near to the site where a gaseous B containing species adsorbs onto the surface. B incorporation at non-lattice positions (e.g. incorporation at the intermediate ring-closed state during; migration along rows on the C$\{100\}$:H 2×1 diamond surface, or at the concave step edge when the dimer bonds are parallel) within diamond may also occur due to the deep energy minima associated with these sites, suggesting that CVD grown diamond containing boron could contain more defects.

References

[1] Yu. A. Mankelevich, M. N. R. Ashfold, D. W. Comerford, J. Ma, and J. C. Richley, *Thin Solid Films* **519**, 4421 (2011).

[2] J. Ma, J. C. Richley, D. R. W. Davies, M. N. R. Ashfold, and Yu. A. Mankelevich, *J. Phys. Chem. A* **114**, 10076 (2010).

[3] A. Cheesman, J. N. Harvey, and M. N. R. Ashfold, *Phys. Chem. Chem. Phys.* **7**, 1121 (2005).

[4] Y. Hannachi, P. Hassanzadeh, and L. Andrews, *J. Phys. Chem.* **98**, 6950 (1994).

[5] W.-H. Fang and S. D. Peyerimhoff, *Mol. Phys.* **93**, 329 (1998).

[6] N. Balucani, F. Zhang, and R. I. Kaiser, *Chem. Rev.* **110**, 5107 (2010).

[7] N. L. Garland, C. T. Stanton, J. W. Fleming, A. Baronavski, and H. Nelson, *J. Phys. Chem.* **94**, 4952 (1990).

[8] J. K. Rice, N. J. Caldwell, and H. H. Nelson, *J. Phys. Chem.* **93**, 3600 (1989).

[9] M. Frenklach and S. Skokov, *J. Phys. Chem. B* **101**, 3025 (1997).

[10] M. Frenklach, S. Skokov, and B. Weiner, *Nature* **372**, 535 (1994).

[11] A. Cheesman, J. N. Harvey, and M. N. R. Ashfold, *J. Phys. Chem. A* **112**, 11436 (2008).

[12] K. Larsson and J. O. Carlsson, *Phys. Rev. B: Condens. Matter* **59**, 8315 (1999).

9

Overview

A combination of both experimental and computational techniques have been used within this thesis to explore the complicated gas phase and gas-surface chemistry which is prevalent during the chemical vapour deposition of diamond films.

Typically gas mixtures used to grow diamond involve gas mixtures of 1-5% CH_4 in H_2. Addition of other species such as argon, boron or oxygen can have a significant impact on the growth rate, quality and properties of the resulting diamond.

A combination of CRDS and OES have been applied to study H_2/CH_4/Ar gas mixtures within MWPE CVD reactors which contain high proportions of Ar (14.7% H_2/ 0.5% CH_4/ 86.8% Ar). Addition of high levels of Ar produced a plasma ball significantly larger than observed in previous work on 4.5% CH_4/ 88.5% H_2/ 7% Ar gas mixtures and greatly increased C_2(a) and CH(X) column densities were recorded. Modelling of such plasmas (Yuri Mankelevich, Moscow State University), in combination with the presented CRDS and OES experimental results, suggests that one of the main effects of Ar addition is the reduction in the overall power density within the reactor. This is a consequence of the reduced power absorption capacity of Ar compared to H_2 and the plasma must subsequently increase in volume to accommodate the same power. As a result of this expansion in volume the maximum T_{gas} is found to vary little as H_2 is progressively replaced by Ar.

CRDS has also been used to study the behaviour of B atoms within both B_2H_6/ H_2/ Ar and B_2H_6 /CH_4 /H_2/ Ar plasmas. B atoms were found to be widely distributed throughout the plasma volume in both cases, although the distribution contracted slightly on the addition of CH_4. Reactions between BH_x species and trace air impurities (predominantly O_2) were deduced to have a significant effect on measured B atom column densities. A number of methods for liberation of BH_x from species such as HBO were also explored using DFT, addition of these reactions to the plasma model provides a method to replicate the trends observed experimentally upon addition of small quantities CH_4.

CH_4/CO_2/H_2 plasmas have also been explored using a combination of OES and CRDS. OES was

used to profile and monitor trends in the emission of excited species within these plasmas. The trends observed were also compared with preliminary column density measurements of C_2(a, v=0) and CH(X, v=0) radicals by CRDS. Obtained emission and column density profiles under our base conditions, as well as changes in emission intensity and column density as the CH_4 to CO_2 ratio was varied, all showed good agreement between the two measurement techniques. However OES and CRDS trends started to show obvious differences when the H_2 flow rate, pressure or MW power were varied, suggesting that the processes governing the creation of ground and/or excited species are changing as these parameters are varied. OES results should therefore be treated with some caution as the trends they reveal may not necessarily reflect similar behaviour of the corresponding ground state species. Additional column density measurements of gas phase species such as H(n=2) atoms, OH and HCO radicals would allow for further experimental insight into the plasma chemistry. These would, however, also need to be combined with computational modelling of these plasmas to gain a more complete understanding of the prevailing chemistry.

In addition to the experimental investigations mentioned above a number of gas-surface and surface reactions were investigated using both QM and QM/MM computational techniques. Firstly, insertion reactions of C_xH_y radicals directly into C-H and C-C bonds on the diamond surface were investigated. Reactions of $^1CH_2$, ^2CH, C(^{3}P) and $^1C_2$ with surface C-H and C-C bonds were investigated and all the reactions were found to be exothermic. Insertion of these species into C-H bonds involved little to no activation barrier, insertion into C-C bonds, in contrast, was found to involve high energy barriers. The C-H insertion reactions are potentially important as they allow the investigated species to add directly to the $\approx$90% of the diamond surface that is terminated with H atoms, rather than the more traditional growth routes involving the ($\approx$10%) of surface radical sites. This increased ability to react with the surface may play a key role in the re-nucleation of diamond under certain plasma conditions (e.g. high Ar fraction).

Corresponding insertion reactions of B and BH atoms have also been investigated using QM and QM/MM techniques. Compared to the equivalent CH_x species, insertion of B(^{2}P) atoms and ^{1}BH radicals into C-H bonds were found to involve much higher energy barriers. Insertion into C-C bonds was again found to involve significant barriers. Insertion of B atoms and BH radicals directly into C-H bonds would provide an alternative route for the addition of boron to the growing diamond surface. Complementing the classic addition routes which rely on the presence of surface radical sites.

Other species such as O(^{1}D) are known to be able to insert directly into C-H bonds, but other species such as NH_x may also be able to participate in this type of reaction. Future computational investi-

gations of both oxygen and nitrogen containing gas phase species and the diamond surface therefore may be worth pursuing to gain a full understanding of the effects which are seen when oxygen and nitrogen are present within the gas-phase.

QM/MM calculations have also been applied to study the migration of CH_2 and BH groups on the $\{111\}$:H and between the $\{100\}$:H 2×1 and $\{111\}$ diamond surfaces. BH migration was also investigated on the $\{100\}$:H 2×1 surface. Migration of CH_2 was found to be relatively facile at the substrate temperatures typically involved in diamond CVD ($\approx$ 1000 K), apart from at a concave step edge with the dimer bonds aligned perpendicular to it. The deep energy well created at this site, by the formation of a bond between the migrating group and the adjacent surface, traps the group in place. This process of trapping at the step edge may well be important in the formation of stepped diamond surfaces and step-flow type growth. Migration of BH groups on and between the surfaces was found to involve much deeper energy minima than calculated for the equivalent CH_2 reactions, suggesting that surface BH groups are not as mobile as CH_2 groups. The ability of these groups to migrate on the surface of diamond may play an important role in governing the overall morphology of crystals grown. Migration of nitrogen or oxygen containing species on the diamond surfaces may also play a part in determining the overall morphology, and future analysis of possible species and their ability to migrate may allow for increased insight into why certain gas mixtures result in different crystal morphologies.

A

Important reactions in the Bristol-Moscow plasma model

Table A.1: Absorbed power densities and reaction rates for important plasma-chemical reactions in the central hot region of the plasma (r=0, z=10.5 mm) for a typical MCD plasma (4.4% CH_4/88.6% H_2/ 7% Ar, p=150 Torr, P=1.5 kW), table reproduced from Mankelevich *et al.* [1]

N	Process	Reaction rate constants (cm^{-3} s^{-1})	Fraction of total power density ($\approx$30 W cm^{-3}) (%)
1	$H_2(v=0)+e \rightarrow H_2(v=1)+e$	2.38×10^{20}	82.96
2	$H_2(v=1)+e \rightarrow H_2(v=0)+e$	4.90×10^{19}	17.02
3	$H_2(J)+e \leftrightarrow H_2(J+2)+e$	7.50×10^{20}	26.71
4	$H_2+e \leftrightarrow H_2+e$, elastic	1.41×10^{22}	5.14
5	$H_2(v=1)+H \rightarrow H_2(v=0)+H$	1.359×10^{23}	
6	$H_2(v=0)+H \rightarrow H_2(v=1)+H$	1.357×10^{23}	
		Dissociation	
7	$H_2+H_2 \rightarrow H+H+H_2$	1.57×10^{19}	
8	$H_2+e \rightarrow H+H+e$	6.02×10^{17}	1.62
9	$CH_4+e \rightarrow CH_3+H+e$	8.04×10^{13}	
10	$C_2H_2+e \rightarrow C_2H+H+e$	2.70×10^{16}	0.09
11	$C_2H+e \rightarrow C_2+H+e$	3.12×10^{14}	
		Ionization	
12	$Ar+e \rightarrow Ar^+ +e+e$	7.11×10^{12}	
13	$Ar^*+e \rightarrow Ar^+ +e+e$	1.10×10^{10}	
14	$H_2^*+e \rightarrow H_2^+ +e+e$	1.82×10^{11}	
15	$H+e \rightarrow H^+ +e+e$	1.60×10^{14}	0.001
16	$H_2+e \rightarrow H_2^+ +e+e$	2.12×10^{14}	0.002
17	$C_2H_2+e \rightarrow C_2H_2^+ +e+e$	1.09×10^{15}	0.008
18	$H(n=2)+H_2 \rightarrow H_3^+ +e$	1.02×10^{15}	
19	$H(n=2)+Ar \rightarrow ArH^+ +e$	3.07×10^{13}	
20	$H(n=3)+H_2 \rightarrow H_3^+ +e$	5.56×10^{13}	
21	$Ar^*+C_2H_2 \rightarrow Ar+C_2H_2^+ +e$	9.44×10^{12}	
22	$H_2^*+C_2H_2 \rightarrow H_2+C_2H_2^+ +e$	3.95×10^{13}	

Table A.1: (*continued*)

N	Process	Reaction rates (cm^{-3} s^{-1})	Fraction of total power density ($\approx$30 W cm^{-3}) (%)
		Recombination	
23	$H_3^+ + e \rightarrow H_2 + H(n=2)$	9.74×10^{11}	
24	$C_2H_2^+ + e \rightarrow C_2H + H$	9.84×10^{14}	
25	$C_2H_3^+ + e \rightarrow C_2H_2 + H$	1.16×10^{15}	
		Excitation/de-excitation	
26	$H_2 + e \rightarrow H_2^* + e$	3.40×10^{16}	0.22
27	$Ar + e \rightarrow Ar^* + e$	8.03×10^{14}	0.0053
28	$Ar + e \rightarrow Ar^{**} + e$	5.59×10^{14}	0.0038
29	$Ar^* + H \rightarrow Ar + H(n=2)$	7.92×10^{14}	
30	$Ar^{**} + H \rightarrow Ar + H(n=2)$	2.45×10^{14}	
31	$H(n=2) + e \rightarrow H(n=3) + e$	3.63×10^{11}	
32	$H(n=3) + e \rightarrow H(n=2) + e$	1.03×10^{11}	
33	$H + e \rightarrow H(n=2) + e$	4.25×10^{16}	0.245
34	$H(n=2) + e \rightarrow H + e$	7.37×10^{11}	
35	$H + e \rightarrow H(n=3) + e$	8.67×10^{14}	0.0055
36	$H(n=2) + H_2 \rightarrow H + H + H$	1.02×10^{15}	
37	$H(n=3) + H_2 \rightarrow H + H + H$	5.56×10^{13}	
		Radiation	
38	$H(n=3) \rightarrow H(n=2) + h\nu$	3.35×10^{14}	
39	$H(n=2) \rightarrow H(n=1) + h\nu$	4.18×10^{16}	
40	$H(n=3) \rightarrow H(n=1) + h\nu$	4.19×10^{14}	
41	$H_2^* \rightarrow H_2 + h\nu$	3.39×10^{16}	
42	$Ar^{**} \rightarrow Ar + h\nu$	3.13×10^{14}	
		Ion Chemistry	
43	$Ar^+ + H_2 \rightarrow ArH^+ + H$	6.36×10^{12}	
44	$Ar^+ + H_2 \rightarrow H_2^+ + Ar$	7.46×10^{11}	
45	$Ar^+ + C_2H_2 \rightarrow C_2H_2^+ + Ar$	1.36×10^{10}	
46	$ArH^+ + H_2 \rightarrow H_3^+ + Ar$	3.72×10^{14}	
47	$H^+ + C_2H_2 \rightarrow C_2H_2^+ + H$	1.60×10^{14}	
48	$H_2^+ + H_2 \rightarrow H_3^+ + H$	2.03×10^{14}	
49	$H_2^+ + Ar \rightarrow ArH^+ + H$	3.69×10^{12}	
50	$H_2^+ + C_2H_2 \rightarrow C_2H_2^+ + H_2$	3.14×10^{12}	
51	$H_2^+ + C_2H_2 \rightarrow C_2H_3^+ + H$	3.14×10^{12}	
52	$H_3^+ + Ar \rightarrow ArH^+ + H_2$	3.30×10^{14}	
53	$H_3^+ + C_2H_2 \rightarrow C_2H_3^+ + H_2$	1.48×10^{15}	

References

[1] Yu. A. Mankelevich, M. N. R. Ashfold, and J. Ma, *J. Appl. Phys.* **104**, 113304 (2008).

B

Constants for CRDS

Table B.1: List of transitions and their associated wave numbers, Einstein A coefficients, upper and lower state degeneracies and PGOPHER coefficients investigated using CRDS spectroscopy. C_2 and CH PGOPHER coefficients are from simulations using PGOPHER and the Einstein A coefficients are from Wills *et al.*[1] Constants relating to the H(n=2) transitions are from the NIST atomic spectra database.[2]

Species	Transition		$\bar{\nu}_{ij}$	A_{ij}	g_j	g_i	p
	Upper level	Lower level	(cm^{-1})	(s^{-1})			at 3000 K
C_2	$d^3\Pi_g$ (v' = 0)	$a^3\Pi_u$ (v"=0)					
	J' = 9	J" = 8	19422.97	7.21×10^6	6	6	0.002447757
	J' = 10	J" = 9	19424.12	7.21×10^6	6	6	0.002705416
	J' = 11	J" = 10	19425.42	7.21×10^6	6	6	0.002963075
	J' = 36	J" = 37	19426.39	7.21×10^6	6	6	0.003478392
CH	$A^2\Delta$ (v'=0)	$X^2\Pi$ (v"=0)					
	J' = 8.5	J" = 7.5	23422.980	1.85×10^6	4	4	0.004860101
			23424.885	1.85×10^6	4	4	0.009200721
	J' = 7.5	J" = 6.5	23426.994	1.85×10^6	4	4	0.004335854
	n=3	n=2					
H	$^2D_{\frac{3}{2}}$	$^2P_{\frac{1}{2}}$	15237.61	5.39×10^7	4	2	
	$^2P_{\frac{3}{2}}$	$^2S_{\frac{1}{2}}$	15237.57	2.25×10^7	4	2	
	$^2S_{\frac{1}{2}}$	$^2P_{\frac{1}{2}}$	15237.51	2.10×10^6	2	2	
	$^2P_{\frac{1}{2}}$	$^2S_{\frac{1}{2}}$	15237.46	2.45×10^7	2	2	
	$^2D_{\frac{5}{2}}$	$^2P_{\frac{3}{2}}$	15237.28	6.47×10^7	6	4	
	$^2D_{\frac{3}{2}}$	$^2P_{\frac{3}{2}}$	15237.24	1.08×10^7	4	4	
	$^2S_{\frac{3}{2}}$	$^2P_{\frac{1}{2}}$	15237.14	4.21×10^6	2	4	

References

[1] J. B. Wills, J. A. Smith, W. E. Boxford, J. M. F. Elks, M. N. R. Ashfold, and A. J. Orr-Ewing, *J. Appl. Phys.* **92**, 4213 (2002).

[2] Yu. Ralchenko, A. Kramida, J. Reader, and NIST ASD Team. (2011), Nist atomic spectra database (ver. 4.1.0), [online] http://physics.nist.gov/asd3, National Institute of Standards and Technology, Gaithersburg, MD, 2011.

C

Calculated rates of C(^{3}P) and CH($X^2\Pi$) insertion into C-H bonds.

Table C.1: Reaction rate coefficients of C(^{3}P) atoms inserting into C-H bonds, calculated from vibrational frequencies computed in the QM calculations using transition state theory.

T (K)	Rate coefficients (cm^3 s^{-1})
800	4.67×10^{-10}
900	6.04×10^{-10}
1000	7.60×10^{-10}
1100	9.34×10^{-10}
1200	1.13×10^{-9}
1300	1.34×10^{-9}
1400	1.56×10^{-9}
1500	1.80×10^{-9}
1600	2.07×10^{-9}

Table C.2: Reaction rate coefficients of CH($X^2\Pi$) radicals inserting into C-H bonds, calculated from vibrational frequencies computed in the QM calculations using transition state theory.

T (K)	Rate coefficients (cm^3 s^{-1})
800	1.85×10^{-9}
900	1.43×10^{-9}
1000	1.20×10^{-9}
1100	1.06×10^{-9}
1200	9.79×10^{-10}
1300	9.30×10^{-10}
1400	9.04×10^{-10}
1500	8.93×10^{-10}
1600	8.93×10^{-10}